

UNIVERSITY OF STRATHCLYDE

DEPARTMENT OF PHYSICS

**Optimisation of Proton Acceleration and
Synchrotron Radiation in Ultraintense
Laser-Solid Interactions**



by

Jack Goodman

in partial fulfilment of the requirements for the degree of
Doctor of Philosophy in Physics

2023

Copyright declaration

This thesis is the result of the author's original research. It has been composed by the author and has not been previously submitted for examination which has led to the award of a degree.

The copyright of the thesis belongs to the author under the terms of the United Kingdom Copyright Act as qualified by University of Strathclyde Regulation 3.50. Due acknowledgement must always be made of the use of any material contained in, or derived from, this thesis.

Signed:

Date:

Abstract

This thesis reports on numerical investigations of laser-solid interactions with peak laser intensities in the approximate range 10^{21} – 10^{24} W cm⁻², where few experiments have yet taken place. Higher laser intensities enable the production of higher energy radiation whilst altering the physics of the interaction. Here, the generation of protons and gamma rays is optimised for laser intensities in the given range, now becoming accessible with improved petawatt and multi-petawatt laser facilities, and the dynamics of the interactions are analysed.

The first investigation presented was centred on maximising the proton energies obtained with thin foil targets. The highest proton energies from CH targets are shown to occur when the foil becomes relativistically transparent as the peak of the temporal laser intensity profile reaches the target, for a wide range of laser intensities and both linear and circular laser light polarisation. The interaction dynamics are discussed, including the changes with earlier or later transparency times. Increased intensity of the laser pulse rising edge is demonstrated to increase the foil thickness which optimises the maximum proton energy, without significantly reducing the maximum proton energy. Finally, radiation reaction is shown to reduce the maximum proton energies from most targets by tens of percent.

The second investigation reported was principally the optimisation of the synchrotron gamma ray emission from foil targets. Bayesian optimisation (a machine learning approach) was applied to optimise various objective functions corresponding to the energy converted into synchrotron radiation, peak angle-resolved emission and number of photons in the high energy spectral tail. Several objectives were also combined and optimised together. The results show the synchrotron emission is generally maximised for oblique incidence with the highest on-target laser intensity. Simultaneous reduction of bremsstrahlung emission also demonstrated optimised results with

ultrathin targets. The role of the angle-of-incidence of the laser onto the target was explored, and 3D simulations enabled the additional role of the laser polarisation state to be determined. These results provide new understanding of gamma ray production in ultraintense laser-solid interactions, which could be used to improve the design of experiments and aid in the interpretation of experimental results.

Role of author

All of the particle-in-cell simulations reported on in this thesis were designed, performed and analysed by the author, with some assistance provided by M. King. The BISHOP code used to submit the simulations corresponding to the 2D parameter space scans and Bayesian optimisation runs in chapter 5 was developed by R. J. Gray and E. J. Dolier.

Publications

Publications reporting on the work presented in this thesis:

1. **Optimisation and control of synchrotron emission in ultraintense laser-solid interactions using machine learning.** **J. Goodman**, M. King, E. J. Dolier, R. Wilson, R. J. Gray, and P. McKenna, High Power Laser Science and Engineering **11**, e34 (2023).
2. **Optimisation of multi-petawatt laser-driven proton acceleration in the relativistic transparency regime.** **J. Goodman**, M. King, R. Wilson, R. J. Gray, and P. McKenna, New Journal of Physics **24**, 053016 (2022).

Additional publications where the author played a supporting role:

1. **Perspectives on laser-plasma physics in the relativistic transparency regime,** M. King, R. Wilson, E. F. J. Bacon, E. J. Dolier, T. P. Frazer, **J. Goodman**, R. J. Gray, and P. McKenna, The European Physical Journal A **59**, 132 (2023).
2. **Influence of target-rear-side short scale length density gradients on laser-driven proton acceleration,** A. Higginson, R. Wilson, **J. Goodman**, M. King, R. J. Dance, N. M. H. Butler, C. D. Armstrong, M. Notley, D. C. Carroll, Y. Fang, X. H. Yuan, D. Neely, R. J. Gray, and P. McKenna, Plasma Physics and Controlled Fusion **63**, 114001 (2021).

Contents

Copyright declaration	i
Abstract	ii
Role of author	iv
Publications	v
List of figures	x
1 Introduction	1
1.1 Thesis outline	7
2 Theory and background physics	8
2.1 Laser pulses	9
2.1.1 Gaussian laser beams	9
2.1.2 Polarisation	12
2.2 Single electron motion	13
2.2.1 Plane wave solutions	13
2.2.2 The ponderomotive force	15
2.3 Plasma formation and characteristics	17
2.3.1 Ionisation	17
2.3.2 Definition of a plasma	19
2.3.3 The Debye length	20
2.3.4 The plasma frequency	21
2.3.5 The propagation of light in plasma	22
2.3.6 Laser self-focussing	23

2.4	Laser absorption and fast electron generation	24
2.4.1	Inverse bremsstrahlung	25
2.4.2	Resonance absorption	25
2.4.3	Vacuum heating	26
2.4.4	$\mathbf{j} \times \mathbf{B}$ absorption	27
2.4.5	Other sources of absorption	27
2.4.6	Fast electron transport	28
2.5	Ion acceleration mechanisms	30
2.5.1	Target normal sheath acceleration	30
2.5.2	Radiation pressure acceleration	33
2.5.3	RSIT-enhanced acceleration	37
2.5.4	Other acceleration mechanisms in near critical density and relativistically transparent plasma	38
2.6	Radiation from accelerating charges	39
2.6.1	Bremsstrahlung	41
2.6.2	Classical synchrotron radiation	43
2.6.3	Quantum synchrotron radiation	45
2.6.4	Radiation reaction	48
2.7	Electron-positron pair production	50
3	Methodology	54
3.1	High power laser systems	55
3.1.1	Chirped pulse amplification (CPA)	55
3.1.2	Intensity contrast improvement	56
3.1.3	State of the art laser systems	59
3.2	High energy radiation detection	60
3.2.1	Detection materials	60
3.2.2	Diagnostics	63
3.3	Particle-in-cell modelling	66
3.3.1	Synchrotron radiation and pair production in EPOCH	68
3.3.2	Limitations and convergence	71
3.3.3	Convergence testing	72

4	Optimisation of multi-petawatt laser-driven proton acceleration with relativistic transparency	78
4.1	Introduction	79
4.2	Simulation parameters	80
4.2.1	General conditions	81
4.2.2	The laser pulse rising edge	81
4.2.3	3D	82
4.2.4	Transparency time	82
4.3	2D — linear polarisation	83
4.3.1	Interaction dynamics with relativistic transparency	83
4.3.2	Proton spectra — linear polarisation	86
4.3.3	Proton tracking — linear polarisation	89
4.4	2D — circular polarisation	92
4.4.1	Proton spectra — circular polarisation	94
4.4.2	Proton tracking — circular polarisation	97
4.5	3D — linear and circular polarisation	99
4.5.1	Proton tracking — 3D	101
4.6	2D — the laser pulse rising edge	103
4.6.1	Proton tracking — the laser pulse rising edge	104
4.7	2D — radiation reaction	106
4.7.1	Electron cooling	107
4.7.2	Proton acceleration with radiation reaction	108
4.8	Scaling with laser intensity	110
4.8.1	Maximum proton energy	110
4.8.2	Optimum target thickness	111
4.9	Summary	112
5	Bayesian optimisation and control of the angular distribution of synchrotron radiation in ultraintense laser-solid interactions	115
5.1	Introduction	116
5.2	Simulation parameters	120
5.3	2D Parameter space scans of gamma ray emission	122
5.3.1	Laser-injected synchrotron emission	124

5.3.2	Pulse duration, focal spot size and defocus	126
5.3.3	Stability	126
5.3.4	Scaling of the synchrotron conversion efficiency	127
5.3.5	Angle-of-incidence	129
5.3.6	Bremsstrahlung emission for varied laser intensity and target thickness	130
5.4	Application of Bayesian optimisation	132
5.4.1	Optimisation of individual synchrotron emission properties . . .	133
5.4.2	Mitigating bremsstrahlung emission	134
5.4.3	Maximum laser intensity	135
5.5	Optimisation in the highly radiative plasma regime	135
5.5.1	Angle-resolved synchrotron emission	136
5.5.2	Mitigating bremsstrahlung emission	138
5.6	Angle-of-incidence dependence of the forward synchrotron emission . . .	139
5.7	Spatial control of synchrotron emission in 3D	142
5.8	Summary	152
6	Conclusion	155
6.1	Proton acceleration	155
6.2	Synchrotron radiation	158
6.3	Final remarks	160
A	List of Acronyms	162
	Bibliography	163

List of Figures

2.1	Gaussian beam	10
2.2	Single electron motion in a linearly polarised plane wave	14
2.3	An illustration of the transverse ponderomotive force	16
2.4	Debye length	20
2.5	Plasma frequency and critical density	21
2.6	Diagrams of the conditions for resonance and vacuum absorption	26
2.7	Target normal sheath acceleration diagram	31
2.8	Radiation pressure acceleration diagrams	34
2.9	Field line diagram of radiation from an accelerating charge	40
2.10	Angular profile of synchrotron radiation	44
2.11	Electron quantum parameter	46
2.12	Quantum synchrotron function	48
3.1	Increase in peak laser intensity over the years	55
3.2	Yee staggered grid	67
3.3	Convergence testing the cell size for proton acceleration	72
3.4	Convergence testing the particles per cell for proton acceleration	73
3.5	Convergence testing of synchrotron and bremsstrahlung radiation in 2D	74
3.6	Convergence testing of synchrotron and bremsstrahlung radiation in 3D	76
4.1	Rising edge profile	82
4.2	2D simulation snapshot	84
4.3	Proton spectra for linear polarisation	87
4.4	Variation of maximum proton energies and conversion efficiency with transparency time for linear polarisation	88

4.5	Electron densities and electric fields with proton tracking for linear polarisation	89
4.6	Acceleration of tracked protons and local electron dynamics for linear polarisation	91
4.7	Proton spectra for circular polarisation	93
4.8	Variation of proton max energies and conversion efficiencies with transparency time for circular polarisation	95
4.9	Electron density and longitudinal field on axis with proton tracking for circular polarisation	97
4.10	Acceleration history of the highest energy protons for circular polarisation	98
4.11	Comparison between 2D and 3D simulations of transparency time and proton max energies	99
4.12	Proton spectra from 3D simulations	100
4.13	Electron density and longitudinal electric field evolution with proton tracking for 3D simulations	101
4.14	Electric field and kinetic energy evolution for the highest energy protons in 3D simulations	102
4.15	Maximum proton energies with and without laser pulse rising edge . . .	104
4.16	Electron density and longitudinal electric field evolution with and without laser pulse rising edge	105
4.17	Proton tracking results with and without laser pulse rising edge	106
4.18	Electron density evolution without and with radiation reaction	107
4.19	Electron energy spectra without and with radiation reaction	108
4.20	Proton acceleration results with radiation reaction	109
4.21	Proton spectra with radiation reaction	110
4.22	Intensity scaling of maximum proton energies and optimum target thickness	111
5.1	Illustration of the Bayesian optimisation loop, and 1D optimisation example	120
5.2	2D parameter scan results for synchrotron conversion efficiency	123
5.3	Scaling of synchrotron conversion efficiency with several laser parameters	128
5.4	Variation of synchrotron conversion efficiency with laser angle-of-incidence onto target	129

5.5	Bremsstrahlung emission	130
5.6	Synchrotron and bremsstrahlung radiation at found optima under weakly radiative conditions	134
5.7	Synchrotron and bremsstrahlung radiation at found optima under highly radiative conditions	137
5.8	Laser-electron interaction at different target angles	140
5.9	Peak angle-resolved synchrotron emission and conversion efficiency in 3D	143
5.10	Angle-resolved synchrotron emission in 3D at $I_L = 1.1 \times 10^{23} \text{ W cm}^{-2}$	146
5.11	Angle-resolved synchrotron emission in 3D at $I_L = 1.1 \times 10^{24} \text{ W cm}^{-2}$	148
5.12	Conversion efficiency to synchrotron radiation at $I_L = 1.1 \times 10^{24} \text{ W cm}^{-2}$	149
5.13	Snapshot of a 3D simulation for $I_L = 1.1 \times 10^{24} \text{ W cm}^{-2}$, p-polarisation and 45° laser incidence	151

CHAPTER 1

Introduction

Particle accelerators are essential in large areas of modern science, healthcare and industry. Many are used for direct applications of the particle source, such as ion implantation, radioisotope production, hadron therapy and the study of particle physics, where the latter uses colliding particle beams; whilst secondary sources of radiation from the accelerated particles are also widely used. For example, synchrotron light sources, such as the Diamond Light Source in the UK, use bending magnets or insertion devices (wigglers and undulators) to induce perpendicular acceleration of a GeV electron beam and cause the generation of one of the brightest sources of x-ray radiation currently possible in the laboratory for a range of applications [1]. Even brighter and shorter (femtosecond) duration x-ray beams are produced with x-ray free electron lasers [2, 3], using coherent radiation from electrons passing through an undulator.

For charged particles moving in a circular path in a particle accelerator, the energy losses due to synchrotron radiation—sometimes called magnetic bremsstrahlung, or nonlinear Thomson/Compton scattering for electrons interacting with intense laser pulses—limit the maximum particle energy. The radiated power, P , is given by the Larmor formula, and it can be shown that $P \propto K^4/m^4R^2$, where K is the kinetic energy, m the rest mass and R the radius of the particle's orbit. Circular accelerators are therefore much more efficient for the acceleration of protons than electrons, which radiate $(m_p/m_e)^4 \approx 10^{13}$ times more power at the same energy. Larger radii are needed to minimise the radiation losses and maximise the particle energy, which is why the largest particle accelerator ever built, the 27 km circumference Large Hadron Collider,

is also the highest energy particle accelerator ever built at 7 TeV for protons, and is the motivation for the larger still Future Circular Collider proposed, with 100 km circumference and expected proton energies of 50 TeV. Radiation losses can be avoided with the use of a linear particle accelerator, but the particles cannot make multiple passes within the accelerator and the length of the accelerator becomes the limiting factor: the maximum gradient of the acceleration structures can only reach as high as $\sim 100 \text{ MV m}^{-1}$ before breakdown occurs [4].

Here, ionised matter known as plasma offers an attractive alternative to radiofrequency cavities, due to the absence of a breakdown limit with increasing electric fields. The force of an intense laser pulse on plasma electrons can cause charge separation fields exceeding TV m^{-1} . Laser-driven plasma accelerators therefore have the potential to offer a much smaller alternative to conventional accelerators at reduced cost. Although, the space needed for the high power laser driver sets a lower limit to the size of these accelerators outside of the electric fields produced in the plasma. This typically corresponds to dimensions of tens of metres, but depends upon the laser technology used and energy of each pulse it produces. The maximum particle energies achievable with these plasma accelerators are limited by the acceleration length; the maximum energy achieved for electrons is 10 GeV [5] in 10 cm of a low density gas using wakefield acceleration [6], and the maximum energy demonstrated for protons is approximately 100 MeV [7] (potentially now 150 MeV [8]) over tens of microns using a combination of acceleration mechanisms in an ultrathin solid target. Naturally, work is underway to improve the acceleration gradient and length [9], and combine multiple plasma accelerating stages [10] for electron wakefield acceleration. However, for protons and ions, whilst there is some potential to use miniature structures to extend the acceleration [11], staging is expected to be inefficient. The reliance upon expansion of the plasma to drive the ion acceleration in most cases makes it difficult to extend the acceleration length, due to the associated reduction in the charged particle densities and electric field strength as the protons/ions accelerate. Thus, the focus of most research at present into laser-driven proton acceleration is the optimisation of a single micron-scale interaction, and the use of higher laser intensities to produce stronger accelerating fields. Although laser-driven proton acceleration is not expected to replace the technology used for state of the art proton colliders for particle physics, the MeV to potentially GeV energies achievable make these sources suitable for a large number of other applications.

The properties of proton beams from laser-solid interactions that set them apart from conventional accelerators include the ultrashort duration (as low as femtoseconds) at source, large number of particles per bunch (up to $\sim 10^{13}$), large energy spread (100%) and large divergence (tens of degrees). The interaction can also, with some simple modifications, be altered to produce fast electrons and bright x-ray (and other frequency) radiation. The multi-modal and principally ultrafast qualities of laser-driven particle accelerators using dense plasma are some of the core motivations for their continued development for applications.

One of the primary motivators for laser-driven ion sources continues to be hadron therapy [12–14]. Ions stopping in matter deliver a considerable fraction of their energy in the Bragg peak close to their stopping point. In radiotherapy, the damage to healthy tissue outside of the target volume is therefore reduced compared to the use of x-ray or electron radiation, reducing the harm to the patient and improving the efficacy of the treatment. Initially, laser-driven ion sources were viewed only as a potential lower cost and size alternative to conventional accelerators. Yet, in recent years the demonstration of reduced damage to tissue surrounding targeted tumours with ultrahigh dose rates in FLASH radiotherapy [15, 16] has provided an additional motivator for the development of laser-driven ion sources, which are capable of fulfilling the dose rate requirements. Although the maximum proton energies achieved are still below the 250 MeV required for treatment of deep-seated tumours, these sources are now being tested on tumours in mice [17] and a facility dedicated to investigation of the radiobiological effects is planned in the UK [18]. Laser-driven ion acceleration experiments on new and upgraded multi-PW facilities should produce protons and carbon ions with more than sufficient energy for deep-seated tumour irradiation, and should indicate the laser capabilities needed to fulfill these requirements. Whilst the high repetition rates becoming available with many new and upgraded laser facilities will enable larger numbers of data points to be obtained in experiments, and improve both the understanding of these ion sources and testing of their application in radiotherapy.

The localised energy deposition of protons and ions is also useful for isochoric heating to generate warm dense matter [19], and has potential use in fast ignition inertial confinement fusion (ICF) [20]. Delivering and harnessing net energy gain from nuclear fusion has long been a key goal of the scientific community. Nuclear fusion has the potential to provide an abundant and sustainable energy source independent of

weather and without long lived radioactive waste, yet high temperature plasma must be maintained at sufficient densities for long enough to release enough energy from the fuel (usually deuterium and tritium) to provide a net energy gain. One of the core approaches being investigated uses a high energy (MJ) laser system to directly illuminate a fuel pellet [21], compressing it to high enough densities and temperatures for the fuel to start burning and ignite, where the alpha particles released from fusion reactions create a self-sustaining burn wave that propagates out from the centre of the fuel capsule. Hydrodynamic instabilities, however, are a major issue, causing asymmetry in the implosion and mixing of outer higher Z layers into the fuel core, increasing the radiative energy losses. The effect of these instabilities, notably the Rayleigh-Taylor and Richtmeyer-Meshkov instabilities leading also to the Kelvin-Helmholtz instability, can be reduced with greater symmetry in the fuel capsule and implosion driver. X-rays from a laser-irradiated hohlraum surrounding the fuel capsule can have improved symmetry compared to direct laser drive [22]. This indirect drive approach has been the core focus of laser-driven fusion research at the National Ignition Facility (NIF) [23, 24], although hydrodynamic instabilities remain a key issue. The demonstration of ignition [25] and energy gain at NIF recently with indirect drive ICF has stimulated renewed interest in inertial fusion energy; private companies are actively developing fusion reactors based on inertial confinement and intense public research continues.

An alternative to achieving such high quality implosion requirements with the central hotspot ignition approach is to use fast ignition [26], in which a short pulse ($\lesssim 10$ ps) laser generates fast electrons or ions which propagate to the capsule core during the implosion where they deposit energy and ignite the fuel. For electron-driven fast ignition, transport of the divergent laser-produced fast electrons to the capsule core remains a fundamental challenge [27, 28]. Protons (or ions), however, can be focussed by accelerating them from a target with a curved rear surface, and their much higher mass reduces deflection in electric and magnetic fields before reaching the capsule core [29]. The use of a hollow cone can also protect the target from which the protons are accelerated, and the concomitant fast electron generation can induce electric fields within the cone that further focus the proton beam [29–31]. The ultrashort duration of laser-driven proton (and electron) sources and the ability to convert $\sim 10\%$ of the laser energy into fast protons (many times higher for electrons) makes them particularly useful for fast ignition, especially considering the proton focussing methods enabled with such

sources.

Other applications include deflectometry of the protons to measure the spatial and temporal evolution of rapidly varying electric and magnetic fields [32]. The protons are initially propagated through a mesh or other structure which attenuates the proton beam, leaving an imprint in its spatial profile that changes as the protons pass through the fields. The small source size and highly laminar qualities of laser-driven protons make them appropriate for imaging. The x-rays produced in the interaction are also useful for radiographic imaging [33]. The generation of large numbers of energetic (MeV) particles of different types and photons makes possible a range of studies on nuclear physics [34], and the high fluxes of radiation produced may be useful for testing the effects on materials planned to be used in harsh environments, such as in nuclear reactors.

In addition to the applications outlined above, laser-solid interactions also offer an opportunity to test and utilise a range of high field physics effects. Due to the increase in achievable laser intensities at experimental facilities over the years to now $\sim 10^{23} \text{ W cm}^{-2}$ [35], the synchrotron emission from electrons in laser-solid interactions may differ from classical expectations, and it is necessary to use quantum electrodynamics (QED) in modelling of the electron motion and radiation. Under these conditions, the synchrotron emission corresponds to nonlinear Compton scattering, and the accompanying radiation reaction (friction) force must be considered. The power of radiation emitted by highly relativistic electrons is sufficient to influence their individual motion, and therefore the plasma dynamics and particle and photon beams produced. Here, the field in the electron rest frame can approach the Schwinger field, $E_S \simeq 1.32 \times 10^{18} \text{ V m}^{-1}$. For such field strengths in vacuum, electron-positron pairs can be created and the electromagnetic field becomes nonlinear. Although the achievable laser intensities at present are well below the $10^{29} \text{ W cm}^{-2}$ required to reach E_S , the presence of relativistic particles and high energy photons makes possible a range of effects described by strong-field QED. These include nonlinear Breit-Wheeler pair production in addition to nonlinear Compton scattering and higher order processes [36]. Laser-plasma interactions therefore offer an opportunity to test theoretical descriptions of radiation reaction and strong-field QED. Collisions between a laser pulse and an well-defined electron beam (from laser wakefield acceleration, for example) may provide a better configuration for testing strong-field QED theories than laser-solid in-

teractions, where simultaneous plasma dynamics are less important and higher electron energies may be reached, yet the latter still offers the possibility of generating intense gamma ray sources and dense electron-positron pair plasmas. As laser intensities in the laboratory increase further, the increased fields are expected to cause a cascade of pair production and synchrotron emission that efficiently absorbs the electromagnetic field. The generation of pair-plasmas in the laboratory will enable experiments to study the physics occurring in astrophysical environments where similar pair-plasmas exist. Finally, the gamma ray and positron beams produced have the potential to be polarised, opening up a number of additional applications for their use.

The key challenges limiting the application of the radiation from laser-solid interactions include increasing the maximum energy and flux of the ion beams. The highest energies have typically been observed when using ultrathin foil targets. Therefore, a component of the research in this thesis was performed to improve the understanding of the acceleration process for the optimised conditions, and to investigate how this changes for the extreme laser intensities that have only just become experimentally attainable in recent years. Similarly, the use of x-rays and gamma-rays from these interactions for a range of applications could become attractive with increased brightness, increased energies and reduced divergence of the beams generated. Synchrotron radiation is expected to supersede bremsstrahlung radiation as the most efficient source of gamma rays in many interactions at the current upper limit of achievable laser intensities. This radiation may be produced with spectral brightness comparable to or greater than conventional synchrotron light sources but less than x-ray free electron lasers; at much higher photon energies corresponding to MeV rather than the keV photons produced from these other sources. Synchrotron radiation may enable the generation of dense electron-positron pair-plasmas and tests of strong-field QED in experiments, but the conditions where it is best produced need to be identified and better understood. As a result, the second component of the research in this thesis corresponds to an investigation of the optimum conditions for the generation of synchrotron radiation, employing machine learning with simulations of a range of conditions now becoming possible at experimental laser facilities.

1.1 Thesis outline

The optimisation of the radiation generation in laser-solid interactions is vital for the development of these sources for applications. Improving the understanding of the interactions is important to achieve this. In this thesis, the results of investigations of the dependence of maximum energy of protons on the onset of relativistic transparency, a key phenomenon in the interaction, and of the optimum conditions for the generation of high energy photons are shown. These results are useful for future experiments at state of the art high power laser facilities. The thesis is structured as follows:

- **Chapter 2:** The theory and background physics important for the discussions of high power laser-solid interactions in later chapters is presented. This includes electron motion in electromagnetic fields, plasma, ion acceleration and radiation.
- **Chapter 3:** The technology behind high power laser systems and experiments, including the detection of radiation, is described, in addition to the numerical methods used to obtain the results in this thesis.
- **Chapter 4:** This chapter presents a study on the effect of the onset time of relativistic transparency on maximum proton energy at intensities relevant to new multi-PW laser facilities.
- **Chapter 5:** Various properties of the synchrotron emission from laser-solid interactions are optimised in simulations with Gaussian process regression. The results inform further simulations which demonstrate control of the spatial profile of the gamma ray emission with laser polarisation and angle-of-incidence.
- **Chapter 6:** The new results reported in this thesis are summarised, and potential future work is discussed.

CHAPTER 2

Theory and background physics

This chapter provides a description of the physics relevant to high power laser-solid interactions. It begins with the mathematics for a Gaussian beam, and the motion of a single electron in response to a high intensity laser pulse. For the laser-plasma interactions in this thesis, the electron motion is essential to the acceleration of ions and generation of radiation. Initially, however, electrons generally must be freed from their bound atomic states. The possible ionisation processes are described, followed by an introduction to the key properties of the plasma state of matter that may subsequently form. The numerous processes that can cause partial absorption of a laser pulse in interaction with a plasma, vital for the transfer of energy into a particle beam or radiation, are then delineated. All of these elements form the prerequisite knowledge for understanding the ion acceleration mechanisms then detailed, and provide the context for the radiation processes later outlined—advancing the understanding of these topics within ultraintense laser-solid interactions is the core of this thesis. Finally, a brief description of possible processes for electron-positron pair production is given, due to the potential for generation of dense pair-plasmas in high field interactions.

Before considering all of the physics in this chapter, however, it is important to know that the interaction of an ultraintense laser pulse with a solid is dominated by the forces of the electric and magnetic fields, \mathbf{E} and \mathbf{B} , respectively, on the charged particles generated. Here, Maxwell's equations are fundamental: in vacuum,

$$\nabla \cdot \mathbf{E} = \rho/\varepsilon_0, \quad (2.1)$$

$$\nabla \cdot \mathbf{B} = 0, \quad (2.2)$$

$$\nabla \times \mathbf{E} = -\frac{\partial \mathbf{B}}{\partial t}, \quad (2.3)$$

$$\nabla \times \mathbf{B} = \mu_0 \mathbf{j} + \mu_0 \varepsilon_0 \frac{\partial \mathbf{E}}{\partial t}, \quad (2.4)$$

where ρ is the charge density, ε_0 is the permittivity of free space, μ_0 is the permeability of free space and \mathbf{j} is the current density.

2.1 Laser pulses

The development of high power lasers made possible the realisation of high intensity laser-plasma physics and, as a result, the laser-driven plasma accelerators upon which this thesis is based. The electromagnetic fields are sufficiently intense to ionise matter, accelerate electrons to relativistic velocities and cause the subsequent generation of TV m⁻¹ electrostatic fields. A mathematical description of high power laser pulses is essential for modelling and understanding the physical processes that occur. Laser pulses are electromagnetic waves, and have no charge or current density ($\rho, j = 0$). Therefore, Maxwell's equations shown above may be simplified, and the curl ($\nabla \times$) of equation 2.3 produces the wave equation:

$$\nabla^2 \mathbf{E} = \mu_0 \varepsilon_0 \frac{\partial^2 \mathbf{E}}{\partial t^2}, \quad (2.5)$$

where the electromagnetic wave propagates at speed $c = 1/\sqrt{\mu_0 \varepsilon_0}$.

2.1.1 Gaussian laser beams

Production of a high intensity ($> 10^{18}$ W cm⁻²) beam of light from a high power laser requires focussing of the laser pulse. Often close to the highest possible laser intensities are required for proton acceleration, and therefore Gaussian optics are commonly used to focus the typically 1 J–1 kJ of light into a near wavelength diameter focal spot. Assuming cylindrical coordinates and uniformity in the polar direction, the electric

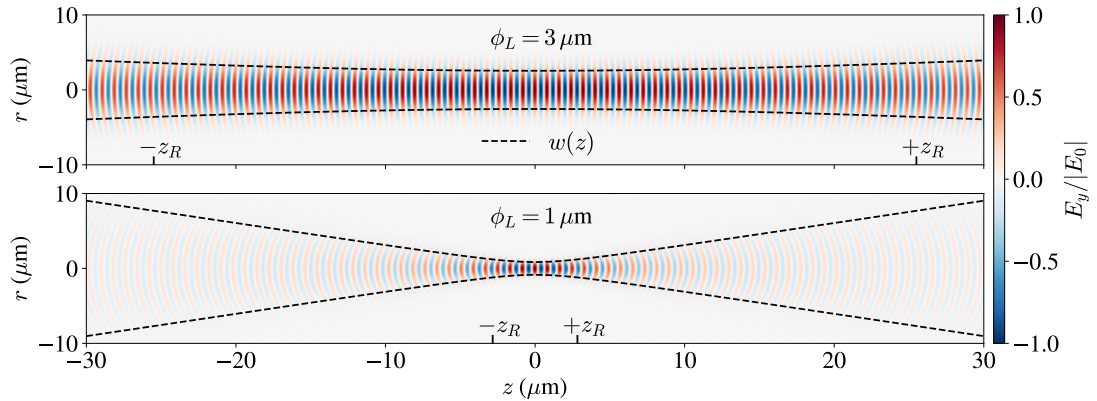


Figure 2.1: The transverse electric field component of a Gaussian beam with spot size $\phi_L = 3 \mu\text{m}$ (top panel) and $\phi_L = 1 \mu\text{m}$ (bottom panel), where $\lambda_L = 800 \text{ nm}$.

field of a Gaussian beam propagating along the z -axis can be written

$$\mathbf{E} = \mathbf{E}_0(r, z) \exp[i(kz - \omega t)], \quad (2.6)$$

where $\mathbf{E}_0(r, z)$ is the positional amplitude of the field and $k = 2\pi/\lambda$ is the wavenumber. Assuming the beam envelope varies slowly such that the paraxial approximation is valid, represented by the condition $|\partial^2 \mathbf{E}_0 / \partial z^2| \ll |k \partial \mathbf{E}_0 / \partial z|$, the electric field can be found by substitution of equation 2.6 into equation 2.5 to produce the paraxial approximation of the Helmholtz equation:

$$\left(\frac{\partial^2}{\partial r^2} + \frac{1}{r} \frac{\partial}{\partial r} + 2ik \frac{\partial}{\partial z} \right) \mathbf{E}_0 = 0. \quad (2.7)$$

This is valid for most practical conditions, although starts to become inaccurate for values of the beam waist at focus $w_0 \sim \lambda$ and smaller, where an accurate description of the fields has been provided by Quesnel *et al.* [37].

Assuming linear polarisation in a direction in the radial plane, the solution of equation 2.7 is

$$\mathbf{E}(r, z) = E_0 \frac{\omega_0}{\omega(z)} \exp \left[-\frac{r^2}{\omega(z)^2} + i \left(kz + \zeta(z) + \frac{kr^2}{2R(z)} \right) \right], \quad (2.8)$$

where E_0 is the amplitude of the electric field at focus ($z, r = 0$). This result is plotted in figure 2.1 for two different values of the full width at half maximum intensity at focus $\phi_L = \sqrt{2 \ln 2} w_0$. Here, $\omega(z) = \omega_0 \sqrt{1 + z^2/z_R^2}$ is the beam waist which expands away from focus, where $z_R = \pi \omega_0^2 / \lambda$ is the Rayleigh length; $R(z) = z(1 + z_R^2/z^2)$ is the

radius of curvature of the wavefronts; and $\zeta(z) = -\arctan(z/z_R)$ is the Guoy phase, which produces a phase shift of π from one side of focus to the other. Although for a fixed laser pulse energy higher intensities are reached with smaller focal spots, figure 2.1 shows that the longitudinal region in which the intensity remains close to its peak value ($|z| < z_R$) considerably reduces. The best focal spot size, and beam divergence, therefore depend upon the specific application. For laser-solid interactions, to accelerate ions or generate intense radiation, the interaction is generally limited to the surface of the target or volume of near critical density (see section 2.3.5; approximately 10^{27} electrons per m^3 for infrared light) plasma over a distance $\lesssim 10 \mu\text{m}$, and focal spots as small as $1 \mu\text{m}$ are useful. However, for laser wakefield acceleration of electrons with a gas target, continuous interaction over as large a distance as possible (typically $\sim 1 \text{cm}$) is required for maximising the electron energies, and therefore much larger focal spots corresponding to $\phi_L > 10 \mu\text{m}$ are generally used.

In experiments, the divergence of the beam and size of the focal spot are controlled primarily by varying the f-number $(f/\#) = f/D$ of the focussing optic, where f is the focal length and D the diameter of the beam. Smaller f-numbers decrease the minimum achievable beam radius. For a diffraction limited beam, $\omega_0 = 2(f/\#)\lambda/\pi$.

Real Gaussian laser pulses produced experimentally are, however, much more complex than the equations in this section show. For perfect focussing the spatial intensity distribution is an airy disk, that is only approximated by a Gaussian at its centre. Outside the central Gaussian peak, the wings of the airy disk and additional light, often produced due to aberrations in the beam, may contain a significant fraction of the laser pulse energy; this light has been shown to become important in laser-solid interactions when sufficiently intense [38]. The temporal profile also contains several components that can be sufficiently intense to ionise matter in addition to an approximately Gaussian peak. This light begins $\sim 1 \text{ns}$ before the fs-ps Gaussian main pulse and its intensity rises from a pedestal for many picoseconds before the main pulse arrives. The finite duration of the pulse causes a spectrum of frequencies, with width given by the time-bandwidth product $\tau_L \Delta\omega = 0.44$ when Fourier transform limited. The frequency of light within the spectrum is also dependent upon time if the temporal chirp is not zero, and either increases or decreases with time depending upon the sign of the chirp parameter.

2.1.2 Polarisation

The structure of the fields of the laser directly influences the response of electrons within them, and can produce vastly different results for different polarisation states. The electric field of an infinite plane wave propagating along the z -axis can be written

$$\mathbf{E} = [E_{0,x} \exp(i\phi_x) \hat{x} + E_{0,y} \exp(i\phi_y) \hat{y}] \exp[i(kz - \omega t)], \quad (2.9)$$

where $E_{0,x}$ and $E_{0,y}$ are the amplitudes of the orthogonal components of the field, and ϕ_x and ϕ_y are the phase offsets. The polarisation of the plane wave may fall into one of three categories:

- *Linear* - the electric field oscillates from positive to negative along a constant direction. This occurs when the components are in phase, $\phi_x - \phi_y = 0$, or if $E_{0,x}$ or $E_{0,y} = 0$.
- *Circular* - the amplitude of the electric field is constant, and its direction completes a full rotation in the xy plane every cycle. Here, $E_{0,x} = E_{0,y}$ and $|\phi_x - \phi_y| = \pi/2$.
- *Elliptical* - all other conditions.

Linear polarisation is the most frequently used in laser-solid interactions due to the greater electron heating it causes, and associated fast ion and radiation generation. The direction of the polarisation vector, however, influences the interaction. Considering a flat surface typical of most solid targets and the laser beam arriving at an oblique angle, if the polarisation vector is parallel with the target surface the laser is s-polarised, whereas if the polarisation vector is in the plane perpendicular to the target surface the laser is p-polarised. The latter case allows the laser electric field to produce forces normal to the surface on the target electrons, and can enhance the absorption of the laser pulse as outlined in section 2.4.

2.2 Single electron motion

A particle with charge q and instantaneous velocity \mathbf{v} moves in electromagnetic fields according to the Lorentz force:

$$\mathbf{F}_L = q(\mathbf{E} + \mathbf{v} \times \mathbf{B}). \quad (2.10)$$

2.2.1 Plane wave solutions

Consider a single electron in a linearly polarised infinite plane wave of the form:

$$\mathbf{E} = E_0 \cos(kx - \omega t) \hat{y}, \quad (2.11)$$

$$\mathbf{B} = B_0 \cos(kx - \omega t) \hat{z}. \quad (2.12)$$

Substitution of the above electric and magnetic fields into the Lorentz force equation, and using $B_0 = E_0/c$, produces the following equations of motion for an electron along each axis:

$$\frac{dp_x}{dt} = -\frac{ep_y E_0}{\gamma m_e c} \cos(kx - \omega t), \quad (2.13)$$

$$\frac{dp_y}{dt} = eE_0 \cos(kx - \omega t) \left(\frac{p_x}{\gamma m_e c} - 1 \right), \quad (2.14)$$

$$\frac{dp_z}{dt} = 0, \quad (2.15)$$

where $\mathbf{p} = (p_x, p_y, p_z)$ is the momentum, $\gamma = (1 - v^2/c^2)^{-1/2}$ the Lorentz factor and m_e the rest mass of an electron. If the electron is assumed to be non-relativistic ($v \ll c$), the force on the electron due to the electric field dominates, and the electron executes oscillations in the polarisation direction with velocity

$$v_y = \frac{eE_0}{m_e \omega} \sin(kx - \omega t). \quad (2.16)$$

It is obvious here that the electron motion must become relativistic for $eE_0/m_e \omega \sim c$ and greater. This threshold is commonly expressed in terms of the dimensionless vector potential

$$a_0 = \frac{eE_0}{m_e c \omega}, \quad (2.17)$$

where $a_0 \sim 1$ and higher corresponds to relativistic intensities. A convenient form of a_0 as a function of the cycle-averaged intensity and wavelength is

$$a_0 = \alpha \sqrt{\frac{I \lambda^2}{1.37 \times 10^{18} \text{ W cm}^{-2} \mu\text{m}^2}}, \quad (2.18)$$

where $\alpha = 1$ for linear polarisation and $\alpha = 1/\sqrt{2}$ for circular polarisation. A $1 \mu\text{m}$ wavelength laser produces relativistic electrodynamics for intensities greater than $10^{18} \text{ W cm}^{-2}$. For the motion of an initially stationary proton to become relativistic a factor of $(m_p/m_e)^2$ higher laser intensity is required, corresponding to more than $10^{24} \text{ W cm}^{-2}$.

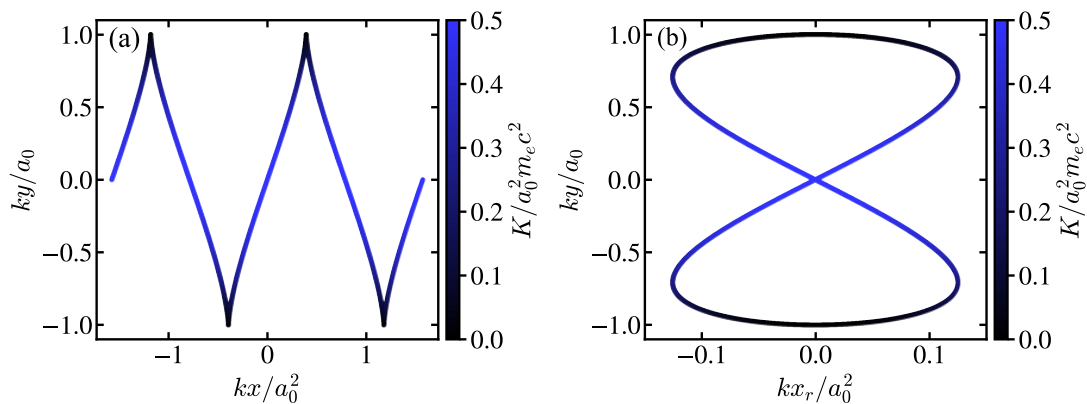


Figure 2.2: The relativistic motion of an electron in a linearly polarised plane wave, in (a) the laboratory frame and (b) the rest frame of the electron drift.

The relativistic motion of an electron can be readily solved by writing the electric and magnetic fields as functions of the vector potential \mathbf{A} , where $\mathbf{E} = -\partial\mathbf{A}/\partial t$ and $\mathbf{B} = \nabla \times \mathbf{A}$. The equations of motion may then be decoupled into components parallel and perpendicular with the laser propagation direction, and the constants of motion found as in the derivation by Gibbon [39], of which the solutions are shown below in dimensionless form. Firstly, for a laser beam propagating along the x -axis the vector potential is defined

$$\mathbf{A} = A_0 \left[\delta \cos \phi \hat{y} + (1 - \delta^2)^{1/2} \sin \phi \hat{z} \right], \quad (2.19)$$

where $\delta = 0$ or ± 1 linear polarisation, $\delta = \pm 1/\sqrt{2}$ for circular polarisation and $\phi =$

$\omega t - kx$ is the phase. For an electron initially at rest,

$$p_x = \frac{a_0^2}{4} \left[1 + (2\delta^2 - 1) \cos 2\phi \right], \quad (2.20)$$

$$p_y = \delta a_0 \cos \phi, \quad (2.21)$$

$$p_z = (1 - \delta^2)^{1/2} a_0 \sin \phi. \quad (2.22)$$

In equation 2.20, the electron is shown to oscillate at 2ω longitudinally for non-circular polarisation, and acquire a constant drift velocity $\beta_D = a_0^2/(a_0^2 + 4)$. Integration of the momentum equations produces the following equations for the electron position:

$$x = \frac{a_0^2}{4} \left[\phi + \frac{1}{2} (2\delta^2 - 1) \sin 2\phi \right], \quad (2.23)$$

$$y = \delta a_0 \sin \phi, \quad (2.24)$$

$$z = - (1 - \delta^2)^{1/2} a_0 \cos \phi. \quad (2.25)$$

These results are plotted in figure 2.2 for a plane wave polarised in the y direction. The electron propagates forwards, with the plane wave, whilst oscillating in the polarisation direction as shown in figure 2.2(a), and reaches a peak energy of $K = a_0^2 m_e c^2 / 2$. In the rest frame of the electron drift, shown in figure 2.2(b), the electron executes a figure-8 motion. The amplitude of the electron motion along y scales linearly with a_0 , and the motion along x increases with a_0^2 such that the motion appears the same as in figure 2.2 for any value of a_0 .

For a circularly polarised plane wave, the electron motion is helical with radius proportional to a_0 in the yz plane, and it rotates with frequency ω . The energy of the electron remains constant at $K = a_0^2 m_e c^2 / 4$.

2.2.2 The ponderomotive force

In the previous section, the motion of an electron in an infinite plane wave was detailed. However, the high power laser pulses employed experimentally in the interactions discussed in this thesis have intensity profiles that are approximately Gaussian in time and space. The electron motion can therefore differ strongly from the plane wave results even neglecting the electric and magnetic fields generated by the plasma in these interactions.

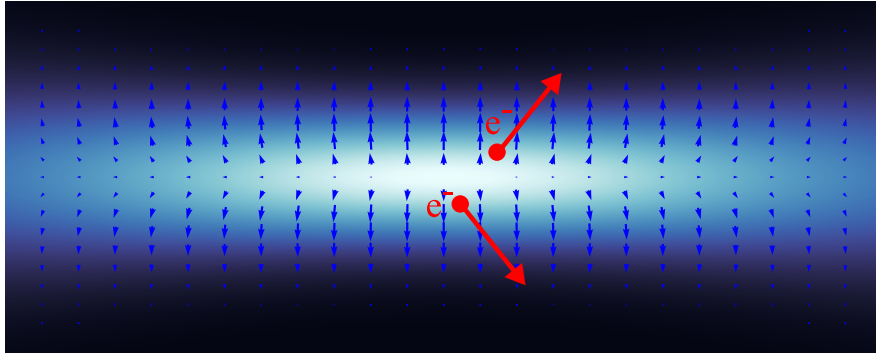


Figure 2.3: An illustration of the ejection of electrons accelerated in a Gaussian beam due to the ponderomotive force. The intensity envelope of a Gaussian beam is shown, and the direction of the ponderomotive force due to the intensity gradient.

An important consequence of the Gaussian spatial profile of the laser pulse is the ponderomotive force, \mathbf{F}_p , represented in figure 2.3, which acts to move electrons to areas of lower intensity. For a constant laser frequency and non-relativistic electrons,

$$\overline{\mathbf{F}}_p = -\frac{e^2}{2m_e\omega^2}\nabla\overline{\mathbf{E}^2}, \quad (2.26)$$

where the overline indicates averaging over the laser period. An electron in a Gaussian beam experiences a smaller restoring force from the laser electric field as it is accelerated away from the centre of focus, resulting in a drift of the electron out of the beam. The ponderomotive force increases with higher intensities and smaller beam waists.

For relativistic laser intensities, equation 2.26 is not valid. The relativistic ponderomotive force may be found by splitting the momentum into fast and slow components: $\mathbf{p} = \mathbf{p}_1 + \mathbf{p}_2$. Here, $\mathbf{p}_2 = \mathbf{A}$ is the fast oscillating component and \mathbf{p}_1 is the slow component, which is related to the ponderomotive force through $d\mathbf{p}_1/dt = \mathbf{F}_p$. The relativistic ponderomotive force averaged over the laser cycle is

$$\overline{\mathbf{F}}_p = -m_e c^2 \overline{\gamma}, \quad (2.27)$$

where $\overline{\gamma} = [1 + (p_1/m_e c)^2 + (e/m_e c)^2 \overline{A_y^2}]^{1/2}$.

The ponderomotive force will cause a nonrelativistic electron to exit a laser beam with a trajectory transverse to the laser propagation direction. The parallel momentum of the electron becomes important for relativistic motion, and the escape angle of the

electron is described by

$$\cos \theta = \sqrt{\frac{\gamma - 1}{\gamma + 1}}. \quad (2.28)$$

Electrons are ejected closer to the laser propagation direction for increasing values of γ .

2.3 Plasma formation and characteristics

2.3.1 Ionisation

Rapid ionisation occurs when matter is irradiated by a high intensity laser pulse, producing the charged particles that subsequently may be accelerated to high energies and also cause the generation of intense radiation. The most intense laser sources available are produced at infrared wavelengths of $\lambda_L \approx 1 \mu\text{m}$. Therefore, the energy of the corresponding photons is generally insufficient for single photon ionisation via the photoelectric effect, and a number of other processes are responsible for ionisation. These are either directly caused by light-matter interaction, or by collisions with accelerated particles.

Multi-photon ionisation

An electron within an atom may briefly absorb a photon with insufficient energy to cause ionisation, before re-emission of the photon a short time later. If many photons are incident upon the atom such that the rate of absorption exceeds the rate of photon re-emission, the electron may cumulatively acquire sufficient energy to escape its bound state. This multi-photon ionisation process leaves the free electron with energy

$$K_f = U_b + n\hbar\omega, \quad (2.29)$$

where $n > 1$ photons are absorbed and $U_b (< 0)$ is the binding energy of the electron. Should the electron absorb more photons and energy than required for ionisation, the excess energy may be converted into kinetic energy of the electron. This latter case corresponds to above threshold ionisation [40, 41], and produces an electron spectrum with peaks separated by the photon energy.

Tunnelling and barrier suppression ionisation

Although increasing the flux of photons may increase the probability of multi-photon and above threshold ionisation, the corresponding intensity of the laser light also increases linearly with the flux, and may become sufficiently intense to modify the electric potential around an atom. Self-generated fields within a plasma can also produce the same effect. A bound electron can therefore experience a reduced potential barrier to escape the atom. In the case of tunnelling ionisation, this increases the probability of the electron to quantum mechanically tunnel through the suppressed potential and escape. With a sufficiently intense laser field, barrier suppression ionisation can occur where the electron escape is facilitated by the complete removal of the barrier.

The laser intensity required to drive the latter process can be found by considering the total electric potential from both the atom and laser:

$$V(x) = -\frac{1}{4\pi\epsilon_0} \frac{Ze^2}{x} - eEx. \quad (2.30)$$

The potential barrier is maximised where $\partial V/\partial x = 0$, at $x_{max} = \sqrt{Ze/E}$. Equating $V(x_{max})$ to the ionisation potential U_b produces the following threshold for the laser intensity:

$$I_{app} \approx 4 \times 10^9 \left(\frac{E_i}{1 \text{ eV}} \right)^4 Z^2 \text{ W cm}^{-2}. \quad (2.31)$$

The appearance intensity for a hydrogen atom is $1.4 \times 10^{14} \text{ W cm}^{-2}$, a factor $\sim 10^{-4}$ of the relativistic electron motion threshold ($a_0 = 1$). Although low contrast ultraintense ($a_0 \gg 1$) laser pulses may enable such ionisation in the amplified spontaneous emission pedestal, such intensities are usually reached within the rising edge of a high contrast pulse picoseconds before the main pulse arrives. As a result, the main pulse usually interacts with pre-ionised matter. Nevertheless, with its arrival light atoms rapidly become fully ionised.

The Keldysh parameter

The Keldysh parameter [42] indicates which of the processes described above is dominant, and is defined as

$$\gamma_K = \sqrt{\frac{|U_b|}{2\phi_p}}, \quad (2.32)$$

where

$$\phi_p = \frac{e^2 E^2}{4m_e \omega^2} \quad (2.33)$$

is the nonrelativistic ponderomotive potential. For $\gamma_K > 1$, multi-photon ionisation dominates; and for $\gamma_K < 1$, where the ratio of the ponderomotive potential to the energy required to free the electron is higher, tunnelling and barrier suppression ionisation dominate.

Collisional ionisation

Free electrons accelerated by the laser, or other fields within a laser-irradiated target, can acquire energies much greater than the ionisation potential of the remaining bound electrons within the target. A collision between a sufficiently energetic free electron and a bound electron can transfer enough energy to the bound electron for it to escape its bound state. The rate of this collisional ionisation is therefore dependent upon the rate of collisions, which varies $\nu \propto n_e / (k_B T_e)^{3/2}$. Increasing the density of energetic electrons thus readily increases the collisional ionisation rate, yet acceleration of electrons to increasingly high energies with higher laser intensities may mitigate collisional ionisation due to the reduction with increasing electron temperature, and cause collisionless processes to increasingly dominate the ionisation. However, collisional ionisation may remain important in thick solid targets where the laser interaction and strongest electrostatic fields are limited to the target surfaces.

2.3.2 Definition of a plasma

The transfer of sufficient energy into a volume of matter can lead to ionisation and the generation of a state of matter beyond the gaseous state known as plasma. To be considered a plasma, an overall quasi-neutral ionised gas must fulfil several criteria defined with the distance beyond which the potential of a charge is shielded, known as the Debye length λ_D , and the relative frequency of different interactions. These are:

- The system has dimensions much larger than the Debye length: $L \gg \lambda_D$.
- The system contains many particles within a sphere with radius equal to the Debye length: $N_D = 4n_e \pi \lambda_D^3 / 3 \gg 1$.
- The frequency of electron plasma waves exceeds the frequency of collisions: $\omega_p \gg \omega_c$.

A plasma is characterised by collective behaviour, where the motion of charged particles is dominated by the electric and magnetic forces instead of collisions.

2.3.3 The Debye length

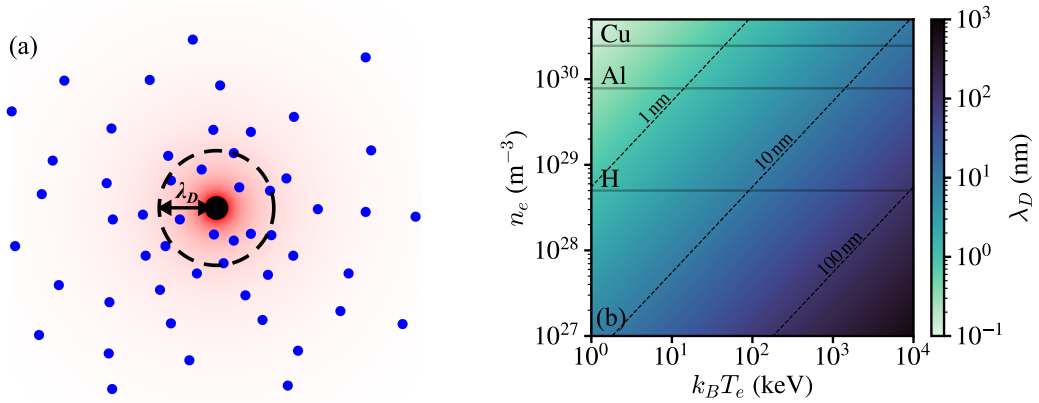


Figure 2.4: (a) An illustration of the shielding of the potential due to a charged particle over the debye length. (b) The debye length for plasma with a range of densities, close to the density of solids, and temperatures, with the density of several solid materials highlighted.

The Debye length, the characteristic distance required to shield the potential of a charge within a plasma, can be derived from the one-dimensional Poisson's equation:

$$\frac{d^2\phi}{dx^2} = \frac{e(n_e - Zn_i)}{\epsilon_0}. \quad (2.34)$$

The ions may be treated as static, $Zn_i = n_{e,0}$, and if the electrons are assumed to follow a Boltzmann distribution, $n_e = n_{e,0}\exp(e\phi/k_B T_e)$, where the potential is small, $e\phi \ll k_B T_e$,

$$\frac{d^2\phi}{dx^2} \approx \frac{n_{e,0}e^2\phi}{\epsilon_0 k_B T_e}. \quad (2.35)$$

The solution of this equation is $\phi = \phi_0 \exp(-|x|/\lambda_D)$, where we arrive at the Debye length

$$\lambda_D = \sqrt{\frac{\epsilon_0 k_B T_e}{n_{e,0} e^2}}. \quad (2.36)$$

This is plotted in figure 2.4(b) for different conditions; it is usually at the nanometre scale for solid density plasmas. Therefore, with dense solids the strongest electric fields are usually limited to the target surfaces. This will become important in section 2.5, where the acceleration of ions due to the surface fields is outlined. Although,

consideration of the Debye length is important in almost all laser-plasma interactions relevant to this thesis. For significantly expanded and heated solids, the Debye length can increase to > 100 nm and charges much further away can influence each other's motion. The small Debye length with dense solids also presents challenges for kinetic simulations, especially at low temperature.

2.3.4 The plasma frequency

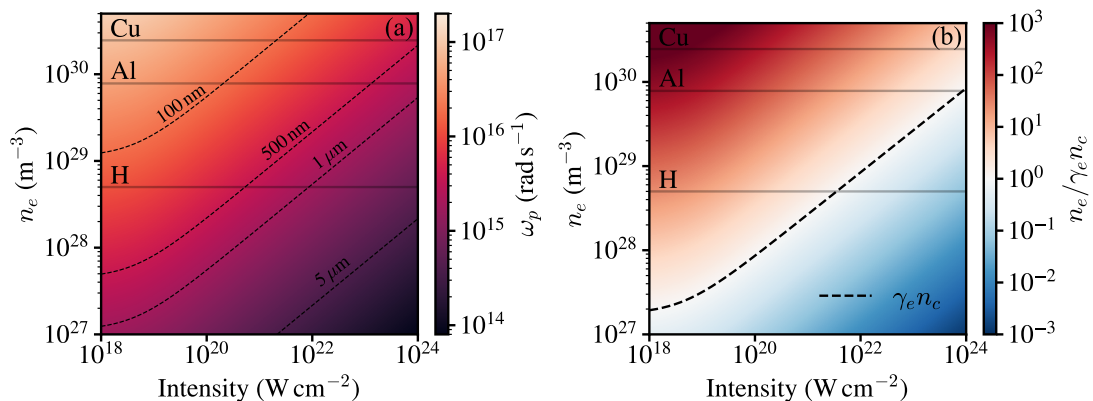


Figure 2.5: (a) The plasma frequency calculated for a range of densities and laser intensities, with contours of the equivalent wavelength. (b) The plasma density normalised by the relativistic critical density. The threshold for relativistic transparency with $\lambda_L = 800$ nm is shown by the $n_e = \gamma_e n_c$ contour. In both plots $\gamma_e = \sqrt{1 + a_0^2/2}$ has been assumed.

The much lower mass of an electron compared to an ion means that within a plasma the ions can often be treated as quasi-static, and the electrons respond to rapidly varying fields. Perturbations in the electron density, with a relatively immobile background of ions, produces electrostatic fields which accelerate electrons to restore equilibrium. In moving towards the equilibrium position the electrons overshoot, and so oscillations of the electron population are initiated. The frequency of such oscillations is the plasma frequency

$$\omega_p = \sqrt{\frac{n_e e^2}{\gamma_e m_e \epsilon_0}}, \quad (2.37)$$

which is shown in figure 2.5(a) for various densities and laser intensities assuming ponderomotive electron energies. The plasma frequency is important when considering the optical properties of a plasma.

The electromagnetic fields of a high intensity laser cause motion of the plasma electrons within them; solid density plasmas often have a plasma frequency much greater

than infrared laser frequencies (see figure 2.5(a)) and the electrons can move to restore equilibrium faster than the laser frequency, preventing its propagation. The relativistic mass increase of the electrons gives them greater inertia, slowing their response to non-equilibrium fields and reducing the plasma frequency. This effect is crucial to many high intensity laser-matter interactions and can enable the transmission of higher wavelengths of light. Higher energy photons corresponding to XUV, x-ray and gamma ray radiation can be much higher frequency than the plasma frequency in even a non-relativistic solid density plasma, and may be transmitted. However, collisions with atoms can absorb them, and become the dominant affect on their propagation. An exponential decay of x-ray radiation is expected with the Beer-Lambert law $I/I_0 = \exp(-\sigma\rho l)$, where σ is the absorption cross section, ρ the mass density and l the length of material propagated through.

2.3.5 The propagation of light in plasma

The dispersion relation of light with frequency ω in plasma is

$$\omega^2 = \omega_p^2 + k^2 c^2, \quad (2.38)$$

where ω_p is the plasma frequency defined above and k is the wavenumber. As a result, the group velocity and phase velocity are

$$\frac{\partial\omega}{\partial k} = c\sqrt{1 - \frac{\omega_p^2}{\omega^2}}, \quad \frac{\omega}{k} = \frac{c}{\sqrt{1 - \frac{\omega_p^2}{\omega^2}}}. \quad (2.39)$$

Here, $\eta = \sqrt{1 - \omega_p^2/\omega^2}$ is the refractive index of the plasma. The refractive index is only real for light with frequency $\omega > \omega_p$, and takes values $\eta < 1$. The group velocity of light in plasma is therefore slower than the speed of light in vacuum, c , and the phase velocity becomes greater than c . This enables various effects which shape a pulse of light as it propagates through plasma, such as self-focussing discussed in the next section, due to the variation of the local electron density and Lorentz factor.

The group and phase velocities become imaginary for $\omega < \omega_p$, and only incident radiation with frequency $\omega > \omega_p$ has real solutions to the above equations and can propagate through the plasma, whilst lower frequencies are evanescent and are typically reflected or absorbed at the plasma surface. This threshold can be restated, using

equation 2.37, in terms of a critical density below which light can propagate:

$$\gamma_e n_c = \frac{\gamma_e m_e \epsilon_0 \omega^2}{e^2} \approx 1.1 \times 10^{27} \gamma_e \left(\frac{1 \mu\text{m}}{\lambda} \right)^2 \text{ m}^{-3} \quad (2.40)$$

The refractive index may be expressed using this critical density as $\eta = \sqrt{1 - n_e/\gamma_e n_c}$.

A plasma with density $n_e < \gamma_e n_c$ is termed underdense, and a plasma with density $n_e > \gamma_e n_c$ is termed overdense. For an infrared laser pulse, $\lambda \approx 1 \mu\text{m}$, the classical critical density, n_c , is much lower than the density of most solids, and such a pulse can only propagate through solids that have been significantly pre-expanded or in which the electrons have been accelerated to sufficiently relativistic velocities. The transmission of light through a classically overdense plasma due to the relativistic motion of the electrons lowering the plasma frequency, such that the plasma is relativistically underdense, is known as *relativistic transparency*. This phenomenon is central to many of the interactions discussed later in this thesis. An overdense plasma may also transmit some light if its thickness is comparable or less than the skin depth, $l_s = c/\omega_p$, such that the evanescent wave remains significant at the rear side.

2.3.6 Laser self-focussing

A Gaussian beam may self-focus into a higher intensity and narrower beam if the refractive index η of the medium in which it propagates peaks in the centre of the beam; a refractive index that decreases radially produces a radially increasing phase velocity, causing the medium to act as a lens. Within a plasma the refractive index $\eta = \sqrt{1 - \omega_p^2/\omega^2} = \sqrt{1 - n_e/\gamma_e n_c}$ is dependent upon the laser frequency, electron density and electron Lorentz factor. A radially increasing electron density induced by, for example, the ponderomotive force may enable self-focussing. Although, relativistic self-focussing due to the maximisation of the electron energy and corresponding increase in the refractive index within the centre of the beam, where the intensity is highest, is often more important to consider.

In competition with self-focussing, a laser beam will naturally diffract as it propagates. For relativistic self-focussing to overcome diffraction a laser power exceeding [43, 44]

$$P_c = \frac{8\pi\epsilon_0 m_e^2 c^5 \omega^2}{e^2 \omega_p^2} \approx 17 \frac{\omega^2}{\omega_p^2} \text{ GW} \quad (2.41)$$

is required. This threshold may be exceeded by several orders of magnitude with

~ 100 TW to PW lasers in the underdense pre-plasma, generated at the surface of a solid target prior to the arrival of the main pulse. However, the degree of self-focussing depends upon the propagation length of the beam inside the underdense plasma, and the density of pre-plasma. For a short pre-plasma ($\sim 10 \mu\text{m}$), self-focussing can substantially increase the laser intensity that reaches the target surface and enhance the acceleration of protons [45]. However, for much longer pre-plasmas ($\sim 100 \mu\text{m}$) that may be produced under low laser contrast conditions, self-focussing may be followed by filamentation of the beam as it continues to propagate, and potentially reduced coupling of laser energy to protons [46]. Self-focussing can become important over distances of several microns in interactions with relativistically transparent ultrathin foils, that are the subject of this thesis, with enhanced proton acceleration demonstrated when the focussed intensity increases within the target [47]. Here, interference of the diffracted laser light as it propagates through the relativistic plasma aperture [48] can also lead to enhanced laser intensities [49], and light reflected from the target surface for oblique incidence may also contribute. Nevertheless, the high laser contrast required to avoid significant pre-expansion of ultrathin foils means that limited pre-plasma is created at the target surface, and almost no self-focussing of the laser pulse arriving on the target may occur.

2.4 Laser absorption and fast electron generation

A laser pulse interacting with a plasma may be absorbed through a number of different processes. These processes belong to one of two categories: collisional, in which laser photons are absorbed during the collision of particles, and collisionless, in which free electrons absorb energy from the laser. Which process dominates depends upon the irradiated material, laser intensity and other conditions of the interaction, yet for the high laser intensities used in this thesis, collisionless absorption (typically $\mathbf{j} \times \mathbf{B}$ outlined below) dominates.

Collisionless absorption of a laser pulse via electron motion generally relies upon the presence of a background plasma, to either reflect the laser light, allowing the electron to escape the laser fields during its oscillation with some energy, or produce electric or magnetic fields that influence the electron motion within the laser and enable net energy gain. The ponderomotive force introduced in section 2.2.2 also enables a single

charged particle in vacuum to escape the laser pulse with some of its energy, and in high intensity laser pulses, intense synchrotron radiation and nonlinear Breit-Wheeler pair production can cause the absorption of much of the laser energy (a description of each of these effects is given in sections 2.6 and 2.7 respectively).

2.4.1 Inverse bremsstrahlung

Inverse bremsstrahlung absorption is the only important process in high intensity laser-plasma interactions that is collisional. A free electron within the laser field collides with an ion and absorbs a photon. This mechanism is important up to laser intensities of $\sim 10^{15} \text{ W cm}^{-2}$, beyond which collisionless processes start to dominate, due to the electron-ion collision frequency scaling with $T_e^{-3/2}$ [50]. Therefore, for relativistically intense laser pulses this need only be considered during the components of the pulse far from the peak intensity. Inverse bremsstrahlung absorption may become important at the edges of the spatial profile of a high intensity laser pulse, outside of the central focal spot, yet for the laser intensities considered in this thesis (10^{20} – $10^{24} \text{ W cm}^{-2}$) the energy contained within such regions of the laser spatial profile near its temporal peak is negligible. Where it is important, however, is in the nanosecond to picosecond pedestal of such intense laser pulses. If sufficiently intense for inverse bremsstrahlung absorption to become important, foil targets can be considerably pre-heated and expand prior to the arrival of the main pulse, thus changing the main interaction. This is especially true for ultrathin foils as used in this thesis, which can expand to peak densities considerably less than solid density.

2.4.2 Resonance absorption

A laser pulse incident upon a plasma of increasing density at some angle θ to the density gradient is reflected at the point, if the plasma density gradient is parallel with x , the x -component of the wavevector $k_x = 0$. Assuming $k_z = 0$, $k_y = \omega \sin \theta / c$ and the dispersion relation in equation 2.38 at the point of reflection becomes $\omega^2 = \omega_p^2 / \cos^2 \theta$. The electron density at which the light is reflected is therefore $n_e = n_c \cos^2 \theta$. For a p-polarised laser pulse, the component of the laser electric field along the density gradient at the turning point excites plasma waves. The electrons experience an enhanced electric field near n_c , where plasma waves are resonantly excited, and absorb energy from the laser pulse as they propagate beyond this point where the electric field

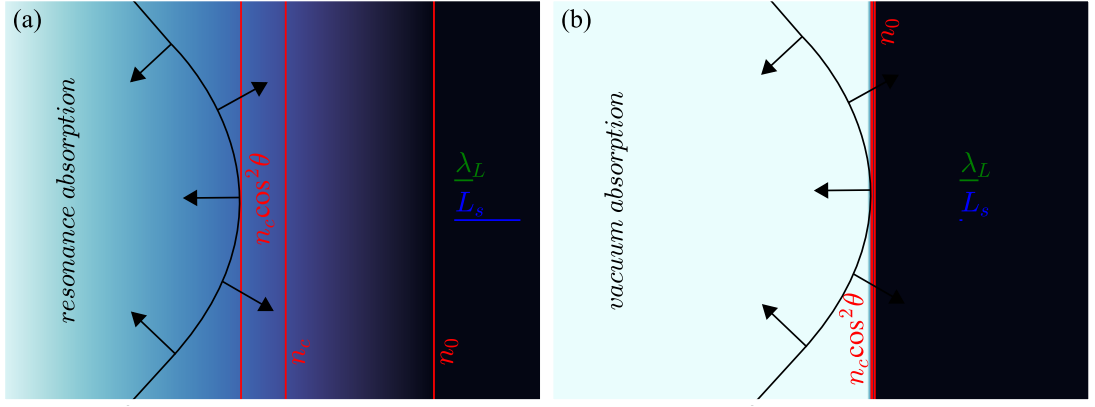


Figure 2.6: Diagrams of the conditions for (a) resonance and (b) vacuum absorption at the surface of a material with a density gradient given by the scale length L_s .

becomes evanescent. This resonance absorption mechanism [51] is important in interactions with solid targets in which the front surface is expanded to have a large density scale length L_s , where $n_e = n_{e,0}\exp(-|x|/L_s)$, and is depicted in figure 2.6(a). The polarisation vector for an s-polarised laser pulse remains parallel with the target surface upon reflection. Therefore, resonance absorption does not occur. For a circularly (or elliptically) polarised laser pulse, a component of the laser polarisation may be parallel to the density gradient upon reflection, and resonance absorption can occur, although may be less efficient than for p-polarisation. Both this resonance absorption and the following vacuum absorption mechanism are expected to be important up to laser intensities $\sim 10^{17} \text{ W cm}^{-2}$, above which relativistic absorption processes are expected to dominate.

2.4.3 Vacuum heating

For a similar set of conditions, shown in figure 2.6(b), to the previous absorption mechanism, the laser pulse may also be absorbed by vacuum (Brunel) heating [52, 53]. A p-polarised laser pulse obliquely incident upon a sharp-edged overdense target extracts electrons from the target surface due to the electric field component directed into the target. These electrons are accelerated in vacuum to roughly the quiver velocity v_{osc} before injection back into the target bulk as the laser electric field changes direction. The electrons propagate beyond the critical density surface where the laser restoring force is reduced, and thus absorb energy from the laser pulse. Both vacuum heating and resonance absorption inject energetic electrons into the target at the laser frequency ω .

Vacuum heating dominates resonance absorption for density scale lengths $L_s < v_{osc}/\omega$.

2.4.4 $\mathbf{j} \times \mathbf{B}$ absorption

If the laser pulse is sufficiently intense that $a_0 \gtrsim 1$, the relativistic electron motion within the laser field enables $\mathbf{j} \times \mathbf{B}$ absorption [54, 55] to become important. This absorption process takes its name from the oscillating magnetic component of the Lorentz force that causes energy to be taken from the laser pulse by plasma electrons; it is expected to dominate for most of the interactions discussed in this thesis, that take place well above the relativistic intensity threshold.

Consider the nonrelativistic form of the ponderomotive force exerted by a laser electromagnetic field with ellipticity ϵ ($0 \leq \epsilon \leq 1$) on an electron along the axis of laser propagation:

$$F_x = -\frac{m_e}{4} \frac{\partial v_L(x)^2}{\partial x} \left(1 - \frac{1 - \epsilon^2}{1 + \epsilon^2} \cos 2\omega t \right), \quad (2.42)$$

where $v_L = eE/m_e\omega$. The first term in the parentheses in this equation produces a drift towards regions of lower intensity. The latter oscillatory term, due to $\mathbf{v} \times \mathbf{B}$ in the Lorentz force, produces oscillations in the electron motion at a frequency of 2ω . The acceleration of electrons close to the plasma surface and injection into the target bulk beyond the critical density surface, in a similar manner to the prior collisionless mechanisms but at twice the frequency, causes laser energy absorption.

If the laser light is linearly polarised ($\epsilon = 0$), the amplitude of the oscillatory component of the force in equation 2.42 is maximised. The amplitude decreases for increasing ellipticity of the laser light polarisation, until it vanishes for circular polarisation ($\epsilon = 1$). For circularly polarised laser light incident onto a flat surface, $\mathbf{j} \times \mathbf{B}$ absorption can only occur when the angle-of-incidence is oblique; however, surface deformation, due to the laser radiation pressure for example, may enable $\mathbf{j} \times \mathbf{B}$ absorption for normal incidence.

2.4.5 Other sources of absorption

The collisionless absorption mechanisms described above rely upon electrons crossing the critical density surface where the laser is reflected. If the radiation pressure is sufficiently high, the reflection of the laser pulse may cause the critical density surface to move forwards with the pulse and transfer energy to the ions as detailed in section

2.5.2. This process becomes more efficient the faster the reflective surface moves with the laser pulse, and therefore generally becomes increasingly important for higher laser intensities.

If the laser pulse impinges on a relativistically transparent target, all of the laser energy may not pass through the target and a large fraction of it can in fact be absorbed. If the target is a thin initially overdense solid that becomes relativistically transparent during its interaction with the laser pulse, only the plasma within the centre of the laser beam may be underdense, and at the edges the plasma may be overdense such that the laser pulse propagates through a relativistic plasma aperture [48]. In this case, the collisionless absorption mechanisms detailed above can occur where the laser interacts with regions of overdense plasma. The ponderomotive force introduced in section 2.2.2 will also eject electrons from the laser beam within the transparent plasma and cause absorption without the electrons having to necessarily cross a surface which reflects the laser light. Furthermore, *direct laser acceleration* may occur when electric or magnetic fields generated in the interaction interfere with the plane wave model of the electron motion in the laser, leading to net energy gain of the particles from the fields and potentially the acceleration of electrons to superponderomotive energies [56]. The case of propagation of a laser pulse through a relativistically underdense channel is well known to improve the acceleration of electrons [57, 58], due to the generation of quasi-static longitudinal and transverse electric fields [58].

2.4.6 Fast electron transport

The fast electrons injected into a solid target by the mechanisms described above can produce a mega-ampere current in a typical interaction. To demonstrate this, consider that a typical laser pulse from a Ti:Sapphire laser system may contain tens of joules in a pulse with duration $\tau_L \sim 30$ fs. A realistic absorption of only 5 J of laser energy (see [59], for example) into an electron population with temperature 5 MeV (corresponding to intensity $a_0 \sim 10$ assuming ponderomotive temperatures) corresponds to 6×10^{12} electrons, and an approximate current of $i \sim 30$ MA. However, the self-induced magnetic field of such a current would be sufficient to turn the electrons back into the reverse direction. Alfvén [60] showed that for a uniform, cylindrically symmetric and

monoenergetic beam of charged particles, a current exceeding

$$i_A = \frac{\beta\gamma m_e c^3}{e} \approx \beta\gamma \times 17 \text{ kA} \quad (2.43)$$

induces a magnetic field that turns particles back towards the source. For a mega-ampere current of fast electrons to propagate through a solid, the space-charge fields induced by the loss of electrons where the current is drawn produce a localised return current in the opposite direction [61]. This contains many more electrons that are less energetic. The net current density is often written

$$\mathbf{j} = \mathbf{j}_f + \mathbf{j}_r \approx 0, \quad (2.44)$$

yet the currents may not exactly balance.

The remaining net current can be strong enough to lead to the generation of significant magnetic fields, which can be described by [62]

$$\frac{\partial \mathbf{B}}{\partial t} = \eta_j (\nabla \times \mathbf{j}_f) + \nabla \eta_j \times \mathbf{j}_f, \quad (2.45)$$

where η_j is the resistivity. Equation 2.45 contains two terms on the right-hand side for magnetic field growth. The first depends on spatial gradients in the fast electron current density and can lead to pinching of the fast electron beam [63]. The second depends on gradients of resistivity, where the fast electrons are forced towards higher resistivity regions. The higher temperature of the plasma within the centre of the electron beam can lead to a lower resistivity in the centre of the beam that increases outwards, depending on the material. The result of this is a magnetic field that causes hollowing of the fast electron beam [64–66].

When the fast electrons reach the rear surface of the solid foil target some may escape leaving the target positively charged, and generating a sheath electric field at the rear surface that accelerates ions. The fast electrons that do not escape may instead be reflected back into the target by the sheath field and the lack of a return current upon reaching the edge of the target. Refluxing can then occur where the formation of a front surface sheath field can trap electrons inside the target as they reflect from both surfaces. The fast electron beam generally has a full angle of divergence $\theta_e > 20^\circ$ [67], and the refluxing fast electrons may spread transversely within the target with

increasing reflections.

2.5 Ion acceleration mechanisms

Direct acceleration of initially stationary ions by the Lorentz force of a laser pulse is important only for intensities $\gtrsim 5 \times 10^{24} \text{ W cm}^{-2}$, which are not at present available at high power laser facilities and are not reached within the studies reported in this thesis. It is therefore the motion of the electrons in response to the laser fields that commonly leads to the acceleration of ions within ultraintense laser-plasma interactions. The resulting imbalance of charge produces electric fields of $\sim \text{MV } \mu\text{m}^{-1}$ within regions of the plasma and accelerates ions to MeV energies. The higher charge-to-mass ratio of protons causes them to often gain the highest energy per nucleon of the accelerated ions, and their preferential acceleration has led to them being the focus of many investigations.

There are many potential ion acceleration mechanisms that describe the specific evolution of the plasma in a given interaction. Although, these mechanisms do not necessarily occur independently. In many cases the ions experience a combination of mechanisms over the duration of the interaction. Here, a description is provided of each of these potential mechanisms, starting with the two most common and well understood.

2.5.1 Target normal sheath acceleration

In target normal sheath acceleration (TNSA) [68], the fast electrons produced by $\mathbf{j} \times \mathbf{B}$ absorption and other mechanisms where the laser impinges on the surface of a solid may continue to propagate and escape through the rear surface. This loss of charge at the rear surface generates a sheath electric field normal to the rear surface, as depicted in figure 2.7, sufficient to ionise atoms and accelerate ions. The surfaces of solid targets usually have a nanometre thick layer of hydrocarbon contaminants, and this commonly results in the acceleration of protons from the ionisation of hydrogen atoms by the sheath electric field at the target surfaces [68–70].

A plasma expansion model of TNSA was provided by Mora [71]. In this 1D fluid model, the plasma is considered isothermal and collisionless. There is only one ion species that is initially cold and at rest, and has density $n_i = n_{i0}$ for $x < 0$ and $n_i = 0$ for $x > 0$. The electrons have a constant temperature, and their density is described

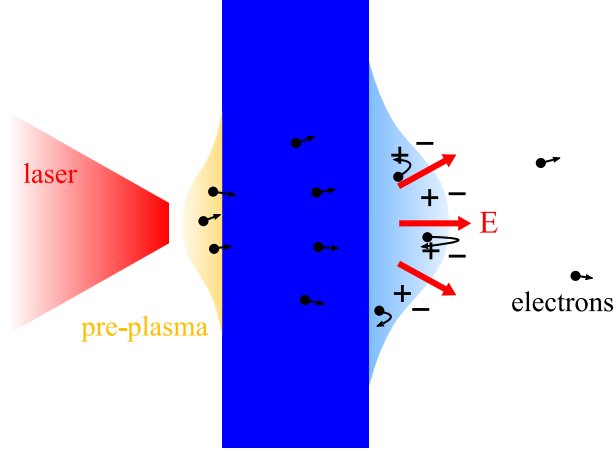


Figure 2.7: A diagram of target normal sheath acceleration showing the electrons accelerated at the target front surface by the laser pulse propagate to the rear side, where they cause the acceleration of ions (light blue) via the charge imbalance induced electric field as they escape the target or reflect close to its edge.

by the Boltzmann distribution $n_e = n_{e0} \exp(e\Phi/k_B T_e)$, where $n_{e0} = Zn_{i0}$ and Φ is the electrostatic potential given by the Poisson equation $\partial^2 \Phi / \partial x^2 = e(n_e - Zn_i) / \epsilon_0$. The details of the derivations can be found in [71]. Here, several important results are presented. The electric field at the ion front is given by

$$E_{front} = \frac{2E_0}{\sqrt{2 \exp(1) + \omega_{pi}^2 t^2}}, \quad (2.46)$$

where $E_0 = \sqrt{n_{e0} k_B T_e / \epsilon_0}$ and $\omega_{pi} = \sqrt{Z n_{e0} e^2 / m_i \epsilon_0}$ is the ion plasma frequency. The velocity of the ion front is

$$v_{front} = 2c_s \ln(\tau + \sqrt{\tau^2 + 1}), \quad (2.47)$$

where $c_s = \sqrt{Z k_B T_e / m_i}$ is the ion acoustic velocity and $\tau = \omega_{pi} t / \sqrt{2 \exp(1)}$. The energy spectrum of the ions is

$$\frac{dN}{dK} = \frac{n_{i0} c_s t}{\sqrt{2K K_0}} \exp\left(-\sqrt{\frac{2K}{K_0}}\right), \quad (2.48)$$

where $K_0 = Z k_B T_e$. Finally, the maximum ion energy is

$$K_{max} = 2K_0 (\ln[2\tau])^2. \quad (2.49)$$

One of the issues with this model is the ions continue to gain energy indefinitely, and a stopping time (usually the laser pulse duration) has to be chosen for its application. An adiabatic model for thin foils was later developed by Mora [72] to address this problem.

Schreiber *et al.* [73] instead modelled the energy gain of ions due to a radially confined surface charge produced by fast electrons at the target rear side. In their quasi-static model, the laser accelerated electrons spread over a circular area with radius

$$r_0 = r_L + l \tan \theta_{1/2} \quad (2.50)$$

at the target rear side, where r_L is the radius of the laser focal spot, l is the target thickness and $\theta_{1/2}$ is the half-angle of the electron propagation through the target. The electrons have the Boltzmann distribution $dN/dK = (N_e/k_B T_e) \exp(-K/k_B T_e)$, where N_e is the total electron number.

When the electrons exit the target rear side into vacuum, a positive charge Qe is left on the rear surface. Solving the Poisson equation for a charge density $Qe/\pi r_0^2$ at $z = 0$ yields

$$-e\Phi(\xi) = K_\infty s(\xi), \quad (2.51)$$

where $\xi = z/r_0$, $E_\infty = Qe^2/2\pi\epsilon_0 r_0$ and $s(\xi) = 1 + \xi - \sqrt{1 + \xi^2}$. Therefore, the energy an ion with charge q_i initially at $z = 0$ can gain is given by $K_i(\xi) = -q_i e\Phi(\xi) = K_{i,\infty} s(\xi)$, where $K_{i,\infty} = q_i k_B T_e r_0 / \lambda_D$. Here, $\lambda_D = \sqrt{2\epsilon_0 k_B T_e / n_{Q0} e^2}$ and n_{Q0} is the electron density at the surface. For a laser power P_L and conversion efficiency η from laser to hot electron energy, it can be derived that

$$K_{i,\infty} = 2q_i m_e c^2 \sqrt{\eta \frac{P_L}{P_R}}, \quad (2.52)$$

where $P_R = m_e c^3 / r_e$, and $r_e = e^2 / 4\pi\epsilon_0 m_e c^2$ is the classical electron radius. The conversion efficiency may be found using the scaling $\eta = 1.2 \times 10^{-15} I_L^{3/4}$ up to $\eta = 0.5$, where I_L is in units of W cm^{-2} . Finally, integration of $d\xi/dt = v(\xi)/r_0$ provides

$$\frac{\tau_L}{\tau_0} = X \left(1 + \frac{1}{2(1-X^2)} \right) + \frac{1}{4} \ln \left(\frac{1+X}{1-X} \right), \quad (2.53)$$

where $\tau_0 = r_0/v(\infty) = r_0/\sqrt{2K_{i,\infty}/m_i}$, $X = \sqrt{K_m/K_{i,\infty}}$ and K_m is the maximum ion

energy. Here, K_m can be approximated as follows [74]:

$$K_m = K_{i,\infty} \tanh^2 \left(\frac{\tau_L}{2\tau_0} \right). \quad (2.54)$$

Many other models of TNSA have been proposed [75–77], where the plasma is treated as either a fluid expanding into vacuum or the ions are accelerated in a static field. Although theoretical models can explain some experimental data, the many assumptions made in their derivation and the many unknown parameters in experiments prevent their use for accurate predictions. Empirical scalings derived from experiments provide an alternative estimate of ion energies. The quantity of data from experiments required to develop accurate scalings of the many available parameters has been limited, due to the low repetition rate of many high power laser systems used over the past few decades. However, the large number of experimental results reported to date has enabled the derivation of increasingly comprehensive scalings of the maximum proton energies [74, 78–81].

The ion (and proton) beams produced by TNSA have a characteristically broad energy spectrum with typically an exponentially decreasing number of ions for increasing ion energy. Protons with energies up to tens of MeV are routinely produced on many current high power laser systems, and the highest proton energy attributed to TNSA demonstrated is 85 MeV at present [82]. Approximately 10^{12} protons with MeV energies are generated during the interaction, and the laser-to-proton energy conversion efficiency may reach as high as 15% [83]. The divergence of the ion beams is usually tens of degrees, where the highest energy ions are in the centre of the beam. The transverse emittance is typically 10^{-1} – 10^{-3} mm mrad, and the highest energy protons are generated from an area of the order of the laser focal spot size [84, 85].

2.5.2 Radiation pressure acceleration

The momentum carried by an electromagnetic wave may be transferred to an object upon reflection or absorption of the wave. For light with intensity I incident normal to a surface, this is equivalent to the radiation pressure

$$P_{rad} = (2R + A) \frac{I}{c} = (1 + R - T) \frac{I}{c}, \quad (2.55)$$

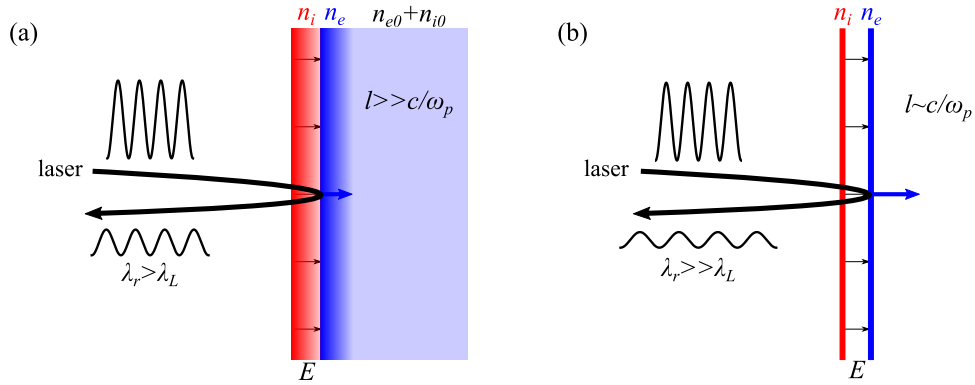


Figure 2.8: Diagrams showing radiation pressure acceleration in the case of (a) hole boring and (b) light sail. The laser pulse is reflected with a wavelength greater than the incident wavelength, thus transferring energy and momentum to the plasma.

where R , T and A are the coefficients of reflection, transmission and absorption, respectively, and $R + T + A = 1$. In high power laser solid interactions, the displacement of electrons at the irradiated surface by radiation pressure can produce space-charge electric fields and accelerate ions at the front surface. The dynamics of this radiation pressure acceleration (RPA) are influenced by the thickness of the solid irradiated. For targets much thicker than the laser skin depth, a laser snowplough through the target generally known as *hole boring* [86, 87] ensues; and for target thicknesses comparable to or less than the laser skin depth, the whole target within the laser focal spot may be simultaneously moved due to *light sail* acceleration [88, 89]. These limits of RPA are shown in figure 2.8.

During hole boring, the ions are reflected from the propagating electrostatic field induced by the laser reflection. The velocity can be derived by first equating the incident light pressure with the momentum flux of the mass flow, in the rest frame of the hole boring front [86, 87],

$$\frac{2I}{c} = 2m_i n_i v_{hb}^2. \quad (2.56)$$

Rearrangement of this equation provides

$$v_{hb} = \sqrt{\frac{I}{m_i n_i c}} = ca_0 \sqrt{\frac{n_c Z m_e}{2n_e A m_p}}, \quad (2.57)$$

where the latter form shown is valid only for linearly polarised light. The ions are reflected from the incoming hole boring front with velocity $v_i = 2v_{hb}$ and energy $K_i = 2m_i v_{hb}^2$.

In the relativistic limit, the Doppler shift causes the radiation frequency in the rest frame of a moving surface to become $\omega' = \omega\sqrt{(1 - \beta)/(1 + \beta)}$. As a result, with conservation of the number of photons, the intensity in the instantaneous rest frame is $I' = I(1 - \beta)/(1 + \beta)$. Therefore, the relativistically correct version of equation 2.56 is [87]

$$\frac{2I(1 - \beta_{hb})}{c(1 + \beta_{hb})} = 2\gamma_{hb}^2 m_i n_i v_{hb}^2. \quad (2.58)$$

Solving this equation produces the relativistically correct hole boring velocity:

$$v_{hb} = c \frac{\sqrt{\Xi}}{1 + \sqrt{\Xi}}, \quad (2.59)$$

where $\Xi = I/m_i n_i c^3$. Finally, a Lorentz transform into the laboratory frame gives the relativistic ion energy as

$$K_i = m_i c^2 \frac{2\Xi}{1 + 2\sqrt{\Xi}}. \quad (2.60)$$

Analysis of equations 2.57 and 2.60 shows that the hole boring velocities and ion energies are greater for higher intensities and lower densities, and in practice they are maximised for near critical density targets. The above derivations have neglected the fast electron pressure $\mathbf{P}_e = -\nabla(n_e T_e)$ which acts against the hole boring, and is important in interactions with strongly heated thin foils. Demonstration of hole boring RPA has been performed by Palmer *et al.* [90] using a 10 μm wavelength CO₂ laser and a gaseous hydrogen target, producing monoenergetic proton spectra at energies close to 1 MeV.

Light sail acceleration of a thin solid foil may be modelled using the following equation of motion:

$$\frac{d(\beta\gamma)}{dt} = \frac{2I(t_{ret})}{m_i n_i l c^2} R(\omega') \frac{1 - \beta}{1 + \beta}, \quad (2.61)$$

where the intensity is a function of the retarded time $t_{ret} = t - x/c$, and $R(\omega')$ is the reflection coefficient in the foil rest frame. Assuming perfect reflectivity, $R = 1$, the target velocity is given by [89, 91]

$$v_{ls} = c \frac{(1 + \varepsilon)^2 - 1}{(1 + \varepsilon)^2 + 1}, \quad \varepsilon = \frac{2\Phi}{m_i n_i l c^2}, \quad (2.62)$$

where $\Phi = \int I dt$ is the laser fluence. Therefore, in this simple model where all of the

ions move with velocity v_{ls} , the ion energy is given by

$$K_i = m_i c^2 \frac{\varepsilon^2}{2(1 + \varepsilon)}. \quad (2.63)$$

The conversion efficiency of laser-to-ion energy is

$$\eta_{ls} = \frac{2\beta_{ls}}{1 + \beta_{ls}}, \quad (2.64)$$

and this may approach unity in the ultrarelativistic limit ($\beta_{ls} \rightarrow c$).

Equation 2.62 implies that the ion velocities and energies continuously increase as $l \rightarrow 0$. However, as the thickness of the foil is reduced, the threshold for self-induced transparency may be reached and the assumption used in the above equations that $R = 1$ is no longer valid. Macchi *et al.* [89] showed that

$$R \simeq \begin{cases} \zeta^2 / (1 + \zeta^2), & \text{if } a_0 < \sqrt{1 + \zeta^2} \\ \zeta^2 / a_0^2, & \text{if } a_0 > \sqrt{1 + \zeta^2} \end{cases} \quad (2.65)$$

where $\zeta = \pi n_e l / n_c \lambda$. The threshold for transparency is therefore $a_0 = \sqrt{1 + \zeta^2} \simeq \zeta$ for $\zeta \gg 1$. This result indicates an optimum thickness for light sail acceleration at

$$l_{opt} = \frac{a_0 n_c \lambda}{\pi n_e}. \quad (2.66)$$

In experiments, as a laser pulse impinges on a thin foil, the $\mathbf{j} \times \mathbf{B}$ heating of electrons can also lead to the onset of transparency, through the expansion and break up of the foil. The reduced heating of the foil for circular polarisation enables thinner foils to be used and is more suitable for light sail acceleration than linear polarisation [92]. The use of circular laser polarisation removes the oscillating component of the ponderomotive force along the laser axis, and prevents $\mathbf{j} \times \mathbf{B}$ heating for normal incidence. However, the transverse intensity gradient across a Gaussian focal spot will lead to deformation of the critical density surface, with the target receding further in the centre of the focal spot than at the edges. Thus, the laser beam may become locally oblique to areas of the target surface and still cause some $\mathbf{j} \times \mathbf{B}$ and vacuum heating. This effect is greatest for the smallest focal spot sizes, and was shown by Dollar *et al.* for $\phi_L = 1.2 \mu\text{m}$ with thin foils [93]. Instabilities across the surface of the target can also occur [94, 95].

Nevertheless, the possibility of producing peaked energy spectra and the rapid scaling of maximum ion energies with intensity [96] makes light sail acceleration a promising candidate for a high energy ion source.

2.5.3 RSIT-enhanced acceleration

Thin solid foil targets, that are commonly used in laser-driven ion acceleration experiments, may become relativistically transparent due to the combination of plasma expansion and relativistic electron heating. This process is often referred to as *relativistic self-induced transparency* (RSIT), and causes the transition from the mix of RPA and TNSA with an overdense plasma to a less well defined acceleration. This regime is often studied with high contrast laser pulses, and requires ultrathin ($l \lesssim 100$ nm) foils for most high power laser facilities available at present. Since RSIT occurs only within the centre of the laser beam, where it is most intense, a relativistic plasma aperture forms in the foil [48, 97]. After the onset of RSIT, the laser pulse may interact directly with the electrons throughout the plasma volume in its path, and cause the production of electrostatic fields that continue the acceleration of ions. The TNSA electric field at the edges of the target may still exist as the target expands, and be fed by further fast electrons attempting to escape the target. Similarly, ions may continue to be accelerated by the charge-separation field induced by radiation pressure whilst they lag behind the displaced electron layer, and if we consider only the radiation pressure arising from reflection, RPA may continue for a short time whilst R remains significant.

The highest proton energies are regularly found for ultrathin foils that experience RSIT, and close to 100 MeV protons have been reported due to an RSIT enhancement of hybrid RPA-TNSA acceleration [7]. For close to picosecond duration laser pulses, the protons may be locally accelerated after the onset of RSIT by a jet of fast electrons within the laser pulse as it propagates through the target [7, 98]. In general, the ion energies are maximised when the target becomes transparent close to the peak of the laser pulse [99]. Yan *et al.* [100] derived an analytical estimate of the onset time of RSIT by assuming a 1D model in which the laser ponderomotive force induces a charge separation force which expands the ion population:

$$t_1 = \left(\frac{12}{\pi^2}\right) \sqrt{\frac{N\tau l}{a_0 c_s}} - \tau, \quad (2.67)$$

where $c_s = \sqrt{Qm_e c^2 a_0 / m_i}$ is the ion sound speed, and $t_1 = 0$ corresponds to the peak of the laser temporal intensity profile. Experimental measurement of the onset time of RSIT, however, is particularly difficult, due to the need for a temporal resolution less than the laser pulse duration, and has only been claimed in one publication [101]. Analysis of the transmitted light with techniques such as spectral interferometry can still yield information on the interaction dynamics though [102].

2.5.4 Other acceleration mechanisms in near critical density and relativistically transparent plasma

Here, a description is provided of the other mechanisms for ion acceleration in targets that are either initially underdense or near critical density, and solid targets that are rendered (relativistically) underdense during the interaction.

In gaseous targets, the arrival of an intense laser pulse can drive a collisionless electrostatic shock [103, 104]. The ions upstream of the propagating shock wave can be reflected at twice the shock velocity, similar to hole boring acceleration, in this process known as *collisionless shock acceleration*.

For targets near critical density, the propagation of the laser pulse through the target may result in the generation of magnetic dipole vortex structures, through the electron motion, that cause the acceleration of ions [105–107]. The collimation of ions along the vortex axis, and the transverse centre of the plasma channel formed during the interaction, is characteristic of this *magnetic vortex acceleration*.

Near critical density targets also enable *synchronised acceleration by slow light (SASL)* [108], also known as *relativistic transparency front (RTF)-RPA* [109]. In this mechanism, the ions are accelerated by the charge separation field induced by the ponderomotive force of the laser pulse pushing electrons into the target. Continuous acceleration is achieved if the front of the laser pulse accelerates into the target together with some ions in this charge separation field, referred to as the ponderomotive sheath. The mechanism bears similarity to hole boring; however, it is a specific case in which the relativistic critical density surface accelerates into the target due to the increase of γ_e , caused by the increasing intensity of the laser pulse.

One of the mechanisms suggested to take place in transparent plasma is *Coulomb explosion* [110, 111], where the removal of electrons leaves behind a positively charged ion core that explodes due to the Coulomb force between the ions. In this scheme, the

use of a double layer target constituting a heavy ion layer and a rear surface hydrogen layer may deliver improved proton acceleration, due to the Coulomb repulsion from the heavy ions. A directed Coulomb explosion may also be achieved if the target initially begins to move with the pulse due to radiation pressure [111].

For completeness, another mechanism suggested to take place in thin foils that experience RSIT is *laser break-out afterburner (BOA)* [112–115]. Yin *et al.* [112] describe the ion acceleration in their study as TNSA whilst the target is overdense; followed by an enhanced TNSA phase as the skin depth becomes comparable to the target thickness and the laser ponderomotive force acts on all the electrons in the target, which may now all be heated to become fast electrons; and finally, after the onset of RSIT, the BOA phase, defined by a Buneman instability that transfers energy from electrons to ions due to the faster drift velocity of the electrons. Although, the presence of a Buneman instability that results in significant ion acceleration within these interactions has not been proven.

2.6 Radiation from accelerating charges

In a laser-solid interaction, electromagnetic radiation is generated from many different sources and at many different wavelengths. This includes THz radiation, atomic line emission and energetic photons from bremsstrahlung emission, due to fast electrons moving through atomic fields, or synchrotron emission, due to fast electrons accelerating in the fields of the laser pulse and other electric and magnetic fields produced in the interaction. Harmonics of the incident laser pulse may be produced through nonlinear Thomson scattering [116, 117], and coherent transition radiation [118, 119] at $2\omega_L$ due to the $\mathbf{j} \times \mathbf{B}$ accelerated electron bunches crossing the rear surface of a solid target into vacuum. Cherenkov radiation may also be produced in the optical range if electrons accelerated in the interaction move through a medium faster than the phase velocity of light in the medium [120, 121]. The radiation of interest in this thesis is the high energy x-rays and gamma rays produced, which themselves are useful for numerous applications including fundamental science, but are also important due to the resulting friction (radiation reaction) force on the emitting particle. Now that peak laser intensities produced in the laboratory have reached values of $I_L \sim 10^{23} \text{ W cm}^{-2}$ [35], the synchrotron emission of electrons in the laser fields may absorb a considerable

fraction of the laser energy and influence the plasma dynamics. Thus it is an important consideration throughout this thesis in which such laser intensities are used, especially in chapter 5 in which the synchrotron emission is optimised. This section provides a description of the relevant radiation processes, including both classical and quantum models of synchrotron emission, differences between which only begin to emerge under much of the conditions considered in this thesis, and radiation reaction.

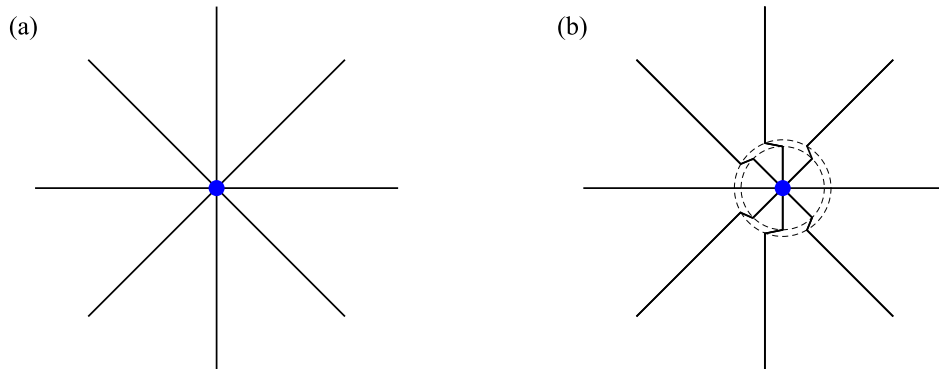


Figure 2.9: (a) The field lines of a moving charge in its rest frame. (b) The field lines after acceleration for a short time.

The power of radiation emitted by an accelerating charge can be derived by considering the changes to the electromagnetic field lines as shown in [122]. A charged particle at the origin of an inertial reference frame will produce a radial electric field $E_r = e^2/4\pi\epsilon_0 r^2$. After acceleration of the particle for a short time Δt by a change in speed Δv , the field lines are radial around the new position of the particle. The information that the charge has moved can only propagate at c . Therefore, for the field lines to remain necessarily continuous, there must be a perturbation of the field that propagates outwards in a thin shell of thickness $c\Delta t$, as shown in figure 2.9. For the field lines to join across this shell, there must be a component of the field orthogonal to the radial direction:

$$E_\theta = \frac{\Delta v t \sin \theta}{c \Delta t} E_r, \quad (2.68)$$

where $t = r/c$ and θ is the angle to the acceleration vector. Inserting E_r and $\Delta v/\Delta t = a$, where $a = (dp/dt)/m$ is the particle acceleration, gives $E_\theta = qa \sin \theta/4\pi c^2 \epsilon_0 r$.

The intensity of the electromagnetic radiation described by E_θ is calculated from the magnitude of the Poynting vector $S = |\mathbf{E} \times \mathbf{B}|/\mu_0 = E^2/\mu_0 c$. Therefore, the radiated

power is

$$P = \int S r^2 d\Omega = \int \frac{q^2 a^2 \sin^2 \theta}{16\pi^2 \epsilon_0 c^3} d\Omega. \quad (2.69)$$

Performing this integration over the solid angle $d\Omega = \sin \theta d\theta d\phi$ yields *Larmor's formula*:

$$P = \frac{q^2 a^2}{6\pi \epsilon_0 c^3}. \quad (2.70)$$

The relativistically correct description of the electromagnetic fields induced by a charged particle is given by the Liénard-Wiechert potentials:

$$\mathbf{A}(\mathbf{r}, t) = \frac{\mu_0 c}{4\pi} \left[\frac{q\boldsymbol{\beta}}{R(1 - \boldsymbol{\beta} \cdot \mathbf{n})} \right]_{ret}, \quad \phi(\mathbf{r}, t) = \frac{1}{4\pi \epsilon_0} \left[\frac{q}{R(1 - \boldsymbol{\beta} \cdot \mathbf{n})} \right]_{ret}, \quad (2.71)$$

where $\mathbf{n} = (\mathbf{r} - \mathbf{r}_s) / |\mathbf{r} - \mathbf{r}_s|$ is the unit vector in the direction from the moving charge to the point of observation, $R = |\mathbf{r} - \mathbf{r}_s|$ and *ret* indicates evaluation at the retarded time $t_r = t - R/c$. The electric and magnetic fields are functions of the vector and scalar potentials as follows: $\mathbf{E} = -\partial\mathbf{A}/\partial t - \nabla\phi$ and $\mathbf{B} = \nabla \times \mathbf{A}$. A simpler method to obtain the power radiated from the acceleration and velocity of the particle measured in the observer's frame of reference is to use the knowledge that the power radiated in equation 2.70 is a Lorentz invariant, and the norm of the acceleration four-vector $\gamma[c\partial\gamma/\partial t, \partial(\gamma\mathbf{v})/\partial t]$ is also invariant. The proper acceleration \mathbf{a}_0 of the particle thus satisfies $|\mathbf{a}_0|^2 = \gamma^4(|\mathbf{a}|^2 + \gamma^2|\boldsymbol{\beta} \cdot \mathbf{a}|^2) = \gamma^4(|\mathbf{a}_\perp|^2 + \gamma^2|\mathbf{a}_\parallel|^2)$, where \mathbf{a}_\parallel and \mathbf{a}_\perp are the components of the acceleration parallel and perpendicular to the velocity, respectively. Substituting this relation for the proper acceleration into equation 2.70 yields

$$P = \frac{q^2 \gamma^4}{6\pi \epsilon_0 c^3} (|\mathbf{a}_\perp|^2 + \gamma^2|\mathbf{a}_\parallel|^2). \quad (2.72)$$

2.6.1 Bremsstrahlung

The generation of large numbers of energetic electrons in laser-solid interactions can provide a bright source of bremsstrahlung radiation at x-ray wavelengths. This emission, often referred to as free-free emission, originates from the scattering of moving electrons due to the Coulomb field surrounding atomic nuclei. A clear introduction to the classical theory of bremsstrahlung radiation has been provided by Longair [122], of which the key results are summarised below.

The spectrum of radiation emitted by a single electron accelerated in the Coulomb

potential of a nucleus can be calculated by using Parseval's theorem and taking the Fourier transform of the acceleration. The acceleration is a function of the impact factor, b , the distance of closest approach between the two particles. This produces a spectrum that is constant at low frequencies and falls exponentially for frequencies ω greater than $\sim \gamma v/b$, which corresponds to the approximate duration of the collision, $\tau = 2b/\gamma v$ [122, 123]. The low frequency ($\omega \ll \gamma v/b$) part of the spectrum is approximately given by

$$I(\omega) = \frac{e^6}{24\pi^4 \epsilon_0^3 c^3 m_e^2} \frac{Z^2}{b^2 v^2}. \quad (2.73)$$

Consider a non-relativistic electron propagating through a density of nuclei n_i in the laboratory frame. The range of impact factors in the electron motion that may produce radiation with frequency ω must be integrated over, and the low frequency spectrum becomes

$$I(\omega) = \frac{e^6}{12\pi^3 \epsilon_0^3 c^3 m_e^2} \frac{Z^2 n_i}{v} \ln \Lambda, \quad (2.74)$$

where $\Lambda = b_{max}/b_{min}$. An appropriate choice for the upper limit of the impact factor, b_{max} , is v/ω , where the spectrum falls off exponentially. For high velocities ($v/c \geq Z/137$), the lower limit to the closest distance of approach is given by the Heisenberg uncertainty principle; it is appropriate to assume $b_{min} = \hbar/2m_e v$, thus $\Lambda = 2m_e v^2/\hbar\omega$.

Although the single electron bremsstrahlung spectrum is informative, it is necessary to integrate over the distribution of electrons to obtain a result that can be used to describe the bremsstrahlung emission from a plasma. Here, the electron velocities may be approximated by a Maxwell-Boltzmann distribution:

$$f(v) dv = n_e \left(\frac{m_e}{2\pi k_B T_e} \right)^{3/2} v^2 \exp\left(-\frac{m_e v^2}{2k_B T_e}\right) 4\pi dv. \quad (2.75)$$

For such a velocity distribution, the spectral emissivity is [122, 124]

$$\kappa = 6.8 \times 10^{-51} Z^2 n_e n_i T_e^{-1/2} \exp\left(-\frac{h\nu}{k_B T_e}\right) g(\nu, T_e) \text{ W m}^{-3} \text{ Hz}^{-1}, \quad (2.76)$$

where $g(\nu, T_e)$ is a Gaunt factor that varies slowly with frequency. For x-ray wavelengths, $g(\nu, T_e) \approx \sqrt{3} \ln(k_B T_e/h\nu)/\pi$.

The key aspects of bremsstrahlung production can be seen in equation 2.76. Higher Z materials much more efficiently produce bremsstrahlung radiation due to the Z^2 scaling; the emission scales linearly with the density of energetic electrons; and the

spectrum falls exponentially for higher frequencies, where the rate that it falls decreases for higher electron temperatures.

2.6.2 Classical synchrotron radiation

Magnetic fields are always present during laser-solid interactions; the induced currents generate magnetic fields and the laser pulse itself contains often the strongest magnetic fields present. As a result, synchrotron radiation is always produced in these interactions from the acceleration of electrons by the magnetic component of the Lorentz force, and any electric field component perpendicular to the electron motion. Although the synchrotron emission is often immeasurable due to the dominance of other radiation sources such as bremsstrahlung when using solid targets, it is expected to become an efficient source of high energy photons for laser intensities $I > 10^{22} \text{ W cm}^{-2}$.

Classical equations for synchrotron radiation can be derived by considering the acceleration of a charge in a constant magnetic field [122, 123, 125]. Here, classical generally refers to a relativistic but not quantum treatment. The equation of motion is

$$m \frac{d(\gamma \mathbf{v})}{dt} = m\gamma \frac{d\mathbf{v}}{dt} + m\gamma^3 \mathbf{v} \frac{(\mathbf{v} \cdot \mathbf{a})}{dt} = q(\mathbf{v} \times \mathbf{B}). \quad (2.77)$$

The acceleration remains perpendicular to the velocity: $\mathbf{v} \cdot \mathbf{a} = 0$. Therefore, the left-hand side simplifies to $m\gamma d\mathbf{v}/dt$. Consider an electron with velocity components parallel and perpendicular to the magnetic field \mathbf{v}_{\parallel} and \mathbf{v}_{\perp} , respectively. The electron maintains a constant pitch angle $\alpha = \arctan(v_{\parallel}/v_{\perp})$ to the magnetic field as it traces a helical path with a constant velocity parallel to the magnetic field. The magnitude of the right-hand side of equation 2.77 becomes $evB \sin \alpha$, and the acceleration measured in the lab frame

$$a_{\perp} = \frac{evB \sin \alpha}{\gamma m_e}, \quad (2.78)$$

where the acceleration parallel to the magnetic field $a_{\parallel} = 0$. Inserting the acceleration components into equation 2.72 gives the power radiated as

$$P = \frac{e^4 B^2 \beta^2 \gamma^2 \sin^2 \alpha}{6\pi \epsilon_0 c m_e^2}. \quad (2.79)$$

The angular distribution of synchrotron radiation in the electron rest frame $dP/d\Omega = e^2 a^2 \sin^2 \theta / 16\pi^2 \epsilon_0 c^3$, where θ is the angle from the acceleration vector, is shown in figure

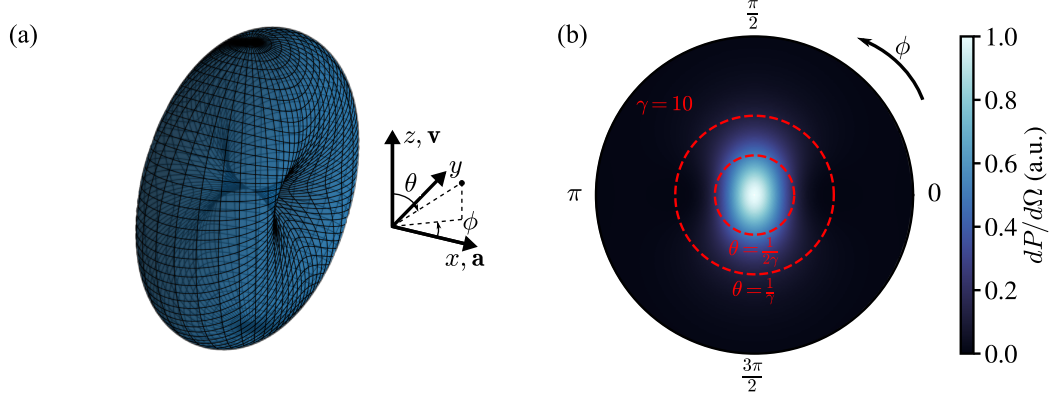


Figure 2.10: The angular profile of synchrotron radiation for an electron in (a) its rest frame and (b) the laboratory frame for $\gamma = 10$.

2.10(a); the $\sin^2 \theta$ dependence minimises the emission along the acceleration vector. A Lorentz transformation of the radiated power into the laboratory frame for acceleration perpendicular to the velocity produces angular profile [123, 126]

$$\frac{dP}{d\Omega} = \frac{e^2}{16\pi^2 \epsilon_0 c} \frac{\left\{ \mathbf{n} \times [(\mathbf{n} - \boldsymbol{\beta}) \times \dot{\boldsymbol{\beta}}] \right\}^2}{(1 - \mathbf{n} \cdot \boldsymbol{\beta})^5} \quad (2.80)$$

$$= \frac{cr_0 m_0 c^2 \beta^4}{4\pi \rho^2} \left[\frac{(1 - \beta \cos \theta)^2 - (1 - \beta^2) \sin^2 \theta \cos^2 \phi}{(1 - \beta \cos \theta)^5} \right], \quad (2.81)$$

where θ and ϕ correspond to the polar and azimuthal angles, respectively, in the coordinate system shown in figure 2.10(a), $r_0 = e^2/4\pi\epsilon_0 m_e c^2$ is the classical electron radius and $\rho = \beta\gamma m_e c/eB$ is the radius of electron motion. For a relativistic electron with $\gamma \gg 1$ the radiation profile becomes peaked along the velocity direction into a cone with opening angle $\theta \sim 1/\gamma$. This is shown in figure 2.10(b) for an electron with $\gamma = 10$. The narrow beam of radiation emitted by relativistic particles means that it can often be considered parallel with the particle motion in modelling of highly relativistic electrons.

The radiated energy per unit frequency per unit solid angle can be calculated from the motion of an electron through the following equation:

$$\frac{d^2 W}{d\omega d\Omega} = \frac{e^2}{16\pi^3 \epsilon_0 c} \left| \int_{-\infty}^{\infty} \frac{\mathbf{n} \times [(\mathbf{n} - \boldsymbol{\beta}) \times \dot{\boldsymbol{\beta}}]}{(1 - \boldsymbol{\beta} \cdot \mathbf{n})^2} \exp \left[i\omega \left(t - \frac{\mathbf{n} \cdot \mathbf{r}(t)}{c} \right) \right] dt \right|^2. \quad (2.82)$$

The $1/(1 - \boldsymbol{\beta} \cdot \mathbf{n})^2$ term in the integral shows the radiation from a relativistic particle in arbitrary motion is generally parallel to the velocity: for $\boldsymbol{\beta} \rightarrow c$ and observation parallel with the velocity, $1 - \boldsymbol{\beta} \cdot \mathbf{n} \rightarrow 0$.

If the electron motion is circular, equation 2.82 is equivalent to

$$\frac{d^2W}{d\omega d\Omega} = \frac{e^2}{16\pi^3\epsilon_0 c} \gamma^2 \left(\frac{\omega}{\omega_c}\right)^2 (1 + \gamma^2\theta^2)^2 \left[K_{2/3}^2(\xi) + \frac{\gamma^2\theta^2}{1 + \gamma^2\theta^2} K_{1/3}^2(\xi) \right], \quad (2.83)$$

where $K_{1/3}$ and $K_{2/3}$ are modified Bessel functions of the second kind, and θ is the angle perpendicular to the plane of orbit. Here, ω_c is the critical frequency:

$$\omega_c = \frac{3c}{2\rho} \gamma^3, \quad (2.84)$$

where ρ is the radius of curvature of the electron motion. The parameter ξ is defined

$$\xi = \frac{\omega}{2\omega_c} (1 + \gamma^2\theta^2)^{3/2}. \quad (2.85)$$

In equation 2.83, the $K_{2/3}$ term corresponds to radiation polarised in the plane of the electron motion, and the $K_{1/3}$ term corresponds to radiation polarised perpendicular to that plane. Integration of equation 2.83 produces the following expression for the spectrum of synchrotron radiation:

$$\frac{dW}{d\omega} = \sqrt{3} \frac{e^2}{4\pi\epsilon_0 c} \gamma \frac{\omega}{\omega_c} \int_{\omega/\omega_c}^{\infty} K_{5/3}(x) dx. \quad (2.86)$$

2.6.3 Quantum synchrotron radiation

For intense laser fields where the energy of the synchrotron radiation approaches the electron energy, it is necessary to use the quantum model of synchrotron radiation [127–129]. Several parameters will be defined here that are used in the quantum synchrotron equations.

The critical field of quantum electrodynamics (QED), above which e^-e^+ pairs are produced from vacuum and the electromagnetic field becomes nonlinear, is the *Sauter-Schwinger field*:

$$E_S = \frac{m_e^2 c^3}{e\hbar} \simeq 1.32 \times 10^{18} \text{ V m}^{-1}. \quad (2.87)$$

The importance of quantum effects for an electron in an electromagnetic field depends upon the field strength in the electron's rest frame. This is defined by the Lorentz-

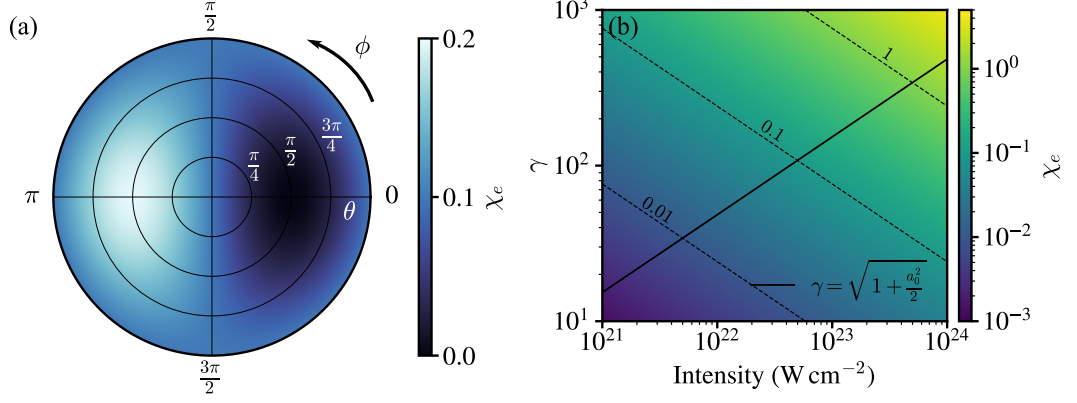


Figure 2.11: (a) The value of χ_e of an electron with $\gamma = 150$ in an electromagnetic field with intensity $I = 10^{23} \text{ W cm}^{-2}$ and wavelength $\lambda = 800 \text{ nm}$ for the range of possible orientations of the electron trajectory, where the field propagates along $\theta = \pi/2$, $\phi = 0$. (b) The value of χ_e for a range of laser intensities and Lorentz factors of an electron assuming counter-propagation to the laser beam.

invariant parameter

$$\chi_e = \frac{e\hbar}{m_e^3 c^4} |F_{\mu\nu} p^\nu| \approx \frac{\gamma}{E_S} |\mathbf{E}_\perp + \mathbf{v} \times \mathbf{B}|, \quad (2.88)$$

where $F_{\mu\nu}$ is the electromagnetic field tensor and p^μ is the electron four-momentum. Similarly, the quantum synchrotron emission equations depend upon the Lorentz-invariant parameter

$$\chi_\gamma = \frac{e\hbar^2}{2m_e^3 c^4} |F^{\mu\nu} k_\nu| = \frac{\hbar\omega}{2m_e c^2} \frac{1}{E_S} \left| \mathbf{E}_\perp + c \frac{\mathbf{k}}{|\mathbf{k}|} \times \mathbf{B} \right|, \quad (2.89)$$

where $\hbar k_\nu$ is the photon four-momentum. The parameters χ_e and χ_γ are also commonly written in other works as η and χ , respectively.

The values of χ_e and χ_γ are clearly dependent upon their trajectory relative to an electromagnetic field. In figure 2.11(a), χ_e is plotted for an electron with $\gamma = 150$ in a laser beam with intensity $I = 10^{23} \text{ W cm}^{-2}$ and wavelength $\lambda_L = 800 \text{ nm}$ propagating along the x -axis ($\theta = \pi/2$, $\phi = 0$). The value of χ_e is minimised for co-propagation with the laser beam, and maximised for counter-propagation ($\theta = \pi/2$, $\phi = \pi$); it is straightforward to show that these cases correspond to $\chi_e = \gamma E(1 \pm \beta)/E_S$. Assuming counter-propagation, χ_e is plotted for a range of electron energies and laser intensities in figure 2.11(b). For ponderomotive electron energies to reach $\chi_e = 0.1$, where the highly radiative regime begins, intensities $I \sim 5 \times 10^{22} \text{ W cm}^{-2}$ are required.

A factor $10\times$ higher laser intensity of $I \sim 5 \times 10^{23} \text{ W cm}^{-2}$ is required to reach $\chi_e = 1$, where the distinctly quantum regime begins. However, this strongly depends upon the trajectory of the electrons relative to the electromagnetic field in the interaction, and is complicated by the large spread of electron energies in laser-solid interactions.

Two approximations are made in the equations presented in this section as described in [129, 130]. Firstly, the *quasi-static/local-constant-field approximation* assumes that the external fields are temporally constant so that instantaneous values of process rates are calculated. This approximation holds where the coherence length of the interaction λ_L/a , where $a = eE/m_e c \omega$, is much smaller than the laser wavelength, corresponding to $a \gg 1$. Secondly, the *weak-field approximation* is made: the effect of the Lorentz-invariant parameters $\mathcal{F} = |E^2 - B^2|/E_S^2$ and $\mathcal{G} = |\mathbf{E} \cdot \mathbf{B}|^2/E_S^2$ on the transition (photon emission) probabilities is neglected [128]. This is valid only when the following conditions are satisfied: $\mathcal{F}, \mathcal{G} \ll 1$ and $\text{Max}(\mathcal{F}, \mathcal{G}) \ll \chi_e^2$.

The spin and polarisation averaged rate of synchrotron emission is [130]

$$\frac{d^2 N}{d\chi_\gamma dt} = \sqrt{3} \frac{\alpha_f c}{\lambda_c} \frac{\chi_e}{\gamma} \frac{F(\chi_e, \chi_\gamma)}{\chi_\gamma}, \quad (2.90)$$

where $\alpha_f = e^2/4\pi\epsilon_0\hbar c$ is the fine-structure constant, λ_c is the Compton wavelength and $F(\chi_e, \chi_\gamma)$ is the quantum synchrotron function. Here,

$$F(\chi_e, \chi_\gamma) = 4 \frac{\chi_\gamma^2}{\chi_e^2} y K_{2/3}(y) + \left(1 - \frac{2\chi_e}{\chi_\gamma}\right) y \int_y^\infty K_{5/3}(x) dx, \quad (2.91)$$

where $y = 4\chi_\gamma/3\chi_e(\chi_e - 2\chi_\gamma)$ and $\chi_\gamma < \chi_e/2$. In the classical limit, $y \simeq 4\chi_\gamma/3\chi_e^2$ and $F(\chi_e, \chi_\gamma) \simeq y \int_y^\infty K_{5/3}(x) dx$.

The variation of the emitted power spectrum $dP/d\omega$ here with frequency is entirely due to the quantum synchrotron function $F(\chi_e, \chi_\gamma)$. This is straightforward to show from equation 2.90: $dP/d\omega = \hbar\omega(d^2 N/d\chi_\gamma dt)(d\chi_\gamma/d\omega) = \sqrt{3}\hbar(\alpha_f c/\lambda_c)(\chi_e/\gamma)F(\chi_e, \chi_\gamma)$, where $d\chi_\gamma/d\omega = \chi_\gamma/\omega$ and $P = \hbar\omega dN/dt$. The quantum synchrotron function is shown in figure 2.12 for $\chi_e = 0.1, 1$ and 10 , assuming an electron with $\gamma = 2000$ and photon emission parallel with the electron motion. For $\chi_e = 0.1$, the classical form of $F(\chi_e, \chi_\gamma)$ appears to produce slightly more emission at high energies. The difference between the classical and quantum solutions becomes much larger for $\chi_e = 1$, where the classical spectrum unphysically extends beyond the energy of the emitting electron but the quantum spectrum does not. These differences grow larger for $\chi_e = 10$ where

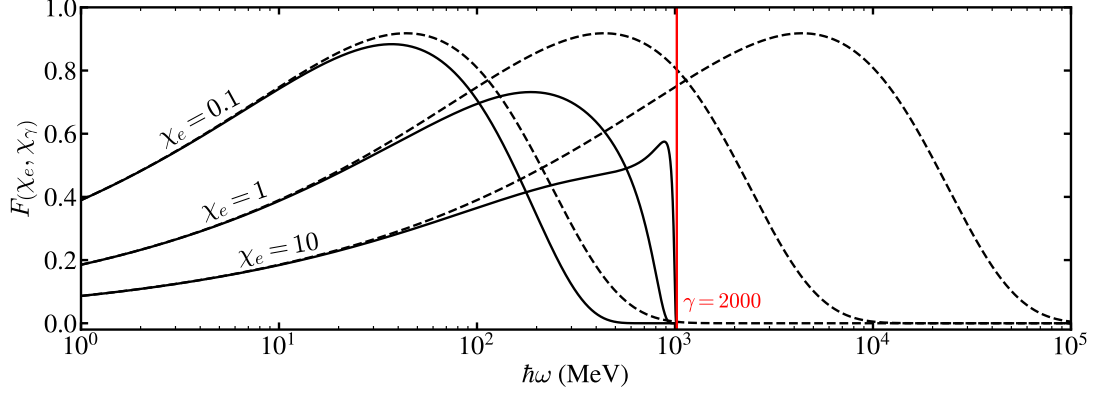


Figure 2.12: The frequency variation of the quantum synchrotron function for an electron with $\gamma = 2000$. The function is plotted for several values of χ_e using the quantum (solid) and classical (dashed) form.

the quantum spectrum becomes peaked close to the electron energy.

The power radiated is

$$P = \frac{4\pi}{3} \frac{\alpha_f m_e c^3}{\lambda_c} \chi_e^2 g(\chi_e), \quad (2.92)$$

where $g(\chi_e)$ is the Gaunt factor:

$$g(\chi_e) = \frac{3^{3/2}}{2\pi} \frac{1}{\chi_e^2} \int_0^{\chi_e/2} F(\chi_e, \chi_\gamma) d\chi_e \quad (2.93)$$

$$\approx \left(1 + 4.8 [1 + \chi_e] \ln [1 + 1.7\chi_e] + 2.44\chi_e^2\right)^{-2/3}. \quad (2.94)$$

The Gaunt factor captures the transition from the classical to the quantum regime. In the classical limit where $\chi_e \ll 1$, $g(\chi_e) = 1$ is constant and the power radiated $P \propto \chi_e^2$. The value of $g(\chi_e)$ starts to reduce for $\chi_e \gtrsim 0.1$, and when $\chi_e \gg 1$, the Gaunt factor is small $g(\chi_e) \ll 1$. In this quantum limit, the power radiated follows a reduced scaling $P \propto \chi_e^{2/3}$.

2.6.4 Radiation reaction

The emission of radiation by an accelerating charged particle causes a recoil force on the emitting particle. This is commonly known as *radiation reaction*, and must be incorporated into the particle equation of motion. The forces acting on the particle can be described with the following equation:

$$m\mathbf{a} = \mathbf{F}_{ext} + \mathbf{F}_{rad}, \quad (2.95)$$

where $\mathbf{F}_{ext} = q(\mathbf{E} + \mathbf{v} \times \mathbf{B})$ is the Lorentz force and \mathbf{F}_{rad} is the radiation reaction force.

In the classical picture, the radiation reaction force can be derived by equating the work done by this force to the radiated energy:

$$\int_{t_1}^{t_2} \mathbf{F}_{rad} \cdot \mathbf{v} dt = - \int_{t_1}^{t_2} P_\gamma dt, \quad (2.96)$$

where $P_\gamma = q^2 a^2 / 6\pi\epsilon_0 c^3$ is the radiated power. The right-hand side may be integrated by parts:

$$-\frac{q^2}{6\pi\epsilon_0 c^3} \int_{t_1}^{t_2} \mathbf{a} \cdot \mathbf{a} dt = -\frac{q^2}{6\pi\epsilon_0 c^3} (\mathbf{a} \cdot \mathbf{v}) \Big|_{t_1}^{t_2} + \frac{q^2}{6\pi\epsilon_0 c^3} \int_{t_1}^{t_2} \dot{\mathbf{a}} \cdot \mathbf{v} dt. \quad (2.97)$$

Assuming the particle undergoes motion such that $\mathbf{a} \cdot \mathbf{v} = 0$, only the latter term on the right-hand side remains and we find the *Abraham-Lorentz* force:

$$\mathbf{F}_{rad} = \frac{q^2}{6\pi\epsilon_0 c^3} \dot{\mathbf{a}}. \quad (2.98)$$

When there are no external fields ($F_{ext} = 0$), one of the solutions of the Abraham-Lorentz equation (equation 2.95 and 2.98) is $\mathbf{a}(t) = \mathbf{a}(t=0) \exp(6\pi\epsilon_0 c^3 t / q^2)$. This a runaway solution, and hence unphysical, since the acceleration increases exponentially whenever it is initially nonzero. Although the runaway solutions can be neglected, this leads to the additional unphysical behaviour of pre-acceleration, where the acceleration depends upon the force applied at all later times [131]. The covariant relativistic version of the Abraham-Lorentz equation is the *Lorentz-Abraham-Dirac* equation [132, 133]:

$$m \frac{d\mu^\mu}{ds} = eF^{\mu\nu} u_\nu + \frac{2}{3} e^2 \left(\frac{d^2 u^\mu}{ds^2} + \frac{du^\nu}{ds} \frac{du_\nu}{ds} u^\mu \right), \quad (2.99)$$

where s is the proper time, u^μ is the four-velocity and $eF^{\mu\nu} u_\nu$ is the Lorentz force of the external fields.

An alternative classical description of the dynamics of an electron, in an external field with radiation reaction, is provided by the *Landau-Lifshitz* equation [125, 133] (in three-vector form [134]):

$$m \frac{du^\mu}{ds} = eF^{\mu\nu} u_\nu + \frac{2}{3} e^2 \left[\frac{e}{m} (\partial_\alpha F^{\mu\nu}) u^\alpha u_\nu - \frac{e^2}{m^2} F^{\mu\nu} F_{\mu\nu} u^\alpha + \frac{e^2}{m^2} (F^{\alpha\nu} u_\nu) (F_{\alpha\lambda} u^\lambda) u^\mu \right]. \quad (2.100)$$

Here, it is assumed that the radiation reaction force is much weaker than the Lorentz

force. Thus enabling the acceleration due to the Lorentz force only, $eF^{\mu\nu}u_\nu/m$, to be substituted into the radiation reaction force to produce the above equation. This corresponds to two conditions: $\lambda \gg \alpha_f \lambda_c$ and $F \ll F_{cr}/\alpha_f$, where λ_c is the Compton wavelength.

In strong-field QED, the emission of radiation is *probabilistic*. Therefore, an electron does not follow a deterministic worldline as in the classical description. Instead, it propagates classically in the electromagnetic field, for the approximations made in the previous section, in between stochastic photon emission in discrete events. The photon emission is modified as described in section 2.6.3, where the emission is reduced by the Gaunt factor (equation 2.93) and the spectrum is limited to the electron energy. A detailed review of quantum radiation reaction has been provided by Piazza *et al.* [133].

2.7 Electron-positron pair production

For laser intensities $I \sim 10^{29} \text{ W cm}^{-2}$ corresponding to the Schwinger limit [135], e^-e^+ pairs can be produced from vacuum. At present, only laser intensities up to $I \sim 10^{23} \text{ W cm}^{-2}$ are possible in high power laser facilities and pair production must be achieved through alternative mechanisms that require energetic photons or electrons. Several processes in laser-matter interactions that result in the production of e^-e^+ pairs are described in this section.

In the Coulomb field of an atomic nucleus, photons with energy $\hbar\omega \geq 2m_e c^2 \approx 1.02 \text{ MeV}$ may be converted into an e^-e^+ pair via the *Bethe-Heitler* process [136]. Although an external source of gamma rays can be used, bremsstrahlung emission from fast electrons is generally the source of such high energy photons in laser solid interactions. The dependence of the interaction on the Coulomb field of the nucleus, and the increased bremsstrahlung emission with higher Z materials, makes high- Z materials more efficient converters [137]. The production of e^-e^+ pairs via the Bethe-Heitler process has been observed in laser-solid experiments [138], and can be achieved through conversion of a laser wakefield accelerated electron beam in a solid [139].

Electrons may also produce e^-e^+ pairs by scattering from the Coulomb field of an atomic nucleus via the *trident* process [129, 140–142]. This occurs via the emission of a virtual photon that generates the e^-e^+ pair.

Perhaps the most efficient source of e^-e^+ pairs in laser-solid interactions may

be possible with the nonlinear *Breit-Wheeler* process [143] and laser intensities $I \gtrsim 10^{23} \text{ W cm}^{-2}$ [141, 144]. In this process, a high energy photon, γ_h , within a strong electromagnetic field comprised of many laser photons, γ_l , is converted into a pair:

$$\gamma_h + n\gamma_l \rightarrow e^- + e^+. \quad (2.101)$$

This process was first observed more than two decades ago at the Stanford Linear Accelerator (SLAC) with the injection of 46.6 GeV electrons into an intense laser pulse [145, 146]. The nonlinear (inverse) Compton scattering of the laser photons from the electrons produces photons with up to GeV energies in this setup which then generate the pairs. In laser-solid interactions, the high energy photons may be supplied by bremsstrahlung emission, or more likely, synchrotron emission, which becomes an extremely bright source of gamma rays at such high laser intensities.

A key goal of fundamental scientific interest, that may become possible with laser-plasma interactions, is observation of the linear Breit-Wheeler process between two real photons: $\gamma + \gamma \rightarrow e^- + e^+$. Although this process may occur in laser-plasma interactions, it is generally expected to be much less efficient than nonlinear Breit-Wheeler (and in some cases Bethe-Heitler) pair production when there is only a single laser driver, due to the collision geometry required to maximise the probability of pair production. The threshold on the energies of the two photons, ε_1 and ε_2 , required for the generation of an electron and positron is $\varepsilon_1 \varepsilon_2 > 2m_e^2 c^4 / (1 - \cos \theta)$, where θ is the angle between the trajectories of the two photons. Clearly counter-propagation of the two photons is preferential for linear Breit-Wheeler pair production, where the energy threshold corresponds to the square of the electron rest mass, with the energy threshold diverging and pair production inhibited for parallel propagation ($\theta = 0$).

The efficient generation of high energy gamma rays in single pulse laser-plasma interactions requires either conversion of a laser wakefield accelerated (LWFA) electron beam into bremsstrahlung radiation in a solid or laser-irradiation of a dense material; the former case produces a collimated beam of photons in the same direction as the incident electrons, and the latter case often produces high energy photons over a wide angle predominantly in the forward direction with the laser pulse, depending upon the conditions, where the angle between the two bright lobes of photons generated may still be limited (typically tens of degrees), and the intersection of this radiation

may also be limited due to its generation in bunches at frequency ω_L with the two different directions separated by half the laser cycle (see for example [147]). Both setups enable Bethe-Heitler pair production as the photons propagate through dense matter, which will produce noise on the measured positron signal, and the latter case nonlinear Breit-Wheeler pair production. The use of a second laser driver to produce a counter-propagating (or at least intersecting with a large angle) source of energetic photons may therefore be necessary to enhance the linear production of Breit-Wheeler pairs.

Pike *et al.* [148] suggested directing the bremsstrahlung emission from a GeV electron beam into the ~ 100 eV radiation field inside a laser-heated hohlraum, yet the application of this technique is limited by the prohibitively high energy and low repetition rate laser systems required to heat the hohlraum. Kettle *et al.* [149] suggested a similar more practical method using the keV x-rays from a germanium target heated by a ~ 100 TW laser. There are two key advantages of these techniques over the collision of two gamma ray beams from two short pulse lasers [150, 151]: the much higher energy of one of the two photons in the collision causes the generated pairs to be emitted over a small angular range, and the wide bath of radiation and long duration of the lower energy photon source makes spatial and temporal overlap easier to attain. Alternatively, the counter-propagation of two laser pulses inside a structured target, comprising a pre-filled channel with diameter comparable to ϕ_L , to produce counter-propagating gamma rays for linear Breit-Wheeler pair production has been proposed [152, 153]. However, alignment of counter-propagating laser pulses with a classically overdense pre-filled channel of width $\sim 5 \mu\text{m}$ provides an additional challenge to the spatial and temporal overlap of the radiation; imperfect alignment and spatial jitter of the laser beams will add to the uncertainty in the results. A more practical method may be possible with a single pulse if the forward-directed radiation is accompanied by the generation of significant backwards directed radiation [154]. The space-charge field at the front of the laser pulse as it propagates through dense plasma has been shown to inject electrons backwards into the laser pulse and thus produce synchrotron radiation in this direction [155]. Careful choice of the target density (and structure) may enable this single pulse scheme to be useful, yet nonlinear Breit-Wheeler pair production is expected to dominate above a certain laser intensity as many high energy photons are generated counter-propagating into the laser pulse.

The electrons and positrons in the pairs created by one of the above processes may themselves radiate photons under acceleration by the electric and magnetic fields they propagate through and produce more pairs. An *electromagnetic cascade* can therefore be triggered, creating a pair plasma analogous to those expected in astrophysical environments and efficiently depleting energy from the laser pulse [144, 156].

Methodology

The results presented later in this thesis were obtained from particle-in-cell (PIC) simulations and a description of the methods used by this class of simulation code is given in this chapter. Firstly, however, it is important to understand how the lasers used to drive the interactions studied are created for experiments. The imperfect nature of real laser pulses arises from a number of physical effects, and can become essential to consider when these non-ideal conditions influence the interaction and its products. In particular, for laser-solid interactions, the light that arrives before the main pulse. The near constant hundreds of picoseconds, or nanosecond, component of this light is commonly parameterised with the intensity contrast ratio compared to the pulse peak. A brief discussion of state of the art systems for high power laser-plasma interactions, corresponding to new multi-petawatt facilities and high repetition rate capabilities, is also given here.

The high energy particles and radiation produced from the interactions examined in this thesis may be detected and the properties of their beams measured with many different diagnostics, each with various advantages and disadvantages which are discussed in this chapter. An essential component of these diagnostics is a detection medium in which the incoming particles or radiation produce a measurable signal. The several most commonly used types of such media are outlined here, which include films with an active layer that must be physically extracted and processed for the signal, and materials that scintillate, producing optical light that can be rapidly captured.

3.1 High power laser systems

Today, there are many petawatt class laser systems around the world in operation [157], with as high as 10 petawatts producible for laser-solid interactions [158]. The generation of such high power laser pulses has been motivated by the prospect of increasingly energetic secondary sources of particles and radiation, and the possibility of accessing conditions where strong-field quantum electrodynamics and radiation reaction become important in the laboratory. The increase of laser power has corresponded to an increase of achievable laser intensity over the years as shown in figure 3.1. This has relied upon a number of technological developments since the first demonstration of a laser in 1960 [159]. Q-switching and modelocking were rapidly developed in the 1960s, but the essential technique that enabled the production of relativistically intense laser pulses and subsequent MeV particle and radiation sources was the development of chirped pulse amplification (CPA) in 1985 [160], that formed part of the work for which the Nobel prize in Physics was awarded in 2018. In this section, a brief description of CPA is given, before discussion of several methods, including optical parametric amplification, for improving the contrast and discussion of the highest power laser systems in operation at present or expected to become operational in the near future.

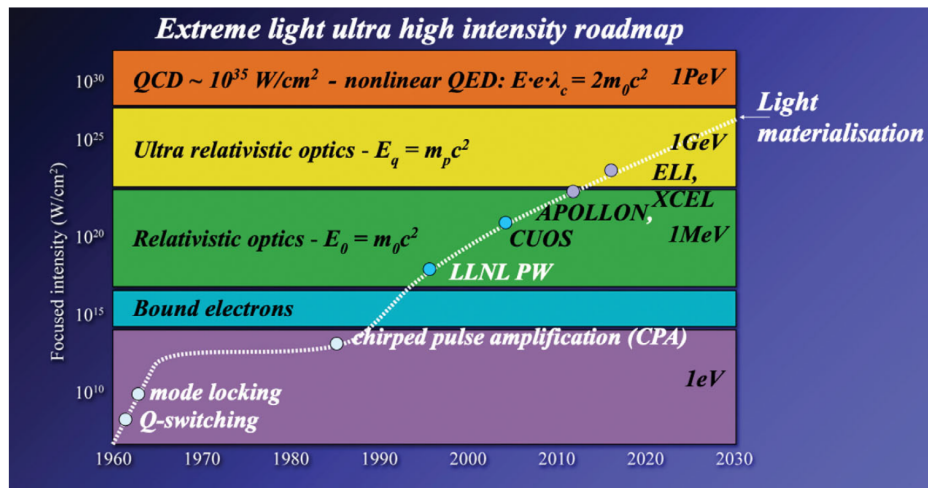


Figure 3.1: The increase in laser intensity over the years, from [161].

3.1.1 Chirped pulse amplification (CPA)

The principal effect limiting the laser intensity that can be used with solid state optics is self-focussing due to the nonlinear and intensity dependent refractive index:

$\eta = \eta_0 + \eta_2 I$, where η_0 is the constant refractive index applicable with low intensities, and η_2 is the nonlinear component. This latter element of the refractive index induces an additional phase shift of intense light as it propagates in a medium, which is characterised by the B-integral:

$$B = \frac{2\pi}{\lambda_L} \int \eta_2 I_L(z) dz. \quad (3.1)$$

Gradients in intensity across the laser spatial profile produce a spatially varying refractive index that can self-focus the laser beam. Similarly, the time dependence of the laser pulse intensity (usually Gaussian) can cause self-phase modulation, where the refractive index varies with time and produces a time dependent phase shift of the laser pulse, which can lead to broadening of the frequency spectrum. For a sufficiently high B-integral, the produced laser beam is degraded and damage to the optics used, the amplification medium in particular, can occur as the laser self-focusses to intensities above their damage threshold. Although the area of the beam and the optics it propagates through may be increased to mitigate this effect, increasing their size can become prohibitively expensive and requires increasingly larger spaces to house the system.

CPA was therefore developed [160], in which the laser pulse is stretched temporally before amplification and compressed afterwards, enabling much higher powers to be produced after amplification without B-integral effects. The pulse is stretched to a duration > 1000 times longer than its initial duration with diffraction gratings that apply a temporal chirp (group velocity dispersion), causing its frequency to vary with time, and compressed similarly with diffraction gratings to reverse the applied chirp.

3.1.2 Intensity contrast improvement

The amplification of stimulated emission from the gain medium can also amplify other light in the system. Excitation of atoms in the gain medium causes the generation of spontaneous emission as the excited states decay; this is emitted in random directions and is incoherent, unlike the stimulated emission which is emitted in phase with the seed pulse propagating through the gain medium. A fraction of the spontaneous emission propagates along the path of the amplified pulse and may be amplified in later stages. The final laser beam that exits the system contains this amplified spontaneous emission (ASE) in the form of a nanosecond duration pedestal in the pulse temporal

intensity profile [162]—parametric fluorescence also contributes to this pedestal if optical parametric amplification is used. The pulse also contains an exponential rise in intensity for up to tens of picoseconds before the main short pulse arrives, known as the coherent pedestal or rising edge [163]. The coherent pedestal originates from uncompensated dispersion in the compressor as the pulse exits the CPA stage; imperfections and damage in the diffraction gratings or imperfect alignment prevent the stretched pulse from being fully compressed. Finally, short pre-pulses (and post-pulses) can occur in the pulse temporal profile that are more intense than the ASE, due to unwanted reflections from optics in the laser chain.

All of these additional components of a high power laser pulse can be sufficiently intense to drive ionisation and plasma formation with the target prior to the arrival to the main pulse [164]. Pre-expansion of the front surface of a solid foil can lead to self-focussing of the laser pulse and influence the coupling of laser energy to fast electrons and the subsequent ion acceleration [46, 165, 166]. Similarly, pre-expansion of the rear surface is known to degrade ion acceleration [167, 168]. The effect of the laser contrast can be most severe for ultrathin foil targets. The laser pre-pulse can destroy such targets if sufficiently intense, or displace the whole target [169]. Pre-expansion to considerably reduced peak densities can also occur [170], and therefore the optimum thickness for proton acceleration is found to increase with more intense contrast [171, 172]. A high contrast ratio is essential for many laser-solid interactions, even more so as peak laser intensities in the laboratory increase and higher contrast ratios are required to prevent breakdown of the target.

A commonly applied technique to improve the laser temporal contrast is to combine optical parametric amplification [173] with CPA (OPCPA) [174–176]. This mitigates the generation of ASE, yet the pump pulse may still generate unwanted light via parametric fluorescence at a typically lower intensity. The dielectric polarisation density which characterises the optical properties of a dielectric crystal can be described by a Taylor series: $\mathbf{P}(t) = \varepsilon_0(\chi^{(1)}\mathbf{E}(t) + \chi^{(2)}\mathbf{E}^2(t) + \dots)$, where $\chi^{(n)}$ are the susceptibilities. For crystals that lack inversion symmetry, $\chi^{(2)}$ is not negligible and a number of nonlinear optical effects such as second harmonic generation and parametric amplification become possible. Optical parametric amplification uses a phase matched pump pulse with higher frequency, ω_p , than the seed pulse to excite the gain medium. The stimulated emission driven by the seed pulse, of frequency ω_s , therefore also generates

another photon, known as the idler, corresponding to the frequency difference between the pump and seed photons: $\omega_p = \omega_s + \omega_i$.

The laser contrast may also be improved with a third order process called cross polarised wave generation (XPW) [177]. Here, a linearly polarised input photon is returned with polarisation rotated by $\pi/2$. Therefore, with the use of several polarisers, the unconverted light can be filtered out. Due to this being a third order process, the output laser pulse has a broadened spectrum and shortened duration. In addition to reducing the intensity of the laser pre-pulse, its duration can be shortened with the use of Pockels cells. These devices comprise an electro-optic crystal that acts as a variable waveplate. Although they are only fast enough to switch approximately a nanosecond, or many hundreds of picoseconds, before the main pulse arrives, they can be used to effectively block all light from the laser before this time.

Lastly, the contrast can be improved using a device known as a plasma mirror that takes advantage of the increase in reflectivity of a material upon becoming ionised and forming a plasma in an intense laser field. Plasma mirrors [178–181] are one of many plasma optics [182] that can control light at intensities beyond the damage threshold of solid-state optics. They are generally composed of a transmissive substrate material such as fused silica upon which the laser light is focussed, before reflection and recollimation when the plasma mirror switches on for sufficiently intense light. The surface is often coated with antireflective material to reduce the amount of light reflected before it switches on and therefore improve the contrast ratio as much as possible. The damage to the surface prevents its use at the same location for repeated shots. This drawback makes plasma mirrors a limiting factor for high repetition rate operation, although the use of liquid crystal films as plasma mirrors [183] may provide a high repetition rate solution if the associated contrast enhancement is necessary. Plasma mirrors typically improve the contrast ratio by 10^2 [181], and switch on < 1 ps before the main pulse [181, 184]. Although, this time can be varied by adjusting the intensity on the plasma mirrors. The use of ellipsoidal plasma mirrors [185, 186] also enables higher laser intensities to be reached. If the incident laser beam is focussed at one of the foci of the ellipse before reaching the ellipsoidal plasma mirror surface and being reflected and focussed at the other focus of the ellipse, the focal spot at the latter focus is narrower causing a potential increase in the laser intensity, which can interact with a locally placed target.

3.1.3 State of the art laser systems

At the time of writing this thesis numerous petawatt class laser systems around the world are planned, are under development, or have recently begun operation. These are either upgrades to existing systems or new facilities designed to enable experiments at higher laser intensities and repetition rates. In the UK, the 500 TW Astra-Gemini and 1 PW Vulcan lasers at the Central Laser Facility will be superseded in the near future by the extreme photonics applications centre (EPAC), that will be capable of delivering 1 PW pulses at 10 Hz. The availability of laser pulses at a multi-Hz rate will enable greater data acquisition and the possibility of applying the particle or photon beams from laser-driven plasma accelerators for a range of purposes in fundamental science and industry. The 350 TW system at the Scottish Centre for the Application of Plasma-based Accelerators (SCAPA), within the University of Strathclyde, is also capable of 5 Hz operation and will support the development of these accelerators and their application. The Vulcan 20-20 project (expected to be completed in 2029) will deliver an upgrade to the existing Vulcan laser facility, with 20 PW pulses and up to 8 additional longer duration beams with a total energy of 20 kJ.

Outside of the UK, the Apollon 10 PW laser [187, 188] in Saclay, France has been operating at the 1 PW level for several years and is nearing completion. ELI-NP [158, 189] in Romania has demonstrated 10 PW and is actively supporting experiments at 1 PW. ELI-Beamlines [190, 191] in the Czech Republic will soon deliver 10 PW pulses, and also supports a 1 PW beamline at 10 Hz [192]. Another pillar of ELI, ELI-ALPS [193], offers a number of high power and high repetition rate laser beams, yet is specialised in the delivery of few cycle pulses for attosecond science. In the United States, the BELLA laser at Berkeley offers 1 PW pulses, and the ZEUS laser at Michigan will soon deliver 3 PW laser pulses. Finally, in Shanghai the SULF 10 PW laser [194] is almost completed, and a 100 PW laser named the station of extreme light is under development [195]. There are many other examples that have not been included here. All of these systems rely upon CPA, and usually OPCPA; their wavelengths are all close to $1\mu\text{m}$, usually 800 nm, and most of them have pulse duration at peak power equal to tens of femtoseconds. With their use, experiments will regularly occur at laser intensities $> 10^{22} \text{ W cm}^{-2}$ similar to the conditions simulated in this thesis, where ion acceleration and gamma ray production will be improved and high field physics will

become important.

3.2 High energy radiation detection

3.2.1 Detection materials

Extraction of a signal for the measurement of a photon or particle beam generally requires some material to be placed in the path of the beam that converts the incident radiation into another form. The deposited energy as photons and fast particles propagate through matter depends upon the cross section for interaction [196], which tends to increase for higher charge particles. High energy photons and electrons exhibit a slowly changing energy deposition curve as they stop in matter, whilst protons and ions deposit a considerable fraction of their energy close to their stopping point. This corresponds to the Bragg peak in their stopping profile, and is due to the interaction cross section increasing rapidly as the ions reach low velocities. The differences in the stopping curves for different incident particles (including differences between ion species) and for different energies of incident radiation makes possible identification of different contributions. Although, unwanted particles can be filtered out as discussed in the next section. It is important to choose a material which is sensitive to the incident radiation of interest, exhibits a change which can be measured and has high dynamic range i.e. does not saturate quickly with increasing flux. The most commonly used materials for detection of high energy particles and photons in laser-solid interactions are outlined here.

Radiochromic film (RCF) [85, 197] is a plastic film that becomes more opaque upon irradiation with ionising radiation. This corresponds to an increase in its optical density:

$$OD = \log_{10} \left(\frac{I_0}{I} \right), \quad (3.2)$$

where I_0 is the intensity of light for complete transmission and I is the intensity of light transmitted. The film is permanently changed after a single use and should not be used again. Given that the information on the energy deposited in the film is given by its optical density, it must be physically removed from the interaction chamber and scanned. The scanners used for RCF usually employ visible light at several different wavelengths. The slow retrieval of information from RCF makes it inappropriate for

high repetition rates, yet its insensitivity to the electromagnetic pulse associated with high power laser-solid interactions, that can interfere with nearby electronics, makes it a robust and reliable choice for use in diagnostics. The spatial resolution can be as low as several microns, enabling detailed spatial information on the incident radiation to be obtained. A number of RCF types are available, such as HDV2 and EBT3 among others, that contain different layers and thicknesses of each layer. RCF is most commonly used for measuring the dose of accelerated protons due to the large energy deposition they deliver close to their stopping point. These films require calibration with conventional accelerators, such as a cyclotron, to enable absolute measurements of proton numbers.

Another often used film that responds to ionising radiation is Fujifilm imaging plate [198, 199]. It is comprised of a phosphor layer supported by a steel base and a magnetic layer; some types have a protective mylar layer on the phosphor surface. The active phosphor layer contains barium fluorobromide with europium ions that have charge +2. The incident radiation can ionise the europium ions further to a +3 charge state by releasing an electron into the conduction band which becomes trapped due to lattice defects, reaching a metastable state corresponding to a colour centre. The electron is released by photostimulated luminescence, where an incident photon re-excites the electron from its metastable state, enabling it to recombine with the hole in the valence band and emit another photon. Similar to RCF, image plate is resistant to electromagnetic pulses and must be physically removed and scanned. However, it must be shielded from ambient light to prevent recombination of the metastable electrons before scanning. Spontaneous emission from the metastable state does occur, and causes the stored signal to reduce exponentially over time [198, 199]. The scanning is therefore best performed a fixed time after exposure, or the signal must be corrected for the different delay times before scanning. Image plate can be erased after scanning with exposure to bright light for more than 15 minutes and can then be reused. The advantages of image plate include high dynamic range and sensitivity, and it is often used for the measurement of x-ray and electron beams.

An alternative to these films that is suitable for higher repetition rates is the use of scintillators. These materials emit visible or UV light when radiation propagates into them and is absorbed. Electrons are excited into the conduction band where they can interact with other particles in the material and generate other electron-hole pairs, until

radiative recombination occurs when the electrons reach the luminescence centres of the material. A characteristic spectrum of light is therefore emitted, and multiple different scintillators can be combined to emit signals at different colours. As particles propagate through a scintillator their energy will be absorbed according to their stopping curve, with protons and ions exhibiting a significant Bragg peak near their stopping point as mentioned previously. For x-rays and gamma rays, however, absorption occurs primarily through the photoelectric effect for energies $\lesssim 100$ keV; Compton scattering becomes important above this threshold, and for energies exceeding 1.02 MeV pair production becomes an important absorption mechanism also. The emitted light can be immediately imaged with a camera, but considerable shielding from other light produced in the interaction is required. The camera can also be susceptible to the electromagnetic pulse from the interaction, which can prevent data acquisition on some shots unless appropriate measures are taken to limit its effect. The recorded camera image can contain many pixels that are saturated or have signal considerably above those surrounding it due to direct hits on the CCD by energetic radiation; shielding the camera or placing it far from the interaction can limit their appearance, yet they can often be digitally filtered from the recorded image. The time dependence of the scintillator emission varies depending upon the material. Although much of the light from the scintillator is often emitted in a fast decaying component within $\lesssim 1 \mu\text{s}$, light can continue to be emitted for a much longer time in a slower decaying component known as afterglow. The afterglow of scintillators may become problematic for multi-Hz repetition rates due to its interference with measurements for successive shots. Different scintillator materials have considerably different amounts of afterglow and light yields for a given energy deposited. Therefore, the most appropriate material can vary depending upon the expected radiation beam and repetition rate. For high fluences, saturation of the light output or the pixel signal in the camera can occur, and the scintillator material may acquire permanent damage. The dynamic range and spatial resolution of RCF and image plate is superior to that achievable with the use of scintillators, yet their low repetition rate make them unsuitable for continued use with modern laser facilities.

A number of other materials and devices can be used for the detection of radiation in high power laser-matter interactions [200, 201]. Notable examples include the micro-channel plate (MCP), which uses a large number of capillaries that multiply electrons

freed from their walls by incident radiation. An electric field is applied between the entrance and exit of the capillaries that causes initially freed electrons to move towards the capillary exits, whilst many of them propagate into the inner walls of the capillaries releasing further electrons that also drift toward the capillary exit. The multiple charges produced for a single incident particle make MCPs useful for detecting low fluences. The electrons exit the capillaries onto a detector; usually a phosphor screen which converts them into visible light that is collected by a camera system. Pixel detectors [196, 202, 203] such as a charge-coupled device (CCD) can also be used with high energy radiation, and single particle detection is possible provided the number of particles per unit area is sufficiently low. Lastly, radiation at MeV energies can cause nuclear activation of appropriately chosen materials, producing characteristic decay radiation that can be measured to infer the incident radiation beam.

3.2.2 Diagnostics

RCF, image plate or scintillators can be placed into successive layers interspersed by other materials to slow the incident radiation in a spectrometer that utilises the different energy deposition curves for radiation of different species and energy to unfold the spectrum—known as calorimeters within particle physics. An example of this is the RCF stack often used to diagnose spatially-resolved proton spectra. The proton Bragg peak enables the maximum proton energy to be well diagnosed due to the absence of signal in the subsequent RCF layer. Electrons and photons with similar energies are often produced, and propagate further through the attenuating layers of the stack. Their contribution can be inferred from the slowly changing signal in the RCF layers at the rear of the stack provided it extends beyond the range of the highest energy protons. Although, when present, the Bragg peak due to protons usually dominates the energy deposited in the thin RCF layers. Scintillators can be used in a similar way, in successive layers with optional filter materials in between, in a linear absorption spectrometer; the row of scintillator and filter layers is usually surrounded with lead to shield the scintillator crystals from other radiation, and one side is left open in view of a camera system which captures the emitted light. In this case, information on the 2D spatial profile of the incident radiation beam is not captured. The diagnostic is usually placed ~ 1 m from the interaction point and subtends only a small solid angle from the source, thus giving a measurement of the radiation energy spectrum

along a chosen direction. When measuring x-ray and gamma ray spectra, magnets are commonly placed before the spectrometer to deflect charged particles. Also, multiple rows can be used in an array configuration (see [204], for example) to potentially gain 1D spatial information and improve the spectral retrieval.

If the 2D spatial profile of radiation is required and precise information on the spectrum is not necessary, a single layer of RCF, image plate or scintillators can instead be used. An array of filters with different thicknesses (assuming the same material) in a repeating pattern in front of the detection layer [205–207] can still enable 2D spatial and spectral information to be retrieved.

A number of diagnostics are made possible with the deflection of charged particles in electric and magnetic fields. Charged particles of the same type but with different energies can be physically separated, enabling the measurement of the energy spectrum, and charged particles can be removed from neutral particle and photon beams allowing them to be diagnosed without additional contributions. It is common practice for measurement of the electron spectrum to reduce the electrons to a narrow beam by passing them through a small hole in an attenuating material, and then to place a dipolar magnetic field in the path of the beam to separate the electrons by their energies, with the least energetic electrons deflected the most. The line of deflected electrons can then be detected with image plate or scintillators. If positrons are generated, they are deflected opposite to the electrons and can be measured with detection materials in their path. For the measurement of proton and ion beams, a similar narrow beam of ions can be passed through a Thomson parabola consisting of both electric and magnetic fields, before the deflected particles reach a 2D detector such as image plate or an MCP system. The use of both electric and magnetic fields enables different ion species and charge states to be spatially separated, due to their different charge-to-mass ratios, where each produces a unique parabolic trace away from the point of no deflection. The disadvantage of both of these techniques is there is no spatial information on the particle beams due to the sample of only a narrow component along one direction. For this reason multiple Thomson parabola spectrometers are often used at different angles in the detection of accelerated ions, with holes placed in RCF stacks for the corresponding components of the beam in the direction of the Thomson parabola spectrometers.

Several alternative diagnostics for fast proton and ion beams include the time-of-flight detector, which uses the delay in time from the appearance of photons generated

in the interaction to the arrival of protons and ions to estimate their velocity and corresponding energy. The further away from the interaction point this is placed the better the energy resolution of the diagnostic due to its fixed temporal resolution. As mentioned previously, the nuclear activation of certain materials can be used to diagnose the ion spectrum, if the cross section for the nuclear reaction is well known and the decay products are measured. This method can also be used for diagnosing multi-MeV photons. Numerous other diagnostics of high energy radiation to those listed here are possible, yet these are the diagnostics that have been most often used for the measurement of radiation from laser-solid interactions, and the diagnostics expected to be first used for the radiation beams produced with new multi-PW laser systems.

The generation of particles and photons with energies in the 100 MeV–1 GeV range (per nucleon for ions) with multi-PW laser systems, as produced in the simulations presented in this thesis, may require or enable different approaches to their measurement. This more energetic radiation will propagate further in matter, and the particles will become harder to deflect and separate with applied electric and magnetic fields. More filtering will be required in calorimeters, and applied magnetic or electric fields may need to be increased unless additional propagation distance is available for the deflection of particles before a detector. A possible solution for ions could be to introduce a filter material to reduce their velocity before they propagate into a Thomson parabola ion spectrometer, time of flight detector or deflecting magnetic field placed before a high energy photon diagnostic. It may even be useful to use a calorimeter instead, to detect the energy deposited before the remaining radiation reaches another diagnostic. If particles and photons cannot be fully separated, Cherenkov or transition radiation could be used to diagnose a charged particle beam amongst intense synchrotron (and bremsstrahlung) radiation. It may also be advantageous to adopt other diagnostic techniques and detection methods used in particle physics [196, 208]. For example, the increased propagation distance in matter with such high ion energies could enable the use of silicon tracking detectors. Although particle identification, spatially-resolved measurements and spectral measurements are readily possible with the range of diagnostics available, the information gathered is usually time-integrated over the femtosecond duration interaction. Therefore, only time-integrated properties of the gamma rays produced are considered in chapter 5, to allow a more direct comparison with experimental results.

3.3 Particle-in-cell modelling

In laser-plasma interactions such an enormous number of real particles are involved that it is impractical to model the motion of each particle individually, and other methods for kinetic modelling of plasmas have been developed. For a plasma in which the effect of collisions is negligible, the Vlasov equation describes the variation of the distribution function of particle momenta and positions with time:

$$\left[\frac{\partial}{\partial t} + \mathbf{v} \cdot \nabla + q (\mathbf{E} + \mathbf{v} \times \mathbf{B}) \cdot \frac{\partial}{\partial \mathbf{p}} \right] f(\mathbf{p}, \mathbf{r}, t) = 0. \quad (3.3)$$

This equation can be modified to account for the effect of collisions with the addition a collision operator, $(\partial f / \partial t)_{coll}$, to the right-hand-side. In particular, for applications such as inertial confinement fusion the Fokker-Planck collision operator is often accurate, and may be combined with equation 3.3 to numerically model various interactions [209]. However, directly solving the Vlasov (or Vlasov-Fokker-Planck) equation can require large computational resources.

Particle-in-cell methods [210, 211] are generally much more efficient for collisionless plasmas. The specific routines used by EPOCH [211], the code used throughout this thesis, are described in this section, yet the methods used by other PIC codes, for example, SMILEI [212], are similar. PIC simulations divide the interaction space into many cells upon which the electric and magnetic fields are calculated self-consistently with the densities and currents of macroparticles, corresponding to many real particles, moving through the simulation space. The macroparticles are initialised with a weight corresponding to the number of real particles they represent, and a shape. The simplest macroparticle shape is a top hat function, where the particle weight is uniform within a finite volume. Higher order b-spline shape functions are commonly used, however, to help mitigate anomalous self-heating of the simulated plasma, which occurs when the Debye length is not well resolved by the grid cells.

The electric and magnetic fields are defined on the Yee staggered grid [213] as shown in figure 3.2. The finite difference time domain (FDTD) method is used to calculate the iterative changes to the electric and magnetic fields with each timestep from the start of the simulation, where the particles are pushed using the Lorentz force at the half timestep. The changes to the fields are simply found from Maxwell's equations with

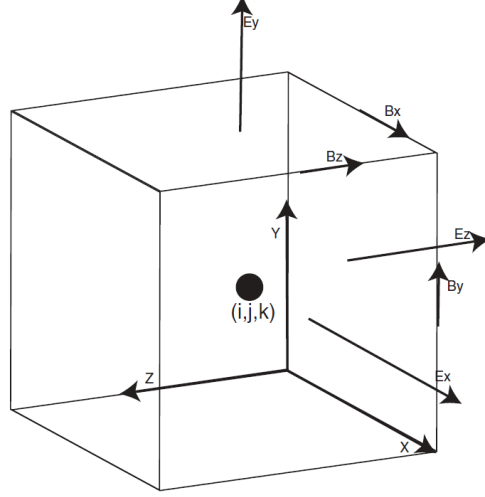


Figure 3.2: Diagram of the Yee staggered grid, from [211].

calculations at half-integer and integer timesteps (superscripts containing n correspond to timesteps):

$$\mathbf{E}^{n+\frac{1}{2}} = \mathbf{E}^n + \frac{\Delta t}{2} \left(c^2 \nabla \times \mathbf{B}^n - \frac{\mathbf{j}^n}{\varepsilon_0} \right), \quad (3.4)$$

$$\mathbf{B}^{n+\frac{1}{2}} = \mathbf{B}^n - \frac{\Delta t}{2} \left(\nabla \times \mathbf{E}^{n+\frac{1}{2}} \right). \quad (3.5)$$

After calculation of the fields at the half timestep, the particle pusher is applied:

$$\mathbf{p}^{n+1} = \mathbf{p}^n + \Delta t \mathbf{F}_L^{n+\frac{1}{2}}, \quad (3.6)$$

where \mathbf{F}_L is the the Lorentz force evaluated for the fields and particle velocity at the half timestep, $n+\frac{1}{2}$. The current is updated by the particle pusher at this step, allowing the fields at the next step to be calculated as follows:

$$\mathbf{B}^{n+1} = \mathbf{B}^{n+\frac{1}{2}} - \frac{\Delta t}{2} \left(\nabla \times \mathbf{E}^{n+\frac{1}{2}} \right), \quad (3.7)$$

$$\mathbf{E}^{n+1} = \mathbf{E}^{n+\frac{1}{2}} + \frac{\Delta t}{2} \left(c^2 \nabla \times \mathbf{B}^{n+1} - \frac{\mathbf{j}^{n+1}}{\varepsilon_0} \right). \quad (3.8)$$

Although collisions are usually not necessary to model in high intensity laser-plasma interactions, binary collisions can be added. Similarly, ionisation can also be modelled (see [211] for details). For the interactions studied in this thesis, where thin targets composed of light elements (hydrogen and carbon) are irradiated by laser intensities well above the relativistic threshold, the targets are assumed to be initially fully ionised.

The energy required to fully ionise the volume of target material simulated is only a small fraction of the laser energy, and the light preceding real laser pulses is expected to ionise and heat the target prior to the main interaction. Ionisation becomes important when modelling interactions with a large volume of high Z material.

3.3.1 Synchrotron radiation and pair production in EPOCH

The additional effects which can become important for the conditions studied in this thesis are synchrotron emission and nonlinear Breit-Wheeler pair production. These processes (and their time inverse) are the first order effects in the Furry picture of QED [36, 214]. Synchrotron emission is included in EPOCH with a semi-classical model where the electrons (and positrons) move classically in between photon emission events that are described by QED (see section 2.6.3 for additional details). Both the emitted photons and generated positrons are treated as macroparticles, and thus have a weight parameter corresponding to the number of real particles they represent. The high energy photons produced are assumed to be emitted parallel with the electron trajectory, and the photon momentum ($\hbar\omega/c$) is subtracted from that of the electron. After emission, the photons do not interact with each other and propagate ballistically, unless they decay into electron-positron pairs via the nonlinear Breit-Wheeler process. The rate of synchrotron emission is

$$\frac{dN_\gamma}{dt} = \sqrt{3} \frac{\alpha_{fc}}{\lambda_c} \frac{\chi_e}{\gamma} \int_0^{\chi_e/2} \frac{F(\chi_e, \chi_\gamma)}{\chi_\gamma} d\chi_\gamma, \quad (3.9)$$

where the parameters are as defined in section 2.6.3. The rate of nonlinear Breit-Wheeler pair production is

$$\frac{dN_\pm}{dt} = 2\pi \frac{\alpha_{fc}}{\lambda_c} \frac{m_e c^2}{\hbar\omega} \chi_\gamma T_\pm(\chi_\gamma), \quad (3.10)$$

where $T_\pm(\chi_\gamma) \approx 0.16 K_{1/3}^2(2/3\chi_\gamma)/\chi_\gamma$ and $K_{1/3}$ is a modified Bessel function of the second kind.

These processes are modelled using a Monte Carlo algorithm. The probability that a particle emits after propagation through a plasma with optical depth τ_{em} is $P = 1 - \exp(-\tau_{em})$. A particle is randomly assigned a probability of emission between 0 and 1, and the optical depth traversed before emission occurs is calculated as $\tau_{em} = -\ln(1 - P)$. For each particle, the optical depth is integrated over time until emission

occurs as soon as $\tau \geq \tau_{em}$:

$$\tau(t) = \int_0^t \frac{dN}{dt}(t') dt', \quad (3.11)$$

where dN/dt is replaced by equation 3.9 or 3.10 for synchrotron emission or pair production respectively.

The photons emitted can take an energy within a range of values. The probability that an electron or positron with the quantum parameter χ_e emits a photon with energy corresponding to χ_γ is

$$p(\chi_e, \chi_\gamma) = \frac{F(\chi_e, \chi_\gamma)}{\chi_\gamma} \left[\int_0^{\chi_e/2} \frac{F(\chi_e, \chi_\gamma)}{\chi_\gamma} d\chi_\gamma' \right]^{-1}. \quad (3.12)$$

Integration of equation 3.12 thus gives the cumulative probability that the emitted photon has an energy corresponding to χ_γ :

$$P(\chi_e, \chi_\gamma) = \int_0^{\chi_\gamma} p(\chi_e, \chi_\gamma') d\chi_\gamma'. \quad (3.13)$$

The energy of the emitted photon is determined by randomly assigning a value for P in equation 3.13 (between 0 and 1), and comparing to tables of this probability function. For nonlinear Breit-Wheeler pair production, the energy of the gamma ray photon is given to the electron and positron created. The energy each of the particles take is calculated with a similar method, where the probability that one of the particles takes a fraction f of the energy, $p(\chi_\gamma, f)$, is used (see figure 7 in [215]).

The inclusion of these first order QED processes in EPOCH with this method requires many assumptions. The assumption that the fields are much weaker than the Schwinger field is appropriate for any experimentally feasible conditions in the near future. However, the local-constant-field approximation (LCFA) that assumes the spatial and temporal variation of the fields has negligible effect on the processes may not always be accurate even for peak laser intensities corresponding to $a_0 \gg 1$, where it is often assumed to be valid; several theoretical investigations show LCFA overestimates photon emission at low energies [216–218]. The assumption of incoherent emission, such that it can be treated individually for different particles, is appropriate where the distance between emitting particles is much larger than the wavelength of the emitted photon. Consider a plasma with electron density $n_e = 100n_c$ for $\lambda_L = 800$ nm (corresponding to $1.75 \times 10^{29} \text{ m}^{-3}$), a photon with wavelength equal to the

average distance between electrons ($n_e^{-1/3}$) has energy 7 keV. This plasma can only be transparent to the laser and therefore produce considerable synchrotron radiation for laser intensities where $a_0 > 100$ ($= n_e/n_c$), yet at such high laser intensities most of the energy converted into synchrotron radiation is expected to go to $\gg 100$ keV photons (see figure 5.6(d) where $a_0 \approx 120$, for example). Although coherent emission may become important for up to keV photons in regions of high density plasma, it is appropriate to assume the bulk of the emission, at much higher energies, is incoherent.

The rates of synchrotron emission and pair production assumed here (equations 3.9 and 3.10) are averaged over photon polarisation and particle spin, yet the dependence of these processes on spin and polarisation can become important [219–224]. Indeed, polarised gamma ray beams and spin-polarised electron and positron beams could be producible with high intensity lasers. Electrons can have either a projection of their spin parallel or antiparallel to a spin basis, \hat{s} , corresponding to a magnetic moment $\boldsymbol{\mu}_e = \pm \frac{1}{2} g_s \mu_B \hat{s}$, where $g_s \approx 2$ is the electron spin g-factor and $\mu_B = e\hbar/2m_e$ is the Bohr magneton. The quantum synchrotron function is given as a function of the initial and final spin, and photon polarisation in [219], showing the value of the function changes with each of these additional parameters. For laser-solid interactions, PIC simulations including the polarisation and spin dependence have demonstrated the ability to generate polarised positrons [225–227]. Although the synchrotron emission and number of positrons produced in simulations neglecting these dependencies may require some correction, the results obtained are still useful for providing a rough indicator of the synchrotron radiation and number of positrons that should be produced, enabling the design of experiments to maximise their generation.

The production of positrons through the linear Breit-Wheeler process ($\gamma + \gamma \rightarrow e^- + e^+$) is also neglected here. The number of positrons created by this process is expected to be small enough to not influence the plasma dynamics and therefore it is not necessary to include in the simulation routines. An estimate of positron production through this linear process can be gained with analysis of the photon dynamics. Bethe-Heitler pair production is also not included in the simulations performed in this thesis. This is appropriate because this pair production mechanism is only important when high energy photons (> 1.02 MeV) propagate through high Z material. Due to the thin targets and light elements used in this work the number of pairs produced in this way is expected to be negligible.

3.3.2 Limitations and convergence

When running PIC simulations it is essential that the resolution of the grid cells is sufficient to accurately resolve the plasma dynamics. This generally means that the dimensions of the grid cells must be less than the Debye length (equation 2.36). Otherwise, self-heating of the plasma can occur within the simulation without any energy input. This presents challenges for simulating dense solids and low temperatures. To avoid such issues high density solids are often modelled at lower densities, and the target is often assumed to be preionised and heated. Target pre-expansion and heating is expected to occur anyway experimentally due to the laser light preceding the short pulse. Although the simulations can be extended for up to approximately a picosecond before the main interaction to enable modelling of the most intense component of the laser rising edge, it is too computationally expensive to model the full temporal-intensity profile of the laser pulse prior to the main interaction. The laser intensity in the nanosecond duration pedestal before the main pulse is often low enough that the target dynamics are dominated by the laser-driven shock. Therefore, hydrodynamic simulations can be used to model this early stage of the interaction, provided the intensity is sufficiently low to avoid significant kinetic effects, and the resulting density profile can be used to initialise the PIC simulation of the main interaction. Alternatively, a reasonable estimate of the front surface density scale length or full target pre-expansion can be used to set an initial density profile.

As well as having sufficient spatial resolution, the simulations must have sufficiently small timesteps. The Courant-Friedrichs-Lewy condition requires the timestep be smaller than the time it takes light to cross a grid cell. The timestep must also be sufficient to resolve both the electron plasma frequency (ω_p) and gyrofrequency ($\omega_c = eB/\gamma m_e$). The number of particles per cell must be sufficient to produce accurate results. This is often tested by increasing the number until the simulation results converge. The noise in the results also reduces with increasing numbers of particles per cell. Ensuring the grid size and timestep are sufficiently small is similarly done individually by testing the convergence of results. Provided that sufficient computational resource is available on a high performance computer to run multidimensional PIC simulations, the limiting factor often becomes the size of the output files, which can occupy terabytes of disk space. Therefore, careful choice of the required output

parameters and the frequency of output must be made.

Accurate PIC simulations do, however, provide a valuable tool for testing theory and providing new understanding of the physics occurring in experiments, where the information available from diagnostics is often limited. PIC simulations enable access to spatially and temporally resolved information with particle tracking and the ability to test configurations not achievable experimentally. They can be used to improve the design of experiments and investigate physical processes over wide parameter ranges rapidly with fewer assumptions than analytical models.

3.3.3 Convergence testing

To test the convergence of the PIC simulations shown in this thesis, the simulations of a small number of cases were repeated using different numbers of particles per cell and cell sizes.

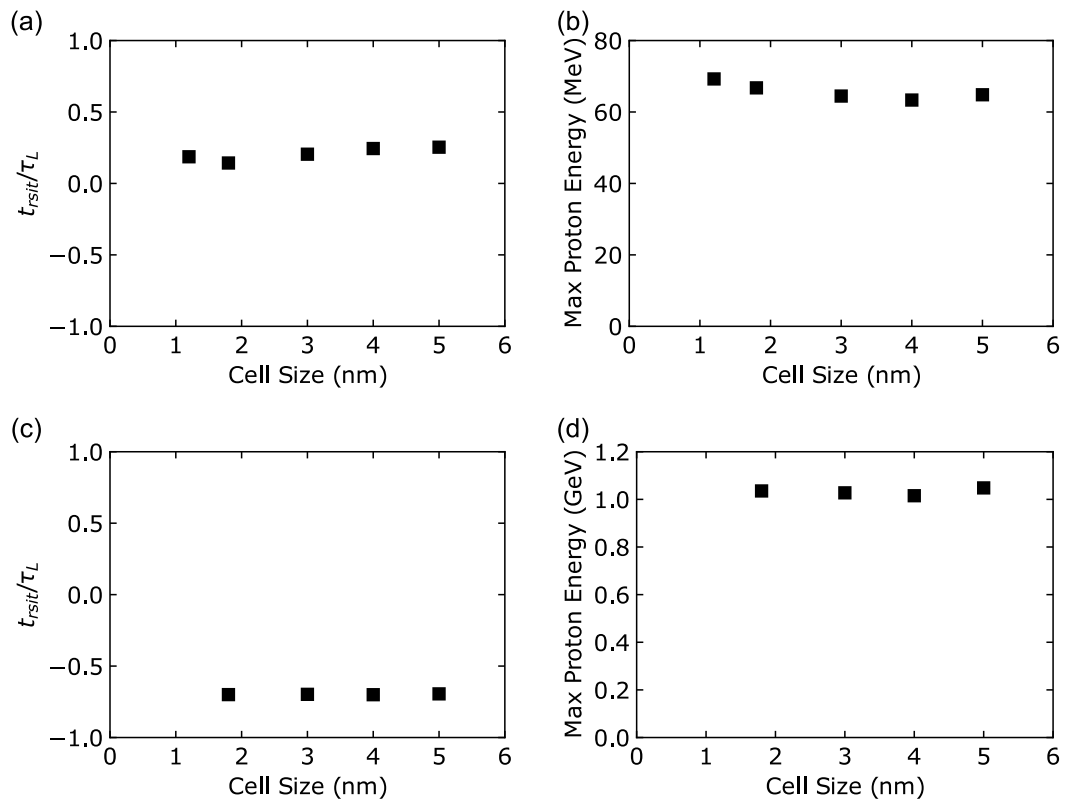


Figure 3.3: (a) Onset time of relativistic transparency and (b) maximum proton energy, as a function of the size of the simulation grid cells, for a $l = 50$ nm target at $a_0 = 16$. (c) and (d) corresponding plots for a $l = 200$ nm target and $a_0 = 310$. The 5 nm cell size corresponds to the result for the 5 nm \times 12 nm cell size used in chapter 4 and all other cell sizes tested correspond to square cells.

For the simulations in chapter 4, the grid cell size used was $5\text{ nm} \times 12\text{ nm}$ and the number of particles per species per cell was 50. Convergence testing of the cell size was carried out by repeating the simulation of a $l = 50\text{ nm}$ and $l = 200\text{ nm}$ target at $a_0 = 16$ and $a_0 = 310$, respectively, with reduced size square cells with widths between 1.2 nm and 4 nm . The laser was linearly polarised in both cases. The maximum proton energies and onset times of relativistic transparency obtained are shown in figure 3.3. The onset time of relativistic transparency varied by 11% of the pulse duration across these simulations for $a_0 = 16$ in figure 3.3(a), and by 0.6% of the pulse duration for $a_0 = 310$ in figure 3.3(c). The maximum proton energies were observed to change by 6.8% and 1.2% for the different laser intensity cases in figure 3.3(b) and (d), respectively. The changes in the results found by varying the cell size were small compared with the variation found in the parameter scans. Therefore, the $5\text{ nm} \times 12\text{ nm}$ cell size was determined to be sufficiently small.

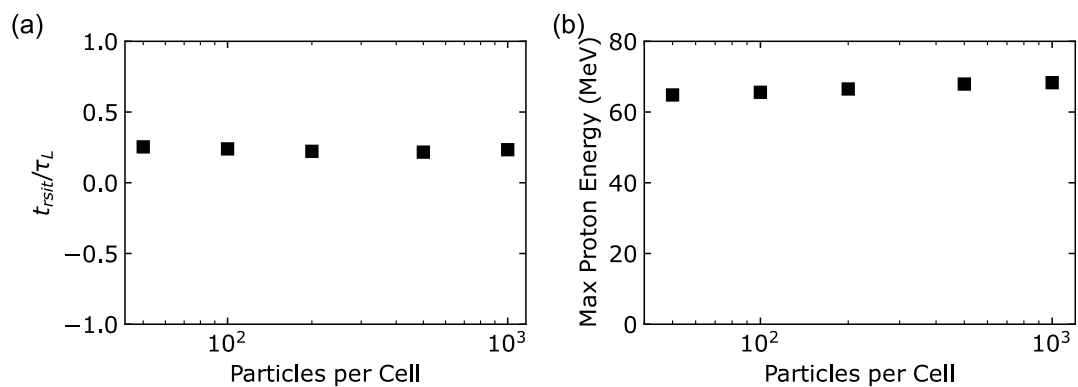


Figure 3.4: (a) Onset time of relativistic transparency and (b) maximum proton energy, as a function of the initial number of particles per cell per species in the simulation, for a $l = 50\text{ nm}$ target at $a_0 = 16$ with linear laser polarisation along the y -axis.

The convergence with number of particles per cell was separately tested for a single case with $l = 50\text{ nm}$, $a_0 = 16$ and linear laser polarisation. The number of particles per cell per species was tested at a number of values between 50 and 1000. The results are shown in figure 3.4. The onset time of relativistic transparency varied by 2.5% whilst the maximum proton energy increased by 5.6%. These changes were also small compared to those observed in the parameter scans in chapter 4, and 50 particles per cell per species was determined to be sufficient for the simulations reported in that chapter.

The simulations presented in chapter 5 were performed to investigate the gener-

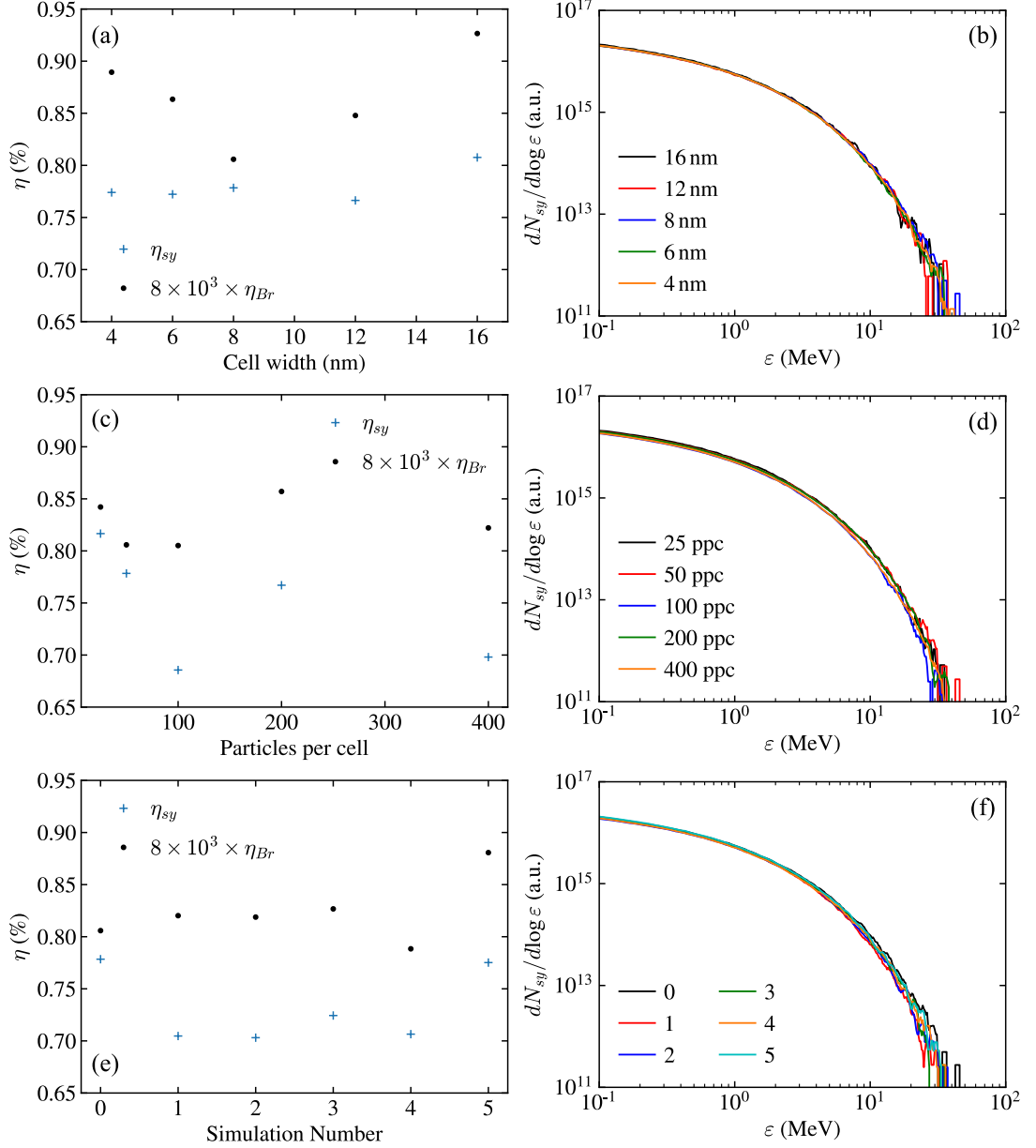


Figure 3.5: Convergence testing results of 2D simulations where $I_L = 10^{22} \text{ W cm}^{-2}$, $\tau_L = 30 \text{ fs}$, $\phi_L = 3 \mu\text{m}$ and $l = 300 \text{ nm}$. (a), (c) and (e) conversion efficiency of laser energy into synchrotron and bremsstrahlung radiation for parameter scans of the simulation cell width, electron particles per cell and number, respectively. (b), (d) and (f) synchrotron radiation energy spectra for each parameter scan, in the same order.

ation of gamma radiation. Therefore, separate testing was completed to assess the convergence of laser energy conversion into synchrotron and bremsstrahlung gamma rays. The 2D simulations were tested using a single case in the approximate centre of the investigated parameter ranges corresponding to laser intensity $10^{22} \text{ W cm}^{-2}$, pulse

duration 30 fs, focal spot FWHM $3\ \mu\text{m}$ and a 300 nm thick target foil. The conversion efficiency of laser energy into synchrotron radiation (η_{sy}), scaled conversion efficiency into bremsstrahlung radiation (η_{Br}) and synchrotron radiation energy spectrum are shown in figure 3.5 for each of the test simulations, where the cell size is $8\ \text{nm} \times 12\ \text{nm}$ and 50 (10) electron particles (ion particles per species) per cell are used unless shown to be varied. The 2:3 ($\Delta x:\Delta y$) aspect ratio of the cells is maintained in the scans of the cell width (Δx) in figure 3.5(a) and (b). The ratio of 5:1 of number of electron particles per cell to ion particles per species per cell is separately maintained in the scans of electron particles per cell in figure 3.5(c) and (d). The apparent noise in the conversion efficiencies for the cell size and particles per cell scans dominates any gradient in the results when the lowest fidelity cases are neglected. The synchrotron radiation energy spectra also show no significant alterations in these scans. The highest fidelity feasible to use with the available computing resources, $8\ \text{nm} \times 12\ \text{nm}$ and 50 (10) electron particles (ion particles per species) per cell, was therefore chosen. The reference case tested here was also repeated a further five times to assess the simulation noise. The results are shown in figure 3.5(e) and (f). The standard deviation of the conversion efficiencies are 4.4% and 3.5% of the mean values for synchrotron and bremsstrahlung radiation, respectively. Although varying the initial laser and target parameters will influence the noise in the simulation, these values provide an estimate of the uncertainty in the results shown in chapter 5.

Convergence tests were also performed for the 3D simulations in chapter 5. A laser intensity of $1.1 \times 10^{23}\ \text{W cm}^{-2}$, pulse duration of 30 fs, focal spot FWHM of $1\ \mu\text{m}$ and target thickness of $1\ \mu\text{m}$ were used. For the cell width scan shown in figure 3.6(a) the cell height was kept at 3 times the cell width, and 12 electron particles per cell were used. The number of ion particles per species per cell was kept at half the electron value for all simulations, and a cell width of 10 nm was used for the scan of electron particles per cell in figure 3.6(b). The range of values for η_{sy} for the cell width parameter scan is 4.1% of the median value over a factor 3 change in the cell width, and the range of values for the particles per cell scan is 7.7% of the median value over a factor 16 change in the number of particles per cell. Given the slow variation in the simulation output the results were taken to be sufficiently converged. A cell width of 10 nm and 12 electron particles per cell was then chosen, corresponding to the highest fidelity possible with the available resources. To characterise the simulation noise a further

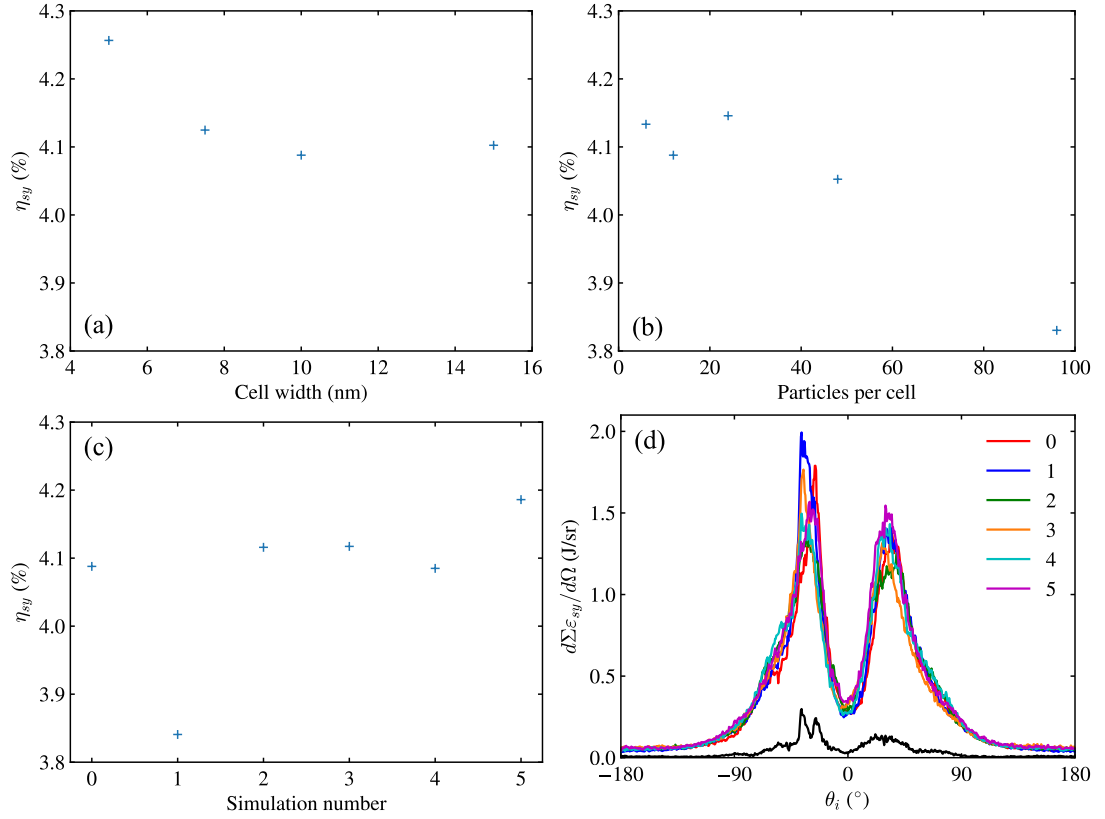


Figure 3.6: Convergence testing results of 3D simulations where $I_L = 1.1 \times 10^{23} \text{ W cm}^{-2}$, $\tau_L = 30 \text{ fs}$, $\phi_L = 1 \mu\text{m}$ and $l = 1 \mu\text{m}$. (a), (c) and (e) conversion efficiency of laser energy into synchrotron and bremsstrahlung radiation for parameter scans of the simulation cell width, electron particles per cell and number, respectively. (d) Angular profile of the radiated synchrotron energy along $\phi = 0$ for each simulation in the noise test, where the standard deviation is shown in black.

five simulations were performed for these parameters. Their results are shown in figure 3.6(c) and (d). The standard deviation of η_{sy} was found to be 2.7% of the mean value. The conversion efficiency results of the 3D simulations in chapter 5 are therefore expected to have a similar fractional uncertainty. The angular profiles of radiated synchrotron energy were also found to have a maximum standard deviation of 0.3 J/sr, corresponding to an approximate fractional uncertainty of 20%. This value can be assumed as an approximate error on the results at the same laser intensity in chapter 5, and an estimate of the error on the results shown in figure 5.11 for $10\times$ higher laser intensity in the absence of further noise testing.

The dimensions of the cells and values of particles per cell tested in this section were kept within a range expected to provide convergent results based upon experience and the discussion in the previous section. Further increasing the cell size or reducing

the number of particles per cell beyond this range is anticipated to generate diverging results.

Optimisation of multi-petawatt laser-driven proton acceleration with relativistic transparency

In this chapter, results for proton acceleration from simulations of laser intensities over several orders of magnitude up to $2 \times 10^{23} \text{ W cm}^{-2}$ incident upon CH foils sufficiently thin for relativistic self-induced transparency to occur are presented. The maximum energy of protons accelerated using current high power lasers with peak intensities up to $\sim 10^{21} \text{ W cm}^{-2}$ has been limited to values $K \lesssim 100 \text{ MeV}$ [7] (perhaps now 150 MeV [8]), and less per nucleon for heavier ions, insufficient for hadron therapy of deep tumours and other potential applications. Increasing the energies achievable is one of the key challenges these sources face. New multi-PW laser facilities with intensities up to $\sim 10^{23} \text{ W cm}^{-2}$ are expected to demonstrate a considerable improvement; however, optimisation of the interaction is essential.

Here, the maximum proton energies achievable with these laser intensities are shown to optimise with the onset time of relativistic transparency. Results for linear and circular polarisation in 2D are presented in sections 4.3 and 4.4, respectively, before comparison with a limited number of 3D simulations capturing the slightly modified and true dynamics of the interaction in section 4.5. The laser pulse rising edge, a component of the light preceding real laser pulses thus an experimental concern, is modelled in section 4.6 and found to increase the optimum target thickness without a

major change to the maximum proton energy. Simulations with and without electron recoil due to synchrotron radiation in section 4.7 for $I_L = 2 \times 10^{23} \text{ W cm}^{-2}$ demonstrate it delays the onset of relativistic transparency, reduces the maximum proton energy (by 10%) and reduces the peak conversion efficiency (by 15%). The optimised maximum proton energies are shown to scale $K \propto I^X$, where $X = 0.53\text{--}0.57$, in section 4.8.

These results were published in *New Journal of Physics* **24**, 053016 (2022).

4.1 Introduction

Target normal sheath acceleration [68, 69, 82, 228] from thin solid foils has been demonstrated as a source of MeV protons for several decades. The surface fields that accelerate the ions are induced by fast electrons propagating out of the target from within. Therefore, the ion energies scale with the fast electron temperature, itself expected to scale with the square root of laser intensity. The leap forward in achievable laser intensities in recent years may enable radiation pressure acceleration [87, 88, 96] to provide higher ion energies, although these processes generally do not occur in isolation and the ions often experience a combination of both [229].

Radiation pressure acceleration can in principle produce a peaked energy spectrum and result in high laser-to-ion energy conversion efficiencies. The highest energies are achieved for ultrathin foils, via the light sail mode of RPA [88, 89, 230]. This is, however, susceptible to instabilities across the target surface and undesirable heating as the target deforms under the radiation pressure [93–95]. For all thicker foils, ions are accelerated at the front surface by hole boring RPA [86, 87, 90]. The onset of relativistic self-induced transparency [231, 232] when the electron density falls below the relativistic critical density ($n_e < \gamma_e n_c$) curtails RPA as the laser light begins to transmit through the target bulk.

The Gaussian laser spatial profile causes the formation of a relativistic plasma aperture through which the light propagates, resulting in diffraction of the laser light and the generation of structures influenced by the light polarisation in the electron and ion beams [48, 97]. The transmitted light may interfere to increase the local laser intensity [49], and contain high order spatial modes [233] and high order harmonics [234]. The direct interaction with and acceleration of electrons by the laser pulse throughout the plasma volume in its path following the onset of RSIT can lead to

improved electric fields and ion energies [7, 99, 235].

The highest proton energies reported to date were measured from ultrathin plastic foils in which a combination of TNSA and RPA is assisted by RSIT [7]. Relativistic transparency of ultrathin foils is well known to offer higher proton energies, with the onset time playing a role [7, 99, 115, 172, 236–238]. However, the contribution of several different mechanisms which occur as the target rapidly expands and is deformed by the electromagnetic force of the laser pulse presents an unstable regime in which optimisation and control of the interaction is challenging. This is further complicated by target pre-expansion due to the laser temporal-intensity contrast in experiments.

The use of laser pulses with peak intensity $I_L \gtrsim 10^{23} \text{ W cm}^{-2}$, which have not been experimentally available until now, will make consideration of radiation reaction due to the synchrotron emission from electrons in the laser field necessary. The production of e^-e^+ pairs will also become important for $I_L \sim 10^{24} \text{ W cm}^{-2}$ and enable the creation of a dense pair plasma [141, 144]. A large fraction of the laser pulse energy may be absorbed by the electron synchrotron emission alone under these conditions [239, 240]. The exploration of the radiation reaction effects on ion acceleration is at an early stage, although numerical modelling for linearly polarised laser pulses has shown it increases the ion energies from relativistically transparent targets and reduces the maximum energies from thicker targets that remain opaque [240–246].

The aim of this chapter is to improve the understanding of the acceleration of protons in relativistically transparent targets for intensities relevant to multi-PW laser facilities. This includes identifying the optimum conditions, examining the role of the laser pulse rising edge and investigating the consequences of radiation reaction.

4.2 Simulation parameters

Laser-driven proton acceleration from CH foil targets was modelled for different conditions of the incident laser pulse intensity, polarisation and temporal-intensity contrast with a series of 2D, and a smaller number of 3D, PIC simulations using the EPOCH code [211]. The target thickness, l , was varied over a range for which the target transitions from initially overdense to relativistically underdense during the interaction.

4.2.1 General conditions

The laser pulse, incident at target normal, propagates along the x -axis with Gaussian temporal and spatial intensity profiles of pulse duration FWHM $\tau_L = 40$ fs, focal spot FWHM $\phi_L = 3 \mu\text{m}$ and wavelength $\lambda_L = 0.82 \mu\text{m}$, similar to laser parameters on multi-PW laser facilities (see for example [188, 189, 247]). Four laser intensities in the range $I_L = 5 \times 10^{20} - 2 \times 10^{23} \text{ W cm}^{-2}$ were simulated for both linear (polarised in the y -direction) and circular polarisation. The simulated laser intensities correspond to $a_0 = 16, 50, 160$ and 310 for linear polarisation and $a_0 = 11, 35, 110$ and 220 for circular polarisation. The CH (equal mix of carbon and hydrogen) foils were initialised as a fully ionised plasma with electron density $n_e = 210n_c$, electron temperature $T_e = 1 \text{ keV}$, ion temperature $T_i = 10 \text{ eV}$ and with 50 particles per cell per species.

The simulation grid cell size was $5 \text{ nm} \times 12 \text{ nm}$ ($x \times y$), with the boundaries of the simulation box all set to free-space. In order to simulate over the required intensity range while making efficient use of computational resources and avoid loss of the highest energy protons from the box edges, the simulation box size was increased with intensity from a minimum of $40 \mu\text{m} \times 36 \mu\text{m}$ up to a maximum of $84 \mu\text{m} \times 96 \mu\text{m}$. To ensure foils with $l \leq 50 \text{ nm}$ were well resolved on the simulation grid, these were simulated with $l = 50 \text{ nm}$ and a reduced density, maintaining the areal density. Ultrathin foils at this scale rapidly expand when irradiated by the leading edge of the laser pulse and therefore modelling them with limited pre-expansion does not significantly change the results. To demonstrate this, a small number of higher resolution (grid cell size of $1.8 \text{ nm} \times 4.32 \text{ nm}$) simulations of non-expanded targets with $l < 50 \text{ nm}$ were conducted and minimal variation was found. All times shown in this chapter, except t_{rsit} , are with respect to the arrival of the peak of the laser temporal profile at $x = 0$, which occurs at $t = 0$.

4.2.2 The laser pulse rising edge

The rising edge of the laser pulse was modelled for linear polarisation, with peak main pulse intensities corresponding to $a_0 = 16$ and 160 , using a sech^2 profile (in addition to the Gaussian main pulse) with peak intensity $0.01I_L$ and pulse duration such that the intensity rises from an initial value of $5 \times 10^{-4}I_L$ at 0.4 ps before the laser peak, as shown by figure 4.1. This profile is similar to typical experimental measurements of

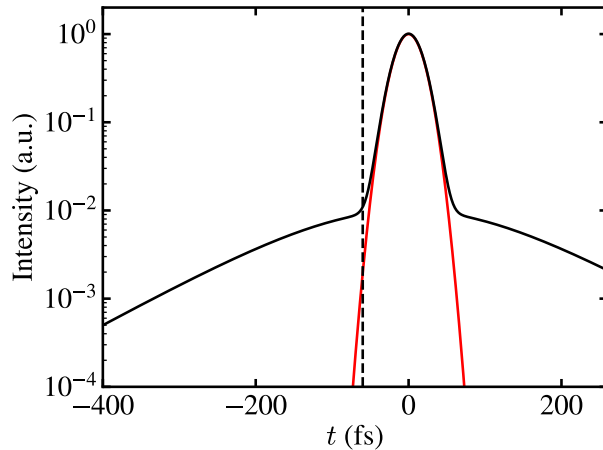


Figure 4.1: The temporal-intensity contrast profile of the 40 fs Gaussian laser pulse without the rising edge (red) and with the rising edge (black). The start time of the simulations without the rising edge is indicated by the vertical dashed line.

the rising edge [184, 248]. The simulation duration before the arrival of the laser peak was extended to accommodate this rising edge profile.

4.2.3 3D

A limited set of 3D simulations were performed for both linear and circular polarisation, for $a_0 = 16$ – 160 and $a_0 = 11$ – 110 , respectively. The simulation box size was increased from $30 \mu\text{m} \times 36 \mu\text{m} \times 36 \mu\text{m}$ ($x \times y \times z$) for the lowest intensities up to $70 \mu\text{m} \times 36 \mu\text{m} \times 36 \mu\text{m}$ at the highest intensities to prevent the loss of protons with low divergence from the laser propagation axis before the end of the simulation. The cell size was $10 \text{ nm} \times 30 \text{ nm} \times 30 \text{ nm}$. To compensate for the reduction in resolution, all targets simulated were initialised with a uniform electron density equal to $70n_c$, and an increased thickness to keep the areal density the same as a $210n_c$ target with the quoted thickness. Corresponding 2D simulations with equivalent pre-expansion but higher resolution ($5 \text{ nm} \times 12 \text{ nm}$) were also performed for comparison.

4.2.4 Transparency time

To calculate the onset time of relativistic transparency, properties of the electron and ion populations were extracted every $\Delta t = 0.5 \text{ fs}$ within a spatial region of $|y| \leq 0.5 \mu\text{m}$ about the laser propagation axis and averaged across the y -direction. The Doppler-

shifted critical density in the rest frame of the moving plasma is calculated

$$n_{c,D}(x) = n_c \frac{1 - \langle \beta_i \rangle(x)}{1 + \langle \beta_i \rangle(x)}, \quad (4.1)$$

where $\langle \beta_i \rangle(x)$ is the average velocity of the ions along the x -axis as a function of their position. The onset of relativistic transparency is determined as the time $n_e / \gamma_e n_{c,D} < 1$. Here, $t_{rsit} = 0$ corresponds to the arrival of the peak of the laser intensity profile at the position of the relativistic critical density surface immediately before relativistic transparency.

4.3 2D — linear polarisation

In this section, the results of proton acceleration in 2D PIC simulations—much more physically accurate than 1D yet still feasible for detailed scans with the available resources—from targets with a range of thicknesses are shown, for a linearly polarised laser pulse with a_0 up to 310. Firstly, the important features of the interaction with the onset of relativistic transparency are described. The proton spectra are shown and the influence of the transparency time is demonstrated. Finally, the changes to the dynamic processes for ion acceleration with the transparency time are shown and discussed for several cases by tracking the acceleration history of the protons that obtain the highest energies.

4.3.1 Interaction dynamics with relativistic transparency

Upon reaching the solid target surface, the linearly polarised laser pulse causes $\mathbf{j} \times \mathbf{B}$ acceleration of electrons, many of which propagate through the target to the rear side where they induce TNSA. At the same time, the pressure on the irradiated target surface caused by reflection (and absorption) of the laser pulse drives forward electrons in a compressed layer. The inward propagating electric field induced by this separation of charge accelerates ions towards the rear surface whilst the laser pulse bores into the target. In the event the initial target thickness is comparable to the laser skin depth ($l_s = c/\omega_p$) or the target remains opaque following hole boring up to the rear surface, the radiation pressure acceleration takes the form of light sail acceleration. The laser pulse is incident at target normal for all cases in this work; therefore, RPA and TNSA act parallel to each other within the centre of the focal spot. The combination of both

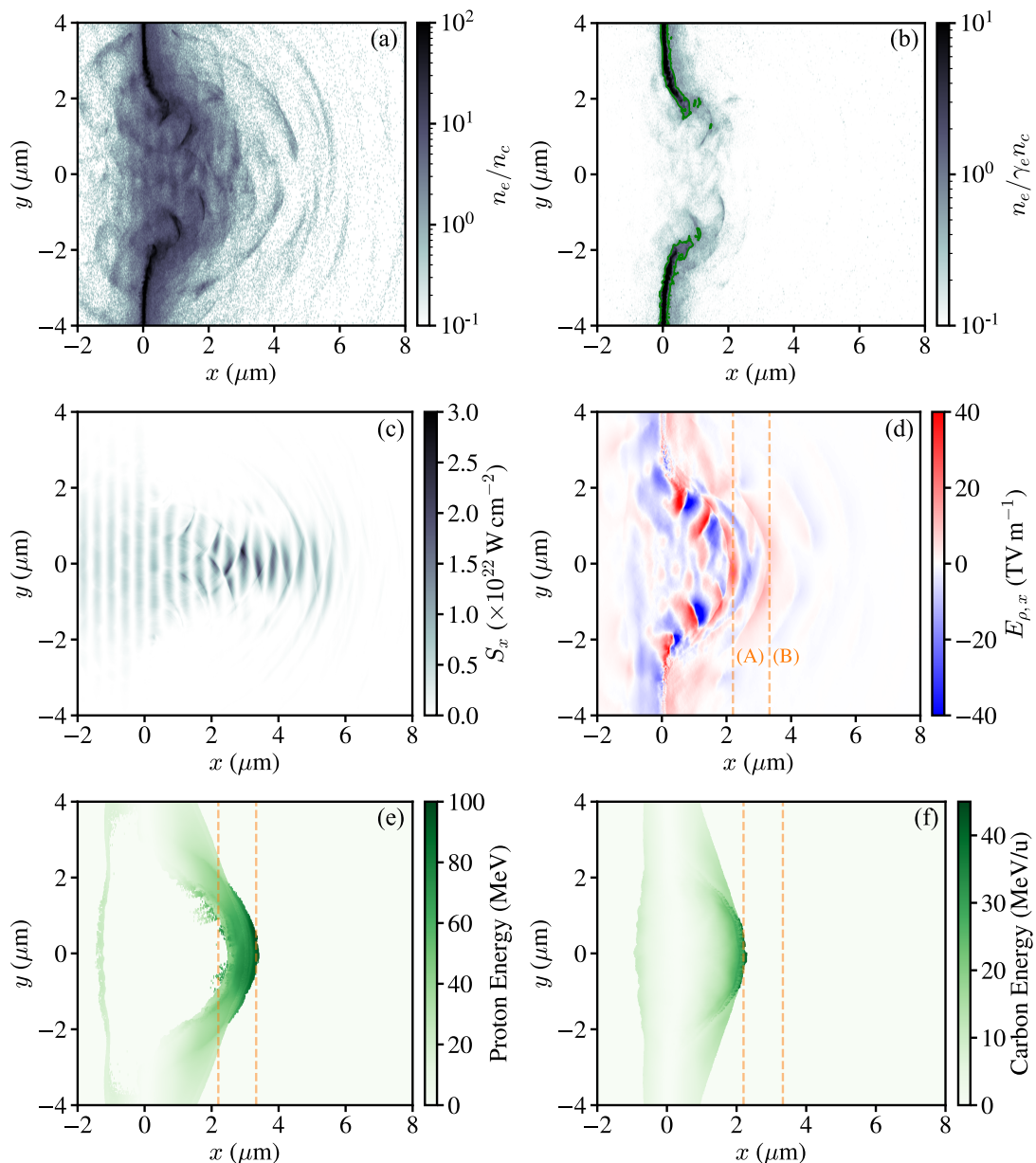


Figure 4.2: Snapshots at $t = 17$ fs after the arrival of the laser peak intensity at $x = 0$, and after the onset of RSIT, for $l = 125$ nm and $a_0 = 50$: (a) electron density; (b) electron density normalised by the relativistic critical density, with contour lines where $n_e = \gamma_e n_c$ (green); (c) x -component of the Poynting vector ($S_x \simeq E_y B_z / \mu_0$); (d) electrostatic field in the x -direction; (e) average proton energy within each grid cell; and (f) average carbon ion energy within each grid cell. Features (A) and (B) in (d)–(f) indicate the positions for $y = 0$ of the positive fields co-moving with the accelerating ions.

processes produces a hybrid acceleration scenario [7, 229], with ions gaining energy from one or both components of the field.

The use of ultrathin foils in this work enables the possibility of relativistic self-

induced transparency as the target is rapidly heated and expands. The reflectivity of the target quickly drops and electrons may be accelerated throughout the bulk plasma, affecting the acceleration processes above. Across the intensity range explored, the highest proton energies are commonly obtained when hybrid RPA-TNSA is interrupted by the onset of relativistic transparency; the onset of propagation of the laser pulse through the classically overdense target during the interaction is well correlated with a rapid increase in the ion energies.

A snapshot of the interaction shortly after the onset of RSIT is shown in figure 4.2 for $a_0 = 50$ and $l = 125$ nm. The electron density in the centre of the laser focal spot has fallen to a value $n_0 \gg n_e \gg n_c$, where $n_0 = 210n_c$ is the initial target density, as displayed in figure 4.2(a). The electrons are able to acquire Lorentz factors $\gamma_e \sim a_0$ within the laser pulse, thus $n_e \ll \gamma_e n_c$ as shown in figure 4.2(b) and the laser pulse is transmitted through—figure 4.2(c). The direct acceleration of electrons within the target bulk causes a shift from surface to volumetric laser absorption. Here, a larger number of high energy electrons escape the target [249]. The propagation of a laser pulse through a relativistically transparent channel of plasma can produce superponderomotive energy electrons through direct laser acceleration [58], or through self-generated magnetic fields and oscillating longitudinal fields caused by reflection from the channel walls [250]. The altered electron dynamics with the onset of relativistic transparency affects the separation of charge and the corresponding fields responsible for ion acceleration.

The longitudinal (x) component of the electrostatic field was calculated by Poisson solving the charge density and is shown in figure 4.2(d). The fields induced by the electron bunches escaping the rear of the target can be clearly seen, and the positive fields in the centre of the laser beam labelled (A) and (B). These fields move with the accelerated protons and carbon ions as shown in figure 4.2(e) and (f), respectively. The dual-peaked field structure shown here after the onset of transparency forms due to the presence of two ion species with different charge-to-mass ratios. The protons are able to respond more rapidly to the fields, leaving the heavier ions behind and causing the generation of an electrostatic field where they separate. This results in buffering of the proton beam [251] which propagates ahead of the carbon ions and is also accelerated by the sheath-like field at the expanding target rear side. Unlike the TNSA model of a thermal population of electrons expanding into vacuum, here the electrons also

experience the electromagnetic force of the transmitted laser pulse acting to accelerate them out of the finite target with the pulse. Most of the proton energy is generally acquired in this phase of the interaction in these 2D simulations; although, the absence of the additional transverse dimension causes higher densities (and intensities) to be maintained as the plasma moves outwards, causing greater acceleration than should occur.

The most rapid acceleration occurs immediately after the onset of RSIT, as the laser pulse breaks through the target and drives electrons forward. The acceleration dynamics are discussed in more detail later, with $a_0 = 50$ examined in this section and cases for other values of a_0 delineated in later sections—the principal difference in the proton acceleration for different values of a_0 is the increased role of RPA for higher intensities.

4.3.2 Proton spectra — linear polarisation

The proton energy spectra from each target thickness for $a_0 = 16, 50, 160$ and 310 are shown on the left in figure 4.3(a), (c), (e) and (g), respectively. For all laser intensities the complete proton spectra are broad and lack monoenergetic features. In each case there is an optimum thickness for which the maximum energy of the spectrum peaks. The angular proton spectra for these optima are shown in figure 4.3(b), (d), (f) and (h). The highest energy protons propagate close to parallel with the target normal and incident laser pulse ($\theta = 0$). A gap in the spectrum is present along the same direction at low energies due to the buffering by carbon ions [251], which may also be supported by bulk target acceleration by RPA at the highest intensities. Higher intensities demonstrate an increased number of highly divergent protons, resulting from the increase of the laser radiation pressure and transverse ponderomotive force causing greater deformation of the target as it breaks out of the rear side. This increases the radius of the characteristic ring of protons at low energies [97, 98, 237] that originates from the electrons driven forwards at the edges of the relativistic plasma aperture.

The full angular proton spectrum is too divergent for applications that require a beam-like source. For this reason, the proton spectrum within a divergence half-angle $\theta_{1/2} < 2.5^\circ$ is considered and shown on the right in figure 4.3(a), (c), (e) and (g). The spectra remain broad and without prominent peaks. However, a gap in the spectrum is produced that is greatest where relativistic transparency occurs for a significant fraction

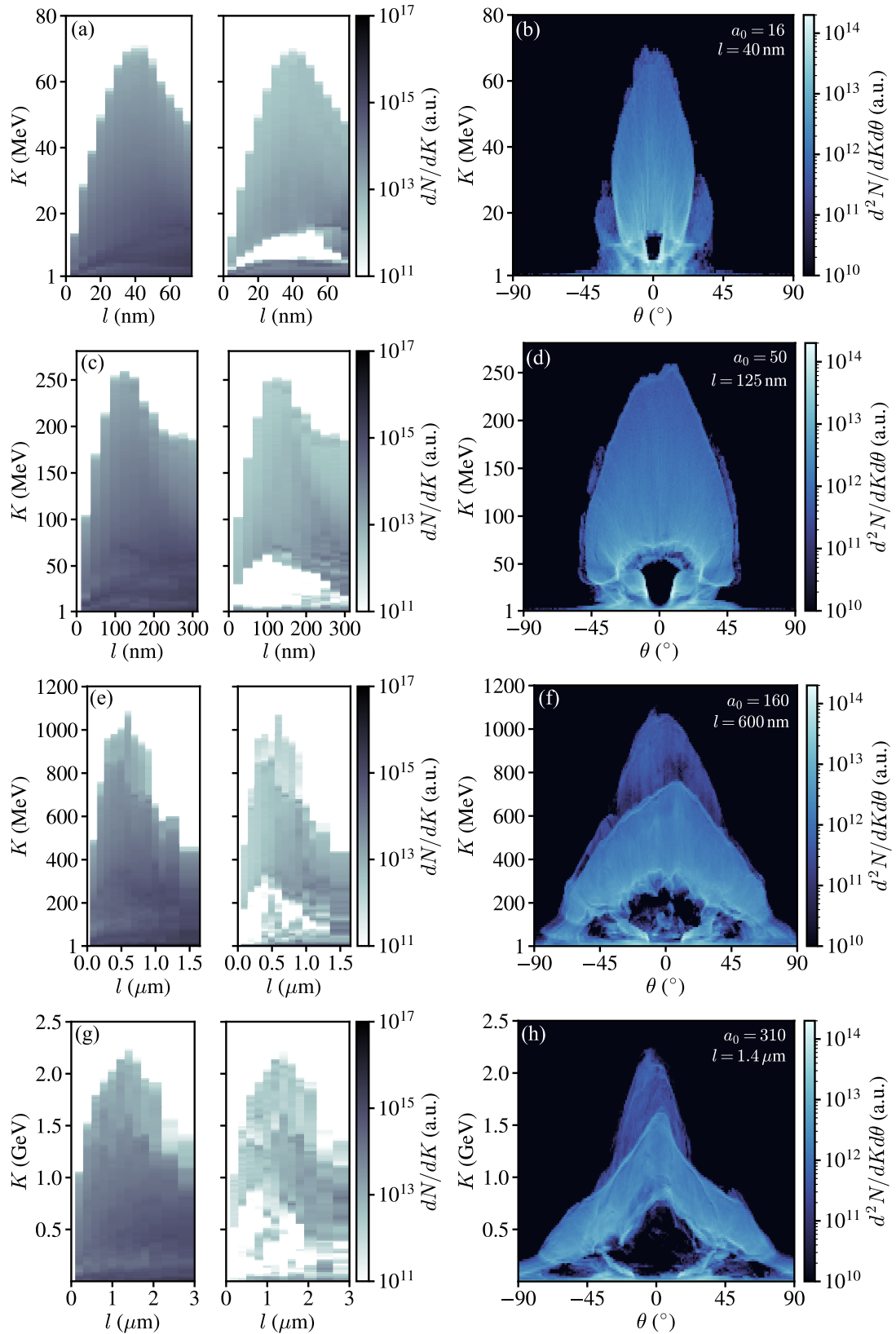


Figure 4.3: Full proton spectra (left panel) and target normal spectra within a divergence half-angle $\theta_{1/2} < 2.5^\circ$ (right panel) for all target thicknesses at $a_0 = 16, 50, 160$ and 310 —(a), (c), (e) and (g), respectively. Angular proton spectra for optimum target thicknesses—(b), (d), (f) and (h).

of the laser pulse.

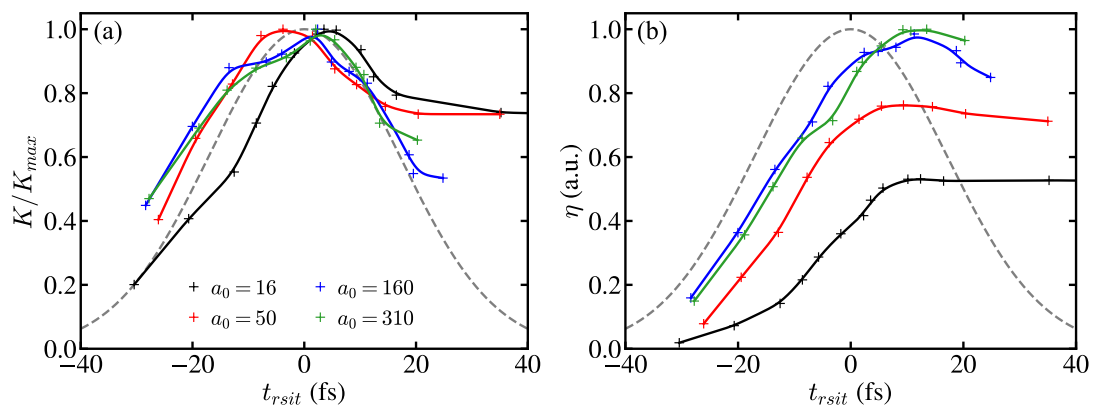


Figure 4.4: (a) Maximum proton energies achieved in each fixed-intensity scan of target thickness normalised to the maximum value for the whole scan K/K_{max} . The temporal profile of the laser intensity is also plotted (grey dashed). (b) The normalised conversion efficiency of laser energy to protons with $K > 1$ MeV.

The maximum proton energy for each spectrum is normalised to the peak value for each a_0 and shown in figure 4.4(a) as a function of the onset time of RSIT—calculated from the time the electron density falls below the relativistic critical density as described in section 4.2.4. The highest proton energies for each value of a_0 are produced when RSIT occurs close to the time the peak intensity of the laser pulse reaches the target ($t_{rsit} = 0$): the onset time of RSIT is critical to the optimisation of ion acceleration up to the intensities expected to be achieved with 10 PW-class lasers. Although radiation reaction is not modelled here, its affect is addressed in section 4.7 and it is found not to invalidate this result.

The conversion efficiency of laser-to-proton energy is important for the delivery of a high dose of protons for applications. It is shown in figure 4.4(b) as a function of the onset time of RSIT and is highest when $t_{rsit} \sim 10$ fs, and remains high for RSIT at later times. A greater fraction of the laser energy is transferred to the hot electron population, which produces electric fields that accelerate the protons, during the interaction when RSIT occurs on the falling edge of the laser pulse. Measurements using a laser system with $\tau_L = 700$ fs and $a_0 = 9$ have shown the overall absorption of the laser pulse peaks for the thinnest target that does not become relativistically transparent [249]. Although the overall trend is similar for all four laser intensities, the relative conversion efficiencies achievable are almost a factor of two higher for $a_0 = 160$ than $a_0 = 16$, with little increase from $a_0 = 160$ to $a_0 = 310$. Radiation reaction will affect these results

at the upper intensity limit.

4.3.3 Proton tracking — linear polarisation

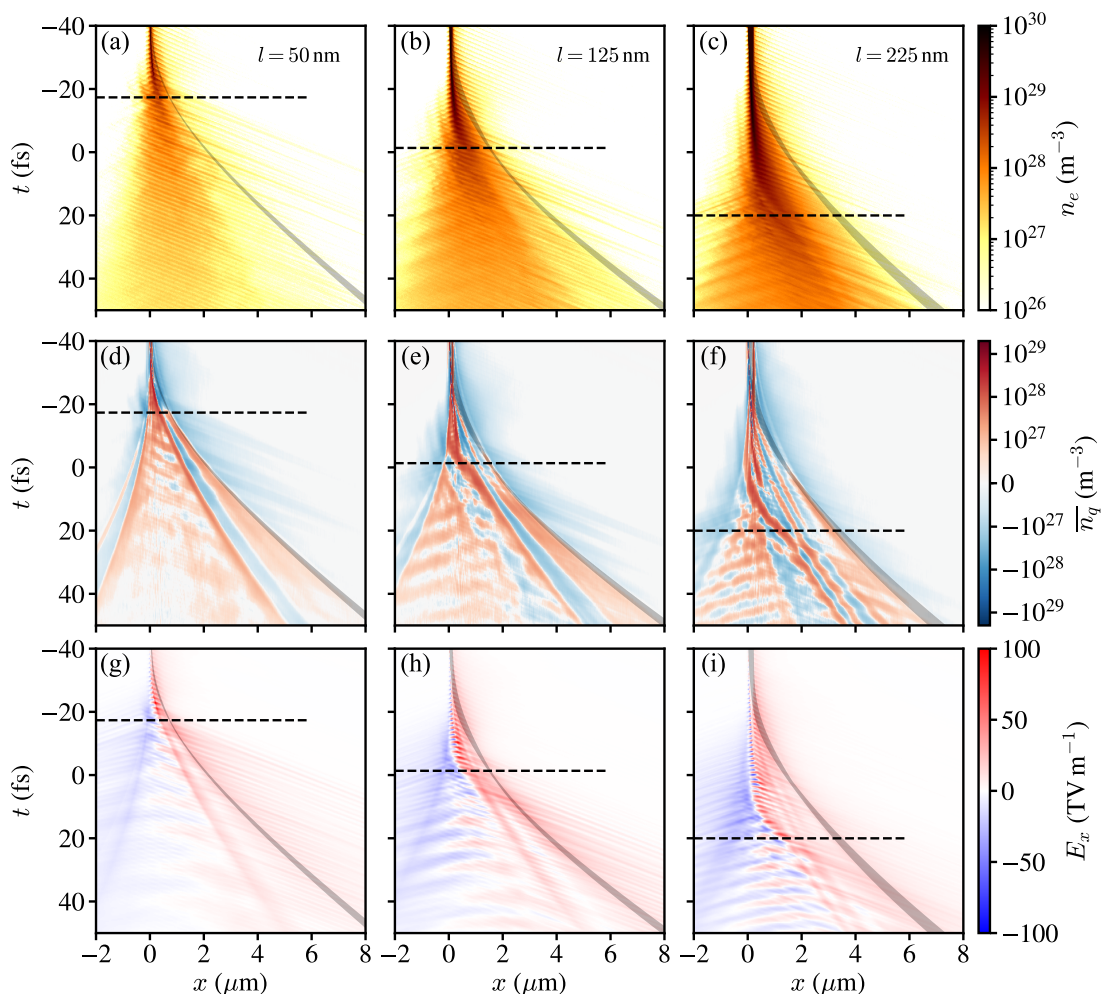


Figure 4.5: (a)–(c) The electron density, (d)–(f) the density of charge averaged over a laser cycle and (g)–(i) the longitudinal component of the electric field. All quantities are shown along the x -axis ($y = 0$) for the stated target thickness (denoted above) and $a_0 = 50$. The region containing the tracked highest energy protons (shaded, grey) and the onset time of RSIT (dashed) are also shown.

To explore the physics giving rise to these results in more detail, a sample of the highest energy protons was tracked in further simulations for $a_0 = 50$ at three example target thicknesses, $l = 50$ nm, 125 nm and 225 nm, corresponding to $t_{rsit} = -19$ fs, -4 fs and 14 fs (early, optimised and late transparency), respectively. The highest energy protons generally propagate close to parallel with the x -axis (see figure 4.3). Therefore, the particle and grid data within $|y| < \phi_L/4$ was extracted, and the protons that are initially within the centre of this region ($|y| < \phi_L/8$) with final energies exceeding 85%

of the maximum proton energy and $\theta_{1/2} < 5^\circ$ were tracked. The electron density, n_e , cycle-averaged charge density, $\overline{n_q}$, and longitudinal electric field, E_x , data was averaged across the y -direction.

The motion of the tracked protons is shown accompanied by the electron density, charge density and longitudinal electric field in figure 4.5. In all cases, the protons may initially experience RPA close to the front surface or TNSA close to the rear side; however, they all move to the target rear and experience TNSA by the time RSIT occurs. The onset of RSIT leads to rapid target expansion (see figure 4.5(a)–(c)), and for the thinnest targets the forward propagation of a large number of electrons at the target rear side beyond the tracked protons. This is also shown in figure 4.5(d)–(f) by the cycle-average charge density $\overline{n_q}$.

The enhancement of ion acceleration with relativistic transparency is caused by this forward acceleration of electrons by the Lorentz force of the transmitted laser pulse; a dense region of negative charge forms at the target rear side, and the depletion of electrons within the target bulk causes dense regions of positive charge due to the carbon ions and protons left behind. This separation of charge enhances the electric field as shown in figure 4.5(g)–(i). This physical picture does not fall within the descriptions of commonly theorised acceleration mechanisms: the target has become strongly transmissive and therefore RPA [87, 89] is mitigated; Coulomb explosion [110, 111] from the remaining ion core ignores the significant fraction of the electric field the protons experience induced by the electrons; the accelerating electric field is caused by the separation of charge at the rear side of a finite target and not a streaming (Buneman) instability as required for BOA [112]; and the protons are not accelerated by co-propagation with the relativistic critical density surface as in SASL/RTF-RPA [108, 109]. Although the dynamics present here appear similar to TNSA [68, 71], the presence of a laser pulse throughout the bulk target modifies the electron motion.

The evolution of E_x local to the tracked protons and their energy is shown in figure 4.6(a) and (b), respectively. In all cases, E_x peaks at 30–40 TV m⁻¹ at between $t = -30$ fs and -15 fs (later with increasing thickness) corresponding to the protons moving through the sheath field at the target rear side. As these protons propagate away from the target the magnitude of the sheath field they experience reduces. A secondary peak in E_x of comparable magnitude follows the onset of transparency for $l = 50$ nm and 125 nm, leading to a rapid increase in the proton energies. For $l = 225$ nm, transparency

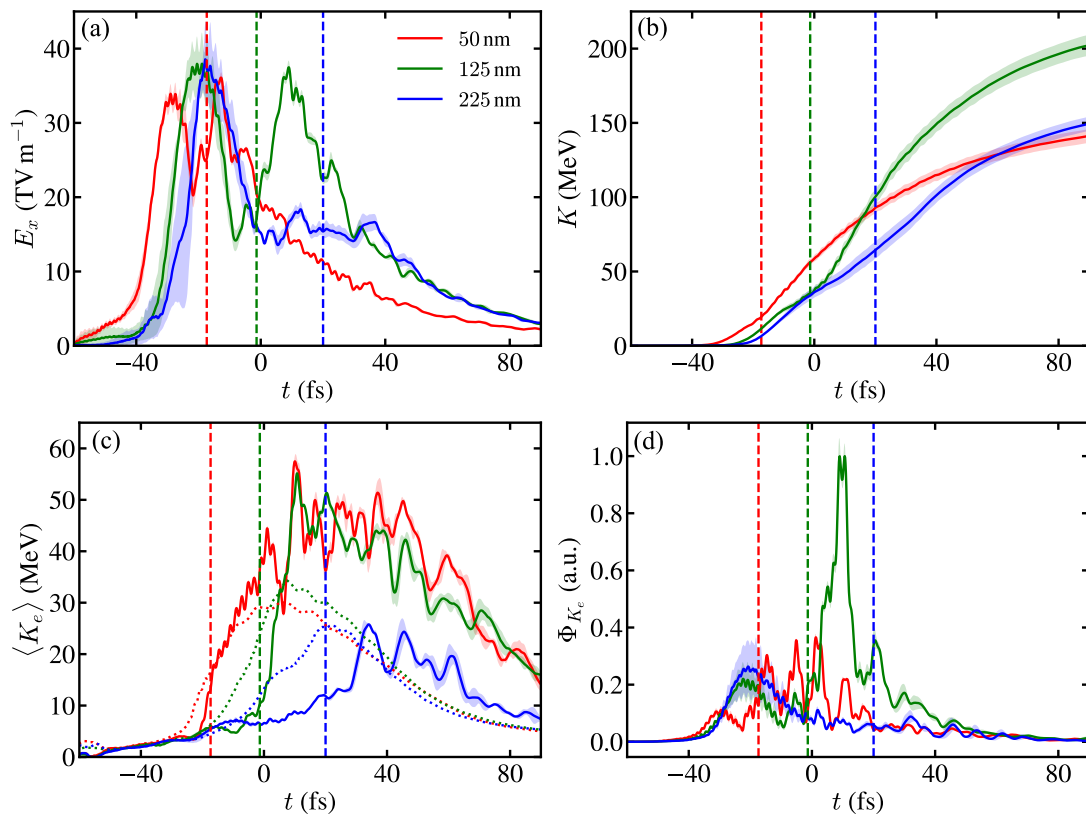


Figure 4.6: The acceleration history of the highest energy protons for $a_0 = 50$: (a) the longitudinal electric field, (b) the proton energy, (c) the mean electron energy and (d) the flux of electron kinetic energy along x . For all, the mean (solid) and standard deviation (shaded) are shown. In (c) both the mean fast electron energy near the tracked protons (solid) and within the whole sample region (dotted) are shown. The vertical dashed lines indicate t_{rsit} .

occurs late in the interaction and only a minor increase in E_x is observed to follow.

The mean fast electron energies within the whole sample region and local (within $\lambda_L/8$ along x) to the tracked highest energy protons are shown in figure 4.6(c). The electrons in the thinner targets reach higher temperatures early in the interaction when the target becomes transparent and the fast electron temperature near the tracked protons is much higher for the $l = 50$ nm and 125 nm targets compared to $l = 225$ nm. The interaction of the laser light within the target volume when transparency occurs enables electrons to readily overcome the electrostatic potential behind the tracked protons at the rear of the target and reach them with high energies. This increases the energy available to be transferred by the electrons to the electric field ahead of the protons and also causes a rapid blowout of electrons from the target as seen in figures 4.5(a), (b), (c) and (d). The displacement of electrons is observed to lead to

high densities of net positive and negative charge respectively behind and in front of the tracked protons after the onset of RSIT in figures 4.5(c) and (d), which produces a strong electrostatic field. Figure 4.6(d) shows the flux of electron kinetic energy in the $+x$ -direction near the protons is significantly greater for the $l = 125$ nm target than the others. For this target, where transparency occurs near the peak of the laser pulse, the laser is able to drive the highest amount of fast electron energy up to the tracked protons at the target rear side, where some of it is transferred to the charge-separation/sheath field and as a result produces the highest energy protons. The break-out of the rear side of the target by the laser pulse is key to the enhancement with relativistic transparency, as demonstrated by Willingale *et al.* [235]. The rapidly decreasing density gradient at the target rear side reduces the ability of the directly accelerated forward current of electrons to draw a return current, and therefore large electric fields form to accelerate the ions. The proton acceleration is optimised when the laser pulse breaks through close to the time it reaches its peak electromagnetic force.

Investigations using longer (hundreds-of-femtosecond to picosecond) duration laser pulses also show improved ion acceleration local to a so-called jet of fast electrons within the laser pulse after the onset of RSIT [7, 98, 252–254]. For oblique incidence of the laser pulse, this can cause the highest energy protons to be produced propagating close to the laser propagation direction instead of along the target normal direction as expected from TNSA [7, 98, 252].

For the early onset of transparency, figure 4.5(a) and (d) shows the densities fall very quickly and thus the transparency-enhanced E_x field is short-lived. For the late onset of transparency with $l = 225$ nm, less fast electron energy reaches the tracked protons in figure 4.6(d), which have been accelerated away from the target by TNSA earlier in the interaction, limiting the value of E_x they experience after t_{rsit} .

The acceleration dynamics for lower intensities, higher intensities, circular polarisation and 3D simulations are discussed in later sections of this chapter.

4.4 2D — circular polarisation

For circularly polarised laser light, electron heating is reduced due to the absence of $\mathbf{j} \times \mathbf{B}$ absorption for normal laser incidence onto a flat surface. The target expansion is slower and thinner targets are required for RSIT, enabling RPA to potentially dominate

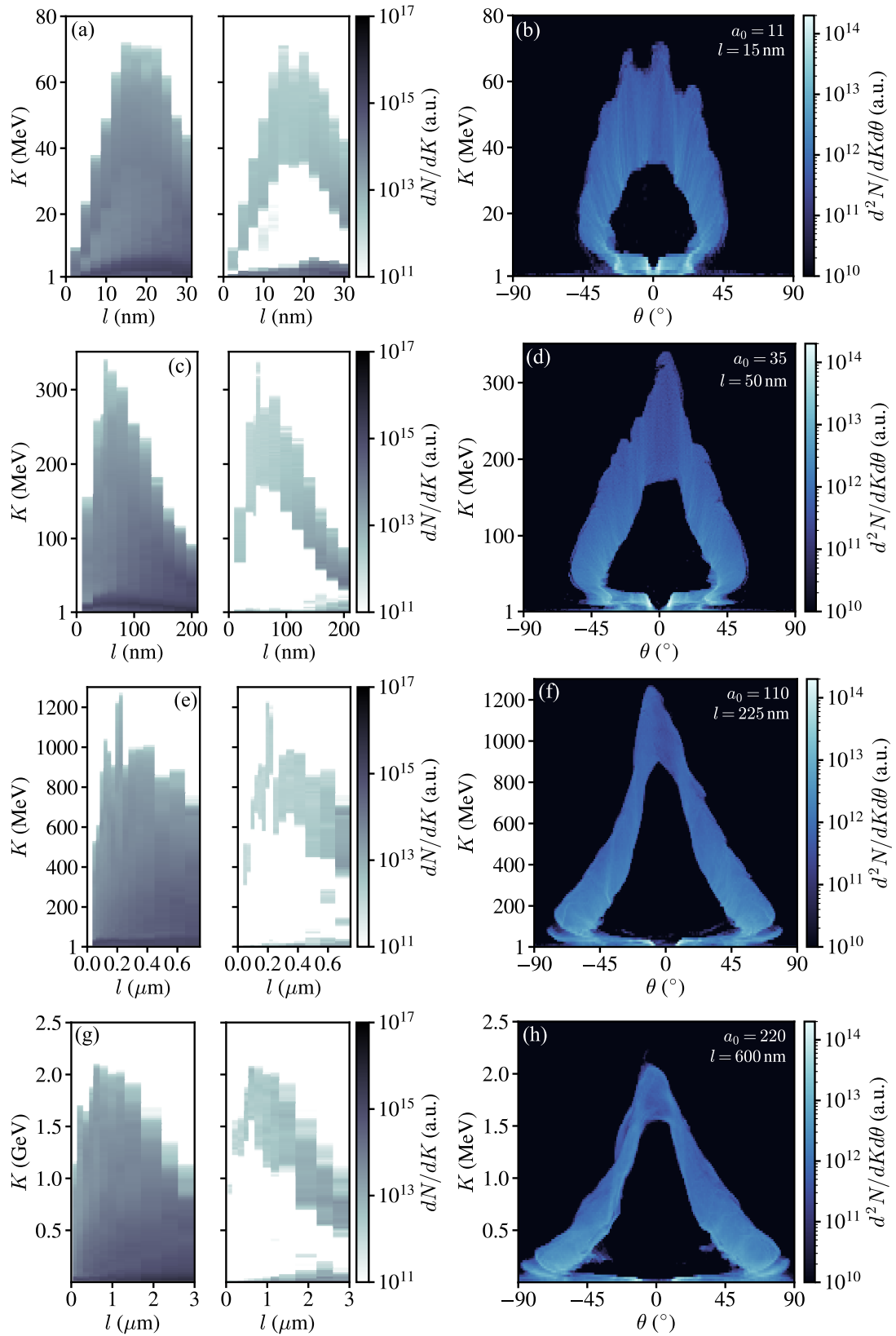


Figure 4.7: Full proton spectra (left panel) and spectra within $\theta_{1/2} < 2.5^\circ$ (right panel) for all target thicknesses at $a_0 = 11, 35, 110$ and 220 —(a), (c), (e) and (g), respectively. Angular proton spectra for optimum target thicknesses—(b), (d), (f) and (h).

the ion acceleration [92]. Here, the effect of RSIT on proton acceleration with circularly polarised laser pulses for a_0 up to 220 is examined in a similar manner to the previous section.

4.4.1 Proton spectra — circular polarisation

The proton energy spectra for $a_0 = 11, 35, 110$ and 220 are shown in figure 4.7(a), (c), (e) and (g), respectively. The complete proton spectra do not contain pronounced spectral peaks. This is also true for the proton spectra sampled within $\theta_{1/2} < 2.5^\circ$. However, these spectra along the target normal direction contain a large empty band of energies from the low energy limit of the spectrum ($K \sim 1$ MeV) covering most of the energy range up to the maximum proton energy in some cases. This feature is most pronounced within the range of targets that become transparent to a substantial fraction of the laser pulse. It results from both buffering by the carbon ions and bulk target acceleration by RPA, which is most effective along the laser propagation direction ($\theta = 0$). The empty band of energies is many times larger than found for linear polarisation in figure 4.3 due to the increased role of RPA for circular polarisation and reduced electron heating.

The angular spectra for the optimum targets at each intensity are shown in figure 4.7(b), (d), (f) and (h). The highest energy protons are produced propagating close to parallel with the target normal and laser propagation direction ($\theta = 0$), and the divergence of the accelerated protons increases with intensity as it does for linear polarisation. The key difference is the absence of protons within large energy ranges which extends to divergence angles up to $\theta \approx 50^\circ$.

The normalised maximum proton energies for each value of a_0 are shown in figure 4.8(a). In a similar manner to linear polarisation, the highest proton energies are achieved when RSIT occurs close to the laser peak and the laser-to-proton energy conversion efficiencies in figure 4.8(b) are maximised when RSIT occurs shortly after the peak. Light sail RPA is central to the interaction dynamics. However, the deformation of the foil caused by the transverse gradients in radiation pressure across the Gaussian focal spot enables substantial electron heating with the circularly polarised light, and the foils can quickly expand as they propagate with the laser pulse resulting in the onset of relativistic transparency. For tightly focussed laser pulses similar to those considered in this work, the presence of some TNSA and the onset of RSIT can become

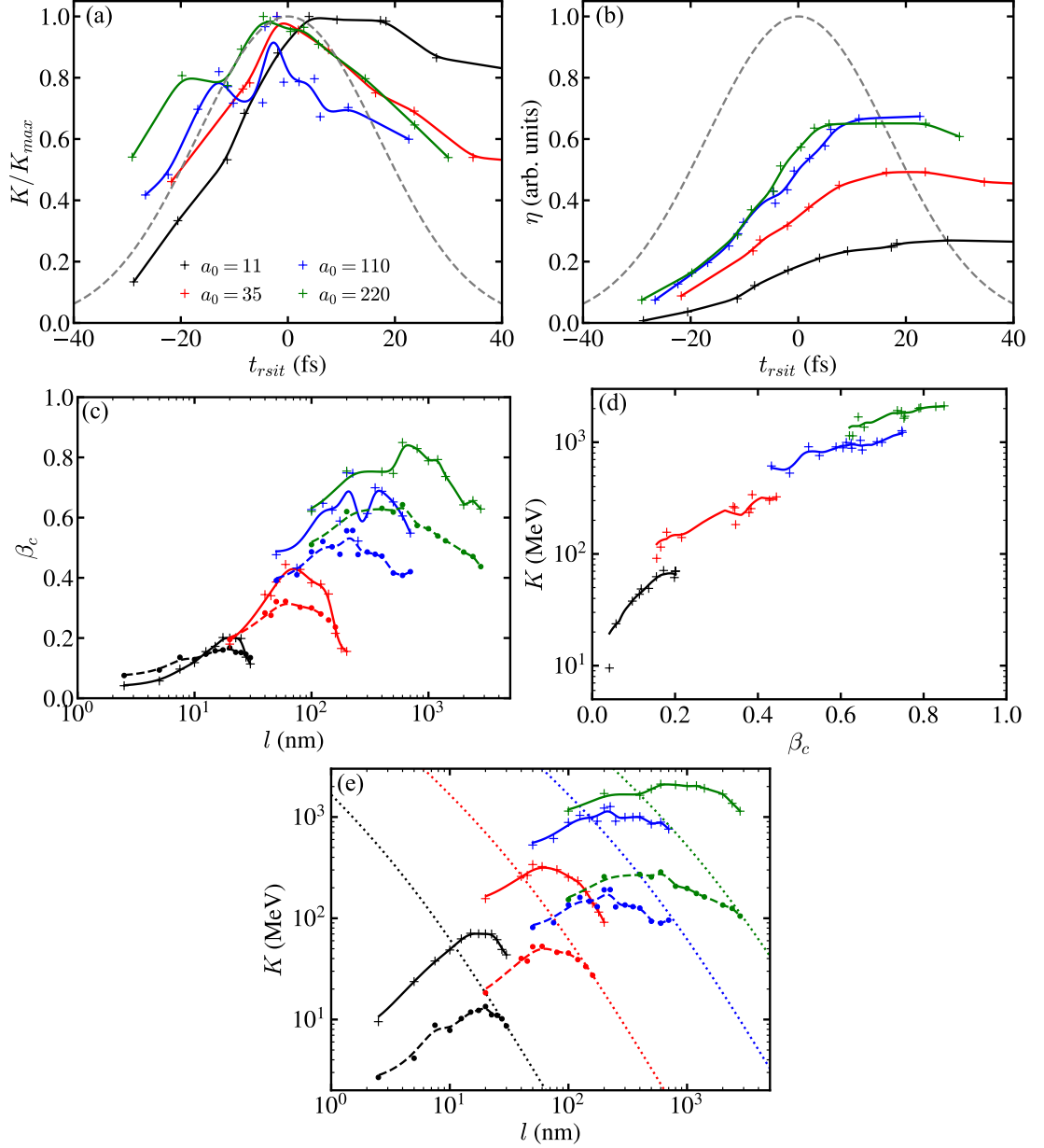


Figure 4.8: (a) Maximum proton energies as a function of t_{rsit} for the target thickness scan at each value of a_0 normalised separately. (b) Conversion efficiency of laser energy to protons with energy > 1 MeV, using the same normalisation factor as for linear polarisation in figure 4.4. (c) Maximum relativistic critical surface velocity, β_c , (solid) and calculated using the light sail model up to t_{rsit} (dashed) as a function of target thickness. (d) The variation of the maximum proton energies with β_c . (e) The maximum proton energies (solid), and those predicted by the light sail model for complete acceleration (dotted) and acceleration stopping at t_{rsit} (dashed).

unavoidable in the interaction when optimising RPA for maximum proton energy with thin foil targets.

The peak velocity of the critical density surface, β_c , indicates the bulk target velocity

caused by RPA and is shown in figure 4.8(c) for all targets. For light sail acceleration, a velocity $\beta_{ls} = [(1 + \varepsilon)^2 - 1]/[(1 + \varepsilon)^2 + 1]$ is expected, where $\varepsilon = 2\Phi_L/\rho l c^2$ [89]. For a Gaussian temporal-intensity profile, the laser fluence that reaches the target before the onset of transparency is

$$\Phi_L = \frac{I_L \tau_L}{4} \left(\frac{\pi}{\ln 2} \right)^{1/2} \left[1 + \operatorname{erf} \left(2\sqrt{\ln 2} \frac{t_{rsit}}{\tau_L} \right) \right]. \quad (4.2)$$

The values of t_{rsit} are used to estimate β_{ls} of each target in figure 4.8(c) alongside β_c . Although they vary similarly with target thickness, β_c far exceeds β_{ls} in most cases, with the difference increasing for higher laser intensities. The light sail model is one-dimensional and assumes a perfectly reflective rigid mirror; it does not account for both the transverse and longitudinal expansion of the target, electron heating, the transverse expansion of the laser pulse far from focus and the possibility of self-focussing of the laser pulse. Rapid transverse expansion of the target is induced as the Gaussian laser pulse forces its way through the target rear side, causing the areal density in the centre of the laser pulse to fall (e.g. by 20–50% for the electrons in the $a_0 = 35$ cases shown in figure 4.9). The targets also experience significant longitudinal expansion, with many of the heavier carbon ions left trailing far behind the moving electron layer, especially close to the onset of RSIT where the electrons also become highly relativistic, which may assist the motion of the critical density surface.

The value of β_c is typically highest for $t_{rsit} \approx 0$, where the proton energies are also highest. The maximum proton energies are shown in figure 4.8(d) as a function of β_c . The proton energies tend to increase with β_c . Therefore, measurements of the reflected laser spectrum could provide a good indicator of the conditions where the proton energies are optimised in experiments. The maximum proton energies are compared against the light sail model both with the complete laser fluence ($\Phi_L = I_L \tau_L \sqrt{\pi/\ln 2}/2$) and with the laser fluence that arrives before the onset of RSIT (equation 4.2) in figure 4.8(e). The optimum target thicknesses predicted using the light sail model with transparency are approximately the same as those from the simulations. However, the energies achieved in the simulations are many times greater.

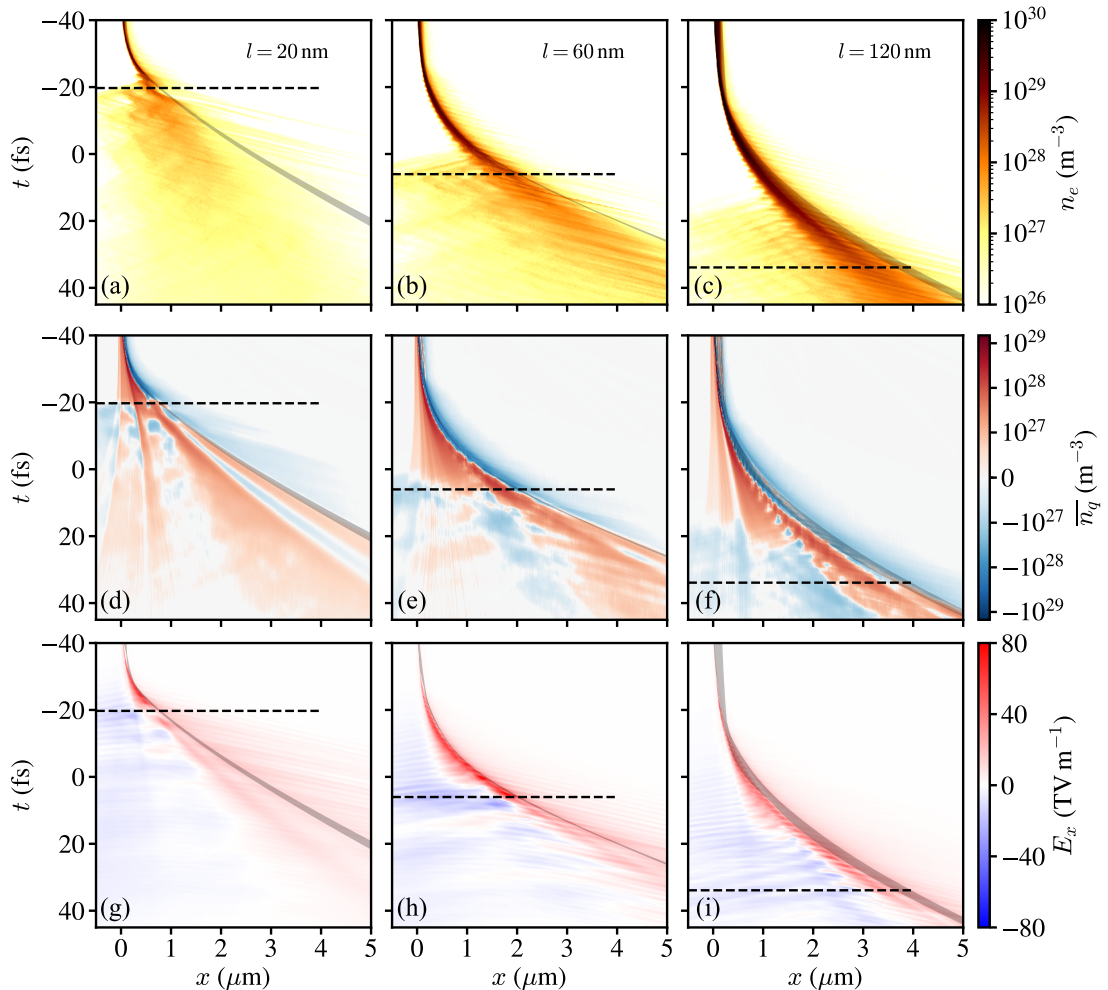


Figure 4.9: (a)–(c) The electron density, (d)–(f) the density of charge averaged over a laser cycle and (g)–(i) the longitudinal component of the electric field. All quantities are shown along the x -axis ($y = 0$) for the target thickness denoted above and $a_0 = 35$. The region containing the tracked highest energy protons (shaded, grey) and the onset time of RSIT (dashed) are also shown.

4.4.2 Proton tracking — circular polarisation

The highest energy protons were tracked for $a_0 = 35$ and $l = 20$ nm, 60 nm and 120 nm in the same manner as for the linear polarisation cases in section 4.3.3. The temporal evolution of n_e , \bar{n}_q and E_x along the x -axis ($y = 0$) for each of these cases is shown in figure 4.9 with the path of the tracked protons. In contrast to the interactions with linearly polarised light in figure 4.5, the bulk target propagates forwards with the laser pulse due to light sail RPA for all cases as shown in figure 4.9(a), (b) and (c). The initial acceleration of the tracked protons is therefore dominated by RPA.

As the target is driven forwards expansion of the rear surface begins, causing TNSA.

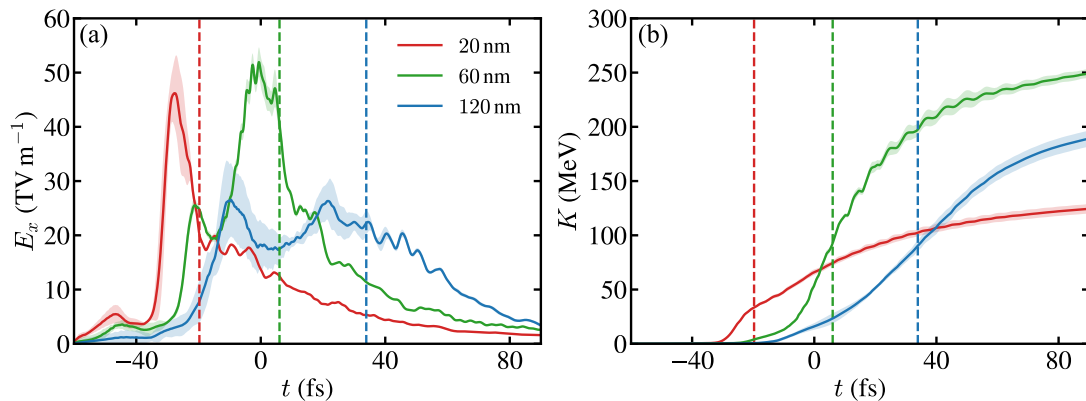


Figure 4.10: Acceleration history of the highest energy protons for $a_0 = 35$: (a) the longitudinal electric field and (b) the proton energy. For both, the mean (solid) and standard deviation (shaded) are shown. The vertical dashed lines indicate t_{rsit} .

Although the RPA and TNSA fields are difficult to distinguish, the tracked protons remain close to the dense electron layer, moving due to the radiation pressure, before RSIT occurs. Therefore, the proton acceleration is dominated by the influence of the radiation pressure. For $l = 120$ nm (late RSIT) in figure 4.9(c), (f) and (i), the protons visibly drift away from the dense electron region well before RSIT. Here, the accumulated electron heating has caused significant expansion of the target and TNSA must be considered important.

After the onset of transparency RPA is curtailed, leaving the protons to be accelerated in the remaining charge separation field after many electrons are pulled back to the trailing ion region and others are accelerated forwards out of the target by the laser fields. This effective sheath field of expanding plasma decays as the densities reduce over time, as collectively shown by all panels of figure 4.9. The bulk target motion induced by radiation pressure prior to transparency causes this sheath field to co-propagate with the accelerating protons, extending the acceleration time. Furthermore, RPA also assists the sheath acceleration by deforming the foil whilst it is opaque to cause $\mathbf{j} \times \mathbf{B}$ heating. The proton energies are highest where the combination of RPA and rear surface acceleration is optimised.

The mean value of E_x and the proton energies over the duration of the interaction are shown in figure 4.10. Unlike for linear polarisation in figure 4.6(a), E_x peaks before the onset of RSIT and it reduces over time afterwards. The protons in the thinner targets experience the strongest E_x fields ($> 40 \text{ TV m}^{-1}$) immediately before transparency. For the 60 nm target, that becomes transparent close to the laser peak,

this enables extremely rapid energy gain of the already fast protons to produce the highest final energies.

4.5 3D — linear and circular polarisation

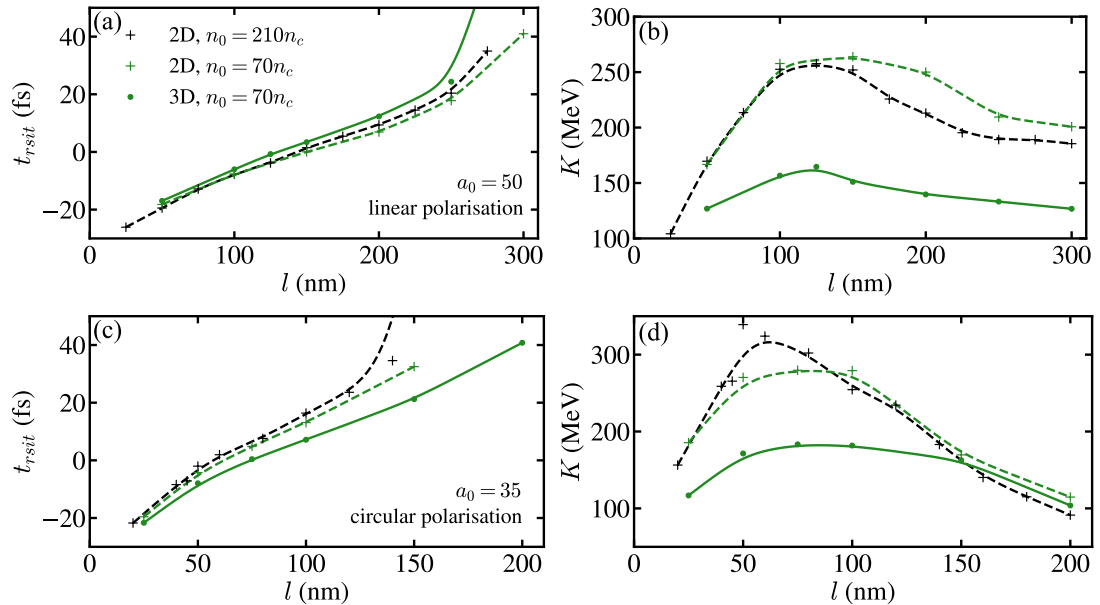


Figure 4.11: The onset times of RSIT, as a function of target thickness, calculated from 3D simulations at a reduced initial density $n_0 = 70n_c$ for (a) linear polarisation and (c) circular polarisation, with the maximum proton energies for (b) linear polarisation and (d) circular polarisation from the same simulations. The results for 2D simulations at the same density and the full solid density of CH are shown for comparison.

To check the accuracy of the 2D simulations, a limited number of 3D simulations were performed for both linear and circular polarisation. The targets were pre-expanded to a reduced initial density of $n_0 = 70n_c$ due to the larger size of the simulation grid cells. Therefore, additional 2D simulations were performed for this density to separate any potential density-dependent effects. A target thickness scan was completed for $I_L = 5 \times 10^{21} \text{ W cm}^{-2}$ for linear and circular polarisation (corresponding to $a_0 = 50$ and $a_0 = 35$, respectively).

Figure 4.11(a) shows the onset time of relativistic transparency, t_{rsit} , is the same in 3D for linear polarisation, and figure 4.11(c) shows t_{rsit} is only brought forward by several femtoseconds for most targets in 3D for circular polarisation. The proton energies in figure 4.11(b) for linear polarisation are reduced by almost a factor of two in

3D for most targets. The origin of this difference is the increased transverse expansion of the targets enabled by the additional dimension. This causes the sheath field at the target rear side to reduce faster with distance from the interaction point ($x \sim 0$). The proton energies in figure 4.11(d) for circular polarisation are reduced for the thinnest targets similarly due to faster target expansion. The variation of proton energy with target thickness remains similar for both polarisations in 3D, and the optimum is still achieved for $t_{rsit} \approx 0$.

The size of the transverse dimensions of the simulation box were reduced in 3D due to the otherwise excessive use of available computing resources. The full angular proton spectra were therefore not captured. The proton spectra along the target normal, where the maximum energies are generally achieved, are shown in figure 4.12 for the optimum targets from figure 4.11, and individual simulations for the optimum target thicknesses obtained in 2D at different intensities—proton acceleration was also not modelled in 3D for $I_L = 2 \times 10^{23} \text{ W cm}^{-2}$ due to the impractical resource required to capture the full interaction. Gaps in the proton energy spectra appear as expected from the 2D results in the previous sections. At the highest intensities, linear polarisation produces partially modulated spectra instead of the exponential decay for $a_0 = 16$. Circular polarisation produces a wide peak-like band of protons at high energies. For all cases, $\sim 10^6$ protons per MeV are captured within the 5° measurement cone at the maximum of the spectrum.

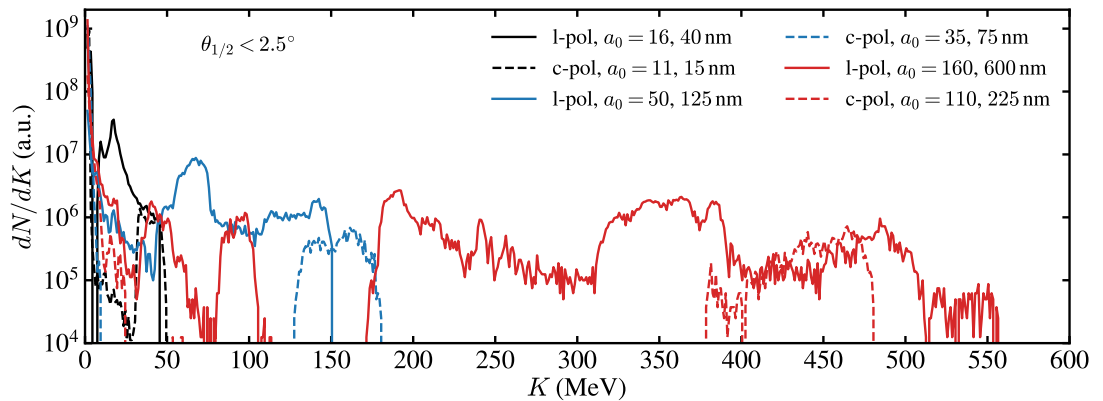


Figure 4.12: Proton energy spectra within a divergence half-angle $\theta_{1/2} < 2.5^\circ$ for the optimised target thicknesses in 3D at the stated intensities and laser light polarisations.

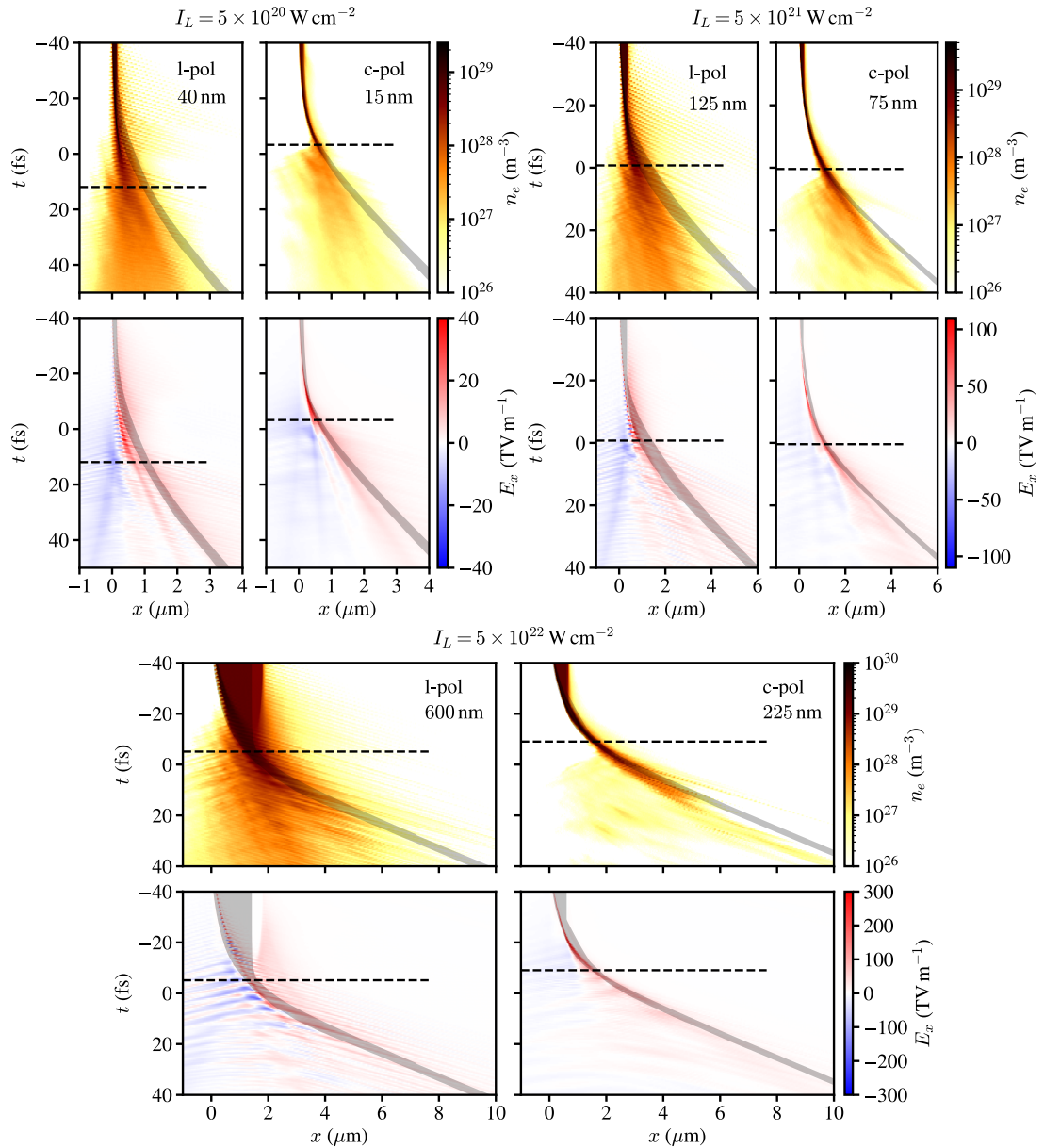


Figure 4.13: The electron density (n_e) and longitudinal electric field (E_x) along the x -axis for the optimum cases at each laser intensity and polarisation case given. The path of the tracked highest energy protons (shaded) and the onset time of RSIT (dashed) are also shown.

4.5.1 Proton tracking — 3D

The highest energy protons were tracked (in the same way as in the previous sections) for examination of the acceleration process. The motion of these protons through n_e and E_x is shown in figure 4.13 for all of the optimised cases. The physical picture is similar to the single intensity cases described in the previous sections, with RPA becoming increasingly important for higher intensities with linear polarisation.

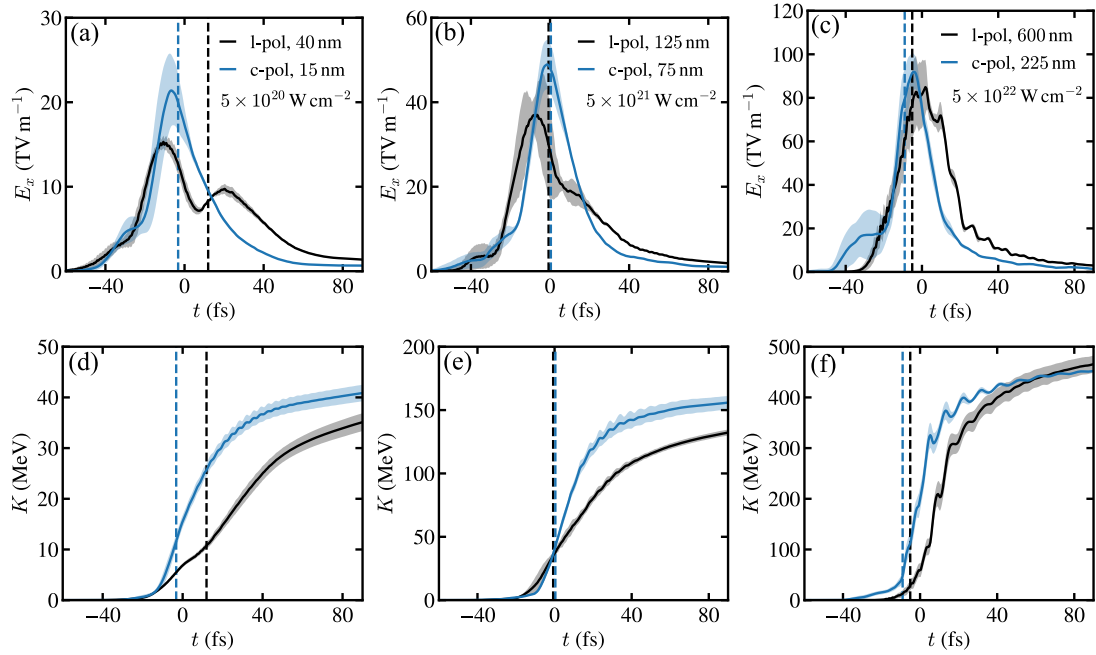


Figure 4.14: The (a)–(c) mean local longitudinal electric field and (d)–(f) mean energy of the tracked highest final energy protons as a function of time for the stated target thickness, polarisation and intensity. The vertical dashed lines indicate t_{rsit} .

The results for circular polarisation at all intensities demonstrate the dominance of RPA up to t_{rsit} , followed by acceleration from the target bulk into the enhanced rear surface electric field as electrons are swept from the target volume out of the rear side after the onset of RSIT. For linear polarisation, prior to the onset of RSIT only some protons experience RPA for $a_0 = 16$, causing injection into the rear surface TNSA field. As the intensity is increased to $a_0 = 160$ this initial phase of the interaction for the fastest protons shifts to RPA dominance. All of the fastest protons originate within the bulk front section of the target, as shown by the shaded region in figure 4.13, and at t_{rsit} they are all in close proximity to the centre of the target. The onset of RSIT drives incredibly rapid target expansion with many fast electrons driven out of the rear side. The remaining dense positively charged region of ions and the electrons at the target rear side produce a powerful charge-separation field that almost instantaneously accelerates the tracked protons to near relativistic velocities. This is much more dramatic than for $a_0 = 16$ and 50, and is aided by the compression of the target into a thinner layer by radiation pressure before release of the electrons with RSIT.

The mean local value of E_x and energy for the tracked populations of protons

are shown in figure 4.14. For all intensities with circular polarisation, a singular peak around t_{rsit} (and $t = 0$) is found, similar to the optimised 2D result in figure 4.10(a). For linear polarisation, a second peak in E_x is produced after RSIT for $a_0 = 16$ as expected from the 2D results in figure 4.17, yet with a lower value of $E_x \approx 10 \text{ TV m}^{-1}$ instead of $E_x \approx 13 \text{ TV m}^{-1}$. For $a_0 = 50$, the enhanced E_x after RSIT is much weaker than seen in 2D in figure 4.6(a), and appears as an extension to the duration of the field rather than a second peak. For $a_0 = 160$, there is a single short peak in E_x of approximately 80 TV m^{-1} just after t_{rsit} that causes 300 MeV to be gained within a timescale of several laser cycles. The temporal profile of E_x is more modulated and temporarily reaches values up to 120 TV m^{-1} in 2D in figure 4.17 for the same laser intensity. In this case, the peak in E_x remains close to t_{rsit} , but does not decay as quickly with time as the 3D case. The key difference between 2D and 3D is the reduced acceleration as the protons move away from the target in 3D, due to the additional transverse dimension causing faster reduction of the particle densities and corresponding fields. However, both demonstrate similar proton acceleration dynamics with the onset of RSIT, where the direct acceleration of electrons as the laser breaks through the target enhances the charge separation fields and concomitant proton acceleration.

4.6 2D — the laser pulse rising edge

The intensity profile of the rising edge of the laser pulse can influence the time in the interaction that the target becomes relativistically transparent and the properties of the proton beam [98, 184, 248, 255]. For ultraintense laser pulses, the laser rising edge can become sufficiently intense picoseconds before the arrival of the main pulse to drive significant pre-heating and pre-expansion of the foil. The laser rising edge has already been observed to limit the energies of protons accelerated from contaminant layers [248] and lead to more efficient acceleration of other ion species [255]. Increased peak laser intensities with the same temporal contrast profile are capable of driving more rapid heating and target pre-expansion, and thus changes to the main interaction for a given target. In this section, additional simulation results with a rising edge added to the laser pulse, as described in section 4.2.2, are presented for $a_0 = 16$ and 160 with linear polarisation.

The maximum proton energies for each target are shown in figure 4.15(a) and (c)

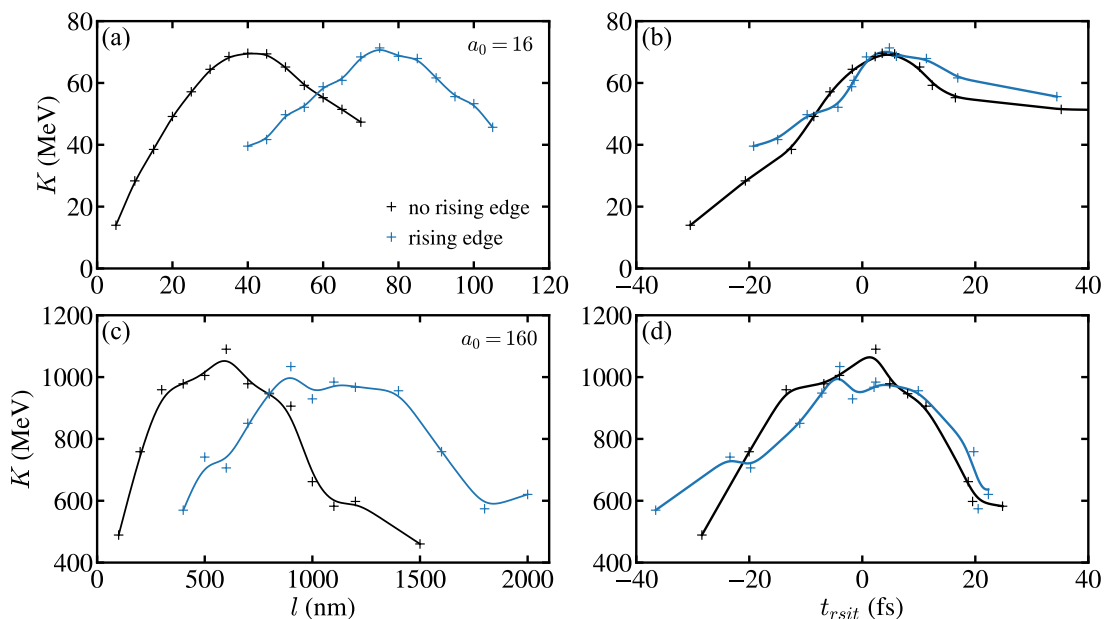


Figure 4.15: Maximum proton energies corresponding to each target thickness simulated for (a)–(b) $a_0 = 16$ and (c)–(d) $a_0 = 160$ with and without modelling the laser rising edge, both for linear polarisation and in 2D.

for $a_0 = 16$ and 160, respectively. The interaction with the rising edge causes an increase of the target thickness for which the proton energies are optimised, but does not considerably affect the overall maximum achievable energies. Recent experimental results show a substantial reduction in the maximum proton energy with lower temporal-intensity contrast, possibly due to a worse contrast profile or 3D effects, but demonstrate the increase to optimum target thickness expected from these simulations [172]. Figure 4.15(b) and (d) show the proton energies are optimised for $t_{rsit} \approx 0$ regardless of whether or not there is a rising edge present; the maximum proton energy is inherently linked to the onset time of RSIT.

4.6.1 Proton tracking — the laser pulse rising edge

The highest energy protons with low divergence were tracked along the x -axis, in the same manner as in the previous sections, in further simulations for target thicknesses close to the optimum, with and without the laser rising edge, at both $a_0 = 16$ and 160. The electron density, cycle-averaged charge density and E_x are shown in figure 4.16 with the path of the tracked protons. For $a_0 = 16$, the rising edge significantly reduces the peak density of the ultrathin target by the time the main pulse reaches it, and for both intensities the rising edge has caused expansion of the critical density surface at

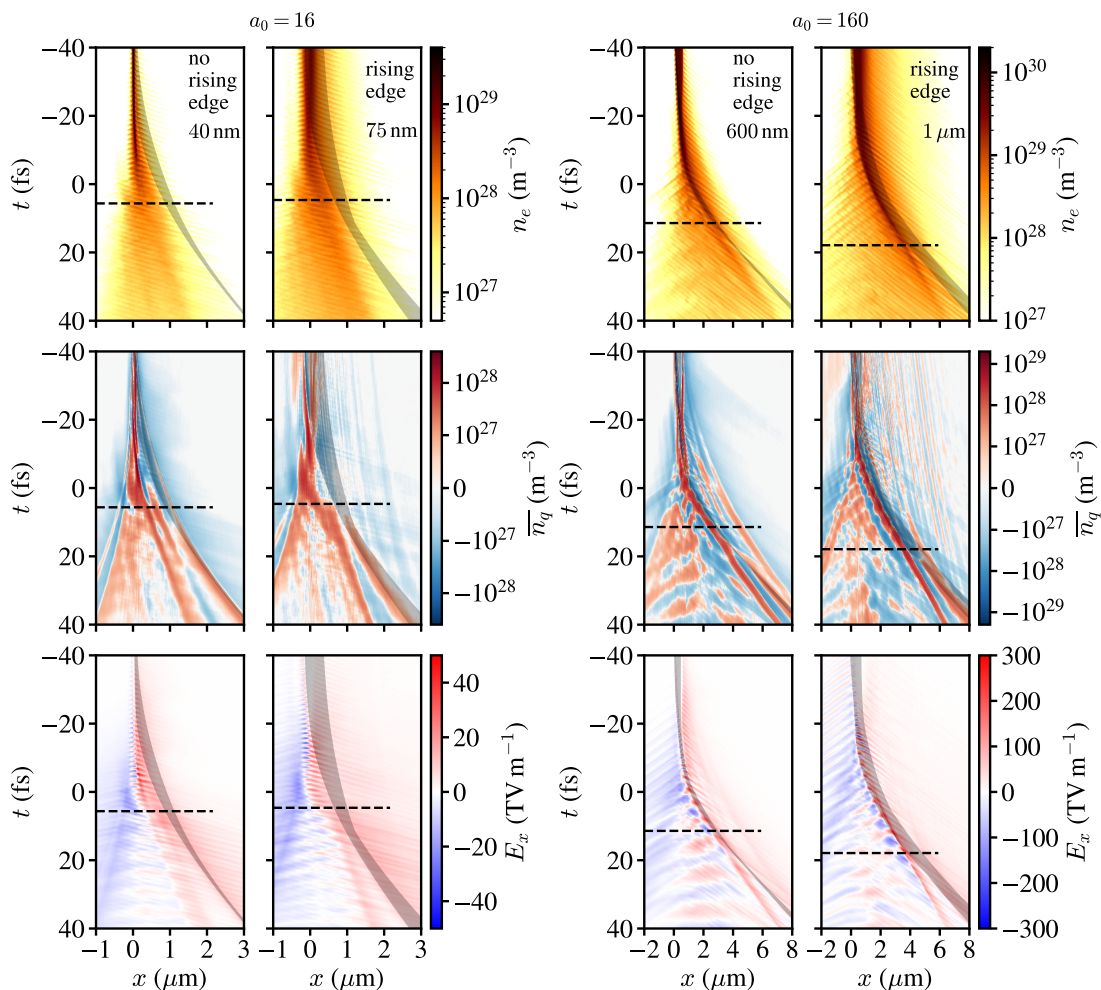


Figure 4.16: The electron density, cycle-averaged charge density and longitudinal electric field along the x -axis with and without modelling the laser rising edge for the stated targets and $a_0 = 16$ (left) and 160 (right). The region containing the tracked highest energy protons (shaded) and the onset time of RSIT (dashed) are also shown.

the target rear side (by $\sim 1 \mu\text{m}$ for $a_0 = 16$ and $\sim 5 \mu\text{m}$ for $a_0 = 160$). The laser pulse rising edge becomes relativistically intense well before the main pulse arrives and induces pre-acceleration by TNSA.

The acceleration process with the main pulse is almost invariant with the addition of the rising edge. For $a_0 = 16$, rear-surface sheath acceleration dominates the interaction. However, the reduced target density from the rising edge enables greater energy to be gained by protons at the front surface via RPA—this still only corresponds to a small fraction of the energies achieved—before injection into the rear side fields, consistent with experimental evidence of faster hole boring with reduced temporal-intensity contrast [256]. For $a_0 = 160$, and both cases, the front surface RPA and rear surface

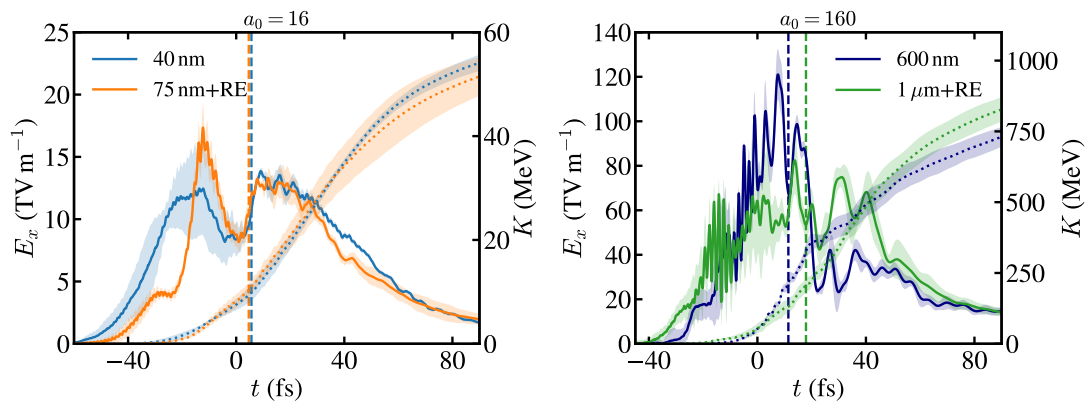


Figure 4.17: The mean local longitudinal electric field (solid) and energy (dotted) of the tracked protons as a function of time from targets with and without modelling the laser rising edge (RE), for the stated values of a_0 . The vertical dashed lines indicate t_{rsit} .

sheath fields merge at $t = -30$ to -20 fs. The tracked protons accelerate in this combined field until t_{rsit} , at which point they detach from the remains of the bulk target and continue their acceleration, from close proximity to the dense positively charged ion layer into the rear surface sheath field enhanced by electrons accelerated forwards directly by the transmitted laser fields. The proton acceleration continues further from the initial target position than the 3D case in figure 4.13 due to the reduced dimensions for transverse expansion.

The mean local E_x and energy of the tracked protons are shown in figure 4.17. The electric field profile is almost identical for $a_0 = 16$, differing only before RSIT as expected from the previous figure. The results for $a_0 = 160$ in both cases show a growing field strength up to immediately before RSIT, and a second peak shortly afterwards. The protons continue to gain energy longer than the 3D cases in figure 4.14 as a result of the exaggerated fields long after t_{rsit} .

4.7 2D — radiation reaction

The degree of synchrotron emission of an electron within an electromagnetic field is characterised by the quantum parameter $\chi_e \simeq (\gamma_e/E_S)|\mathbf{E}_\perp + \mathbf{v} \times \mathbf{B}|$, where $E_S = 1.32 \times 10^{18} \text{ V m}^{-1}$ is the Schwinger field [135, 257]. For laser intensities $I_L \sim 10^{23} \text{ W cm}^{-2}$, $\chi_e \sim 0.1$, depending upon the relative trajectory of the laser light and electron, and the power of synchrotron emission is considerable. Therefore, radiation reaction is

important. The loss of electron energy to radiation is expected to degrade acceleration from opaque targets and enable improved acceleration with RSIT [240–246].

In this section, further simulation results for linear polarisation and $a_0 = 310$ including radiation reaction in the EPOCH code as described in [130] are presented. These conditions correspond to the highest laser intensity considered here and strongest electron heating, for which the effects of radiation reaction are expected to be greatest.

4.7.1 Electron cooling

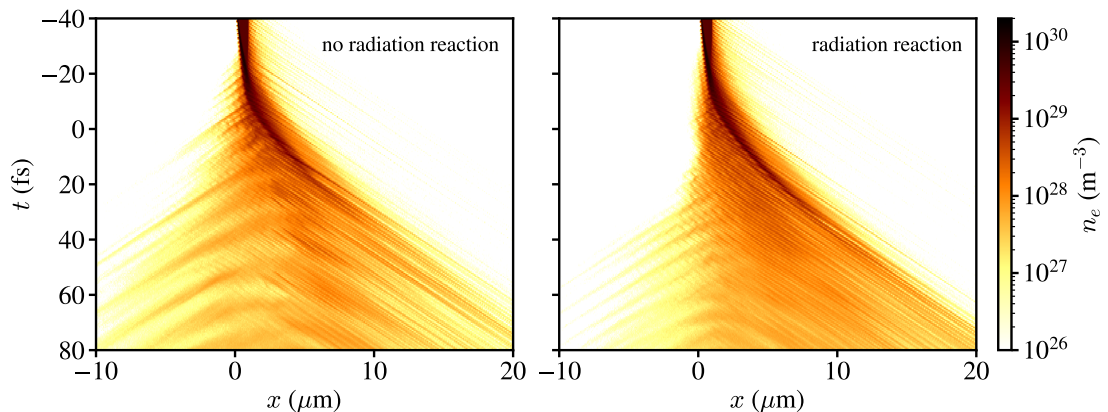


Figure 4.18: The electron density along the x -axis for $l = 1 \mu\text{m}$ and $a_0 = 310$ without and with radiation reaction.

The evolution of the electron density along the laser propagation direction is shown for an example target with $l = 1 \mu\text{m}$ in figure 4.18 for simulations with and without radiation reaction. Electron motion counter to the laser pulse (in the $-x$ -direction) is strongly inhibited by radiation reaction, as expected. The density of electrons co-propagating with the laser pulse is higher with radiation reaction, and the cooling of the electrons causes the target to remain as a well-defined thin high density layer for longer. The intensity threshold for radiation reaction to overcome the transverse ponderomotive force and cause radiative trapping of electrons within the laser pulse was derived by Ji *et al.* [258] as $a_{th} \sim (\phi_L / \sqrt{2 \ln 2} r_e)^{1/3}$, where $r_e = e^2 / 4\pi\epsilon_0 m_e c^2$ is the classical electron radius. Here, $a_{th} \sim 1000 > a_0$ and the radiative trapping effect is not significant, yet radiation reaction does slow the ponderomotive escape of electrons and cause them to be contained within the laser pulse for longer.

The energy spectra of the electrons for all modelled targets are shown in figure 4.19. The number of electrons with energies $K \lesssim 0.1 \text{ GeV}$ increases upon en-

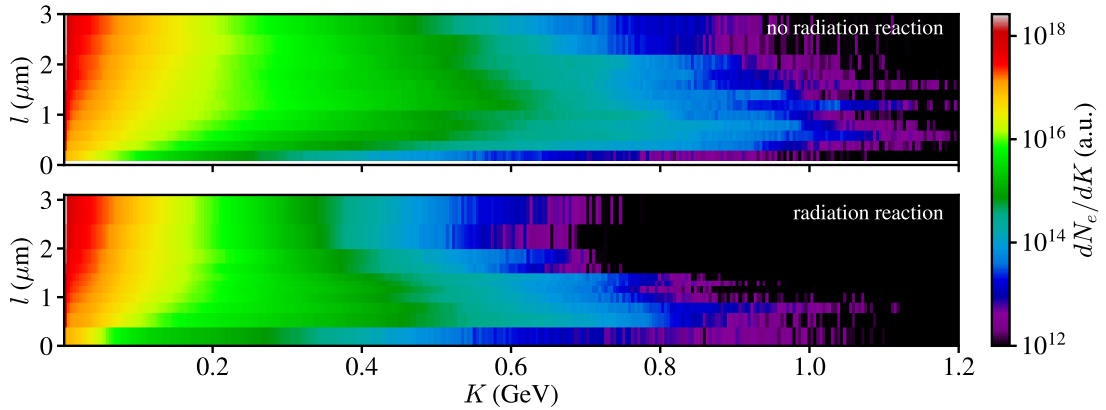


Figure 4.19: The electron energy spectra at $t = 17$ fs for all modelled target thicknesses, with and without radiation reaction.

ablating radiation reaction. However, the highest energy electrons above this range are considerably depleted. The power radiated by an electron scales rapidly with the electron energy. Assuming highly relativistic electrons ($\gamma \propto K$) with the same instantaneous trajectory and electromagnetic field, $\chi_e \propto K$ and the radiated power $P = 4\pi\alpha_f m_e c^3 \chi_e^2 g(\chi_e) / 3\lambda_c \propto K^X$, where $X = 2$ in the classical limit ($\chi_e \ll 1$) and $X = 2/3$ in the quantum limit ($\chi_e \gg 1$). As a result, the temperature of the electron spectrum is less than otherwise expected, and an accurate electron temperature scaling at these intensities will require inclusion of radiative energy losses, unlike those derived for lower laser intensities [86, 259, 260].

4.7.2 Proton acceleration with radiation reaction

The maximum proton energies for a range of target thicknesses with and without radiation reaction are shown in figure 4.20(a). In almost all cases the maximum proton energy reduces with radiation reaction, and the peak value reduces from 2.2 GeV for $l = 1.4 \mu\text{m}$ to 2 GeV for $l = 1 \mu\text{m}$. The difference is greatest for $l = 2.8 \mu\text{m}$, where K reduces by $\sim 50\%$. The radiative cooling of electrons is expected to greatly impair rear surface sheath acceleration, which is important for proton acceleration in thick targets. The mitigation of the electron heating and expansion is evident in the delayed onset of RSIT shown in figure 4.20(b). Although synchrotron emission affects the interaction, figure 4.20(c) shows its optimisation with $t_{rsit} \approx 0$ is maintained. The growing partition of laser energy into high energy photons [261] causes the conversion efficiency to fast protons to reduce compared to that expected otherwise; the peak value is lowered by

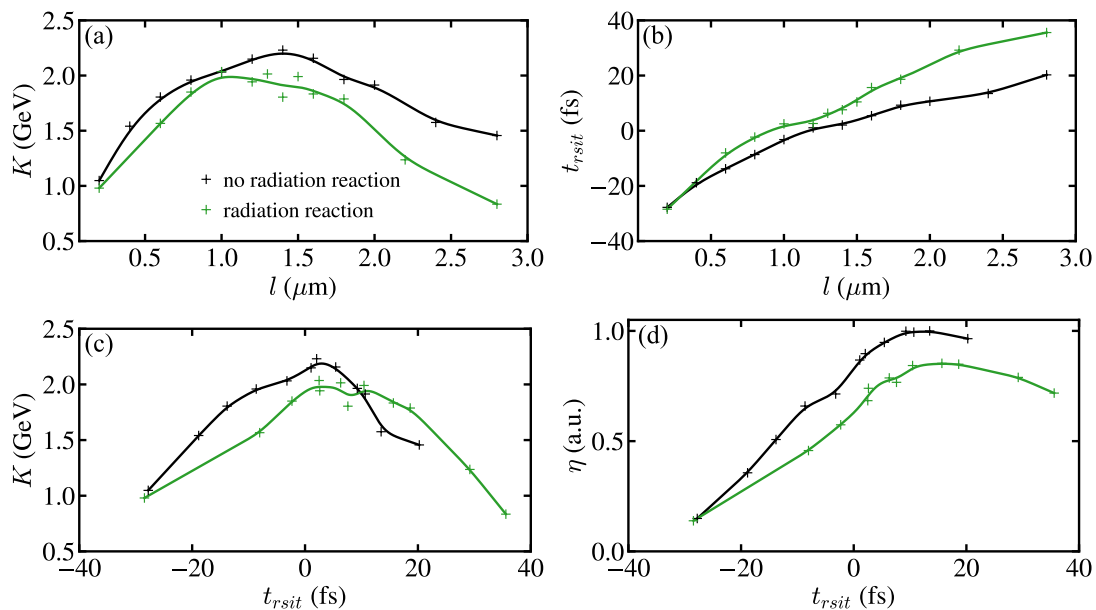


Figure 4.20: (a)–(c) The maximum proton energies and onset times of RSIT for a range of targets with and without radiation reaction, where $a_0 = 310$ and the laser pulse is linearly polarised. (d) The conversion efficiency of laser-to-proton energy as a function of t_{rsit} .

$\sim 15\%$ in Figure 4.20(d).

The angle-resolved proton spectrum for the optimum $l = 1 \mu\text{m}$ target with radiation reaction in figure 4.21(a) shows spectral bunching of the protons along the target normal ($\theta = 0$) into two peaks covering ~ 200 MeV each that were not seen in the optimum case without radiation reaction shown in figure 4.3(h). Modulations in the proton spectra along the target normal were seen in the spectra of some targets without radiation reaction in figure 4.3(g) and could be an indicator of radiation pressure acceleration. However, they appear more pronounced in this case. The spectra for other targets with radiation reaction are shown in figure 4.21(b). The influence of radiation reaction on the angle-resolved spectral shape of the proton beam through the electron dynamics remains an avenue for further investigation.

The improvements to the maximum proton energies with radiation reaction in relativistically transparent targets previously observed were found either in 1D PIC simulations and models [241, 245, 246], 2D PIC simulations at lower density ($16n_c$) and higher intensity ($10^{24} \text{ W cm}^{-2}$) [246], or up to 3D simulations (at density $64n_c$) using a classical model [244]. The use of 1D PIC simulations prevents transverse expansion of the electrons (and protons). As a result, the accelerating fields can be substantially

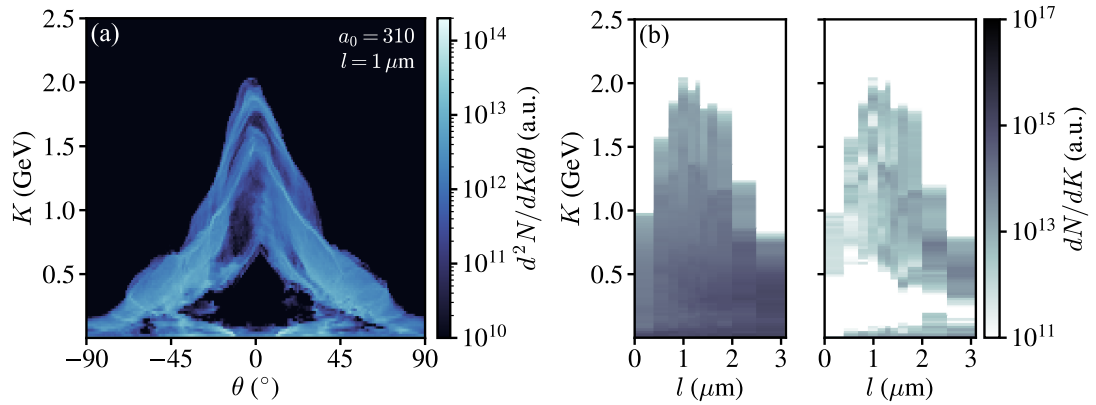


Figure 4.21: (a) The angle-resolved proton spectrum for the optimum target thickness with radiation reaction. (b) The full proton spectra (left panel) and within a divergence half-angle $\theta_{1/2} < 2.5^\circ$ (right panel) for all targets modelled with radiation reaction.

higher than in 2D and 3D simulations. Modelling densities much lower than solid density mitigates RPA with such high intensities, and potentially TNSA and RSIT-enhanced acceleration, especially if the targets remain so thin as to transmit the laser pulse almost completely. Much higher intensities than considered here considerably increase the radiation friction force (and pair production should be included in the modelling). Finally, classical models are insufficient for $I_L \geq 10^{23} \text{ W cm}^{-2}$ and are expected to exaggerate the radiation friction force. Experimental measurements and detailed 3D simulations and models of the interaction with the appropriate conditions are necessary.

4.8 Scaling with laser intensity

4.8.1 Maximum proton energy

The maximum proton energies achieved in each target thickness scan are shown in figure 4.22(a) for both laser polarisations—the same laser intensities were considered, resulting in a horizontal offset in a_0 —and 2D and 3D simulations. Here, the results with radiation reaction are shown for $a_0 = 310$ for linear polarisation, and target thickness scans were only performed in 3D for $a_0 = 50$ (linear polarisation) and $a_0 = 35$ (circular polarisation) with the optimum target thicknesses from the 2D simulations used for the remaining points. The proton energy scaling is almost independent of polarisation and dimensionality across this wide intensity range, with all intensity scalings in the range

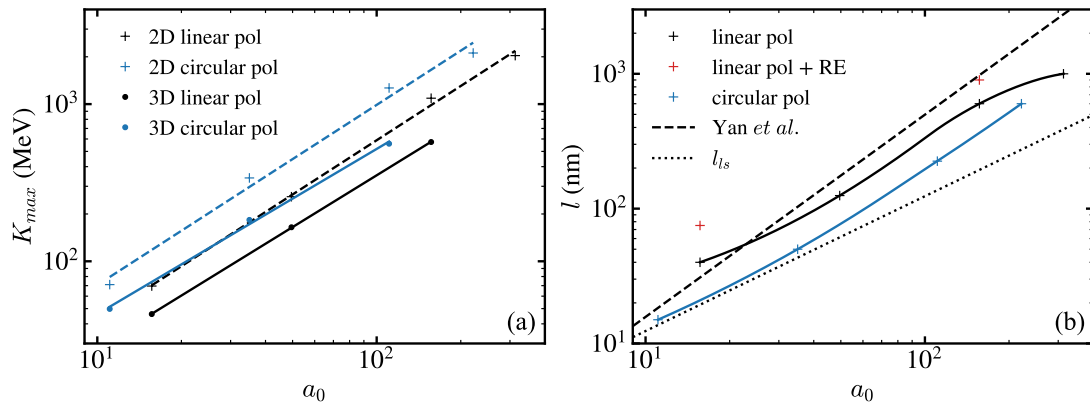


Figure 4.22: (a) The maximum proton energy as a function of a_0 for each polarisation in 2D and 3D simulations, with derived power law scalings ($K_{max} \propto I_L^X$, where $X = 0.53$ – 0.57). (b) The optimum target thickness from the 2D simulations as a function of a_0 , for each polarisation, and the simulations with linear polarisation where the laser pulse rising edge was included (RE). Predictions using the model of Yan *et al.* [100] for transparency occurring at the peak intensity of the laser pulse are included (dashed), and the analytically predicted optimum target thickness for light sail RPA $l_{ls} = a_0 n_c \lambda_L / \pi n_e$ (dotted) [89]. For $a_0 = 310$, the results with radiation reaction are shown.

$$K_{max} \propto I_L^X \text{ where } X = 0.53\text{--}0.57.$$

4.8.2 Optimum target thickness

The optimum target thicknesses from the 2D simulations are shown in figure 4.22(b). It was shown earlier that these correspond to the onset of RSIT close to the peak of the laser pulse. The reduced electron heating and expansion rate for circular polarisation causes optimisation with thinner targets. The analytical model for the onset time of RSIT by Yan *et al.* [100] was used to show predicted target thicknesses for transparency to the laser peak. Although similar values to the optimum target thickness for linear polarisation at the lowest intensities considered are produced, a much faster scaling with intensity ($\propto I_L^{3/4}$) than the simulations causes them to diverge with increasing laser intensity. This is compounded by the reduction of the optimum target thickness due to radiation reaction for $a_0 = 310$, where the absence of radiation reaction in the model makes it insufficient.

The results in section 4.4 (and 4.5) indicate the fastest protons for circular polarisation are not purely accelerated by light sail RPA, yet the analytical optimum thickness derived from consideration of the onset of transmission of the foil $l_{ls} = a_0 n_c \lambda_L / \pi n_e$

[89] matches the results well for $a_0 = 11$ and 35. For higher intensities the transverse plasma expansion and electron heating become increasingly important, and the simulation results depart further from this prediction that does not consider these effects.

The laser pulse rising edge was demonstrated to increase the optimum target thickness due to the hastened onset of RSIT. However, the change in the optimum thickness in experiments will depend upon the full laser temporal-intensity contrast profile, and the rising edge may be considerably different to that assumed here. Prediction of the optimum target thickness for a given material and set of laser parameters is therefore difficult; it may only be possible with characterisation of the unique temporal-intensity contrast profile of the high intensity pulses produced by a given laser system and numerical modelling of each stage of the interaction. In any case, the results shown here with the effect of laser contrast demonstrate optimum proton acceleration when RSIT is simultaneous with the arrival of the peak of the laser pulse holds.

4.9 Summary

In summary, the maximum energy to which protons are accelerated in thin solid CH foils has been demonstrated, with precise calculation of the onset time of RSIT in 2D and 3D PIC simulations, to be highest when RSIT is simultaneous with the arrival of the peak of the laser temporal-intensity profile. Importantly, this was shown across the intensity range 5×10^{20} – 2×10^{23} W cm⁻², for both linear and circular laser polarisation, with modelling of the rising edge contrast and lastly, with radiation reaction accounted for.

A detailed examination of the acceleration dynamics for linear polarisation showed a combination of RPA and TNSA preceding the onset of RSIT, with the dominant mechanism in this phase switching from TNSA for $a_0 = 16$ to combined RPA-sheath acceleration as the protons move with the compressed electron layer for $a_0 = 160$. RSIT was found to enhance the proton acceleration through the direct acceleration of electrons in the plasma volume as it breaks out of the target rear side; the removal of electrons leaves behind a dense positively charged region of ions that repels the protons, and the increased density of electrons moving out of the target at the rear side causes a greater attraction force on the protons. This is optimised essentially, for the same target material, where the peak electromagnetic force of the laser pulse breaks

through the rear side of the highest density of plasma, inducing the most enhanced charge-separation fields as the electrons are accelerated from the thin target.

Circularly polarised laser light causes the target dynamics to be dominated by light sail acceleration prior to RSIT, with some sheath acceleration. The proton acceleration continues after the onset of RSIT with the forward acceleration of some electrons throughout the target by the transmitted pulse, similar to the case for linear polarisation. The multidimensional target expansion and relativistic heating cause the relativistic critical density surface to move faster than the light sail model predicts prior to RSIT, and more energy is gained by the fastest protons in the RSIT phase, yet the peak critical surface velocity was shown to be an indicator of optimum acceleration. Measurements of the reflected laser spectrum could provide an alternative route to identifying optimisation.

The presence of an extended laser pulse rising edge with high intensity was shown to increase the optimum target thickness whilst allowing comparable proton energies to be achieved. Although the pre-expansion it induces may be compensated for with hydrogen atoms in the bulk target material, proton (or other ion) acceleration relying upon surface contaminant layers will be significantly impacted by TNSA pre-acceleration, if a considerable fraction of the laser pulse energy is contained within the rising edge above the relativistic intensity threshold.

Synchrotron radiation was shown with 2D simulations for $a_0 = 310$ to delay RSIT, and reduce the maximum achievable proton energy (by 10%) and laser-to-proton energy conversion efficiency (by 15%). Here, electron motion not parallel with the laser pulse is greatly impeded, slowing target expansion and reducing both the peak energy and temperature of the electron spectrum.

The critical influence of relativistic transparency on proton acceleration has been further delineated here. Although its onset time may be difficult to measure experimentally due to the ultrashort timescales and (time-dependent) absorption of the pulse after it begins, the results shown demonstrate the transmitted and reflected laser light should contain information on the proton acceleration. Even if information is difficult to directly extract from measurements of this light, the data could be used in the development of neural network models for non-invasive measurement of the accelerated particle beam, similar to [262], or for comparison with 3D simulations. Nevertheless, the onset time of RSIT is vital to consider in laser-solid interactions at multi-PW laser

facilities, and in optimisation of laser-driven ion sources for applications that require high energy ion beams.

Bayesian optimisation and control of the angular distribution of synchrotron radiation in ultraintense laser-solid interactions

Bremsstrahlung radiation has offered the most efficient source of high energy photons (> 100 keV) from solid targets irradiated at high power laser facilities, which have generally been limited to peak intensities up to $I_L \sim 10^{21} \text{ W cm}^{-2}$ until recent years. A new class of high power laser facilities offering peak intensities $I_L > 10^{22} \text{ W cm}^{-2}$ are now becoming available, at which the rapid increase in synchrotron radiation from electrons with intensity of the electromagnetic field may enable the possibility of such radiation to dominate other sources. The synchrotron radiation produced in laser-solid interactions is expected to provide a bright source of MeV photons with ultrashort duration, which could be used for positron production, photonuclear reactions and other applications. However, development for applications will require a target suitable for high repetition rate, such as tape drive targets or liquid jets, and optimisation of the generated high energy photon source.

In this chapter, a numerical investigation of the optimum parameters for the generation of synchrotron radiation in ultraintense laser pulse interactions with thin planar foils is reported. In a number of 2D parameter space scans of 2D particle-in-cell simulations, the target foil thickness, the angle-of-incidence of the laser pulse, and the laser pulse duration, focal spot size, focal point and peak intensity are varied to show the ef-

fect on the photon emission for p-polarised light (section 5.3). For constant laser pulse energy, the conversion efficiency to synchrotron radiation is found to be highest for parameters that maximise the peak laser intensity incident on the target surface, and oblique incidence provides a 60% increase to the maximum conversion efficiency compared to normal incidence for the conditions tested. A Gaussian process (GP) regression algorithm is then applied to control the input parameters for a series of simulations to optimise various physical properties of this source of high-energy photons individually. Multi-variate objective functions containing several different physical properties are then optimised, in which the bremsstrahlung emission is minimised whilst maximising parameters of the synchrotron emission (sections 5.4 and 5.5). The discovery of the angle-of-incidence as a critical input parameter in maximising the directional emission of synchrotron radiation leads to further investigation and discussion of its influence on the interaction (section 5.6), and motivates 3D PIC simulations for different laser light polarisation states to demonstrate control of the spatial profile of synchrotron emission (section 5.7).

The results shown here were published in *High Power Laser Science and Engineering* **11**, e34 (2023).

5.1 Introduction

Irradiation of a solid target with a relativistically intense laser pulse typically produces a large number of photons with energies extending to the multi-MeV range, due to bremsstrahlung radiation from laser-accelerated electrons propagating through the target [263–265], and x-ray line emission from excited atomic states [266]. These bright sources of x-rays and gamma rays have potential applications including radiography [33, 267–269], initiating photonuclear reactions [263, 270] and producing beams of positrons through the Bethe-Heitler process [140, 142, 241, 271, 272]. New multi-PW laser systems offer increased achievable peak laser intensities of $\sim 10^{23} \text{ W cm}^{-2}$ [35]; with such intense laser light, higher energy photons will be produced than previously possible in these interactions, and the dominant mechanism for high energy photon generation is expected to become synchrotron emission (nonlinear Compton scattering) from ultrarelativistic plasma electrons.

The energy electrons can gain in a high intensity laser field scales with the parameter

$a_0 = eE_L/m_e c \omega_L \gg 1$. In moving to higher intensity laser pulses, electrons may become increasingly relativistic and generate more synchrotron radiation due to the increase in the field strength in their rest frame. This is expressed by the electron quantum parameter:

$$\chi_e = \frac{\gamma_e}{E_S} \sqrt{(\mathbf{E}_\perp + \mathbf{v}_e \times \mathbf{B})^2 + E_\parallel^2 / \gamma_e^2}, \quad (5.1)$$

where \mathbf{E}_\perp is the electric field perpendicular to the electron motion, E_\parallel is the magnitude of the electric field parallel to the electron motion and $E_S = 1.32 \times 10^{18} \text{ V m}^{-1}$ is the Schwinger field for which electron-positron pairs are produced from vacuum [135, 257, 273]. Here, χ_e is dominated by the perpendicular fields for relativistic electrons ($\chi_e \simeq (\gamma_e/E_S)|\mathbf{E}_\perp + \mathbf{v}_e \times \mathbf{B}|$), and is maximised for electrons counter-propagating with a laser pulse, where $\chi_e \simeq \gamma_e E(1 + \beta_e)/E_S$.

For $\chi_e \gtrsim 0.1$, the electric field in the rest frame of the electron approaches the Schwinger field and a large fraction of the incident laser pulse energy may be converted into synchrotron gamma rays, the radiation reaction force on the emitting electrons becomes important and the high energy photons in the laser field may produce electron-positron pairs through the multi-photon Breit-Wheeler process [36, 143]. These strong-field QED effects are expected to be a common feature of laser-plasma interactions for laser intensities $I_L > 10^{23} \text{ W cm}^{-2}$ [141, 144].

All-optical demonstrations of radiation reaction with peak laser intensities of $\sim 10^{21} \text{ W cm}^{-2}$ have been performed [274, 275], in which an electron beam produced with laser wakefield acceleration was collided with a laser pulse. Although higher laser intensities are generally required for the synchrotron radiation to have a significant influence on the electron motion and dominate other sources of high energy photons, such as bremsstrahlung emission, in laser-solid interactions, theoretical and numerical studies indicate the generation of a high power gamma ray flash with of the order of 10% conversion efficiency from the laser energy possible [147, 155, 261, 276–278]. A large number of different interaction geometries and schemes have been proposed to enhance the gamma ray generation and associated pair production: counter-propagating laser pulses [152, 239, 279] (and foils [280]), a prefilled channel target [151, 152, 281, 282] (or cone [283]), a hollow cone target [284], radial laser polarisation [278, 285], focussing and compressing the laser pulse as tightly as possible into the λ^3 regime [278, 285], oblique incidence [286, 287] (with two laser pulses [288]), relativistically underdense targets [281], moving targets that become relativistically transparent [289],

near critical density plasma with a solid target to reflect the pulse [283, 290–292], a solid target with front surface pre-plasma [293, 294], various microstructured or wire targets [295–297], a concave target surface [298] and laser focussing with a relativistic plasma mirror [299]. However, thus far experimental demonstration of a gamma ray source from a laser-solid interaction in which synchrotron radiation is dominant as compared to other generated sources, such as bremsstrahlung, has not occurred. This is key not only for the development of a new source of gamma radiation but also for experimental investigations of the underlying physics. Numerical modelling and theory shows bremsstrahlung emission is reduced by using a lower atomic number, Z , target material (given the emitted power scales with Z^2) [142, 300–303]. The use of thinner targets also considerably reduces bremsstrahlung production [301, 302, 304], including ultrathin (nanometer scale) solid foils [304].

When an ultrathin foil is irradiated by a high power laser pulse, the combined expansion of the target and heating of the electrons to relativistic velocities can reduce the plasma frequency ($\omega_{pe} = \sqrt{n_e e^2 / \epsilon_0 \gamma_e m_e}$) to less than the laser frequency, and enable laser light propagation through the target plasma in the process known as relativistic (self-induced) transparency [231, 232], as discussed in section 2.3.5. The synchrotron emission can be particularly efficient in relativistically transparent targets, where much of the radiation is emitted by electrons that counter-propagate into the laser pulse due to the space charge field at the front of the pulse, producing an angularly wide beam in the backwards (with respect to the laser propagation) direction [155, 277, 304], in a process termed re-injected electron synchrotron emission (RESE) [155]. Solid targets also produce forward emitted synchrotron radiation from the reflected light interacting with electrons in the skin depth, and oblique lobes either side of the laser propagation direction that are usually symmetric [277, 302, 304, 305]. Although the conversion efficiency to synchrotron radiation is often lower for opaque targets compared to the maximum possible for those that experience RSIT, the introduction of a long pre-plasma density scale length on the target front surface can provide a large volume of transparent plasma to interact directly with the laser field and strongly increase the conversion efficiency [276, 277, 293, 294].

There are many other laser and target parameters that can influence the generation of synchrotron radiation in these interactions, and finding the optimum conditions over a parameter search space with a large number of dimensions would be extremely

costly and time consuming to achieve manually. In recent years, it has become possible to apply machine learning-based techniques as an efficient method of searching this multi-dimensional parameter space to find input conditions for desired output source parameters. Bayesian optimisation [306, 307] is one such technique that is useful when the objective function chosen to be optimised, such as the yield of gamma rays, is susceptible to noise and is costly to evaluate. This approach has already been demonstrated to improve electron and x-ray beams from wakefield accelerators [308, 309], and laser-driven proton acceleration in simulations [310]. Other machine learning techniques that have been applied in the study of laser-plasma accelerators include neural networks [311, 312] and evolutionary algorithms [313–316].

The beam of high energy particles or photons generated in these interactions is defined by many properties, such as the conversion efficiency, energy spectrum and divergence. For some applications, it is necessary to achieve several beam properties within a specific range and thus tune a number of the beam properties simultaneously. Often in such a scenario, these properties are individually optimised in different regions of the search space. Multi-objective optimisation [317–320] involves finding a finite set of solutions that are located on the optimum edges of the objective space, known as the Pareto front, where one of the objectives cannot be improved without a trade-off in another. However, if only a single solution is desired, such as in the case of an automated laser-driven particle or radiation source guided by machine learning, it is not necessary to find a large set of solutions to choose between and the problem can be reduced to the optimisation of a single objective function. Although, this presents the challenge of combining the multiple objectives into a single composite function that is optimised at the most desirable location on the unknown Pareto front. Experimental optimisation of laser-plasma accelerated electrons has been demonstrated with such a function incorporating multiple electron beam properties [308], and in a simulation-based study [320], different functions based on the same physical properties are demonstrated to optimise at different locations on the Pareto front found using multi-objective optimisation.

This chapter presents the results obtained from applying machine learning to the optimisation of synchrotron radiation produced in simulations of laser-foil interactions. In addition to identifying optimal conditions for synchrotron gamma ray generation, and simultaneous reduction of bremsstrahlung radiation, this chapter also aims to improve the understanding of the plasma dynamics that cause synchrotron radiation. This

includes exploring the dependencies of the angular radiation profile on the incidence angle of the laser upon the initially flat foil surface.

5.2 Simulation parameters

The fully relativistic PIC code EPOCH [211] was used in 2D and 3D to model the gamma ray generation. Synchrotron and bremsstrahlung photon data for energies $\varepsilon \geq 100$ keV was output individually. The techniques used for calculating synchrotron emission in the EPOCH code are described in reference [130], and those used for calculating bremsstrahlung emission are described in references [301, 321]. Radiation reaction was included, but pair production was not.

For the 2D simulations, the spatial grid had dimensions $30 \mu\text{m} \times 20 \mu\text{m}$ ($x \times y$) and cell size $8 \text{ nm} \times 12 \text{ nm}$, with free-space boundaries. To simulate an experimentally practical low- Z target material, solid density plastic (CH) was chosen and modelled as a uniform, fully ionised plasma with electron density $n_e = 3.5 \times 10^{29} \text{ m}^{-3}$, neutralised by an equal ratio of C^{6+} and H^+ ions. The initial electron and ion temperatures were $T_e = 3 \text{ keV}$ and $T_i = 100 \text{ eV}$, respectively, with 50 electron macroparticles per cell and 10 ion macroparticles per cell per species. The target parameters were the thickness, l , and the angle between the normal to the target surface and the x -axis, θ_i . The laser pulse was propagated along the x -axis to the target, and had wavelength $\lambda_L = 800 \text{ nm}$, and a

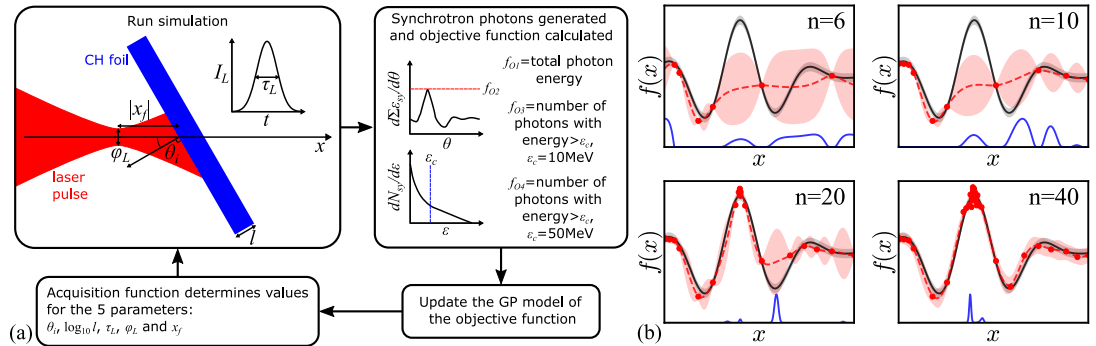


Figure 5.1: (a) The Bayesian optimisation loop and schematic of the simulation setup. The synchrotron photon energy spectrum ($dN_{sy}/d\varepsilon$) and angle-resolved yield ($d\sum \varepsilon_{sy}/d\theta$) generated in each simulation are depicted to illustrate several of the objective functions. (b) An example of Bayesian optimisation of a noisy 1D function showing the true function (black), the model (red) and the acquisition function (blue) for different numbers of iterations (n), where the shaded regions indicate uncertainties.

Gaussian temporal-intensity profile with full width at half maximum (FWHM) τ_L . The laser pulse was focused at $x = x_f$, where $x = 0$ corresponds to the target irradiated (front) surface (the laser pulse focuses behind the target surface for $x_f > 0$, and in front of the target for $x_f < 0$) and x_f is the defocus parameter. At focus, the laser pulse has a Gaussian spatial-intensity profile with diameter ϕ_L (FWHM). The values of l , θ_i , τ_L , x_f and ϕ_L used are stated in each section.

The 3D simulations used a spatial grid with dimensions $20 \mu\text{m} \times 15 \mu\text{m} \times 15 \mu\text{m}$ ($x \times y \times z$) and cell size $10 \text{ nm} \times 30 \text{ nm} \times 30 \text{ nm}$. The target density was reduced to an electron density of $n_e = 1.74 \times 10^{29} \text{ m}^{-3}$ due to the increased cell size, whilst maintaining the areal density of the quoted target thicknesses in section 5.7 by modelling an increased (approximately doubled) thickness. There were 12 electron macroparticles per cell and 6 ion macroparticles per cell per species.

The BISHOP code was used in conjunction with EPOCH to automate the 2D PIC simulations in 2D grid scans of various parameters, and for the Bayesian optimisation of various objectives using a Gaussian process regression algorithm [322], in the same manner as the code was used in reference [310]. For all optimisation scans, 30 initial simulations are performed with randomly generated input parameters (10 more than used previously [310] due to one more input parameter), the objective function is evaluated from the simulation data and the algorithm produces a probability distribution of all potential functions that could fit the results to create a model of the objective function. An acquisition function calculated from the model then determines the next set of input parameters to simulate. Acquisition functions corresponding to the upper confidence bound, expected improvement and probability of improvement methods are calculated. One of these is chosen at each iteration in a process known as hedging, which outperforms the use of individual acquisition functions in identifying the optimum in the minimum number of iterations [323]. With each iteration the model is updated and the acquisition function guides the parameters towards the optimum of the objective function. Up to 200 simulations were run for each objective function used to identify their respective optimum. The optimisation parameters were θ_i , $\log_{10} l$, τ_L , ϕ_L and x_f , illustrated in figure 5.1(a). The logarithm of target thickness was used to ensure ultrathin targets that undergo RSIT cover a significant fraction of the search space. Several of the objective functions used (defined in sections 5.4 and 5.5), which correspond to important parameters of the synchrotron emission, are also shown: the

synchrotron yield, peak angle-resolved yield and number of photons in the high energy spectral tail for different cut-off values. An example demonstration of Bayesian optimisation of an arbitrary 1D function susceptible to noise is shown in figure 5.1(b) for different numbers of iterations.

Previously, the same approach was applied for the optimisation of laser-driven ion acceleration [310] using a single physical parameter in the objective function (maximum ion energy). Here, this method is applied both for single and multiple physical parameters in the objective function, enabling the exploration of different objective functions to influence the trade-off in one required beam parameter against another.

5.3 2D Parameter space scans of gamma ray emission

Before optimising the interaction, the influence of a number of input parameters, including each of the chosen optimisation parameters, was first explored in 2D parameter space scans. The target thickness was one of the varied parameters in each scan, enabling separation of the effect of RSIT, which depends upon target thickness, from the effect of varying each of the other parameters. Initially, in figure 5.2(a)–(c) a pulse with $\tau_L = 30$ fs, $\phi_L = 3$ μm , and $x_f = 0$ incident at target normal ($\theta_i = 0$) was considered, and simulated for peak laser intensities $I_L = 3.16 \times 10^{21}$ – 10^{23} W cm^{-2} , covering a range for which synchrotron radiation may become measurable, up to where it is expected to dominate. Target thicknesses between 50 nm and 5 μm were simulated, encompassing relativistically transparent to opaque targets across the intensity range, demonstrated by the percentage laser energy transmission in figure 5.2(a) and also shown by the white contours of these values in figure 5.2(a)–(c).

To produce considerable synchrotron radiation, highly relativistic electrons are required in a strong electromagnetic field. The amplitude of the laser electromagnetic field is usually much greater than any self-generated electric or magnetic fields. For a constant laser intensity, the number of electrons accelerating in the laser fields and their energy are generally the dominant influence on the total energy converted into synchrotron radiation ($\chi_e \propto \gamma_e$, ε_e for relativistic electrons). The variation of synchrotron conversion efficiency with target thickness in figure 5.2(c) is therefore due to the changing population of electrons that move through the laser fields; the coupling of laser energy to electrons is known to change between relativistically transparent and

opaque targets [249]. In figure 5.2(b), the total electron energy in the transparent plasma in front of the relativistic critical density surface (x_c , where $n_e = \gamma_e n_c$) and in the laser skin depth ($\delta_s = c/\omega_{pe}$) integrated over the period of synchrotron emission (estimated as $-\tau_L/2 < t < \tau_L$, where the laser peak intensity reaches $x = 0$ at $t = 0$)

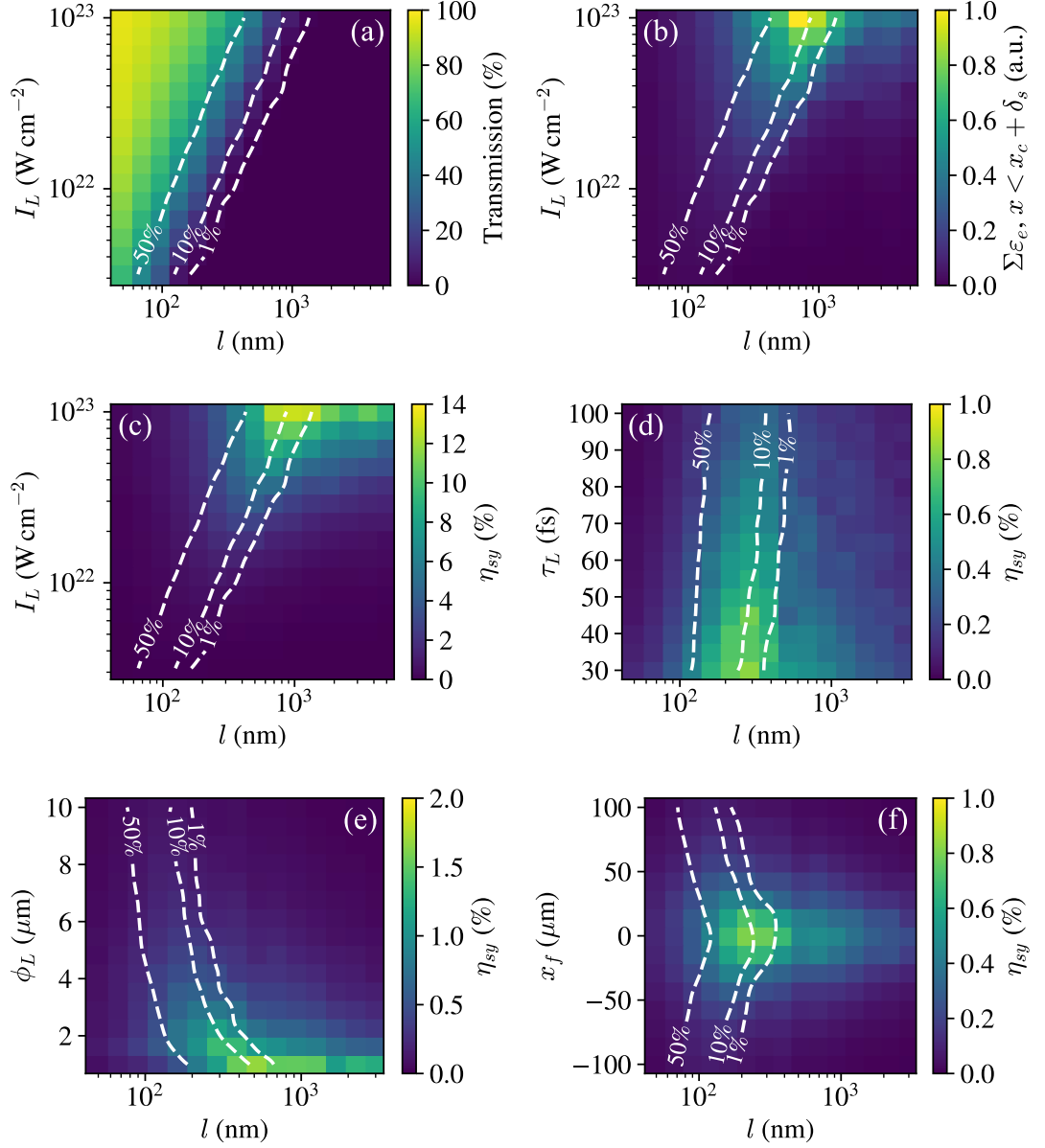


Figure 5.2: (a) Percentage transmission of the laser pulse, (b) total electron energy in front of the plasma critical surface and in the laser skin depth averaged over the period of synchrotron emission, and (c) laser-to-synchrotron photon energy conversion efficiency, all for varying target thickness and laser intensity. (d)–(f) Laser-to-synchrotron photon energy conversion efficiency for varying pulse duration, focal spot size, and defocus, respectively, with target thickness.

is shown. The highest total electron energy, in the plasma accessible to the laser field, for each I_L simulated is on average found when the laser energy transmission is 13%, where the points either side of the maximum provide transmission bounds of 2.6% and 29% for the maximum. This agrees well with the laser-to-synchrotron radiation energy conversion efficiency, η_{sy} , values in figure 5.2(c), which are maximised for 11% transmission, with the adjacent points providing a range between 1.9% and 26%. In the absence of any pre-plasma, for targets that remain opaque the interaction is limited to electrons within the laser skin depth, and any electrons that are accelerated into the laser pulse by self-generated fields in the plasma. For targets that become relativistically transparent, the laser can interact with a larger number of electrons, and those electrons can reach higher energies with direct laser acceleration. The synchrotron conversion efficiency thus increases. If the target is so thin that it transmits a large fraction of the laser energy ($\gtrsim 50\%$), the total synchrotron emission reduces due to the reduced number of emitting electrons. The propagation direction of the electrons is also important. In highly transparent targets the electrons are usually accelerated forwards with the laser pulse. The sustained rear surface sheath field can reflect many fast electrons backwards into the laser for thicker targets, which increases the synchrotron radiation they emit. The return current within the laser pulse can also contain a large number of highly relativistic electrons for relativistically underdense targets (see figure 1(b) in [304], and compare to figure 3(b2) for a relativistically overdense target), which may be responsible for the substantial backwards-directed synchrotron radiation in targets that undergo RSIT.

5.3.1 Laser-injected synchrotron emission

As previously discussed in section 5.1, there are many mechanisms that produce synchrotron radiation in these interactions. Here, it is necessary to provide a description of the process that produces the dominant source of synchrotron emission at the highest laser intensities considered. In this work, the transverse laser electric field directly injects plasma electrons in its path further into the laser spatial profile, whilst they accelerate and subsequently produce copious synchrotron radiation in the strong electric and magnetic fields. In the absence of pre-plasma, this laser-injected emission process increases rapidly for solid targets with laser intensity as a result of the longer cavity formed in the target by the increasing laser radiation pressure. The formation of a cav-

ity is essential for normal incidence onto an opaque flat surface to enable the extraction and acceleration of electrons within the laser pulse. Electrons are pulled transversely towards the centre of the focal spot by the laser electric field as it interacts with the walls of the plasma cavity, with the electron trajectory and the side of the focal spot and target cavity the electrons are injected from determined by the instantaneous direction of the laser electric field. These electrons are accelerated to high energies by the laser and space-charge fields as they move further into the focal spot, causing the production of synchrotron gamma rays within the intense fields that takes an angular profile dependent upon the laser polarisation. For linear polarisation, electrons are injected from opposite sides of the plasma cavity as the electric field oscillates, producing two forward-propagating lobes approximately symmetric about the laser propagation axis (for normal incidence onto a symmetric target only), which are separately modulated at the laser frequency and are separated by half a laser cycle.

This laser-injected emission process is different to edgeglow emission reported in [277, 305], in which the transverse ponderomotive clearing of electrons by the laser pulse generates transverse space charge fields that reintroduce electrons into the channel formed in the target. Here, the laser electric field usually dominates any other transverse electric fields at the edges of the channel, causing modulation of the channel surface and preventing electrons from entering the channel when the polarisation vector of the laser is directed away from the surface. The dominance of the laser fields over space charge fields in driving the electron injection and synchrotron emission in this work is demonstrated by the considerable synchrotron emission produced by electrons accelerated along the surface of targets at oblique incidence without the formation of a channel later in this chapter, and the polarisation-dependent angular profiles of the emission demonstrated in section 5.7. The transverse space charge fields are expected to be most important in interactions with targets that are initially near classical critical density, that immediately become relativistically underdense with the arrival of the laser pulse, and where the electron density is low enough for the electron and ion motion to begin to decouple, producing a densely positively charged channel. Only solid density targets were considered in this work, and the main influence of the space charge fields in the generation of synchrotron radiation is the assistance to the electron acceleration provided within their direct laser acceleration. Although the emitting electrons are accelerated within a plasma channel, these electrons do not generally undergo large

amplitude betatron oscillations as in [58] and related work. The maximum length of the channels formed in this work is approximately $5 \mu\text{m}$ (for the pre-expanded target $l = 3 \mu\text{m}$ results shown in figures 5.11–5.13), much less than the many tens of microns and longer relativistically underdense channels that such oscillations are usually observed in. Particle tracking showed the individual electron motions varied significantly. The self-formed channel evolves rapidly and the generation of rapidly changing space charge fields within the dense targets used can quickly change the trajectory of the electrons, producing considerably different paths for each particle. The most radiating electrons, however, tend to cross the laser focal spot at some point during their motion, as outlined in the description above. The emergence of laser-injected emission due to hole boring [86, 87] causes the conversion efficiency for opaque targets to approach the highest achievable with transparent targets at $I_L \sim 10^{23} \text{ W cm}^{-2}$, as shown in figure 5.2(c).

5.3.2 Pulse duration, focal spot size and defocus

In figure 5.2(d)–(f), the synchrotron conversion efficiency is shown, where the laser energy is kept constant in the 2D simulation geometry corresponding to peak intensity $I_L = 3 \times 10^{22} (30 \text{ fs}/\tau_L)(1 \mu\text{m}/\phi_L) \text{ W cm}^{-2}$ varying linearly with $1/\phi_L$. The values of the other parameters used are $\tau_L = 30 \text{ fs}$, $\phi_L = 3 \mu\text{m}$ and $x_f = 0$, unless scanned. The highest conversion efficiencies for figure 5.2(d)–(f) are on average found for laser transmission values of 10%, 11% and 15%, respectively, similar to the laser intensity scan results. The cause of this optimisation is expected to be the same as the discussion given for those results in section 5.3. The maximum conversion efficiencies in these scans are achieved for the minimum pulse duration, spot size and defocus, for each of which the laser intensity is maximised. Increasing the distance of focus from the target surface increases the beam width upon the surface, and in figure 5.2(f) such changes exhibit similar results to variation of the spot size in figure 5.2(e), with η_{sy} independent of the direction of the defocus.

5.3.3 Stability

Although these results indicate that the most efficient synchrotron radiation source for a fixed laser pulse energy corresponds to the shortest pulse duration and smallest focal spot size focused onto the surface of a partially transmissive foil, the small Rayleigh length, $z_R = \pi\phi_L^2/2\lambda_L \ln 2$, for a near-wavelength ϕ_L makes the interaction highly sus-

ceptible to small changes in the defocus. This was tested in 3D simulations, using the same configuration as in section 5.7, for $\phi_L = 1 \mu\text{m}$, $I_L = 1.1 \times 10^{23} \text{ W cm}^{-2}$, linear (along y) polarisation, normal incidence and one Rayleigh length, $2.83 \mu\text{m}$, of defocus. For $x_f = 0$, z_R and $-z_R$, the synchrotron conversion efficiency is 4.32%, 4.50% and 1.67%, respectively, corresponding to a change of +4% and -61% for the positive and negative defocus, respectively. In addition, the rapid variation of η_{sy} with changes to the transmission also makes such a source susceptible to changes in the plasma expansion dynamics. If source stability is required, a larger than near-wavelength sized focal spot is recommended. If laser intensities $\sim 10^{23} \text{ W cm}^{-2}$ are achievable, η_{sy} is more stable to changes in l for <10% transmissive targets due to the dominance of laser-injected synchrotron emission induced by hole boring of the target. This may be achievable for lower peak laser intensities if a lower density target material is used, or for solid targets with a preformed front surface structure, such as in reference [298].

5.3.4 Scaling of the synchrotron conversion efficiency

The 2D parameter space scans provide target thickness-dependent scalings of η_{sy} with each of the other parameters. In figure 5.3, these are presented for peak laser intensity, pulse duration and spot size, with power law fit values given for the value of l that maximises η_{sy} (black line), and for an indicative opaque target (red line; $l = 5 \mu\text{m}$ for figure 5.3(a), and $l = 3 \mu\text{m}$ for figure 5.3(b) and (c)). In figure 5.3(a), $\eta_{sy} \propto I_L^{1.8}$ for $l = 5 \mu\text{m}$ and $\eta_{sy} \propto I_L^{1.4}$ for the optimum thicknesses, in agreement with the $\eta_{sy} \propto I_L^{1.5}$ scalings reported in references [261, 302]. In both cases, the rate of increase slows as I_L approaches $10^{23} \text{ W cm}^{-2}$. The faster scaling for $l = 5 \mu\text{m}$ and the convergence of the two lines of fit in figure 5.3(a) results from the reduced role of target expansion in the optimisation of the synchrotron emission with increasing laser intensity, due to the increasing importance of the radiation pressure and the increasing relativistically-corrected critical density.

The use of ultrathin targets can increase η_{sy} by almost an order of magnitude compared with $l = 5 \mu\text{m}$ for the lowest intensities considered here, and therefore such targets provide the most accessible route to generating synchrotron radiation in laser-solid interactions. Synchrotron emission can be increased for the case of thick targets is the laser pulse interacts with a significant pre-plasma at the front surface, which can be produced by the laser light preceding the main pulse if the temporal-intensity

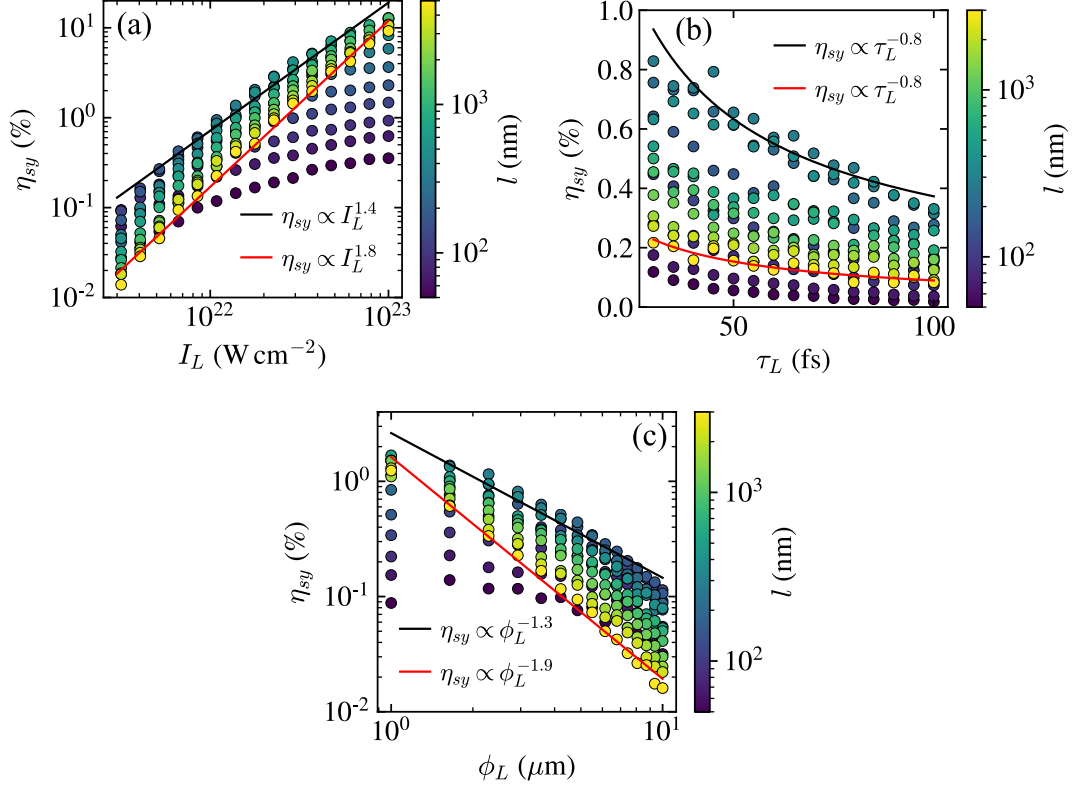


Figure 5.3: Scaling of the laser-to-synchrotron energy conversion efficiency with (a) peak laser intensity, (b) pulse duration and (c) focal spot FWHM, for varying target thickness. Power law fits are shown for the optimum target thicknesses (black) and for the thickest targets used (red; $l = 5 \mu\text{m}$ for (a) and $l = 3 \mu\text{m}$ for (b) and (c)).

contrast is low enough. This was not modelled in our simulations, which only included the main Gaussian peak in the temporal profile of the laser pulse. In experiments, increasing the peak laser intensity by orders of magnitude may require increasing the temporal-intensity contrast to prevent pre-expansion of the target or the creation of a significant pre-plasma at the front surface. Otherwise, the optimum conditions for synchrotron generation are expected to change.

For constant laser pulse energy, the pulse duration is found to play a weaker role, with $\eta_{sy} \propto \tau_L^{-0.8}$ for both $l = 3 \mu\text{m}$ and the transparent optimum thicknesses in figure 5.3(b). In contrast, the conversion efficiency depends strongly on ϕ_L , with $\eta_{sy} \propto \phi_L^{-1.9}$ for $l = 3 \mu\text{m}$ and $\eta_{sy} \propto \phi_L^{-1.3}$ for the optimum thicknesses in figure 5.3(c). In a similar manner to the intensity scan, the transition from RESE-dominated synchrotron emission for $\phi_L = 10 \mu\text{m}$ to laser-injection dominated emission for $\phi_L = 1 \mu\text{m}$ produces these different scalings. The faster $I_L \propto \phi_L^{-2}$ dependence of the pulse intensity on the

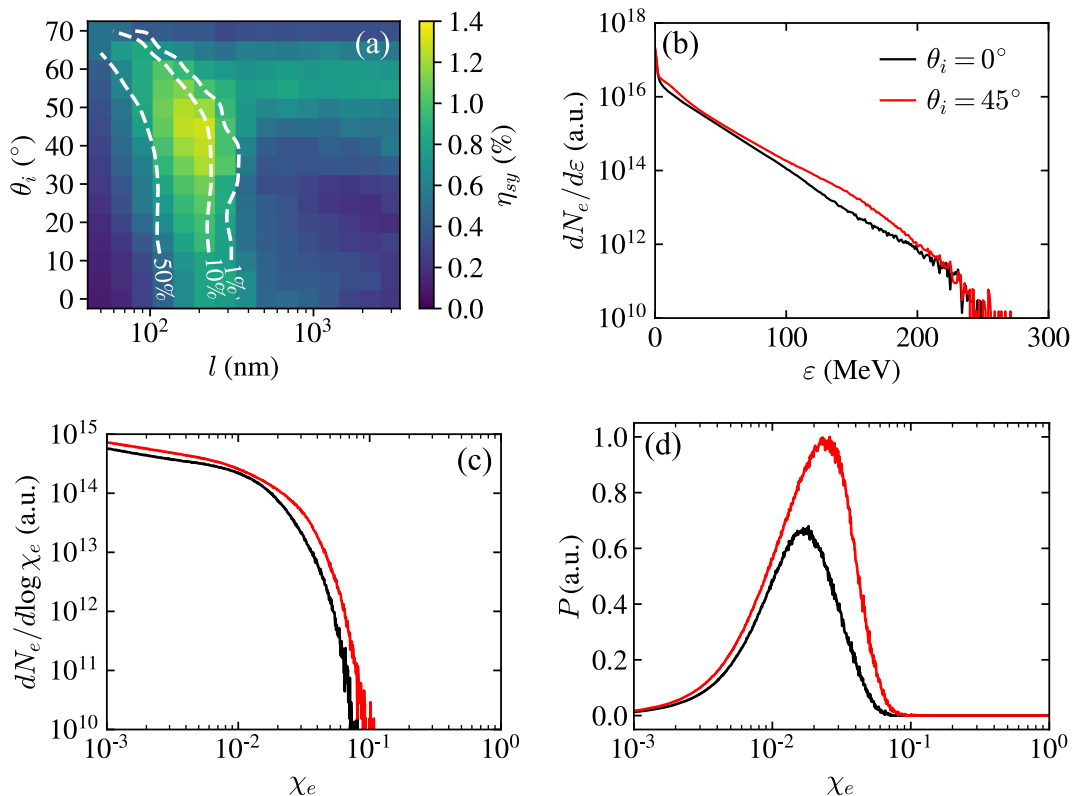


Figure 5.4: (a) Laser-to-synchrotron photon energy conversion efficiency for varying angle-of-incidence and target thickness. (b) Electron spectra, sampled over the whole simulation space, averaged over the period of synchrotron emission for a 200 nm foil at normal and 45° incidence, (c) the corresponding time-averaged spectra of χ_e values and (d) the power of synchrotron radiation calculated from (c).

focal spot size in 3D for constant pulse energy may provide a different η_{sy} scaling with ϕ_L , yet the smallest possible spot size (for constant energy) is still expected to generate the most synchrotron radiation as shown here in 2D.

5.3.5 Angle-of-incidence

The results for the final optimisation parameter, the angle-of-incidence of the laser pulse on the target, are shown in figure 5.4. In figure 5.4(a), the synchrotron conversion efficiency is maximised for $\theta_i = 45^\circ$ and $l = 216$ nm, and is 60% higher than reached for normal incidence. Similar to the other parameters, η_{sy} is highest for targets which on average transmit 14% of the laser light. To explore why the angle-of-incidence improves η_{sy} , the electron energy spectra and spectra of χ_e values were averaged over the period of synchrotron emission and are shown in figure 5.4(b) and (c), respectively, for additional simulations using $l = 200$ nm and $\theta_i = 0^\circ, 45^\circ$. The fast electron population contains

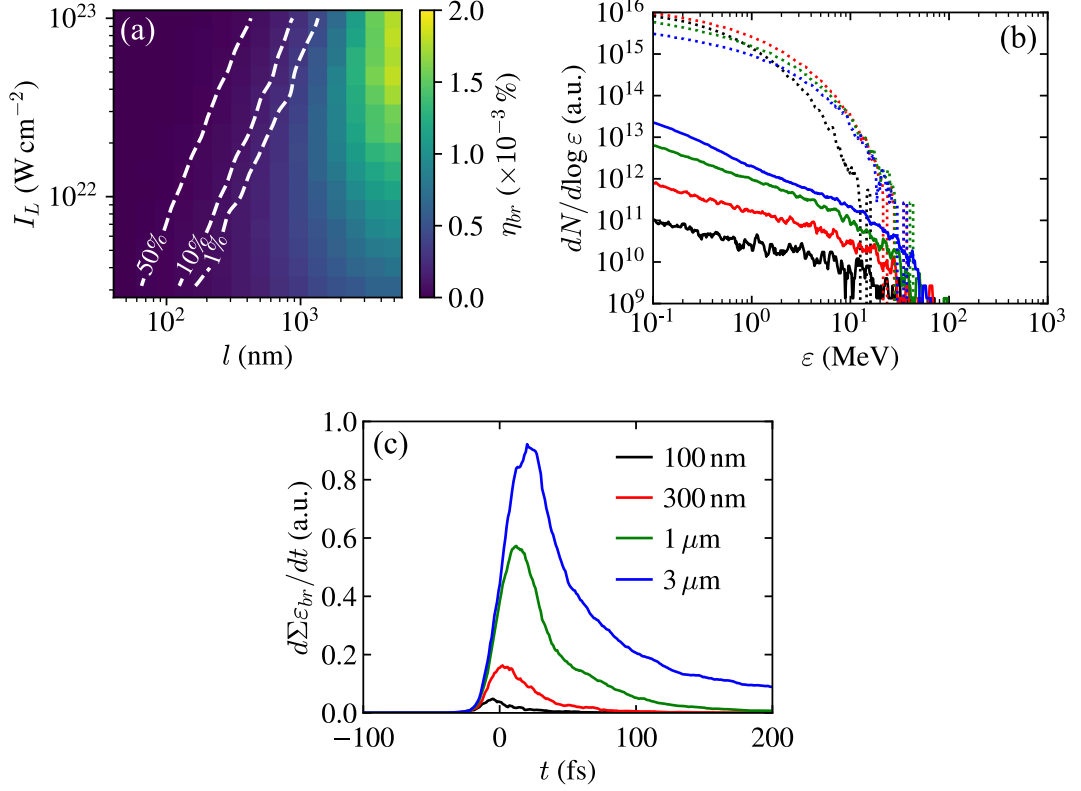


Figure 5.5: (a) Laser-to-bremsstrahlung radiation energy conversion efficiency for varying laser intensity and target thickness. (b) Energy spectra for bremsstrahlung photons (solid) and synchrotron photons (dotted) for different target thicknesses. (c) The rate of energy conversion to bremsstrahlung radiation.

36% more energy for $\theta_i = 45^\circ$ compared to 0° , because the p-polarised light improves energy coupling to electrons, and a much larger number of $\epsilon > 100$ MeV electrons are produced. This contributes to the enhanced spectrum of χ_e values, increasing the generation of synchrotron radiation. In figure 5.4(d), the power of synchrotron radiation for the χ_e spectrum is shown. This was calculated using the power for a single electron, $P = 4\pi\alpha_f m_e c^3 \chi_e^2 g(\chi_e)/3\lambda_c$ (see section 2.6.3). Electrons with $\chi_e > 0.01$ dominate the increased emission for $\theta_i = 45^\circ$. Therefore, the high energy component of the electron spectrum is responsible for the bulk of the enhanced emission.

5.3.6 Bremsstrahlung emission for varied laser intensity and target thickness

Until now, the discussion has focused on the generation of synchrotron radiation and how this depends on key laser and plasma parameters. Gamma radiation will, however,

also be produced via bremsstrahlung emission in these interactions. Distinguishing between these two photon sources is important for the design of experiments that aim to investigate either mechanism.

In this investigation, thin foils of a low- Z material have been selected to minimise the production of bremsstrahlung radiation. In figure 5.5(a), the conversion efficiency to bremsstrahlung radiation, η_{br} , is shown for different values of the target thickness and peak laser intensity. Generally, the conversion efficiency is observed to increase with each of these parameters, except where the laser energy starts to be transmitted. In such targets the bremsstrahlung emission is expected to decrease due to the increased loss of fast electrons and the reduced absorption of the pulse into electrons as the transmission becomes large.

In figure 5.5(b), the energy spectra of the bremsstrahlung and synchrotron radiation is shown for various target thicknesses, where $I_L = 10^{22} \text{ W cm}^{-2}$. In all cases, the synchrotron radiation dominates by many orders of magnitude. The conversion efficiency to synchrotron radiation scales very quickly with peak laser intensity, and therefore the difference is expected to become even greater for higher intensities. The bremsstrahlung emission can take place for many picoseconds in laser-solid interactions [303], due to the presence of a hot electron population trapped inside the target [324]. However, in figure 5.5(c), the rate of energy conversion to bremsstrahlung radiation, $d \sum \varepsilon_{br} / dt$, where ε_{br} is the bremsstrahlung photon energy, for different target thicknesses is shown to quickly reduce after the peak of the laser temporal intensity profile reaches the target at $t = 0$. Only for the thickest target tested, $l = 3 \mu\text{m}$, does the emission rate remain important at the end of the simulation; extrapolating this for a further 6 ps (an estimate of the duration of the fast electron population corresponding to the longest duration of K_α emission measured in reference [324]) increases η_{br} from $1.0 \times 10^{-3}\%$ to $8.6 \times 10^{-3}\%$. This is still dominated by the corresponding value of $\eta_{sy} = 0.27\%$. The simulations here capture the brightest period of bremsstrahlung emission, enabling parameters that minimise its production whilst maximising properties of the synchrotron emission to be found in the following sections, to inform the design of experiments to generate the purest source and clearest signature of synchrotron radiation.

5.4 Application of Bayesian optimisation

The scans discussed thus far vary only two input parameters at a time, linearly over a 15×15 grid corresponding to 225 simulations. To perform a systematic grid scan of this type with 15 values for each of the five input parameters under consideration would require $15^5 = 759,375$ simulations, this was not feasible with the computational resources available. Instead, Gaussian process regression was used to identify the values of the input parameters that maximise a given objective function within 200 simulations.

The parameter search space was defined as $0^\circ \leq \theta_i \leq 70^\circ$, $50 \text{ nm} \leq l \leq 10 \mu\text{m}$, $30 \text{ fs} \leq \tau_L \leq 100 \text{ fs}$, $1 \mu\text{m} \leq \phi_L \leq 6 \mu\text{m}$, and $-50 \mu\text{m} \leq x_f \leq 50 \mu\text{m}$. The laser energy was kept constant in the same way as in the previous section, by setting $I_L = 3 \times 10^{22} (30 \text{ fs}/\tau_L) (1 \mu\text{m}/\phi_L) \text{ W cm}^{-2}$. The objective functions used are shown in table 5.1, with the values of the input parameters for their optima. The objective functions that include only one physical property of the photon emission are: the total energy of synchrotron emission (f_{O1}), where ε_{sy} is the synchrotron photon energy; the maximum of the angle-resolved energy of synchrotron emission, $d \sum \varepsilon_{sy}/d\theta$, (f_{O2}) where θ is the angle in the xy -plane from the positive x -axis; and the total number of synchrotron photons, N_{sy} , with energy exceeding 10 MeV (f_{O3}). Finding the conditions where the most laser energy is converted into synchrotron radiation is useful for identifying where radiation reaction is important, and the effects on the plasma dynamics are greatest. Application of the synchrotron radiation for the generation of positrons or otherwise generally requires a bright and collimated source, hence the optimisation of the angle-resolved energy. The unique aspect of nonlinear Compton scattering sources compared

Objective Function	Parameter Values at Optimum				
	θ_i ($^\circ$)	$\log_{10}(l [\text{m}])$	τ_L (fs)	ϕ_L (μm)	x_f (μm)
	0–70	–(7.3–5)	30–100	1–6	–50–50
$f_{O1} = \sum \varepsilon_{sy}$	41.1	–5	42.8	1	0.7
$f_{O2} = \max(d \sum \varepsilon_{sy}/d\theta)$	26.4	–5	30	1	0.57
$f_{O3} = N_{sy}, \varepsilon_{sy} > 10 \text{ MeV}$	24.4	–6.26	30	1	0.63
$f_{M1} = f_{O2}/\sum \varepsilon_{br}$	70	–7.3	30	1	–4.33
$f_{M2} = A(f_{O2}) f_{O2}/\sum \varepsilon_{br}$	40.6	–6.64	30	1	0.14
$f_{M3} = f_{O2} f_{O3}$	18.3	–5.23	30	1	0.85
$f_{M4} = f_{O2} f_{O3}/\sum \varepsilon_{br}$	30.9	–6.45	30	1	0.92

Table 5.1: The objective functions maximised with Bayesian optimisation and the parameters of the found optimum for each. Here, $I_L = 3 \times 10^{22} (30 \text{ fs}/\tau_L) (1 \mu\text{m}/\phi_L) \text{ W cm}^{-2}$.

to conventional synchrotron sources and free electron lasers is the much higher energy of the photons, which can be many MeV compared to keV.

To optimise multiple properties of the photon emission, a series of different objective functions were considered. These include the ratio of the peak angle-resolved energy of synchrotron emission to the total bremsstrahlung radiation energy (f_{M1}), and the same function multiplied by the acceptance function $A(f_{O2})$, (f_{M2}). The acceptance function is defined as $A(f) = 1/(1 + \exp(-(20/f_{max})(f - 0.5f_{max})))$, where f is a given objective function and f_{max} is the maximum value of the objective function found separately, in a previous optimisation scan. The acceptance function strongly reduces the value of the overall function for $f < f_{max}/2$, to guide the optimisation towards results where $f > f_{max}/2$. In addition, the product of the peak angle-resolved energy of synchrotron emission and the number of synchrotron photons above 10 MeV (f_{M3}), and this function divided by the total bremsstrahlung radiation energy (f_{M4}) were optimised.

5.4.1 Optimisation of individual synchrotron emission properties

The resulting synchrotron and bremsstrahlung photon energy spectra, the angle-resolved energy of synchrotron radiation and the integrated power spectrum of synchrotron radiation are shown in figure 5.6(a)–(d), respectively, for the optimum of each objective function. In maximising the total energy of synchrotron radiation with f_{O1} , the synchrotron spectrum with the highest number of photons < 2 MeV is produced, such photons require less electron energy to be generated and thus can be generated in such high numbers to dominate the total synchrotron energy, accounting for 54% for f_{O1} . This also corresponds to the only optimum where the pulse duration is greater than the minimum of 30 fs, at 42.8 fs. The conversion efficiency here is 1.07% compared to the next highest at 1.03% for f_{O3} . In optimising the maximum of $d \sum \varepsilon_{sy}/d\theta$ and the number of > 10 MeV synchrotron photons, similar peaks in $d \sum \varepsilon_{sy}/d\theta$ at $\theta \approx -50^\circ$ are found in figure 5.6(c). The angular profiles differ mainly by the energy emitted in the backwards direction ($|\theta| > 90^\circ$) due to the dependency of the RESE mechanism on target thickness, enhanced for f_{O3} . The optimum for f_{O1} only reaches approximately half of the peak value of $d \sum \varepsilon_{sy}/d\theta$ compared to f_{O2} and f_{O3} . The only sizeable difference in the parameters here, besides the small increase in τ_L , is the change from $\theta_i = 41.1^\circ$ to $\theta_i \approx 25^\circ$. The production of more directional synchrotron emission with changes to the angle-of-incidence has been reported in references [286, 287, 325], in which a single

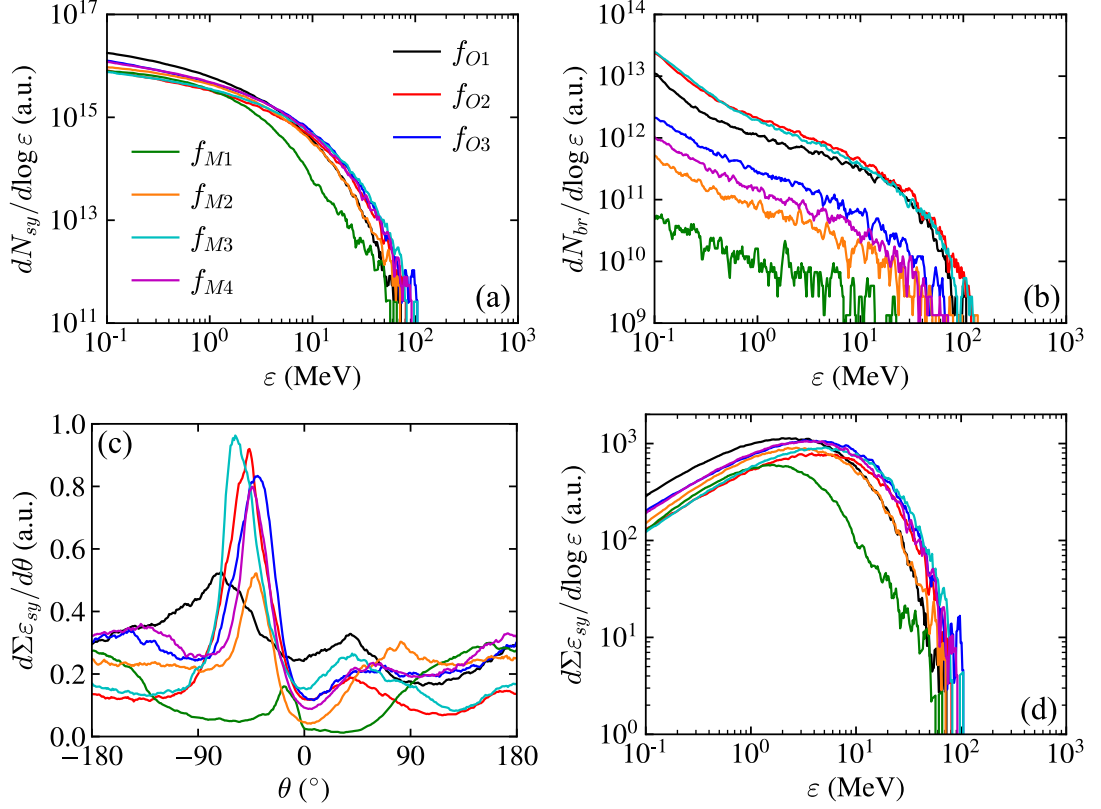


Figure 5.6: Synchrotron and bremsstrahlung radiation for the objective function optima in table 5.1, for which $I_L = 3 \times 10^{22} (30 \text{ fs}/\tau_L) (1 \mu\text{m}/\phi_L) \text{ W cm}^{-2}$. (a) Synchrotron photon energy spectra, (b) bremsstrahlung photon energy spectra, (c) angular profiles of total emitted synchrotron photon energy and (d) the energy content of the synchrotron spectrum.

lobe structure was also reported. It is discussed in further detail in section 5.6.

5.4.2 Mitigating bremsstrahlung emission

By maximising the ratio of the directional synchrotron emission to the overall bremsstrahlung emission with f_{M1} , the bremsstrahlung has been strongly suppressed as shown in figure 5.6(b), at the cost of reducing the peak value of $d\Sigma \epsilon_{sy}/d\theta$ and the synchrotron spectrum in figure 5.6(a) and (d). The optimum parameters here in table 5.1 correspond to the maximum possible angle-of-incidence and minimum target thickness. The optimisation of the objective function has been dominated by the gains obtained by reducing the bremsstrahlung emission as much as possible. The optimum found, however, has synchrotron radiation dominated by emission in the backwards direction ($|\theta| > 90^\circ$) corresponding to RESE, unlike the stronger forward-directed ($|\theta| < 90^\circ$) emission found with the other objective functions. Including the acceptance function

with f_{M2} , an optimum with greater bremsstrahlung emission is found. However, a much higher peak value of $d\sum\varepsilon_{sy}/d\theta$ is obtained, as shown in figure 5.6(c). The use of an acceptance function here demonstrates a method of setting an acceptable limit on the trade-off in one of the physical properties included in a composite objective function in optimising the overall function.

The objective functions f_{O2} and f_{O3} are already optimised for similar parameters, and in optimising their product f_{M3} , similar optimum parameters and photon properties were found at the optimum as shown in figure 5.6. Optimisation of this product divided by the total bremsstrahlung emission using f_{M4} effectively reduces the weight of the bremsstrahlung reduction term in comparison to f_{M1} , and produces photon distributions close to the f_{O2} , f_{O3} and f_{M3} optima with much less bremsstrahlung emission. This optimum is at a different location in the parameter space to the previous efforts to reduce the bremsstrahlung emission (f_{M1} and f_{M2}), and in a different part of the objective space; some increase to bremsstrahlung emission has enabled considerably improved synchrotron radiation to be generated.

5.4.3 Maximum laser intensity

For all of these optimisation results, the best focal spot size corresponds to the minimum, $\phi_L = 1\ \mu\text{m}$. In most cases the pulse duration also corresponds to the minimum, $\tau_L = 30\ \text{fs}$. Also, in most cases, the focal point is $\sim 0.6\ \mu\text{m}$, shifting the laser focus close to the new critical surface position after the initial hole boring. The objective functions used here for improving synchrotron radiation are almost universally optimised for the highest on-target intensity.

5.5 Optimisation in the highly radiative plasma regime

The optimisation results discussed thus far are for conditions where only a small fraction of the laser energy is converted into synchrotron radiation ($\lesssim 1\%$). A much more efficient source of synchrotron radiation can be produced under similar conditions with higher laser pulse energy, where the radiation reaction force starts to become important to the plasma dynamics. The laser energy was increased by a factor of 10, corresponding to $I_L = 3 \times 10^{23} (30\ \text{fs}/\tau_L)(1\ \mu\text{m}/\phi_L)\ \text{W cm}^{-2}$ for which the synchrotron emission is expected to become extremely powerful, and further optimisation scans were performed

to identify the impact on the optimum input parameters. The objective functions f_{O1} , f_{O2} , f_{M1} and f_{M2} were used again. Instead of f_{O3} , the total number of synchrotron photons with energy above 50 MeV (f_{O4}) was optimised, due to the higher energy photon spectra produced under these conditions. Similar optimum parameters were obtained, as shown in table 5.2, with the highest intensity combination of τ_L , ϕ_L and x_f values for most objective functions. An optimum defocus of close to $2 \mu\text{m}$ is found for objective functions f_{O1} , f_{O2} and f_{O4} , several times greater than the lower intensity cases in table 5.1. This is due to the increased hole boring velocity, induced by the higher laser intensity, leading to greater recession of the relativistic critical density surface at the target front side.

5.5.1 Angle-resolved synchrotron emission

The optimum of f_{O2} corresponds to the maximum pulse duration of 100 fs. Similar peak values of $d \sum \varepsilon_{sy} / d\theta$ were obtained across the permitted range of values for the pulse duration. However, the direction of peak emission moves from $\theta \approx -50^\circ$ for $\tau_L \approx 30$ fs, to $\theta \approx 0^\circ$ for $\tau_L \approx 100$ fs. Emission in the same direction as the laser pulse propagation ($\theta = 0^\circ$) has previously been associated with skin depth emission from the electrons near the front of the laser pulse in the reflected light [277, 305]. However, the peak in the angle-resolved emission for the optimum of f_{O2} is a result of the stronger deformation of the target for the longer pulse duration (similar to the higher laser energy case in 3D shown in 5.13). A deeper channel in the target is formed, and dense electron bunches injected into the laser pulse from the closer edge of the channel on the $y > 0$ side of the focal spot, by the positive half-cycle of the laser electric field, propagate almost parallel with the laser pulse close to the channel surface whilst being accelerated to

Objective Function	Parameter Values at Optimum				
	θ_i ($^\circ$)	$\log_{10}(l$ [m])	τ_L (fs)	ϕ_L (μm)	x_f (μm)
	0–70	–(7.3–5)	30–100	1–6	–50–50
$f_{O1} = \sum \varepsilon_{sy}$	38	–5.6	30	1	1.76
$f_{O2} = \max(d \sum \varepsilon_{sy} / d\theta)$	45.6	–5	100	1	1.93
$f_{O4} = N_{sy}, \varepsilon_{sy} > 50 \text{ MeV}$	0	–5.22	30	1	1.89
$f_{M1} = f_{O2} / \sum \varepsilon_{br}$	70	–7.3	30	5.33	–50
$f_{M2} = A(f_{O2}) f_{O2} / \sum \varepsilon_{br}$	54.3	–5.91	30	1	0.19

Table 5.2: The objective functions used for optimisation with laser intensity of $3 \times 10^{23} (30 \text{ fs} / \tau_L) (1 \mu\text{m} / \phi_L) \text{ W cm}^{-2}$, and the parameters of the found optima.

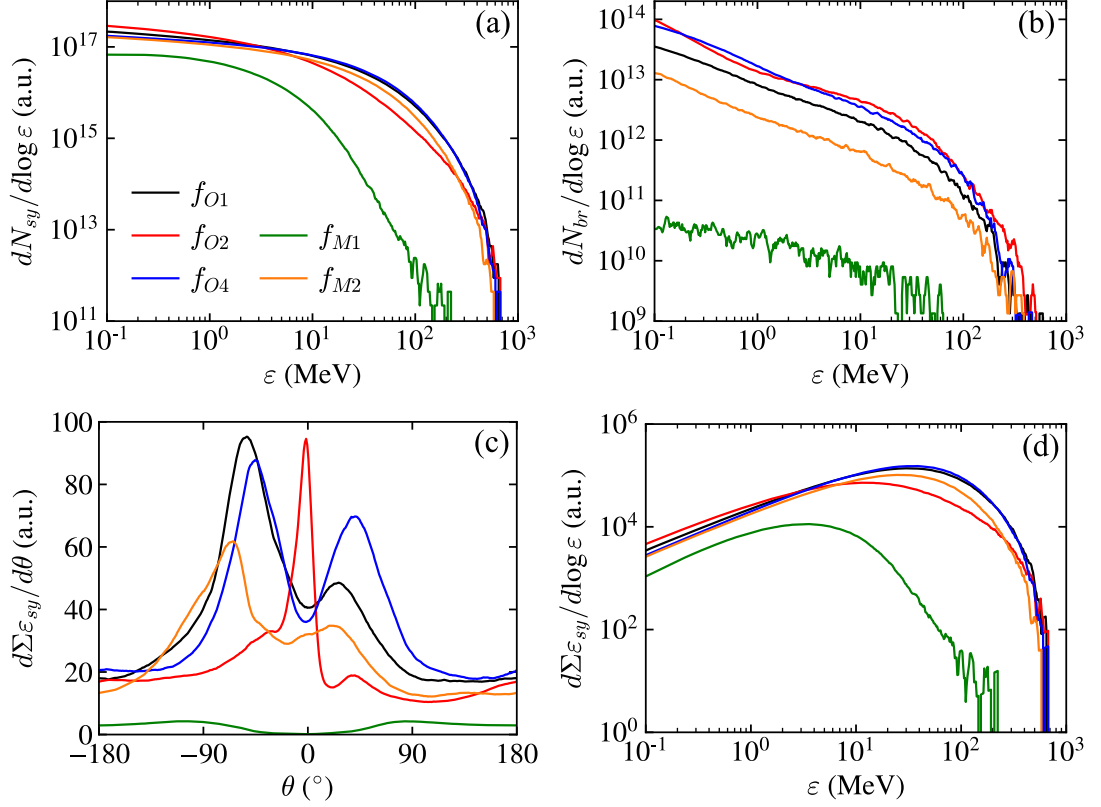


Figure 5.7: Synchrotron and bremsstrahlung radiation for the objective function optima in table 5.2, for which $I_L = 3 \times 10^{23} (30 \text{ fs}/\tau_L)(1 \mu\text{m}/\phi_L) \text{ W cm}^{-2}$. (a) Synchrotron photon energy spectra, (b) bremsstrahlung photon energy spectra, (c) angular profiles of total emitted synchrotron photon energy and (d) energy content of the synchrotron spectrum.

highly relativistic velocities. These electrons subsequently emit synchrotron radiation near parallel with the laser propagation axis. This appears to be the same mechanism that produces synchrotron emission close to parallel with the laser pulse in 3D shown in figure 5.11, and discussed in further detail with figure 5.13. In comparison to the lower laser intensity case in figure 5.6(c), with the same normalisation constant, a $\times 100$ enhancement in the peak value is obtained for only a $\times 10$ higher energy laser pulse. Although the maximum synchrotron photon energies obtained for this optimum set of parameters are similar to the other spectra in figure 5.7(a) and (d), the spectrum is shifted to lower photon energies, containing the most radiation below 2 MeV.

Optimisation of total synchrotron emission with f_{O1} produces a peak in the angle-resolved synchrotron emission of similar magnitude to the optimum for f_{O2} in figure 5.7(c), inadvertently maximising both objectives. This optimum exhibits a pronounced double-peaked structure in the angular emission characteristic of synchrotron radiation

from solid targets [147, 261, 277, 281, 302, 305]. However, the 38° angle-of-incidence has resulted in the suppression of the lobe in the direction closer to the perpendicular of the rotated target surface and the enhancement of the lobe closer to the parallel. This behaviour is also present in figure 5.6(c), although the weakened lobe is less discernible due to the more comparable backwards-directed radiation. The effect of varying the angle-of-incidence on the synchrotron angular profile is discussed in more detail in the next sections. The optimum for f_{O1} also produces a near identical synchrotron spectrum to that for f_{O4} , where the high energy spectral tail is optimised with a thicker target and normal incidence.

5.5.2 *Mitigating bremsstrahlung emission*

The optimum parameters to reduce bremsstrahlung radiation whilst maximising angle-resolved synchrotron emission with f_{M1} still correspond to the minimum target thickness (50 nm) and maximum angle-of-incidence (70°). However, in this case the optimum occurs for the largest possible defocus, $x_f = -50 \mu\text{m}$, and almost the maximum spot size, $\phi_L = 5.33 \mu\text{m}$. Irradiating such an ultrathin target with the minimum possible beam width results in the foil rapidly expanding, becoming transparent very early in the interaction and reducing coupling into synchrotron radiation. Increasing the beam size on the target increases the target volume that the laser pulse interacts with, at the cost of reduced laser intensity. A larger ϕ_L also increases the Rayleigh length, extending the longitudinal distance over which synchrotron radiation is produced. This enhances the overall synchrotron emission faster than any potential increase to the bremsstrahlung emission. The faster increase of bremsstrahlung emission compared to synchrotron emission with thicker targets always leads to the thinnest targets maximising their ratio.

The angle-resolved synchrotron emission for the optimum of f_{M1} in figure 5.7(c) is maximised for $|\theta| \approx 90^\circ$, in contrast to the lower laser pulse energy case in figure 5.6(c), which peaks for $|\theta| \approx 180^\circ$. The objective function f_{M2} , that includes an acceptance function to guide the optimisation towards results above a threshold value for f_{O2} , was used again for the higher laser energy case. An increase to the peak angle-resolved synchrotron emission in figure 5.7(c) was successfully demonstrated, with much higher bremsstrahlung emission as shown in figure 5.7(b).

The optimisation results found here indicate the need to maximise the laser intensity

interacting with the surface of solid targets to produce the most powerful sources of synchrotron radiation. Rotation of the target in the plane of polarisation of the laser pulse can produce the highest peak angle-resolved synchrotron emission, and the use of ultrathin foils is an effective method of reducing the bremsstrahlung emission to generate a purer source of synchrotron emission. The optimisation of multiple objectives in a single objective function can be effectively controlled with careful definition of the objective function, use of such methods is demonstrated to generate comparable to best-case synchrotron emission in sub- μm foils where the bremsstrahlung emission is still strongly mitigated.

5.6 Angle-of-incidence dependence of the forward synchrotron emission

The Bayesian optimisation results have shown the angle-of-incidence to be a critical parameter influencing the spatial profile of the synchrotron emission. To examine this dependence in more detail, additional 2D simulations were performed for laser parameters $I_L = 3 \times 10^{22} \text{ W cm}^{-2}$, $\tau_L = 30 \text{ fs}$, $\phi_L = 1 \mu\text{m}$ and $x_f = 0$ (close to most of the optima), and $l = 3 \mu\text{m}$ (an arbitrary thickness opaque target).

In figure 5.8(a), the maximum value of $d \sum \varepsilon_{sy} / d\theta$ is shown for different directions of the emitted synchrotron photons, θ_{sy} , as a function of the angle-of-incidence. The photons are grouped into those propagating with direction $90^\circ > \theta_{sy} > 0^\circ$ and $0^\circ > \theta_{sy} > -90^\circ$, corresponding to the directions in which the two lobes are usually produced due to laser-injected emission. These directions are hereafter referred to as $\theta_{90,0}$ and $\theta_{0,-90}$, respectively, for brevity. The optimisation results from table 5.1 and figure 5.6(c) are added as data points. The observed lobes are of similar magnitude for normal incidence. As the target is rotated to give the normal to the front surface direction $\theta_n = \theta_i - 180^\circ$, the magnitude of the lobe propagating in $\theta_{0,-90}$ (closer to parallel with the target surface) is enhanced by more than a factor of two when it peaks for $\theta_i = 22.5^\circ$. Many of the Bayesian optimisation results are for similar values of θ_i , albeit with greater directional synchrotron emission achieved due to changes to some of the parameters and many iterations. At the same time the magnitude of the $\theta_{90,0}$ -directed emission is reduced, this begins to reverse for $\theta_i = 37.5^\circ - 52.5^\circ$ until the emission in both directions shown reduces in magnitude and begins to converge for increasing θ_i .

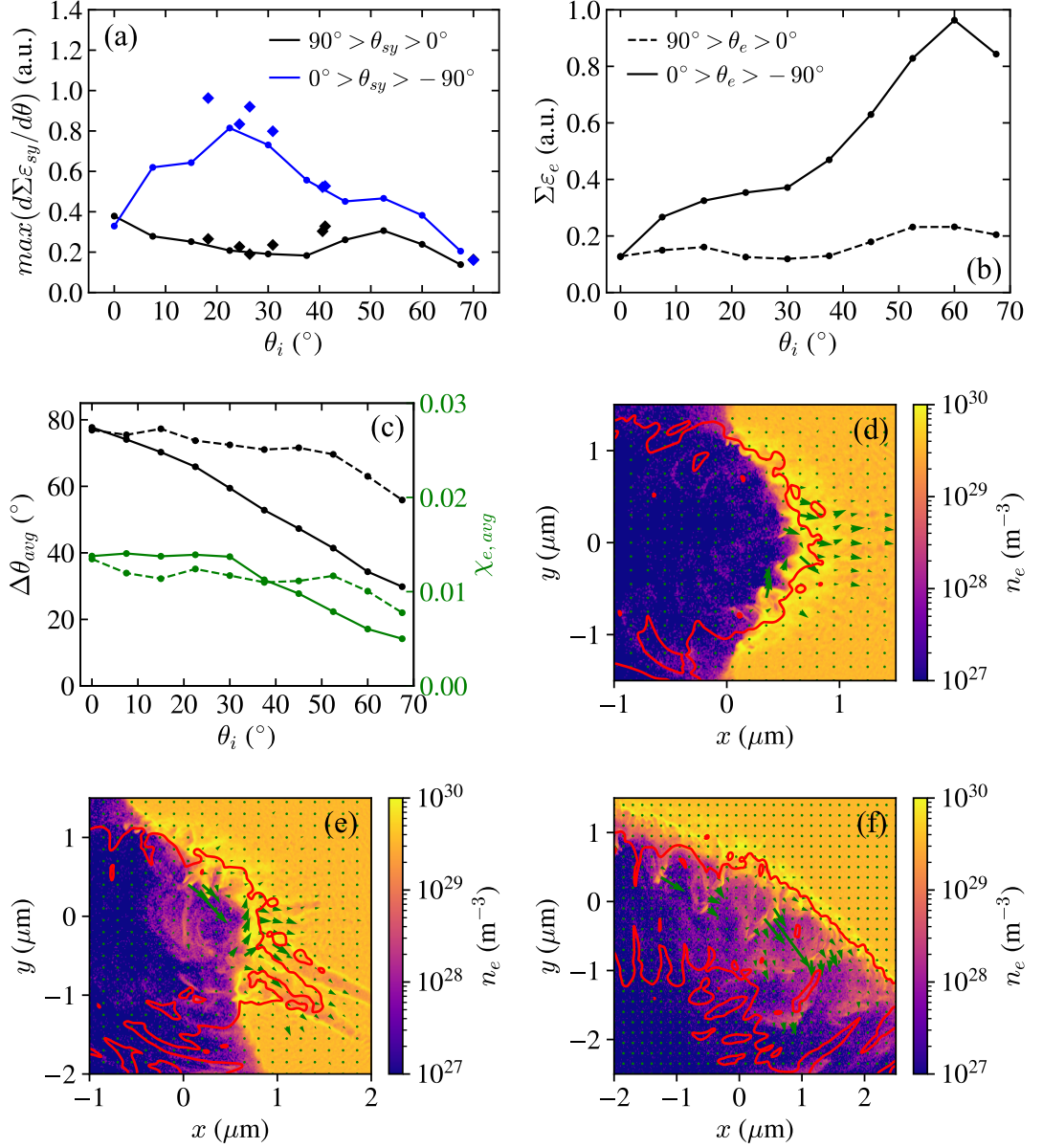


Figure 5.8: (a) Maximum value of $d\Sigma\varepsilon_{sy}/d\theta$ as a function of the angle-of-incidence, for synchrotron photons emitted in angular ranges $\theta_{90,0}$ (black) and $\theta_{0,-90}$ (blue), where $l = 3\ \mu\text{m}$, $I_L = 3 \times 10^{22}\ \text{W cm}^{-2}$, $\phi_L = 1\ \mu\text{m}$, $\tau_L = 30\ \text{fs}$ and $x_f = 0$. The optima in figure 5.6 are also shown (diamonds). (b) Total energy in electrons with $\varepsilon > 10\ \text{MeV}$ in a local intensity $I > 10^{21}\ \text{W cm}^{-2}$ propagating with angle θ_e in the ranges $\theta_{90,0}$ (dashed) and $\theta_{0,-90}$ (solid) averaged over the period of synchrotron emission. (c) Energy-weighted mean angle between the electron trajectory and the propagation direction of the local electromagnetic field (left axis) and mean electron quantum parameter (right axis) for each group of electrons in (b). (d)–(f) The electron density for $\theta_i = 0^\circ$, 22.5° and 60° , respectively, where the total momentum of fast electrons (arrows; green) and $I = 10^{21}\ \text{W cm}^{-2}$ contour (red) is also shown.

The synchrotron radiation is caused by highly relativistic electrons within the laser field, and the direction of the emitted radiation is predominantly in the electron direction of motion, θ_e . The effect of varying the angle-of-incidence is examined by considering the electrons with energy > 10 MeV in local electromagnetic fields with intensity $> 10^{21}$ W cm $^{-2}$. The total energy of such electrons propagating in the same direction as each of the synchrotron lobes was averaged over the period of synchrotron emission and is shown in figure 5.8(b). For normal incidence, the total electron energy in each direction is equal, and as the target is rotated, the electron population that propagates in the $\theta_{0,-90}$ direction rapidly acquires several times more total energy and continues to gain energy until $\theta_i = 60^\circ$. By contrast, the total energy of the electron population that propagates in the $\theta_{90,0}$ direction over the interaction changes very little with θ_i , with a minimum for $\theta_i \approx 30^\circ$ and a second peak at $\theta_i \approx 52.5^\circ$. Although these changes match some of those for the peak angle-resolved synchrotron emission in figure 5.8(a), they do not explain why the $\theta_{0,-90}$ -directed emission peaks for $\theta_i = 22.5^\circ$ and why the peak emission in both directions reduces for θ_i approaching 70° .

The quantum parameter χ_e indicates synchrotron emission increases for higher γ_e , and for higher $|\mathbf{E}_\perp + \mathbf{v}_e \times \mathbf{B}|$. The orientation of the electron motion to the fields, $\Delta\theta$, is therefore important to consider (χ_e is maximised for antiparallel propagation, $\Delta\theta = 180^\circ$, and minimised for parallel propagation, $\Delta\theta = 0$). Figure 5.8(c) shows the energy-weighted average absolute angle between the direction of motion of the electrons and the local electromagnetic field, calculated from the Poynting vector $\mathbf{S} = \mathbf{E} \times \mathbf{B}/\mu_0$. For the $\theta_{0,-90}$ -propagating electron population, the average angle between the electrons and the field exhibits an approximately linear decrease for $\theta_i = 0$ to 70° . For the same field magnitude and γ_e , this would reduce the synchrotron radiation. The energy-weighted average value of χ_e for the electrons propagating in each direction is also shown in figure 5.8(c); $\chi_{e,avg}$ changes very little for $\theta_i = 0-30^\circ$, but is strongly reduced for greater θ_i . The optimisation of the magnitude of the angle-resolved synchrotron emission in $\theta_{0,-90}$ is a result of the balance of the greater energy in the population of electrons propagating in the same direction with the reduced average emission parameter. For the $\theta_{90,0}$ -directed electron population, the angle to the field $\Delta\theta$ and the average emission parameter $\chi_{e,avg}$ only begin to strongly reduce for $\theta_i > 52.5^\circ$, which reflects the behaviour of the associated synchrotron emission in figure 5.8(a).

Example snapshots of the electron density on the simulation grid are shown in

figure 5.8(d)–(f) close to the time of peak synchrotron emission, for $\theta_i = 0, 22.5^\circ$ and 60° , respectively. The red contours correspond to $I = 10^{21} \text{ W cm}^{-2}$, and the arrows show the total momentum of fast electrons in each $150 \text{ nm} \times 150 \text{ nm}$ region. For normal incidence in figure 5.8(d), every half laser cycle the electric field pulls electrons from the edges towards the centre, with the electrons periodically coming from different sides of the focal spot due to the oscillating direction of the laser electric field. This results in periodic synchrotron radiation at the laser frequency with the lobes separated by half a laser cycle, as observed in reference [147]. The shallow depth of the front surface plasma cavity means that only electrons propagating at a steep angle with the incoming laser pulse move into this region and experience the highest fields.

When the target is rotated to $\theta_i = 22.5^\circ$ (see figure 5.8(b)) the laser electric field can pull electrons from a greater area, and accelerate them along the surface of the target further forwards with the pulse. As a result, the coupling of laser energy to $\theta_{0,-90}$ -propagating electrons is enhanced, and the synchrotron emission in this direction. For $\theta_i = 60^\circ$ (see figure 5.8(c)), the laser pulse is no longer reflected back in the $|\theta| > 90^\circ$ direction, but along the surface of the target, reducing enhancement of the synchrotron radiation from counter-propagation of the reflected light with the laser-injected electrons propagating along the target surface. These electrons now move with the laser pulse, reducing their values of χ_e , as shown in figure 5.8(c), and producing less synchrotron radiation.

The Bayesian optimisation results in table 5.2 and figure 5.7(c) indicate a laser intensity dependence of the optimum angle-of-incidence for producing the highest peak angle-resolved synchrotron emission, with the best results for $\theta_i \approx 42^\circ$ in comparison to $\theta_i \approx 25^\circ$ for the lower laser intensity case. The hole boring velocity increases for increasing laser intensity, causing the formation of a longer channel in the target and changing the evolution of the geometry of the interaction, and hence the optimum value of θ_i . The hole boring velocity also reduces for higher densities. Therefore, the optimum value of θ_i is also expected to be dependent upon the target density.

5.7 Spatial control of synchrotron emission in 3D

The influence of the angle-of-incidence on the spatial profile of synchrotron emission was explored in 3D with further simulations. The synchrotron emission is dominated by

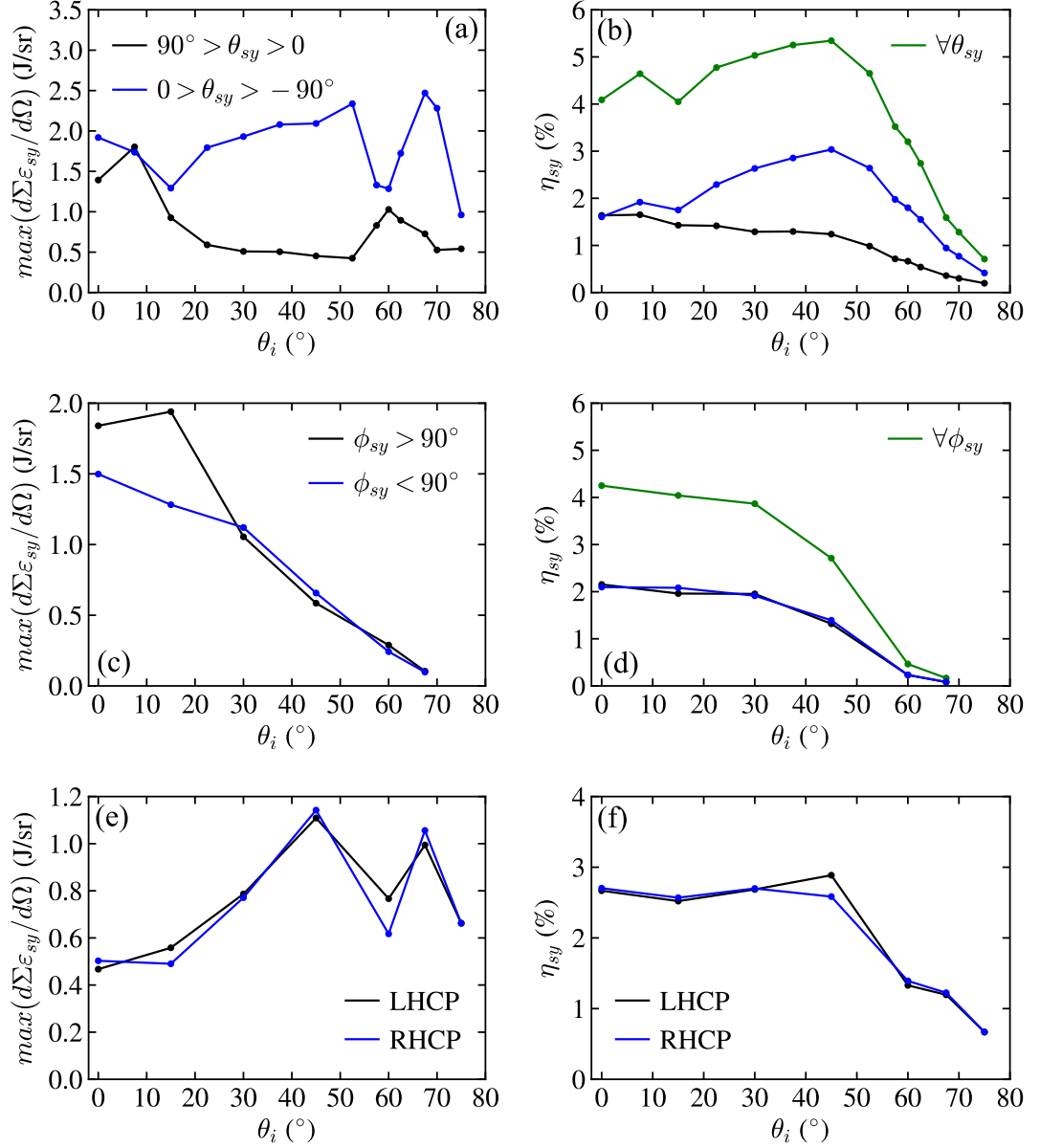


Figure 5.9: 3D simulation results for synchrotron photon emission for different laser light polarisation states. Peak angle-resolved synchrotron energy emitted in each direction for (a) p-polarisation, (b) s-polarisation and (c) left-hand and right-hand circular polarisation. (d)–(f) Conversion efficiency to synchrotron radiation for p-, s- and both RHCP and LHCP polarisation, respectively.

electrons accelerated and injected from the edges further into the laser spatial profile due to interaction with the laser electric field, and therefore the spatial profile of synchrotron emission should change as the polarisation of the laser light changes. As a result, the polarisation was varied between p-, s-, left-hand c- and right-hand c- polarised laser light to test the effect on the spatial profile of synchrotron emission for varying angle-

of-incidence.

A lower initial plasma density of $100 n_c$ was simulated due to the high computational resources required to model higher plasma densities accurately in 3D. This may produce differences in the variation of the laser-injected synchrotron emission with angle-of-incidence as discussed at the end of the previous section. A single target thickness of $1 \mu\text{m}$ was chosen, due to the increased resources required to simulate thicker targets. Therefore, the synchrotron emission was not optimised with target thickness (or transparency) for each angle-of-incidence tested. Transparency occurs for each polarisation state at normal incidence, eventually becoming opaque as the angle-of-incidence is increased, and is polarisation dependent. The laser parameters were $I_L = 1.1 \times 10^{23} \text{ W cm}^{-2}$, $\tau_L = 30 \text{ fs}$, $\phi_L = 1 \mu\text{m}$ and $x_f = 0$, corresponding to a pulse energy of 39.8 J .

The spatial profiles of synchrotron emission are shown as a function of θ , the azimuthal angle from the positive x -axis in the xy plane where $-180^\circ \leq \theta \leq 180^\circ$, and ϕ , the polar angle from the positive z -axis where $0 \leq \phi \leq 180^\circ$. The angle-of-incidence corresponds to rotation in the xy plane.

Figure 5.9(a) shows the maximum angle-resolved energy of synchrotron emission of the two azimuthally defined regions corresponding to $\theta_{90,0}$ and $\theta_{0,-90}$, as in the 2D results, as a function of the angle-of-incidence for p-polarisation. In a similar manner to the 2D results, the magnitude of the emission in each direction for near normal incidence is approximately equal. For increasing values of θ_i , the magnitude of the $\theta_{90,0}$ -directed emission drops very rapidly, and the magnitude of the $\theta_{0,-90}$ -directed emission achieves a peak at $\theta_i = 52.5^\circ$. The peak emission is only $\sim 0.5 \text{ J sr}^{-1}$ higher than the result for normal incidence, less than the factor of 2 improvement observed in 2D. The magnitude of the angle-resolved emission in each direction appears to converge around $\theta_i = 60^\circ$, before the magnitude of the $\theta_{0,-90}$ lobe unexpectedly peaks again for $\theta_i = 67.5^\circ$; such behaviour was not observed in the 2D simulations shown in figure 5.8(a). The conversion efficiency for p-polarisation is shown in figure 5.9(d), the overall synchrotron conversion efficiency peaks for $\theta_i = 45^\circ$, at the same time that the conversion efficiency to $\theta_{0,-90}$ -directed emission peaks at approximately twice its normal incidence value.

For an s- (along z) polarised laser pulse the synchrotron lobes are oriented perpendicular to those for p-polarisation because they are generated along the axis of

polarisation of the laser light. Therefore, each lobe is defined by their polar angle, ϕ . In figure 5.9(b) the lobes begin at normal incidence with approximately equal magnitude (the difference is due to noise in the simulations or partially asymmetric dynamics that depend upon the initial phase of the laser) and have similar values to those for p-polarisation. However, for increasing θ_i the magnitude of the emission in each polar direction tends to reduce. The overall conversion efficiency to synchrotron radiation also reduces in a similar way in figure 5.9(e) and remains equal for each polar direction. Rotation of the target causes the laser pulse to be spread over a larger area, and to be reflected obliquely. As a result, the radiation pressure that is required for forming a cavity in the target and producing strong laser-injected emission is lowered. Furthermore, because the laser pulse is polarised parallel with the target surface, its electric field cannot directly force electrons away from the surface and further into its spatial profile without surface deformation.

Finally, in figure 5.9(c) and (f), results for both left-hand circular polarisation (LHCP) and right-hand circular polarisation (RHCP) are shown. For c-polarisation, two lobes are not produced for normal incidence but an annular structure instead [261], due to the rotating electric field pulling electrons into the focal spot from all around the sides of the hole bored cavity each laser cycle. The magnitude of the angle-resolved energy of synchrotron emission in the full angular range is shown in figure 5.9(c). For normal incidence it is $\sim 1 \text{ J sr}^{-1}$ lower than for linear polarisation, at $\sim 0.5 \text{ J sr}^{-1}$. However, this more than doubles with rotation of the target to $\theta_i = 45^\circ$. The magnitude of the emission reduces for $\theta_i = 60^\circ$ before peaking again for 67.5° in a similar way to the p-polarisation results. The conversion efficiency in figure 5.9(f) remains approximately constant for $\theta_i = 0\text{--}45^\circ$, before it quickly reduces for larger θ_i . The results here for LHCP and RHCP are almost identical, as expected: only the rotation direction of electrons in the laser fields is changed.

The results in figure 5.9 indicate p-polarisation for $\theta_i \approx 45^\circ\text{--}52.5^\circ$ produces the optimal combination of peak angle-resolved energy of synchrotron emission and conversion efficiency for the target simulated. However, they do not capture all of the changes to the spatial structure of the synchrotron emission. In figure 5.10 the angle-resolved synchrotron emission in the forward direction ($|\theta| < 90^\circ$) is shown for each polarisation and a range of values of θ_i .

For p-polarisation a double lobe structure is shown for $\theta = 0\text{--}45^\circ$, in which the

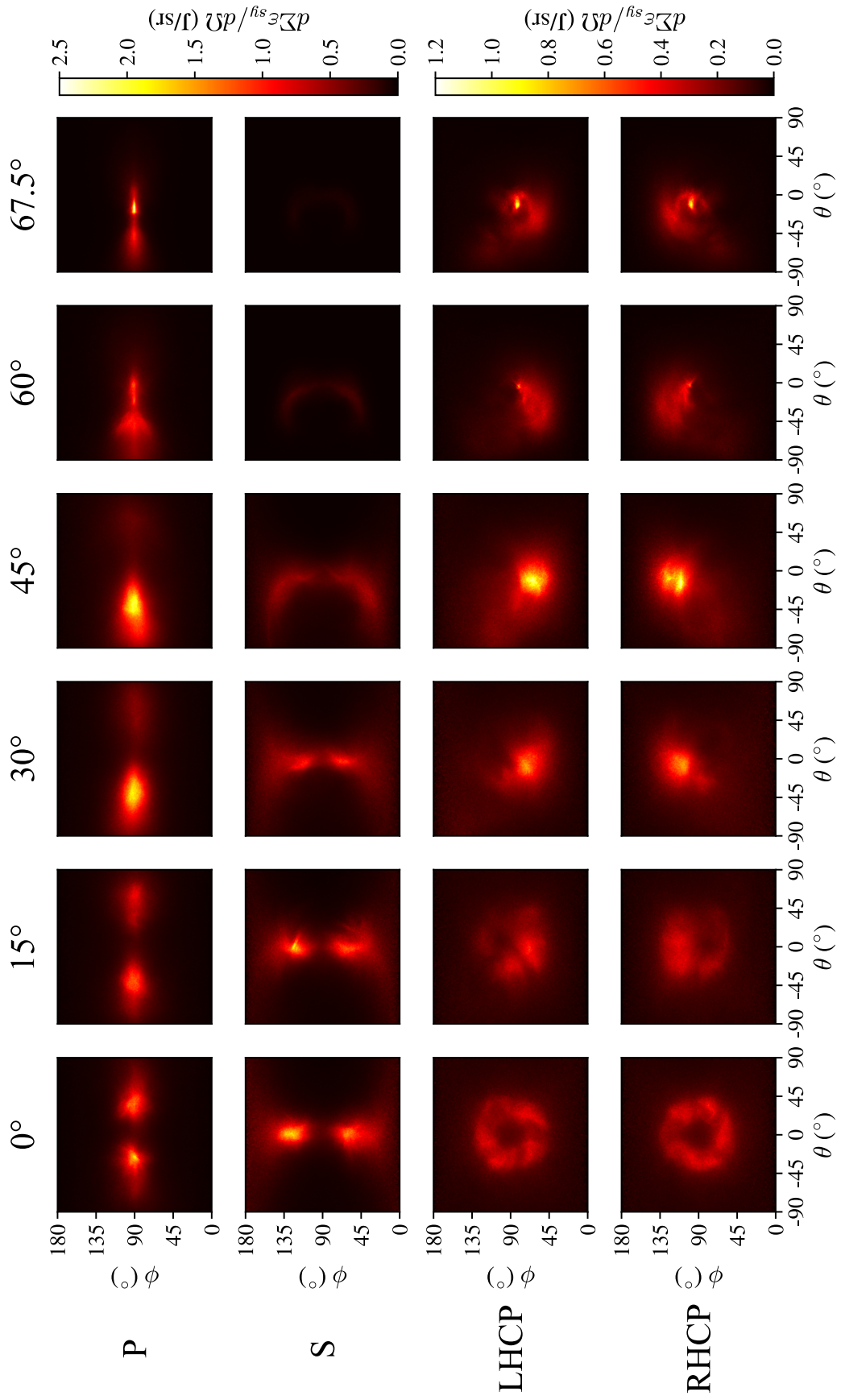


Figure 5.10: Angular profiles of the total energy of synchrotron emission in the forward direction ($|\theta| < 90^\circ$) in 3D simulations for different laser light polarisation states and angles-of-incidence, where $I_L = 1.1 \times 10^{23} \text{ W cm}^{-2}$.

$\theta_{0,-90}$ lobe gains energy up to 45° , whilst the $\theta_{90,0}$ lobe disappears. For $\theta_i = 60^\circ$ the angular structure changes, a beam of synchrotron radiation narrow in ϕ ($|\phi - 90^\circ| < 5^\circ$) is produced for $\theta = -25^\circ - 0^\circ$, becoming wider like the original lobe structure for lower θ , and the magnitude is strongly reduced (as seen in figure 5.9(a)). Lastly, for $\theta_i = 67.5^\circ$, the full synchrotron emission profile becomes narrower in ϕ and strongest for θ between -20° and -10° . This variation with θ_i is not replicated with s-polarisation, where only the double lobe structure is produced and reduces in magnitude for increasing θ_i , although curves towards the $-\theta$ direction.

For $\theta_i = 67.5^\circ$, the angle between the laser propagation direction and target surface becomes 22.5° , approaching the divergence half-angle of the laser pulse, $\theta_{div} = \sqrt{2 \ln 2} \lambda_L / \pi \phi_L = 17.2^\circ$. When a component of the laser polarisation is in the plane of target rotation, as is the case for p- and c- polarisation, the laser electric field can inject electrons from close to the target surface further into the laser pulse as it focuses. The electrons are accelerated along the target surface, over a distance much greater than ϕ_L , towards the focal point where they emit powerful synchrotron radiation in the intense fields. Because the accelerated electron bunches that reach the centre of the laser focus have a narrow divergence, the beam of synchrotron radiation also has a narrow divergence. For the larger θ_i value of 75° , this mechanism is degraded, as shown in figure 5.9(a). The expansion of electrons from the target surface affects the laser beam propagation, and the reduced difference in the propagation direction of the laser pulse and electrons moving parallel with the surface acts to reduce χ_e and the synchrotron emission.

For LHCP and RHCP in figure 5.10, synchrotron radiation is generated with an annular spatial profile for normal incidence. Rotation of the target, however, produces an asymmetry in the angular distribution of radiation. One section of the annular structure becomes thicker and brighter, the hole of the annulus moves away from $\theta = 0$ and $\phi = 90^\circ$, and the opposite side of the annulus becomes thinner and dimmer. The spatial profile of the synchrotron radiation now shows its dependence upon the direction of rotation of circular polarisation, the profile is flipped in ϕ from LHCP to RHCP. For increasing target rotation, the annular structure disappears and a broad arc of synchrotron radiation is formed with a brighter spot in a single direction. Rotation of the target reduces the number of electrons on one side of the focal spot, thus reducing the number of electrons drawn into the spot by the laser electric field on this side.

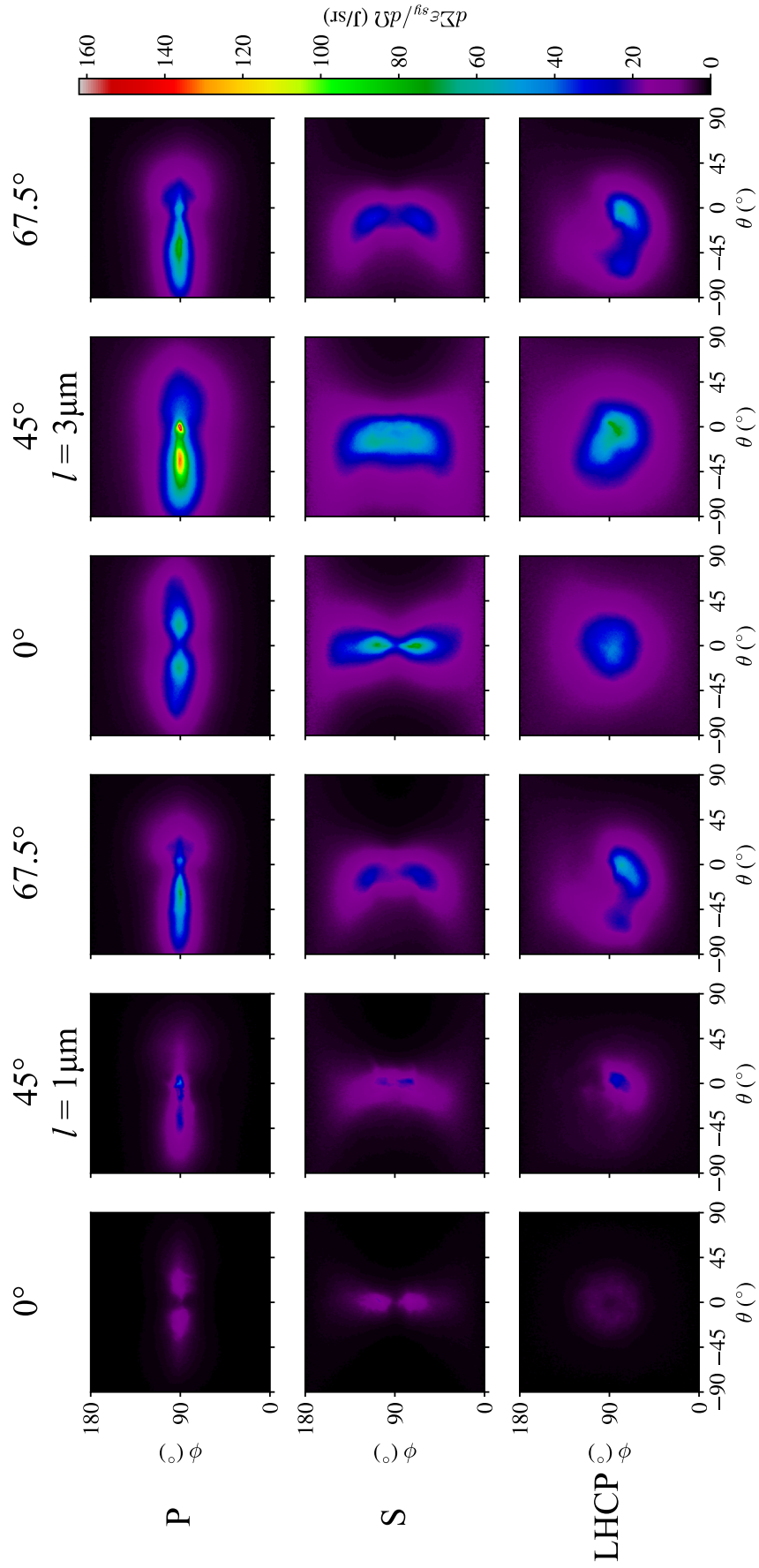


Figure 5.11: Angular profiles of the total energy of synchrotron emission in the forward direction ($|\theta| < 90^\circ$) in 3D simulations for different laser light polarisation states and angles-of-incidence, where $I_L = 1.1 \times 10^{24} \text{ W cm}^{-2}$.

As the electric field rotates it pulls most electrons from the rotated ($\theta_i > 0$) target into the focal spot after it points in the $+y$ direction, this results in the production of angular distributions of electrons in the field that are either directed in $+z$ ($\phi < 90^\circ$) or $-z$ ($\phi > 90^\circ$) depending on the direction of rotation of the electric field. For LHCP, the electric field next rotates towards the $-z$ direction, accelerating electrons in the $+z$ direction and generating synchrotron radiation in the same direction as those electrons. The situation is reversed for RHCP, directing electrons in the field in the $-z$ direction and the concomitant synchrotron radiation.

For $\theta_i \geq 60^\circ$, the narrow enhanced beam of synchrotron radiation obtained from acceleration of electrons along the target surface with the edge of the focusing laser beam appears, similar to the changes to the angular synchrotron profile for p-polarisation. However, due to the electron motion induced by the rotation of the electric field vector, the synchrotron radiation is emitted a small angle above the xy plane for LHCP, and below the xy plane for RHCP.

A limited number of 3D simulations were performed for $I_L = 1.1 \times 10^{24} \text{ W cm}^{-2}$, corresponding to a laser energy of 398 J, to identify if the spatial structures in the synchrotron emission change when the target is greatly deformed by the radiation pressure and ponderomotive force. The angle-resolved total energy of synchrotron emission for these simulations is shown in figure 5.11. Both an $l = 1 \mu\text{m}$ and $3 \mu\text{m}$ target were simulated due to the high laser transmission of the former target for normal incidence at this intensity. The values of θ_i were limited to 0° , 45° and 67.5° .

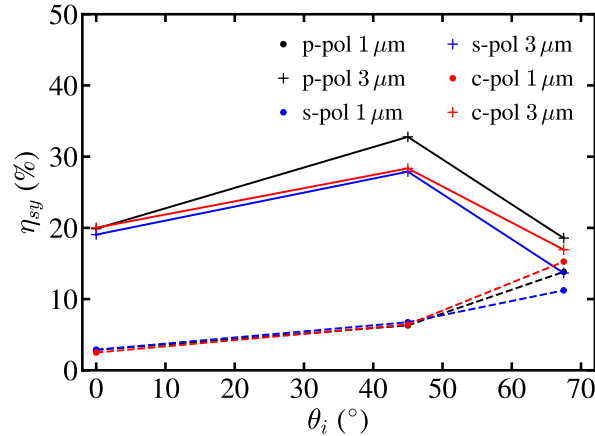


Figure 5.12: The conversion efficiency of laser energy to synchrotron radiation for different laser light polarisation states and target thicknesses where $I_L = 1.1 \times 10^{24} \text{ W cm}^{-2}$.

The double lobes for p- and s- polarisation were generated closer to the laser prop-

agation direction, and the synchrotron emission for s-polarisation is less suppressed for $l = 3 \mu\text{m}$ with increasing θ_i compared to figure 5.10 due to the increased target deformation improving electron injection into the laser beam. For c-polarisation, the emission is also more collimated with the laser pulse, and the annular structure for normal incidence only appears for $l = 1 \mu\text{m}$, with the $l = 3 \mu\text{m}$ target producing a spot centred close to the laser propagation direction. Hollowing of the synchrotron emission profile along the laser propagation direction for c-polarisation may enable the onset of relativistic transparency for a significant duration of the interaction to be inferred from experimental measurements. For all of these polarisation states and $l = 1 \mu\text{m}$, the peak angle-resolved emission is enhanced for the larger values of θ_i due to the increased target material within the path of the laser pulse. For p- and c- polarisation with $l = 3 \mu\text{m}$, the angle-resolved emission is highest for $\theta_i = 45^\circ$, the same as the lower intensity case in figure 5.10 neglecting the narrow enhanced emission for $\theta_i = 67.5^\circ$ which is not produced here. The conversion efficiencies shown in figure 5.12 demonstrate the overall emission is highest with all three polarisations for $\theta_i = 45^\circ$ with $l = 3 \mu\text{m}$.

The highest angle-resolved synchrotron emission of 160 J sr^{-1} was generated for p-polarisation, $\theta_i = 45^\circ$ and $l = 3 \mu\text{m}$. However, this corresponds to a narrow beam centred at $\theta \approx 0$ and $\phi \approx 90^\circ$, instead of an oblique single lobe as in figure 5.10 for lower intensity. The emission here is driven by electrons from the $y > 0$ side of the target injected into the laser pulse and co-propagating with it as it moves further into the target; the same mechanism that drives similar emission for the optimum of f_{O2} in figure 5.7(c).

Figure 5.13 shows a snapshot of the 3D interaction whilst this radiation is generated. The electron bunches accelerated along the closer surface of the channel formed in 5.13(a) can reach Lorentz factors several times greater than $a_0 = 720$ as shown in 5.13(b). The electric and magnetic field components corresponding to the incident laser pulse, E_y and B_z , are shown in figure 5.13(c) and (d), respectively. Assuming the electrons propagate with velocity $v \simeq c$ along x , the perpendicular fields that cause synchrotron emission $|\mathbf{E}_\perp + \mathbf{v} \times \mathbf{B}| \simeq \sqrt{(E_y - cB_z)^2 + (E_z + cB_y)^2}$. The values of this are shown in figure 5.13(e). For incoming light propagating through vacuum $E_y = cB_z$ and $\sqrt{(E_y - cB_z)^2 + (E_z + cB_y)^2} = 0$. However, in these interactions the fields may be altered by the scattering or generation of light, strong currents and space-charge fields. In this case, the dominant contribution to $|\mathbf{E}_\perp + \mathbf{v} \times \mathbf{B}|$ is caused by $|E_y - cB_z|$ close to

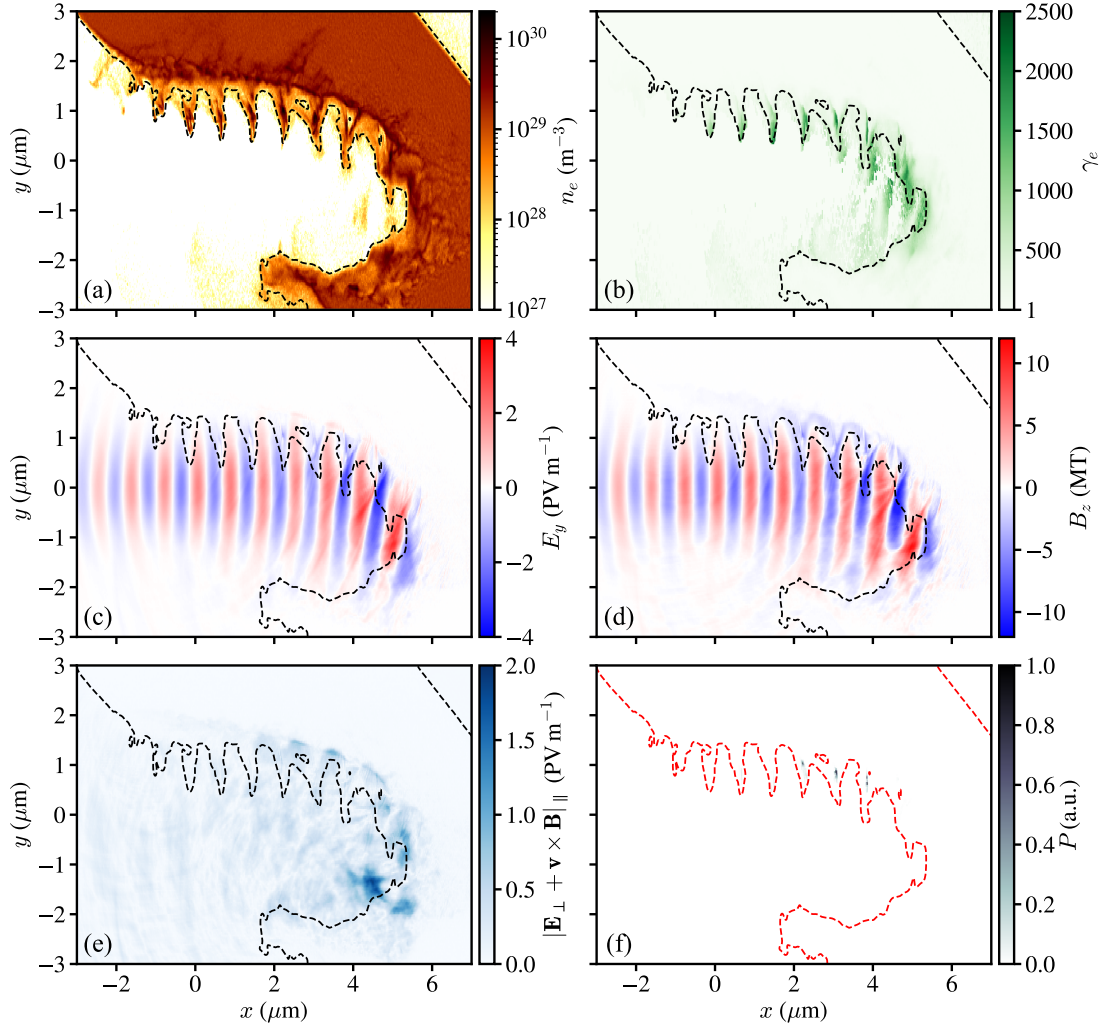


Figure 5.13: (a) The electron density, (b) electron Lorentz factor, (c) y -component of the electric field and (d) z -component of the magnetic field for p-polarisation, $\theta_i = 45^\circ$ and $I_L = 1.1 \times 10^{24} \text{ W cm}^{-2}$. For electron propagation along the x -axis at ultrarelativistic velocities ($\mathbf{v} \simeq c\hat{x}$), the value of $|\mathbf{E}_\perp + \mathbf{v} \times \mathbf{B}| \simeq \sqrt{(E_y - cB_z)^2 + (E_z + cB_y)^2}$ is shown in (e). Lastly, in (f) the normalised synchrotron power estimated from cell-averaged quantities assuming propagation along x , in regions where electrons propagate close to parallel with (within 5°) the $+x$ direction. The contours show where $n_e = 10n_c$, and all quantities are shown 18 fs after the laser peak reaches $x = 0$.

the channel surface. Here, any reflection of the laser light may increase $|E_y - cB_z|$, and strong space-charge fields may be induced as the radiation pressure and ponderomotive force push electrons outwards; figure 5.13(c) shows positive E_y fields are generated along the upper channel surface where the electron density is high for $x = 2\text{--}5 \mu\text{m}$. A strong negative B_z , however, is also shown to be present here along the upper channel surface near the series of electron bunches. This magnetic field is responsible for a

significant fraction of $|\mathbf{E}_\perp + \mathbf{v} \times \mathbf{B}|$ in this region that causes synchrotron emission through the parameter χ_e . Strong magnetic fields are known to be generated in laser-solid interactions due to the large current densities [326–328]. In particular, magnetic fields along the z -direction (or equivalent) have been observed in simulations of direct laser acceleration in relativistically underdense channels [329, 330]. Although analysis of the currents and magnetic field generation is beyond the scope of this work, the results here demonstrate the self-generated magnetic fields to be important. In addition to causing synchrotron emission, the magnetic field also acts to confine the electron bunches within the channel. To show the source of the enhanced synchrotron radiation along the laser direction of propagation, the expected power of synchrotron emission was calculated using $P \propto n_e \chi_e^2 g(\chi_e)$ assuming motion parallel with the x -axis, for grid cells where the averaged electron velocities correspond to trajectories within 5° of the $+x$ direction. The normalised power is shown in figure 5.13(f) and is dominated by the ultrarelativistic electrons within the bunches accelerated along the channel surface that are closest to the closed end of the channel. Although pair production was not modelled in the simulations discussed in the chapter, inclusion of nonlinear Breit-Wheeler pair production in several test simulations for the same conditions as used here produced the same angular profiles of synchrotron emission.

5.8 Summary

In summary, Bayesian optimisation has been applied to the generation of synchrotron radiation in ultrahigh intensity laser interactions with CH foils in 2D PIC simulations. Optimisation of individual properties was shown, and control of the simultaneous optimisation of the individual objectives of maximising synchrotron production and minimising bremsstrahlung emission was demonstrated with changes to the objective function, including the use of an acceptance function.

The angle-of-incidence was identified from the optimisation results as a critical parameter for achieving the highest angle-resolved synchrotron emission. Further 2D and 3D simulations showed the optimisation of the synchrotron emission spatial profile into a single forward-directed lobe, due to the improved acceleration of electrons along the target surface. The angular distribution of the synchrotron emission for p-, s-, left-hand c- and right-hand c- polarisation was demonstrated in 3D for angles-of-

incidence up to 75° . Here, the electrons injected from the target surface into the focal spot during the interaction due to the laser electric field dominate the emission and cause the angular synchrotron profiles generated. Changing the direction of rotation of the electric field vector for circular polarisation showed a synchrotron spatial profile mirrored in the z (polar) direction to be produced. Furthermore, rotation of the target to bring the surface close to the divergence half-angle of the tightly-focused laser pulse for $I_L = 1.1 \times 10^{23} \text{ W cm}^{-2}$ was observed to produce a narrow beam of synchrotron radiation from the electrons accelerated along the surface during focusing, for p- and c- polarisation. For $I_L = 1.1 \times 10^{24} \text{ W cm}^{-2}$, and a target thick enough to avoid significant transparency, the most angle-resolved emission was found for 45° incidence and produced a profile peaked close to the laser propagation direction. Analysis of the interaction dynamics showed highly energetic electrons are accelerated near parallel with the laser pulse along the closer side of the channel, formed in the target due to the radiation pressure and ponderomotive force. The emission here was found to be assisted by a current-driven magnetic field.

Many target designs for synchrotron production in laser-solid interactions utilise microstructures such as pre-formed channels, cones or wires in which the acceleration of electrons along a surface or within a channel occurs in a similar way to the optimised conditions found here. The manufacture and alignment, however, of such small target structures is a considerable challenge that may limit the achievable repetition rate and consistency of the radiation beams produced. The generation of a self-formed channel in an (oblique) target, within which the synchrotron radiation is produced, as in this work may provide a simpler and more repeatable alternative to complex target structures. The density of the target could also be varied to improve the synchrotron emission: reducing the target density with the use of cryogenic hydrogen or foam targets instead of foils would improve the channel formation and could increase the conversion of laser energy to synchrotron radiation.

The changes induced in the synchrotron spatial profile with laser polarisation and angle-of-incidence may enable such radiation to be more easily distinguishable from bremsstrahlung emission in experiments, and enhance studies of the QED-plasma physics in these interactions. The demonstrated control of the synchrotron emission is also useful for the application of this intense source of high energy photons. The work presented here may be extended by searching for conditions that optimise the generation

of electron-positron pairs through the linear or nonlinear Breit-Wheeler process. The influence of additional parameters such as the front surface density scale length, the spatial-intensity contrast [38] (including asymmetries in the focal spot) and different target structures could also be explored.

Conclusion

The research presented in this thesis has explored the optimisation of radiation sources from laser-solid interactions at peak laser powers up to 20 PW. The results will improve the understanding of proton acceleration and the generation of synchrotron radiation in experiments at state of the art high power laser facilities. They are summarised in this chapter.

6.1 Proton acceleration

The maximum energy of protons accelerated from CH foils was optimised by varying the foil thickness in a series of PIC simulations. This was repeated for realistic laser parameters with a number of peak intensities across a range up to $2 \times 10^{23} \text{ W cm}^{-2}$. In all cases, the maximum energy of the proton spectra peaked for a thickness where significant laser transmission occurred. Importantly, the maximum proton energies were demonstrated to peak when relativistic transparency occurs simultaneously with the arrival of the peak laser intensity on the target for $I_L = 5 \times 10^{20} - 2 \times 10^{23} \text{ W cm}^{-2}$ with both linear and circular laser polarisation. Relativistic transparency is well known to offer increased proton energies, but the rapidly evolving plasma dynamics make identification of the mechanism responsible a challenge. Particle tracking enabled examination of the acceleration history of the history energy protons, which showed a mix of processes occur. For linear polarisation, prior to the onset of RSIT these protons usually experience a combination of RPA and TNSA. At the lower limit of the intensity range

TNSA generally dominates the initial phase of the interaction here, whilst close to the upper limit the protons experience combined RPA-TNSA as they move with the compressed electron layer. With the onset of RSIT, electrons throughout the target volume in the path of the laser pulse are directly accelerated by the laser thus enhancing the rear surface sheath field, in part due to the dense positively charged ion region they leave behind. The enhancement with relativistic transparency heavily relies upon the laser pulse propagating through a rapidly decreasing density gradient, where the return current is limited by the reduced number of electrons causing strong charge separation fields to be generated that accelerate the protons and ions, which corresponds to it exiting the rear of the thin foil targets used here. For circular polarisation, the initial phase of the acceleration for the highest energy protons is dominated by RPA, which occurs predominantly through the light sail mechanism due to the ultrathin foils used here. Although the target rapidly expands when RSIT occurs, the Lorentz force of the transmitted laser pulse continues to push many electrons forwards and the protons continue to be accelerated at the rear of the target.

The presence of an extended laser pulse rising edge with high intensity, which may often be present in experiments, increased the optimum target thickness but the maximum proton energy achievable did not considerably change. The other elements of the laser contrast that arrive a picosecond or more before the main pulse are therefore expected to be more important to consider in experiments, provided the rising edge is not significantly more intense than that simulated here. Acceleration of protons from the contaminant layer on the target rear surface will, however, be significantly degraded by pre-acceleration away from the target by TNSA during the laser pulse rising edge. As the plasma electrons begin to radiate strongly at the highest laser intensity considered in this work, the radiation reaction was shown to delay the onset of RSIT and reduce both the maximum achievable proton energy and conversion efficiency. Radiation reaction was also found to reduce the maximum proton energy from the thickest target by approximately 50%. Therefore, relativistic transparency will become even more important for obtaining high proton energies in experiments with such high laser intensities, where TNSA in thick targets will become inefficient. In several cases, peaks in the proton energy spectra were observed along the direction of propagation of the laser pulse. The generation of peak proton energy spectra would be useful for applications that require a large dose of protons at a single energy. It is currently unclear if these

peaks are a result of RPA or radiation reaction, yet production of these artefacts in 3D simulations and improved understanding of their generation could provide sufficient evidence to search for their production in experiments.

The onset time of relativistic transparency has been demonstrated as a critical factor in proton acceleration for a wide range of conditions. Therefore, it will be important to consider in future experiments where relativistic transparency occurs. This may be the case not only for proton acceleration, but also the acceleration of heavy ions and the generation of other radiation from these interactions. Diagnosing the transparency time experimentally is, however, a difficult challenge. The transmitted pulse will have experienced temporally varying absorption, and other light that has not propagated through the relativistically transparent target may also be present. This includes evanescent light that can escape the rear of the target and transition radiation. Measuring changes in the transparency time over timescales much shorter than the laser pulse duration is also a technical challenge that may prove difficult to overcome. In the presence of these obstacles, perhaps the most useful way to use the transmitted laser light is to inform an artificial neural network model of the interaction or proton beams produced. Spectral interferometry of the transmitted laser pulse with a separate pulse at a fixed delay would also provide some information on changes to the temporal structure of the transmitted laser pulse, and the data could additionally be used to inform a machine learning model. Measurements of the reflected light could be used in a similar way, especially for circular polarisation where the proton energies demonstrate a dependence on the peak critical surface velocity.

Given the protons are accelerated by charge separation from the electrons, which are directly accelerated by the Lorentz force of the transmitted laser pulse, the spatial profile of the proton beam can be controlled to some degree by varying the laser polarisation. Indeed, proton beams have been manipulated in the past by varying between linear, elliptical and circularly polarised light [97], yet other polarisation states or high order modes of the incident laser beam such as radial polarisation or Laguerre-Gaussian modes may have the potential to improve the proton beams provided similar laser intensities are attainable.

The use of ultrathin targets to enable RSIT does present several issues. These targets are fragile and it is currently unclear if there is a method of using them successfully at high repetition rate, which may limit their applications. Although the optimum tar-

get thickness increases with intensity, this still only reaches values of $\sim 1 \mu\text{m}$ in this work, whilst the most established method using solid targets at high repetition rate, tape drive targets, are limited to thicknesses $\gtrsim 10 \mu\text{m}$. The use of lower densities corresponding to tens of n_c would enable thicker alternative targets. Production of foams at this density would still require a suitable method of deploying them at high repetition rate. Cryogenic hydrogen ribbons or liquid jet targets could also be useful, but a method to control the thickness and reduce it to values thin enough for RSIT would be needed.

The work presented in chapter 4 could be developed further by considering the acceleration of heavier ions, or by considering optimisation of the proton beam for a specific application. The understanding of interactions at $I_L \gtrsim 10^{23} \text{W cm}^{-2}$ is also currently limited, and further simulations in 3D with strong-field QED effects would help inform upcoming experiments.

6.2 Synchrotron radiation

The generation of synchrotron radiation from planar foil targets was optimised in 2D PIC simulations using Gaussian process regression. Various properties of the synchrotron emission were optimised individually by varying the objective function, including the overall conversion of laser energy to synchrotron photons, the peak directional emission of synchrotron radiation and the number of synchrotron photons above an energy threshold. Optimisation of multiple properties of the emission was demonstrated, including the simultaneous optimisation of synchrotron radiation and mitigation of bremsstrahlung radiation. The use of an acceptance function to set a lower threshold value for one of the optimised parameters was demonstrated. Input parameter scans also showed the scaling of the synchrotron conversion efficiency with several parameters. For increasing laser intensities, the synchrotron emission resulting from electrons entering the laser focal spot from the sides of the channel bored in the target becomes increasingly important.

The optimised results were generally found for conditions that maximise the laser intensity incident on the target surface, and oblique incidence of the laser pulse. Further 2D simulations showed that oblique incidence improves the coupling of laser energy to electrons, but as the angle-of-incidence with respect to the target normal in-

creases the electron propagate closer to the parallel with the laser pulse, eventually reducing the synchrotron emission. Optimisation of the synchrotron radiation with an oblique angle-of-incidence was also found in a series of 3D PIC simulations. Due to the role of the laser polarisation observed in the simulations, further 3D simulations were performed for s-, right-hand c- and left-hand c- polarisation. The results of which demonstrated the polarisation dependence of the emission. Finally, 3D simulations for $I_L = 1.1 \times 10^{24} \text{ W cm}^{-2}$ showed similar results, yet the most synchrotron emission was observed near parallel with the incident laser pulse for p-polarisation with the laser at 45° incidence to the target. In this case, highly relativistic electrons propagate near parallel with the laser pulse along one side of the channel formed in the target, and emit synchrotron radiation in part due to a current-generated magnetic field.

The use of ultrathin targets that undergo RSIT greatly reduces the bremsstrahlung emission compared to thicker targets, and will be useful for exploring the generation of synchrotron radiation and its applications in a less noisy environment. For applications that require the brightest beam of synchrotron radiation, however, the Bayesian optimisation results show the use of thick targets that remain opaque can produce somewhat more directional synchrotron emission. The use of tape drive targets with the laser at oblique incidence could therefore provide a good method of producing bright synchrotron radiation, where the target is relatively robust and where high repetition rates are readily achievable. Although schemes involving microstructured targets, multiple laser pulses or both could enhance the synchrotron emission, the spatial and temporal alignment of multiple laser pulses or alignment of a single laser pulse with a micron scale structure would be challenging. Large variations would be expected in the radiation produced, and the maximum repetition rate of successful shots with structured targets may be limited if the pointing stability of the laser is not much smaller than the transverse dimensions of the target structures. The generation of optimal synchrotron radiation in this thesis was found to be dependent upon the laser forming a channel in the target. Therefore, the synchrotron emission could be further improved on from the results in chapter 5 by utilising alternative lower density targets, where channel formation is improved, to the CH foils modelled in this work. For example, cryogenic hydrogen ribbons, liquid jets, foams, high pressure gases or tape drive targets with a pre-expanded front surface could offer a simple and more repeatable alternative to structured targets, if the challenging laser alignment and pointing stability requirements

with micro-structured targets cannot be overcome.

Extensions to the work presented in this thesis could include implementation of the polarisation and spin-dependent properties of the synchrotron emission, which would enable exploration and optimisation of polarised gamma ray sources. Similarly, machine learning methods could be applied to simulations to find conditions that optimise the generation of positron beams and their polarisation. Although p-polarisation of the laser pulse was found to produce the most synchrotron emission in the 3D simulations discussed in chapter 5, other polarisation states and high order modes of light could be explored. An optimisation technique could also be applied to 3D simulations, and in experiments now that laser facilities capable of producing intensities exceeding $10^{23} \text{ W cm}^{-2}$ are coming online. In particular, multi-objective optimisation via Bayesian optimisation or other methods could be implemented to identify the Pareto front with a number of objectives.

6.3 Final remarks

Research on laser-driven plasma accelerators has spanned many decades. Now, with the availability of high peak power and repetition rate lasers, the potential to soon apply these radiation sources to help solve a range of challenges exists. The laser intensities reachable in the laboratory are now high enough that proton and ion energies surpassing the energy requirements for hadrontherapy of deep seated tumours may be possible, and tests of the medical applications of laser-produced ion sources combined with further development may finally enable them to contribute to this aspect of healthcare. In addition, these laser intensities are also opening up an exciting new area of experimental physics, where tests of strong-field QED physics are possible, and effects within this high field regime could be leveraged to produce new intense sources of high energy particles and photons. A key part of developing laser-driven radiation sources for applications is optimising the interaction to produce a stable source of radiation at the required energies and at high flux. The work in this thesis has gone some way to understanding how the range of proton energies achievable can be increased and the interaction dynamics responsible. In addition to improving the understanding of the generation of synchrotron radiation in these accelerators and identifying conditions under which the brightness of the gamma ray beam could be maximised. It is hoped

that the results discussed in this thesis help inform and understand many experiments in the future.

APPENDIX A

List of Acronyms

ASE	Amplified Spontaneous Emission
BOA	Laser Break-Out Afterburner
CCD	Charge-Coupled Device
CPA	Chirped Pulse Amplification
ELI	Extreme Light Infrastructure
EPOCH	Name of a particle-in-cell code
FWHM	Full-Width-Half-Maximum
ICF	Inertial Confinement Fusion
LCFA	Local-Constant-Field Approximation
LHCP	Left-Hand Circular Polarisation
MCP	Micro-Channel Plate
NIF	National Ignition Facility
OPCPA	Optical Parametric Chirped Pulse Amplification
PIC	Particle-In-Cell
QED	Quantum Electrodynamics
RCF	Radiochromic Film
RESE	Re-injected Electron Synchrotron Emission
RHCP	Right-Hand Circular Polarisation
RPA	Radiation Pressure Acceleration
RSIT	Relativistic Self-Induced Transparency
RTF	Relativistic Transparency Front
SASL	Synchronised Acceleration by Slow Light
TNSA	Target Normal Sheath Acceleration

Bibliography

- [1] E. J. Jaeschke, S. Khan, J. R. Schneider, and J. B. Hastings, *Synchrotron light sources and free-electron lasers: accelerator physics, instrumentation and science applications* (Springer, 2016).
- [2] B. W. J. McNeil and N. R. Thompson, *Nature Photonics* **4**, 814 (2010).
- [3] C. Pellegrini, A. Marinelli, and S. Reiche, *Reviews of Modern Physics* **88**, 015006 (2016).
- [4] V. A. Dolgashev, *Applied Sciences* **13**, 10849 (2023).
- [5] C. Aniculaesei, T. Ha, S. Yoffe, L. Labun, S. Milton, E. McCary, M. M. Spinks, H. J. Quevedo, O. Z. Labun, R. Sain, A. Hannasch, R. Zgad Zaj, I. Pagano, J. A. Franco-Altamirano, M. L. Ringuette, E. Gaul, S. V. Luedtke, G. Tiwari, B. Ersfeld, E. Brunetti, H. Ruhl, T. Ditmire, S. Bruce, M. E. Donovan, M. C. Downer, D. A. Jaroszynski, and B. M. Hegelich, *Matter and Radiation at Extremes* **9**, 014001 (2023).
- [6] T. Tajima and J. M. Dawson, *Physical Review Letters* **43**, 267 (1979).
- [7] A. Higginson, R. J. Gray, M. King, R. J. Dance, S. D. R. Williamson, N. M. H. Butler, R. Wilson, R. Capdessus, C. Armstrong, J. S. Green, S. J. Hawkes, P. Martin, W. Q. Wei, S. R. Mirfayzi, X. H. Yuan, S. Kar, M. Borghesi, R. J. Clarke, D. Neely, and P. McKenna, *Nature Communications* **9**, 724 (2018).
- [8] T. Ziegler, I. Göthel, S. Assenbaum, C. Bernert, F.-E. Brack, T. E. Cowan, N. P. Dover, L. Gaus, T. Kluge, S. Kraft, F. Kroll, J. Metzkes-Ng, M. Nishiuchi, I. Prencipe, T. Püschel, M. Rehwald, M. Reimold, H.-P. Schlenvoigt, M. E. P. Umlandt, M. Vescovi, U. Schramm, and K. Zeil, “Laser-driven high-energy proton beams from cascaded acceleration regimes”, 2023.

-
- [9] J. P. Palastro, J. L. Shaw, P. Franke, D. Ramsey, T. T. Simpson, and D. H. Froula, *Physical Review Letters* **124**, 134802 (2020).
- [10] C. A. Lindstrøm, *Physical Review Accelerators and Beams* **24**, 014801 (2021).
- [11] S. Kar, H. Ahmed, R. Prasad, M. Cerchez, S. Brauckmann, B. Aurand, G. Cantono, P. Hadjisolomou, C. L. S. Lewis, A. Macchi, G. Nersisyan, A. P. L. Robinson, A. M. Schroer, M. Swantusch, M. Zepf, O. Willi, and M. Borghesi, *Nature Communications* **7**, 10792 (2016).
- [12] W. D. Newhauser and R. Zhang, *Physics in Medicine & Biology* **60**, R155 (2015).
- [13] R. Mohan and D. Grosshans, *Advanced Drug Delivery Reviews* **109**, 26 (2017).
- [14] T. D. Malouff, A. Mahajan, S. Krishnan, C. Beltran, D. S. Seneviratne, and D. M. Trifiletti, *Frontiers in Oncology* **10**, 82 (2020).
- [15] V. Favaudon, L. Caplier, V. Monceau, F. Pouzoulet, M. Sayarath, C. Fouillade, M.-F. Poupon, I. Brito, P. Hupé, J. Bourhis, J. Hall, J.-J. Fontaine, and M.-C. Vozenin, *Science Translational Medicine* **6**, 245ra93 (2014).
- [16] A. E. Mascia, E. C. Daugherty, Y. Zhang, E. Lee, Z. Xiao, M. Sertorio, J. Woo, L. R. Backus, J. M. McDonald, C. McCann, K. Russell, L. Levine, R. A. Sharma, D. Khuntia, J. D. Bradley, I. Simone Charles B., J. P. Perentesis, and J. C. Breneman, *JAMA Oncology* **9**, 62 (2023).
- [17] F. Kroll, F.-E. Brack, C. Bernert, S. Bock, E. Bodenstein, K. Brüchner, T. E. Cowan, L. Gaus, R. Gebhardt, U. Helbig, L. Karsch, T. Kluge, S. Kraft, M. Krause, E. Lessmann, U. Masood, S. Meister, J. Metzkes-Ng, A. Nossula, J. Pawelke, J. Pietzsch, T. Püschel, M. Reimold, M. Rehwald, C. Richter, H.-P. Schlenvoigt, U. Schramm, M. E. P. Umlandt, T. Ziegler, K. Zeil, and E. Beyreuther, *Nature Physics* **18**, 316 (2022).
- [18] G. Aymar, T. Becker, S. Boogert, M. Borghesi, R. Bingham, C. Brenner, P. N. Burrows, O. C. Ettliger, T. Dascalu, S. Gibson, T. Greenshaw, S. Gruber, D. Gujral, C. Hardiman, J. Hughes, W. G. Jones, K. Kirkby, A. Kurup, J.-B. Lagrange, K. Long, W. Luk, J. Matheson, P. McKenna, R. McLauchlan, Z. Najmudin, H. T. Lau, J. L. Parsons, J. Pasternak, J. Pozimski, K. Prise, M. Puchalska, P. Ratoff, G. Schettino, W. Shields, S. Smith, J. Thomason, S. Towe, P. Weightman, C. Whyte, and R. Xiao, *Frontiers in Physics* **8** (2020).

-
- [19] P. K. Patel, A. J. Mackinnon, M. H. Key, T. E. Cowan, M. E. Foord, M. Allen, D. F. Price, H. Ruhl, P. T. Springer, and R. Stephens, *Physical Review Letters* **91**, 125004 (2003).
- [20] M. Roth, T. E. Cowan, M. H. Key, S. P. Hatchett, C. Brown, W. Fountain, J. Johnson, D. M. Pennington, R. A. Snavely, S. C. Wilks, K. Yasuike, H. Ruhl, F. Pegoraro, S. V. Bulanov, E. M. Campbell, M. D. Perry, and H. Powell, *Physical Review Letters* **86**, 436 (2001).
- [21] J. Nuckolls, L. Wood, A. Thiessen, and G. Zimmerman, *Nature* **239**, 139 (1972).
- [22] J. Lindl, *Physics of Plasmas* **2**, 3933 (1995).
- [23] J. Lindl, O. Landen, J. Edwards, E. Moses, and N. Team, *Physics of Plasmas* **21**, 020501 (2014).
- [24] O. A. Hurricane, P. K. Patel, R. Betti, D. H. Froula, S. P. Regan, S. A. Slutz, M. R. Gomez, and M. A. Sweeney, *Reviews of Modern Physics* **95**, 025005 (2023).
- [25] H. Abu-Shawareb et al. (Indirect Drive ICF Collaboration), *Physical Review Letters* **129**, 075001 (2022).
- [26] M. Tabak, J. Hammer, M. E. Glinsky, W. L. Kruer, S. C. Wilks, J. Woodworth, E. M. Campbell, M. D. Perry, and R. J. Mason, *Physics of Plasmas* **1**, 1626 (1994).
- [27] A. Kemp, F. Fiuza, A. Debayle, T. Johzaki, W. Mori, P. Patel, Y. Sentoku, and L. Silva, *Nuclear Fusion* **54**, 054002 (2014).
- [28] A. Robinson, D. Strozzi, J. Davies, L. Gremillet, J. Honrubia, T. Johzaki, R. Kingham, M. Sherlock, and A. Solodov, *Nuclear Fusion* **54**, 054003 (2014).
- [29] M. H. Key, R. R. Freeman, S. P. Hatchett, A. J. MacKinnon, P. K. Patel, R. A. Snavely, and R. B. Stephens, *Fusion Science and Technology* **49**, 440 (2006).
- [30] T. Bartal, M. E. Foord, C. Bellei, M. H. Key, K. A. Flippo, S. A. Gaillard, D. T. Offermann, P. K. Patel, L. C. Jarrott, D. P. Higginson, M. Roth, A. Otten, D. Kraus, R. B. Stephens, H. S. McLean, E. M. Giraldez, M. S. Wei, D. C. Gautier, and F. N. Beg, *Nature Physics* **8**, 139 (2012).
- [31] C. McGuffey, J. Kim, M. S. Wei, P. M. Nilson, S. N. Chen, J. Fuchs, P. Fitzsimmons, M. E. Foord, D. Mariscal, H. S. McLean, P. K. Patel, R. B. Stephens, and F. N. Beg, *Scientific Reports* **10**, 9415 (2020).

-
- [32] L. Romagnani, J. Fuchs, M. Borghesi, P. Antici, P. Audebert, F. Ceccherini, T. Cowan, T. Grismayer, S. Kar, A. Macchi, P. Mora, G. Pretzler, A. Schiavi, T. Toncian, and O. Willi, *Physical Review Letters* **95**, 195001 (2005).
- [33] C. Courtois, R. Edwards, A. Compant La Fontaine, C. Aedy, M. Barbotin, S. Bazzoli, L. Biddle, D. Brebion, J. L. Bourgade, D. Drew, M. Fox, M. Gardner, J. Gazave, J. M. Lagrange, O. Landoas, L. Le Dain, E. Lefebvre, D. Mastrosimone, N. Pichoff, G. Pien, M. Ramsay, A. Simons, N. Sircombe, C. Stoeckl, and K. Thorp, *Physics of Plasmas* **18**, 023101 (2011).
- [34] F. Negoita, M. Roth, P. G. Thirolf, S. Tudisco, F. Hannachi, S. Moustazis, I. Pomerantz, P. Mckenna, J. Fuchs, K. Sphor, G. Acbas, A. Anzalone, P. Audebert, S. Balascuta, F. Cappuzzello, M. O. Cernaianu, S. Chen, I. Dancus, R. Freeman, H. Geissel, P. Ghenuche, L. Gizzi, F. Gobet, G. Gosselin, M. Gugiu, D. Higginson, E. D’Humières, C. Ivan, D. Jaroszynski, S. Kar, L. Lamia, V. Leca, L. Neagu, G. Lanzalone, V. Meot, S. R. Mirfayzi, I. O. Mitu, P. Morel, C. Murphy, C. Petcu, H. Petrascu, C. Petrone, P. Raczka, M. Risca, F. Rotaru, J. J. Santos, D. Schumacher, D. Stutman, M. Tarisien, M. Tataru, B. Tatulea, I. C. E. Turcu, M. Versteegen, D. Ursescu, S. Gales, and N. V. Zamfir, arXiv preprint arXiv:2201.01068 (2022).
- [35] J. W. Yoon, Y. G. Kim, I. W. Choi, J. H. Sung, H. W. Lee, S. K. Lee, and C. H. Nam, *Optica* **8**, 630 (2021).
- [36] A. Fedotov, A. Ilderton, F. Karbstein, B. King, D. Seipt, H. Taya, and G. Torgrimsson, *Physics Reports* **1010**, 1 (2023).
- [37] B. Quesnel and P. Mora, *Physical Review E* **58**, 3719 (1998).
- [38] R. Wilson, M. King, N. M. H. Butler, D. C. Carroll, T. P. Frazer, M. J. Duff, A. Higginson, R. J. Dance, J. Jarrett, Z. E. Davidson, C. D. Armstrong, H. Liu, S. J. Hawkes, R. J. Clarke, D. Neely, R. J. Gray, and P. McKenna, *Scientific Reports* **12**, 1910 (2022).
- [39] P. Gibbon, *Short pulse laser interactions with matter: an introduction* (Imperial College Press, 2005).
- [40] J. H. Eberly and J. Javanainen, *European Journal of Physics* **9**, 265 (1988).

-
- [41] R. R. Freeman and P. H. Bucksbaum, *Journal of Physics B: Atomic, Molecular and Optical Physics* **24**, 325 (1991).
- [42] L. V. Keldysh, “Ionization in the field of a strong electromagnetic wave”, in , *Selected Papers of Leonid V Keldysh*, 0 (World Scientific, 2023), pp. 56–63.
- [43] P. Sprangle, C.-M. Tang, and E. Esarey, *IEEE Transactions on Plasma Science* **15**, 145 (1987).
- [44] G. A. Mourou, T. Tajima, and S. V. Bulanov, *Reviews of Modern Physics* **78**, 309 (2006).
- [45] D. B. Zou, H. B. Zhuo, X. H. Yang, F. Q. Shao, Y. Y. Ma, T. P. Yu, H. C. Wu, Y. Yin, Z. Y. Ge, and X. H. Li, *Physics of Plasmas* **21**, 063103 (2014).
- [46] R. J. Gray, D. C. Carroll, X. H. Yuan, C. M. Brenner, M. Burza, M. Coury, K. L. Lancaster, X. X. Lin, Y. T. Li, D. Neely, M. N. Quinn, O. Tresca, C.-G. Wahlström, and P. McKenna, *New Journal of Physics* **16**, 113075 (2014).
- [47] T. P. Frazer, R. Wilson, M. King, N. M. H. Butler, D. C. Carroll, M. J. Duff, A. Higginson, J. Jarrett, Z. E. Davidson, C. Armstrong, H. Liu, D. Neely, R. J. Gray, and P. McKenna, *Physical Review Research* **2**, 042015 (2020).
- [48] B. Gonzalez-Izquierdo, R. J. Gray, M. King, R. J. Dance, R. Wilson, J. McCreddie, N. M. H. Butler, R. Capdessus, S. Hawkes, J. S. Green, M. Borghesi, D. Neely, and P. McKenna, *Nature Physics* **12**, 505 (2016).
- [49] M. Jirka, O. Klimo, and M. Matys, *Physical Review Research* **3**, 033175 (2021).
- [50] P. Mora, *The Physics of Fluids* **25**, 1051 (1982).
- [51] J. P. Freidberg, R. W. Mitchell, R. L. Morse, and L. I. Rudstinski, *Physical Review Letters* **28**, 795 (1972).
- [52] F. Brunel, *Physical Review Letters* **59**, 52 (1987).
- [53] P. Gibbon and A. R. Bell, *Physical Review Letters* **68**, 1535 (1992).
- [54] W. L. Kruer and K. Estabrook, *The Physics of Fluids* **28**, 430 (1985).
- [55] S. Wilks and W. Kruer, *IEEE Journal of Quantum Electronics* **33**, 1954 (1997).
- [56] A. P. L. Robinson, A. V. Arefiev, and D. Neely, *Physical Review Letters* **111**, 065002 (2013).

-
- [57] A. Pukhov, Z.-M. Sheng, and J. Meyer-ter-Vehn, *Physics of Plasmas* **6**, 2847 (1999).
- [58] A. V. Arefiev, V. N. Khudik, A. P. L. Robinson, G. Shvets, L. Willingale, and M. Schollmeier, *Physics of Plasmas* **23**, 056704 (2016).
- [59] Y. Ping, R. Shepherd, B. F. Lasinski, M. Tabak, H. Chen, H. K. Chung, K. B. Fournier, S. B. Hansen, A. Kemp, D. A. Liedahl, K. Widmann, S. C. Wilks, W. Rozmus, and M. Sherlock, *Physical Review Letters* **100**, 085004 (2008).
- [60] H. Alfvén, *Physical Review* **55**, 425 (1939).
- [61] A. R. Bell, J. R. Davies, S. Guerin, and H. Ruhl, *Plasma Physics and Controlled Fusion* **39**, 653 (1997).
- [62] M. N. Quinn, “Investigations of fast electron transport in intense laser-solid interactions”, PhD thesis (University of Strathclyde, 2011).
- [63] X. H. Yuan, A. P. L. Robinson, M. N. Quinn, D. C. Carroll, M. Borghesi, R. J. Clarke, R. G. Evans, J. Fuchs, P. Gallegos, L. Lancia, D. Neely, K. Quinn, L. Romagnani, G. Sarri, P. A. Wilson, and P. McKenna, *New Journal of Physics* **12**, 063018 (2010).
- [64] J. R. Davies, J. S. Green, and P. A. Norreys, *Plasma Physics and Controlled Fusion* **48**, 1181 (2006).
- [65] P. A. Norreys, J. S. Green, J. R. Davies, M. Tatarakis, E. L. Clark, F. N. Beg, A. E. Dangor, K. L. Lancaster, M. S. Wei, M. Zepf, and K. Krushelnick, *Plasma Physics and Controlled Fusion* **48**, L11 (2006).
- [66] D. A. MacLellan, D. C. Carroll, R. J. Gray, N. Booth, M. Burza, M. P. Desjarlais, F. Du, B. Gonzalez-Izquierdo, D. Neely, H. W. Powell, A. P. L. Robinson, D. R. Rusby, G. G. Scott, X. H. Yuan, C.-G. Wahlström, and P. McKenna, *Physical Review Letters* **111**, 095001 (2013).
- [67] J. S. Green, V. M. Ovchinnikov, R. G. Evans, K. U. Akli, H. Azechi, F. N. Beg, C. Bellei, R. R. Freeman, H. Habara, R. Heathcote, M. H. Key, J. A. King, K. L. Lancaster, N. C. Lopes, T. Ma, A. J. MacKinnon, K. Markey, A. McPhee, Z. Najmudin, P. Nilson, R. Onofrei, R. Stephens, K. Takeda, K. A. Tanaka, W. Theobald, T. Tanimoto, J. Waugh, L. Van Woerkom, N. C. Woolsey, M. Zepf, J. R. Davies, and P. A. Norreys, *Physical Review Letters* **100**, 015003 (2008).

-
- [68] S. C. Wilks, A. B. Langdon, T. E. Cowan, M. Roth, M. Singh, S. Hatchett, M. H. Key, D. Pennington, A. MacKinnon, and R. A. Snavely, *Physics of Plasmas* **8**, 542 (2001).
- [69] R. A. Snavely, M. H. Key, S. P. Hatchett, T. E. Cowan, M. Roth, T. W. Phillips, M. A. Stoyer, E. A. Henry, T. C. Sangster, M. S. Singh, S. C. Wilks, A. MacKinnon, A. Offenberger, D. M. Pennington, K. Yasuike, A. B. Langdon, B. F. Lasinski, J. Johnson, M. D. Perry, and E. M. Campbell, *Physical Review Letters* **85**, 2945 (2000).
- [70] M. Allen, P. K. Patel, A. Mackinnon, D. Price, S. Wilks, and E. Morse, *Physical Review Letters* **93**, 265004 (2004).
- [71] P. Mora, *Physical Review Letters* **90**, 185002 (2003).
- [72] P. Mora, *Physical Review E* **72**, 056401 (2005).
- [73] J. Schreiber, F. Bell, F. Grüner, U. Schramm, M. Geissler, M. Schnürer, S. Ter-Avetisyan, B. M. Hegelich, J. Cobble, E. Brambrink, J. Fuchs, P. Audebert, and D. Habs, *Physical Review Letters* **97**, 045005 (2006).
- [74] K. Zeil, S. D. Kraft, S. Bock, M. Bussmann, T. E. Cowan, T. Kluge, J. Metzkes, T. Richter, R. Sauerbrey, and U. Schramm, *New Journal of Physics* **12**, 045015 (2010).
- [75] J. E. Crow, P. L. Auer, and J. E. Allen, *Journal of Plasma Physics* **14**, 65 (1975).
- [76] M. Passoni, L. Bertagna, and A. Zani, *New Journal of Physics* **12**, 045012 (2010).
- [77] M. Passoni, C. Perego, A. Sgattoni, and D. Batani, *Physics of Plasmas* **20**, 060701 (2013).
- [78] J. Fuchs, P. Antici, E. d’Humières, E. Lefebvre, M. Borghesi, E. Brambrink, C. A. Cecchetti, M. Kaluza, V. Malka, M. Manclossi, S. Meyroneinc, P. Mora, J. Schreiber, T. Toncian, H. Pépin, and P. Audebert, *Nature Physics* **2**, 48 (2006).
- [79] L. Robson, P. T. Simpson, R. J. Clarke, K. W. D. Ledingham, F. Lindau, O. Lundh, T. McCanny, P. Mora, D. Neely, C.-G. Wahlström, M. Zepf, and P. McKenna, *Nature Physics* **3**, 58 (2007).

-
- [80] M. Borghesi, Nuclear Instruments and Methods in Physics Research Section A: Accelerators, Spectrometers, Detectors and Associated Equipment **740**, Proceedings of the first European Advanced Accelerator Concepts Workshop 2013, 6 (2014).
- [81] M. Zimmer, S. Scheuren, T. Ebert, G. Schaumann, B. Schmitz, J. Hornung, V. Bagnoud, C. Rödel, and M. Roth, Physical Review E **104**, 045210 (2021).
- [82] F. Wagner, O. Deppert, C. Brabetz, P. Fiala, A. Kleinschmidt, P. Poth, V. A. Schanz, A. Tebartz, B. Zielbauer, M. Roth, T. Stöhlker, and V. Bagnoud, Physical Review Letters **116**, 205002 (2016).
- [83] C. M. Brenner, A. P. L. Robinson, K. Markey, R. H. H. Scott, R. J. Gray, M. Rosinski, O. Deppert, J. Badziak, D. Batani, J. R. Davies, S. M. Hassan, K. L. Lancaster, K. Li, I. O. Musgrave, P. A. Norreys, J. Pasley, M. Roth, H.-P. Schlenvoigt, C. Spindloe, M. Tatarakis, T. Winstone, J. Wolowski, D. Wyatt, P. McKenna, and D. Neely, Applied Physics Letters **104**, 081123 (2014).
- [84] T. E. Cowan, J. Fuchs, H. Ruhl, A. Kemp, P. Audebert, M. Roth, R. Stephens, I. Barton, A. Blazevic, E. Brambrink, J. Cobble, J. Fernández, J.-C. Gauthier, M. Geissel, M. Hegelich, J. Kaae, S. Karsch, G. P. Le Sage, S. Letzring, M. Manclossi, S. Meyroneinc, A. Newkirk, H. Pépin, and N. Renard-LeGalloudec, Physical Review Letters **92**, 204801 (2004).
- [85] F. Nürnberg, M. Schollmeier, E. Brambrink, A. Blažević, D. C. Carroll, K. Flippo, D. C. Gautier, M. Geißel, K. Harres, B. M. Hegelich, O. Lundh, K. Markey, P. McKenna, D. Neely, J. Schreiber, and M. Roth, Review of Scientific Instruments **80**, 033301 (2009).
- [86] S. C. Wilks, W. L. Kruer, M. Tabak, and A. B. Langdon, Physical Review Letters **69**, 1383 (1992).
- [87] A. P. L. Robinson, P. Gibbon, M. Zepf, S. Kar, R. G. Evans, and C. Bellei, Plasma Physics and Controlled Fusion **51**, 024004 (2009).
- [88] T. Esirkepov, M. Borghesi, S. V. Bulanov, G. Mourou, and T. Tajima, Physical Review Letters **92**, 175003 (2004).
- [89] A. Macchi, S. Veghini, and F. Pegoraro, Physical Review Letters **103**, 085003 (2009).

-
- [90] C. A. J. Palmer, N. P. Dover, I. Pogorelsky, M. Babzien, G. I. Dudnikova, M. Ispiriyani, M. N. Polyanskiy, J. Schreiber, P. Shkolnikov, V. Yakimenko, and Z. Najmudin, *Physical Review Letters* **106**, 014801 (2011).
- [91] J. F. L. Simmons and C. R. McInnes, *American Journal of Physics* **61**, 205 (1993).
- [92] C. Scullion, D. Doria, L. Romagnani, A. Sgattoni, K. Naughton, D. R. Symes, P. McKenna, A. Macchi, M. Zepf, S. Kar, and M. Borghesi, *Physical Review Letters* **119**, 054801 (2017).
- [93] F. Dollar, C. Zwick, A. G. R. Thomas, V. Chvykov, J. Davis, G. Kalinchenko, T. Matsuoka, C. McGuffey, G. M. Petrov, L. Willingale, V. Yanovsky, A. Maksimchuk, and K. Krushelnick, *Physical Review Letters* **108**, 175005 (2012).
- [94] C. A. J. Palmer, J. Schreiber, S. R. Nagel, N. P. Dover, C. Bellei, F. N. Beg, S. Bott, R. J. Clarke, A. E. Dangor, S. M. Hassan, P. Hilz, D. Jung, S. Kneip, S. P. D. Mangles, K. L. Lancaster, A. Rehman, A. P. L. Robinson, C. Spindloe, J. Szerypo, M. Tatarakis, M. Yeung, M. Zepf, and Z. Najmudin, *Physical Review Letters* **108**, 225002 (2012).
- [95] Y. Wan, I. A. Andriyash, W. Lu, W. B. Mori, and V. Malka, *Physical Review Letters* **125**, 104801 (2020).
- [96] S. Kar, K. F. Kakolee, B. Qiao, A. Macchi, M. Cerchez, D. Doria, M. Geissler, P. McKenna, D. Neely, J. Osterholz, R. Prasad, K. Quinn, B. Ramakrishna, G. Sarri, O. Willi, X. Y. Yuan, M. Zepf, and M. Borghesi, *Physical Review Letters* **109**, 185006 (2012).
- [97] B. Gonzalez-Izquierdo, M. King, R. J. Gray, R. Wilson, R. J. Dance, H. Powell, D. A. MacLellan, J. McCreadie, N. M. H. Butler, S. Hawkes, J. S. Green, C. D. Murphy, L. C. Stockhausen, D. C. Carroll, N. Booth, G. G. Scott, M. Borghesi, D. Neely, and P. McKenna, *Nature Communications* **7**, 12891 (2016).
- [98] H. W. Powell, M. King, R. J. Gray, D. A. MacLellan, B. Gonzalez-Izquierdo, L. C. Stockhausen, G. Hicks, N. P. Dover, D. R. Rusby, D. C. Carroll, H. Padda, R. Torres, S. Kar, R. J. Clarke, I. O. Musgrave, Z. Najmudin, M. Borghesi, D. Neely, and P. McKenna, *New Journal of Physics* **17**, 103033 (2015).

-
- [99] A. Henig, D. Kiefer, K. Markey, D. C. Gautier, K. A. Flippo, S. Letzring, R. P. Johnson, T. Shimada, L. Yin, B. J. Albright, K. J. Bowers, J. C. Fernández, S. G. Rykovanov, H.-C. Wu, M. Zepf, D. Jung, V. K. Liechtenstein, J. Schreiber, D. Habs, and B. M. Hegelich, *Physical Review Letters* **103**, 045002 (2009).
- [100] X. Q. Yan, T. Tajima, M. Hegelich, L. Yin, and D. Habs, *Applied Physics B* **98**, 711 (2010).
- [101] S. Williamson, R. Wilson, M. King, M. Duff, B. Gonzalez-Izquierdo, Z. Davidson, A. Higginson, N. Booth, S. Hawkes, D. Neely, R. Gray, and P. McKenna, *Physical Review Applied* **14**, 034018 (2020).
- [102] V. Bagnoud, J. Hornung, T. Schlegel, B. Zielbauer, C. Brabetz, M. Roth, P. Hilz, M. Haug, J. Schreiber, and F. Wagner, *Physical Review Letters* **118**, 255003 (2017).
- [103] D. Haberberger, S. Tochitsky, F. Fiuza, C. Gong, R. A. Fonseca, L. O. Silva, W. B. Mori, and C. Joshi, *Nature Physics* **8**, 95 (2012).
- [104] O. Tresca, N. P. Dover, N. Cook, C. Maharjan, M. N. Polyanskiy, Z. Najmudin, P. Shkolnikov, and I. Pogorelsky, *Physical Review Letters* **115**, 094802 (2015).
- [105] A. V. Kuznetsov, T. Z. Esirkepov, F. F. Kamenets, and S. V. Bulanov, *Plasma Physics Reports* **27**, 211 (2001).
- [106] S. V. Bulanov and T. Z. Esirkepov, *Physical Review Letters* **98**, 049503 (2007).
- [107] T. Nakamura, S. V. Bulanov, T. Z. Esirkepov, and M. Kando, *Physical Review Letters* **105**, 135002 (2010).
- [108] A. V. Brantov, E. A. Govras, V. F. Kovalev, and V. Y. Bychenkov, *Physical Review Letters* **116**, 085004 (2016).
- [109] I. Göthel, C. Bernert, M. Bussmann, M. Garten, T. Miethlinger, M. Rehwald, K. Zeil, T. Ziegler, T. E. Cowan, U. Schramm, and T. Kluge, *Plasma Physics and Controlled Fusion* **64**, 044010 (2022).
- [110] E. Fourkal, I. Velchev, and C.-M. Ma, *Physical Review E* **71**, 036412 (2005).
- [111] S. S. Bulanov, A. Brantov, V. Y. Bychenkov, V. Chvykov, G. Kalinchenko, T. Matsuoka, P. Rousseau, S. Reed, V. Yanovsky, D. W. Litzenberg, K. Krushelnick, and A. Maksimchuk, *Physical Review E* **78**, 026412 (2008).

-
- [112] L. Yin, B. J. Albright, B. M. Hegelich, and J. C. Fernández, *Laser and Particle Beams* **24**, 291 (2006).
- [113] B. J. Albright, L. Yin, K. J. Bowers, B. M. Hegelich, K. A. Flippo, T. J. T. Kwan, and J. C. Fernández, *Physics of Plasmas* **14**, 094502 (2007).
- [114] L. Yin, B. J. Albright, B. M. Hegelich, K. J. Bowers, K. A. Flippo, T. J. T. Kwan, and J. C. Fernández, *Physics of Plasmas* **14**, 056706 (2007).
- [115] B. M. Hegelich, I. Pomerantz, L. Yin, H. C. Wu, D. Jung, B. J. Albright, D. C. Gautier, S. Letzring, S. Palaniyappan, R. Shah, K. Allinger, R. Hörlein, J. Schreiber, D. Habs, J. Blakeney, G. Dyer, L. Fuller, E. Gaul, E. Mccary, A. R. Meadows, C. Wang, T. Ditmire, and J. C. Fernandez, *New Journal of Physics* **15**, 085015 (2013).
- [116] Y. Y. Lau, F. He, D. P. Umstadter, and R. Kowalczyk, *Physics of Plasmas* **10**, 2155 (2003).
- [117] D. Umstadter, *Journal of Physics D: Applied Physics* **36**, R151 (2003).
- [118] C. Bellei, S. R. Nagel, S. Kar, A. Henig, S. Kneip, C. Palmer, A. Sävert, L. Willingale, D. Carroll, B. Dromey, J. S. Green, K. Markey, P. Simpson, R. J. Clarke, H. Lowe, D. Neely, C. Spindloe, M. Tolley, M. C. Kaluza, S. P. D. Mangles, P. McKenna, P. A. Norreys, J. Schreiber, M. Zepf, J. R. Davies, K. Krushelnick, and Z. Najmudin, *New Journal of Physics* **12**, 073016 (2010).
- [119] C. Bellei, J. R. Davies, P. K. Chauhan, and Z. Najmudin, *Plasma Physics and Controlled Fusion* **54**, 035011 (2012).
- [120] F. Brandl, G. Pretzler, D. Habs, and E. Fill, *Europhysics Letters* **61**, 632 (2003).
- [121] M. Manclossi, J. J. Santos, D. Batani, J. Faure, A. Debayle, V. T. Tikhonchuk, and V. Malka, *Physical Review Letters* **96**, 125002 (2006).
- [122] M. S. Longair, *High energy astrophysics*, 3rd ed. (Cambridge University Press, 2011).
- [123] J. Jackson, *Classical electrodynamics*, 4th ed. (Wiley, New York, 1999).
- [124] G. B. Rybicki and A. P. Lightman, *Radiative processes in astrophysics*, 3rd ed. (John Wiley & Sons, 1991).
- [125] L. Landau and E. Lifshitz, *The classical theory of fields*, 4th ed. (Butterworth-Heinemann, 1980).

-
- [126] A. Hofmann, in *Synchrotron acceleration and free electron lasers*, CERN Accelerator School (1989), pp. 115–141.
- [127] T. Erber, *Reviews of Modern Physics* **38**, 626 (1966).
- [128] V. I. Ritus, *Journal of Soviet Laser Research* **6**, 497 (1985).
- [129] J. G. Kirk, A. R. Bell, and I. Arka, *Plasma Physics and Controlled Fusion* **51**, 085008 (2009).
- [130] C. Ridgers, J. Kirk, R. Ducloux, T. Blackburn, C. Brady, K. Bennett, T. Arber, and A. Bell, *Journal of Computational Physics* **260**, 273 (2014).
- [131] D. A. Burton and A. Noble, *Contemporary Physics* **55**, 110 (2014).
- [132] P. A. M. Dirac, *Proceedings of the Royal Society of London. Series A. Mathematical and Physical Sciences* **167**, 148 (1938).
- [133] A. Di Piazza, C. Müller, K. Z. Hatsagortsyan, and C. H. Keitel, *Reviews of Modern Physics* **84**, 1177 (2012).
- [134] S. V. Bulanov, T. Z. Esirkepov, M. Kando, J. K. Koga, and S. S. Bulanov, *Physical Review E* **84**, 056605 (2011).
- [135] J. Schwinger, *Physical Review* **82**, 664 (1951).
- [136] H. Bethe, W. Heitler, and P. A. M. Dirac, *Proceedings of the Royal Society of London. Series A, Containing Papers of a Mathematical and Physical Character* **146**, 83 (1934).
- [137] K. Nakashima and H. Takabe, *Physics of Plasmas* **9**, 1505 (2002).
- [138] H. Chen, S. C. Wilks, J. D. Bonlie, S. N. Chen, K. V. Cone, L. N. Elberson, G. Gregori, D. D. Meyerhofer, J. Myatt, D. F. Price, M. B. Schneider, R. Shepherd, D. C. Stafford, R. Tommasini, R. Van Maren, and P. Beiersdorfer, *Physics of Plasmas* **16**, 122702 (2009).
- [139] G. Sarri, K. Poder, J. M. Cole, W. Schumaker, A. Di Piazza, B. Reville, T. Dzelzainis, D. Doria, L. A. Gizzi, G. Grittani, S. Kar, C. H. Keitel, K. Krushelnick, S. Kuschel, S. P. D. Mangles, Z. Najmudin, N. Shukla, L. O. Silva, D. Symes, A. G. R. Thomas, M. Vargas, J. Vieira, and M. Zepf, *Nature Communications* **6**, 6747 (2015).
- [140] E. P. Liang, S. C. Wilks, and M. Tabak, *Physical Review Letters* **81**, 4887 (1998).

-
- [141] A. R. Bell and J. G. Kirk, *Physical Review Letters* **101**, 200403 (2008).
- [142] B. Martinez, M. Lobet, R. Duclous, E. d’Humières, and L. Gremillet, *Physics of Plasmas* **26**, 103109 (2019).
- [143] G. Breit and J. A. Wheeler, *Physical Review* **46**, 1087 (1934).
- [144] C. P. Ridgers, C. S. Brady, R. Duclous, J. G. Kirk, K. Bennett, T. D. Arber, A. P. L. Robinson, and A. R. Bell, *Physical Review Letters* **108**, 165006 (2012).
- [145] D. L. Burke, R. C. Field, G. Horton-Smith, J. E. Spencer, D. Walz, S. C. Berridge, W. M. Bugg, K. Shmakov, A. W. Weidemann, C. Bula, K. T. McDonald, E. J. Prebys, C. Bamber, S. J. Boege, T. Koffas, T. Kotseroglou, A. C. Melissinos, D. D. Meyerhofer, D. A. Reis, and W. Ragg, *Physical Review Letters* **79**, 1626 (1997).
- [146] C. Bamber, S. J. Boege, T. Koffas, T. Kotseroglou, A. C. Melissinos, D. D. Meyerhofer, D. A. Reis, W. Ragg, C. Bula, K. T. McDonald, E. J. Prebys, D. L. Burke, R. C. Field, G. Horton-Smith, J. E. Spencer, D. Walz, S. C. Berridge, W. M. Bugg, K. Shmakov, and A. W. Weidemann, *Physical Review D* **60**, 092004 (1999).
- [147] P. Hadjisolomou, T. M. Jeong, and S. V. Bulanov, *Scientific Reports* **12**, 17143 (2022).
- [148] O. J. Pike, F. Mackenroth, E. G. Hill, and S. J. Rose, *Nature Photonics* **8**, 434 (2014).
- [149] B. Kettle, D. Hollatz, E. Gerstmayr, G. M. Samarin, A. Alejo, S. Astbury, C. Baird, S. Bohlen, M. Campbell, C. Colgan, D. Dannheim, C. Gregory, H. Harsh, P. Hatfield, J. Hinojosa, Y. Katzir, J. Morton, C. D. Murphy, A. Nurnberg, J. Osterhoff, G. Pérez-Callejo, K. Pöder, P. P. Rajeev, C. Roedel, F. Roeder, F. C. Salgado, G. Sarri, A. Seidel, S. Spannagel, C. Spindloe, S. Steinke, M. J. V. Streeter, A. G. R. Thomas, C. Underwood, R. Watt, M. Zepf, S. J. Rose, and S. P. D. Mangles, *New Journal of Physics* **23**, 115006 (2021).
- [150] X. Ribeyre, E. d’Humières, O. Jansen, S. Jequier, V. T. Tikhonchuk, and M. Lobet, *Physical Review E* **93**, 013201 (2016).
- [151] O. Jansen, T. Wang, D. J. Stark, E. d’Humières, T. Toncian, and A. V. Arefiev, *Plasma Physics and Controlled Fusion* **60**, 054006 (2018).

-
- [152] Y. He, T. G. Blackburn, T. Toncian, and A. V. Arefiev, *Communications Physics* **4**, 139 (2021).
- [153] Y. He, T. G. Blackburn, T. Toncian, and A. Arefiev, *Physics of Plasmas* **29**, 053105 (2022).
- [154] Y. He, I.-L. Yeh, T. G. Blackburn, and A. Arefiev, *New Journal of Physics* **23**, 115005 (2021).
- [155] C. S. Brady, C. P. Ridgers, T. D. Arber, A. R. Bell, and J. G. Kirk, *Physical Review Letters* **109**, 245006 (2012).
- [156] E. N. Nerush, I. Y. Kostyukov, A. M. Fedotov, N. B. Narozhny, N. V. Elkina, and H. Ruhl, *Physical Review Letters* **106**, 035001 (2011).
- [157] C. N. Danson, C. Haefner, J. Bromage, T. Butcher, J.-C. F. Chanteloup, E. A. Chowdhury, A. Galvanauskas, L. A. Gizzi, J. Hein, D. I. Hillier, N. W. Hopps, Y. Kato, E. A. Khazanov, R. Kodama, G. Korn, R. Li, Y. Li, J. Limpert, J. Ma, C. H. Nam, D. Neely, D. Papadopoulos, R. R. Penman, L. Qian, J. J. Rocca, A. A. Shaykin, C. W. Siders, C. Spindloe, S. Szatmári, R. M. G. M. Trines, J. Zhu, P. Zhu, and J. D. Zuegel, *High Power Laser Science and Engineering* **7**, e54 (2019).
- [158] C. Radier, O. Chalus, M. Charbonneau, S. Thambirajah, G. Deschamps, S. David, J. Barbe, E. Etter, G. Matras, S. Ricaud, V. Leroux, C. Richard, F. Lureau, A. Baleanu, R. Banici, A. Gradinariu, C. Caldararu, C. Capiteanu, A. Naziru, B. Diaconescu, V. Iancu, R. Dabu, D. Ursescu, I. Dancus, C. A. Ur, K. A. Tanaka, and N. V. Zamfir, *High Power Laser Science and Engineering* **10**, e21 (2022).
- [159] T. H. Maiman, *Nature* **187**, 493 (1960).
- [160] D. Strickland and G. Mourou, *Optics Communications* **55**, 447 (1985).
- [161] G. Mourou, *Reviews of Modern Physics* **91**, 030501 (2019).
- [162] H. Kiriya, Y. Miyasaka, A. Kon, M. Nishiuchi, A. Sagisaka, H. Sasao, A. S. Pirozhkov, Y. Fukuda, K. Ogura, K. Kondo, N. Nakanii, Y. Mashiba, N. P. Dover, L. Chang, M. Kando, S. Bock, T. Ziegler, T. Püschel, H.-P. Schlenvoigt, K. Zeil, and U. Schramm, *Photonics* **10**, 997 (2023).

- [163] C. Hooker, Y. Tang, O. Chekhlov, J. Collier, E. Divall, K. Ertel, S. Hawkes, B. Parry, and P. P. Rajeev, *Optics Express* **19**, 2193 (2011).
- [164] H. Daido, M. Nishiuchi, and A. S. Pirozhkov, *Reports on Progress in Physics* **75**, 056401 (2012).
- [165] P. McKenna, D. C. Carroll, O. Lundh, F. Nürnberg, K. Markey, S. Bandyopadhyay, D. Batani, R. G. Evans, R. Jafer, S. Kar, D. Neely, D. Pepler, M. N. Quinn, R. Redaelli, M. Roth, C.-G. Wahlström, X. H. Yuan, and M. Zepf, *Laser and Particle Beams* **26**, 591 (2008).
- [166] K. A. Ivanov, S. A. Shulyapov, P. A. Ksenofontov, I. N. Tsymbalov, R. V. Volkov, A. B. Savel'ev, A. V. Brantov, V. Y. Bychenkov, A. A. Turlin, A. M. Lapik, A. V. Rusakov, R. M. Djilkibaev, and V. G. Nedorezov, *Physics of Plasmas* **21**, 093110 (2014).
- [167] J. Fuchs, C. A. Cecchetti, M. Borghesi, T. Grismayer, E. d'Humières, P. Antici, S. Atzeni, P. Mora, A. Pipahl, L. Romagnani, A. Schiavi, Y. Sentoku, T. Toncian, P. Audebert, and O. Willi, *Physical Review Letters* **99**, 015002 (2007).
- [168] A. Higginson, R. Wilson, J. Goodman, M. King, R. J. Dance, N. M. H. Butler, C. D. Armstrong, M. Notley, D. C. Carroll, Y. Fang, X. H. Yuan, D. Neely, R. J. Gray, and P. McKenna, *Plasma Physics and Controlled Fusion* **63**, 114001 (2021).
- [169] D. Batani, R. Jafer, M. Veltcheva, R. Dezulian, O. Lundh, F. Lindau, A. Persson, K. Osvay, C.-G. Wahlström, D. C. Carroll, P. McKenna, A. Flacco, and V. Malka, *New Journal of Physics* **12**, 045018 (2010).
- [170] M. L. Zhou, J. H. Bin, D. Haffa, X. Q. Yan, and J. Schreiber, *Plasma Physics and Controlled Fusion* **59**, 055020 (2017).
- [171] M. Kaluza, J. Schreiber, M. I. K. Santala, G. D. Tsakiris, K. Eidmann, J. Meyer-ter-Vehn, and K. J. Witte, *Physical Review Letters* **93**, 045003 (2004).
- [172] N. P. Dover, T. Ziegler, S. Assenbaum, C. Bernert, S. Bock, F.-E. Brack, T. E. Cowan, E. J. Ditter, M. Garten, L. Gaus, I. Goethel, G. S. Hicks, H. Kiriya, T. Kluge, J. K. Koga, A. Kon, K. Kondo, S. Kraft, F. Kroll, H. F. Lowe, J. Metzkes-Ng, T. Miyatake, Z. Najmudin, T. Püschel, M. Rehwald, M. Reimold,

- H. Sakaki, H.-P. Schlenvoigt, K. Shiokawa, M. E. P. Umlandt, U. Schramm, K. Zeil, and M. Nishiuchi, *Light: Science & Applications* **12**, 71 (2023).
- [173] G. Cerullo and S. De Silvestri, *Review of Scientific Instruments* **74**, 1 (2003).
- [174] A. Dubietis, G. Jonušauskas, and A. Piskarskas, *Optics Communications* **88**, 437 (1992).
- [175] I. Ross, P. Matousek, M. Towrie, A. Langley, and J. Collier, *Optics Communications* **144**, 125 (1997).
- [176] S. Witte and K. S. E. Eikema, *IEEE Journal of Selected Topics in Quantum Electronics* **18**, 296 (2012).
- [177] A. Jullien, O. Albert, F. Burgy, G. Hamoniaux, J.-P. Rousseau, J.-P. Chambaret, F. Augé-Rochereau, G. Chériaux, J. Etchepare, N. Minkovski, and S. M. Saltiel, *Optics Letters* **30**, 920 (2005).
- [178] G. Doumy, F. Quéré, O. Gobert, M. Perdrix, P. Martin, P. Audebert, J. C. Gauthier, J.-P. Geindre, and T. Wittmann, *Physical Review E* **69**, 026402 (2004).
- [179] C. Thaury, F. Quéré, J.-P. Geindre, A. Levy, T. Ceccotti, P. Monot, M. Bougeard, F. Réau, P. d'Oliveira, P. Audebert, R. Marjoribanks, and P. Martin, *Nature Physics* **3**, 424 (2007).
- [180] H. Vincenti, S. Monchocé, S. Kahaly, G. Bonnaud, P. Martin, and F. Quéré, *Nature Communications* **5**, 3403 (2014).
- [181] A. Kon, M. Nishiuchi, Y. Fukuda, K. Kondo, K. Ogura, A. Sagisaka, Y. Miyasaka, N. P. Dover, M. Kando, A. S. Pirozhkov, I. Daito, L. Chang, I. W. Choi, C. H. Nam, T. Ziegler, H.-P. Schlenvoigt, K. Zeil, U. Schramm, and H. Kiriyama, *High Power Laser Science and Engineering* **10**, e25 (2022).
- [182] C. Riconda and S. Weber, *Matter and Radiation at Extremes* **8**, 023001 (2023).
- [183] P. L. Poole, A. Krygier, G. E. Cochran, P. S. Foster, G. G. Scott, L. A. Wilson, J. Bailey, N. Bourgeois, C. Hernandez-Gomez, D. Neely, P. P. Rajeev, R. R. Freeman, and D. W. Schumacher, *Scientific Reports* **6**, 32041 (2016).
- [184] L. Obst, J. Metzkes-Ng, S. Bock, G. E. Cochran, T. E. Cowan, T. Oksenhendler, P. L. Poole, I. Prencipe, M. Rehwald, C. Rödel, H.-P. Schlenvoigt, U. Schramm, D. W. Schumacher, T. Ziegler, and K. Zeil, *Plasma Physics and Controlled Fusion* **60**, 054007 (2018).

-
- [185] A. Kon, M. Nakatsutsumi, S. Buffechoux, Z. L. Chen, J. Fuchs, Z. Jin, and R. Kodama, *Journal of Physics: Conference Series* **244**, 032008 (2010).
- [186] R. Wilson, M. King, R. J. Gray, D. C. Carroll, R. J. Dance, C. Armstrong, S. J. Hawkes, R. J. Clarke, D. J. Robertson, D. Neely, and P. McKenna, *Physics of Plasmas* **23**, 033106 (2016).
- [187] D. Papadopoulos, J. Zou, C. Le Blanc, G. Chériaux, P. Georges, F. Druon, G. Mennerat, P. Ramirez, L. Martin, A. Fréneaux, A. Beluze, N. Lebas, P. Monot, F. Mathieu, and P. Audebert, *High Power Laser Science and Engineering* **4**, e34 (2016).
- [188] K. Burdonov, A. Fazzini, V. Lelasseux, J. Albrecht, P. Antici, Y. Ayoul, A. Beluze, D. Cavanna, T. Ceccotti, M. Chabanis, A. Chaleil, S. N. Chen, Z. Chen, F. Consoli, M. Cuciuc, X. Davoine, J. P. Delaneau, E. d’Humières, J.-L. Dubois, C. Evrard, E. Filippov, A. Freneaux, P. Forestier-Colleoni, L. Gremillet, V. Horny, L. Lancia, L. Lecherbourg, N. Lebas, A. Leblanc, W. Ma, L. Martin, F. Negoita, J.-L. Paillard, D. Papadopoulos, F. Perez, S. Pikuz, G. Qi, F. Quéré, L. Ranc, P.-A. Söderström, M. Scisciò, S. Sun, S. Vallières, P. Wang, W. Yao, F. Mathieu, P. Audebert, and J. Fuchs, *Matter and Radiation at Extremes* **6**, 064402 (2021).
- [189] S. Gales, K. A. Tanaka, D. L. Balabanski, F. Negoita, D. Stutman, O. Tesileanu, C. A. Ur, D. Ursescu, I. Andrei, S. Ataman, M. O. Cernaianu, L. D’Alessi, I. Dancus, B. Diaconescu, N. Djourellov, D. Filipescu, P. Ghenuche, D. G. Ghita, C. Matei, K. Seto, M. Zeng, and N. V. Zamfir, *Reports on Progress in Physics* **81**, 094301 (2018).
- [190] S. Weber, S. Bechet, S. Borneis, L. Brabec, M. Bučka, E. Chacon-Golcher, M. Ciappina, M. DeMarco, A. Fajstavr, K. Falk, E.-R. Garcia, J. Grosz, Y.-J. Gu, J.-C. Hernandez, M. Holec, P. Janečka, M. Jantač, M. Jirka, H. Kadlecova, D. Khikhlikha, O. Klimo, G. Korn, D. Kramer, D. Kumar, T. Lastovička, P. Lutoslawski, L. Morejon, V. Olšovcová, M. Rajdl, O. Renner, B. Rus, S. Singh, M. Šmid, M. Sokol, R. Versaci, R. Vrána, M. Vranic, J. Vyskočil, A. Wolf, and Q. Yu, *Matter and Radiation at Extremes* **2**, 149 (2017).

-
- [191] N. Jourdain, U. Chaulagain, M. Havlík, D. Kramer, D. Kumar, I. Majerová, V. T. Tikhonchuk, G. Korn, and S. Weber, *Matter and Radiation at Extremes* **6**, 015401 (2020).
- [192] S. Borneis, T. Laštovička, M. Sokol, T.-M. Jeong, F. Condamine, O. Renner, V. Tikhonchuk, H. Bohlin, A. Fajstavr, J.-C. Hernandez, N. Jourdain, D. Kumar, D. Modřanský, A. Pokorný, A. Wolf, S. Zhai, G. Korn, and S. Weber, *High Power Laser Science and Engineering* **9**, e30 (2021).
- [193] S. Kühn, M. Dumergue, S. Kahaly, S. Mondal, M. Füle, T. Csizmadia, B. Farkas, B. Major, Z. Várallyay, E. Cormier, M. Kalashnikov, F. Calegari, M. Devetta, F. Frassetto, E. Månsson, L. Poletto, S. Stagira, C. Vozzi, M. Nisoli, P. Rudawski, S. Maclot, F. Campi, H. Wikmark, C. L. Arnold, C. M. Heyl, P. Johnsson, A. L’Huillier, R. Lopez-Martens, S. Haessler, M. Bocoum, F. Boehle, A. Vernier, G. Iaquaniello, E. Skantzakis, N. Papadakis, C. Kalpouzos, P. Tzallas, F. Lépine, D. Charalambidis, K. Varjú, K. Osvay, and G. Sansone, *Journal of Physics B: Atomic, Molecular and Optical Physics* **50**, 132002 (2017).
- [194] Z. Gan, L. Yu, C. Wang, Y. Liu, Y. Xu, W. Li, S. Li, L. Yu, X. Wang, X. Liu, J. Chen, Y. Peng, L. Xu, B. Yao, X. Zhang, L. Chen, Y. Tang, X. Wang, D. Yin, X. Liang, Y. Leng, R. Li, and Z. Xu, “The shanghai superintense ultrafast laser facility (sulf) project”, in *Progress in ultrafast intense laser science xvi*, edited by K. Yamanouchi, K. Midorikawa, and L. Roso (Springer International Publishing, Cham, 2021), pp. 199–217.
- [195] X. Wang, X. Liu, X. Lu, J. Chen, Y. Long, W. Li, H. Chen, X. Chen, P. Bai, Y. Li, Y. Peng, Y. Liu, F. Wu, C. Wang, Z. Li, Y. Xu, X. Liang, Y. Leng, and R. Li, *Ultrafast Science*, 9894358 (2022).
- [196] H. Kolanoski and N. Wermes, *Particle Detectors: Fundamentals and Applications* (Oxford University Press, 2020).
- [197] D. S. Hey, M. H. Key, A. J. Mackinnon, A. G. MacPhee, P. K. Patel, R. R. Freeman, L. D. Van Woerkom, and C. M. Castaneda, *Review of Scientific Instruments* **79**, 053501 (2008).
- [198] T. Bonnet, M. Comet, D. Denis-Petit, F. Gobet, F. Hannachi, M. Tarisien, M. Versteegen, and M. M. Aleonard, *Review of Scientific Instruments* **84**, 013508 (2013).

-
- [199] P. Martin, H. Ahmed, D. Doria, A. Alejo, R. Clarke, S. Ferguson, J. Fernández-Tobias, R. R. Freeman, J. Fuchs, A. Green, J. S. Green, D. Gwynne, F. Hanton, J. Jarrett, D. Jung, K. F. Kakolee, A. G. Krygier, C. L. S. Lewis, A. McIlvenny, P. McKenna, J. T. Morrison, Z. Najmudin, K. Naughton, G. Nersisyan, P. Norreys, M. Notley, M. Roth, J. A. Ruiz, C. Scullion, M. Zepf, S. Zhai, M. Borghesi, and S. Kar, *Review of Scientific Instruments* **93**, 053303 (2022).
- [200] M. Roth, *Journal of Instrumentation* **6**, R09001 (2011).
- [201] P. Bolton, M. Borghesi, C. Brenner, D. Carroll, C. De Martinis, F. Fiorini, A. Flacco, V. Floquet, J. Fuchs, P. Gallegos, D. Giove, J. Green, S. Green, B. Jones, D. Kirby, P. McKenna, D. Neely, F. Nuesslin, R. Prasad, S. Reinhardt, M. Roth, U. Schramm, G. Scott, S. Ter-Avetisyan, M. Tolley, G. Turchetti, and J. Wilkens, *Physica Medica* **30**, 255 (2014).
- [202] N. Wermes, *Nuclear Instruments and Methods in Physics Research Section A: Accelerators, Spectrometers, Detectors and Associated Equipment* **512**, Proceedings of the 9th European Symposium on Semiconductor Detectors: New Developments on Radiation Detectors, 277 (2003).
- [203] M. Garcia-Sciveres and N. Wermes, *Reports on Progress in Physics* **81**, 066101 (2018).
- [204] K. T. Behm, J. M. Cole, A. S. Joglekar, E. Gerstmayr, J. C. Wood, C. D. Baird, T. G. Blackburn, M. Duff, C. Harvey, A. Ilderton, S. Kuschel, S. P. D. Mangles, M. Marklund, P. McKenna, C. D. Murphy, Z. Najmudin, K. Poder, C. P. Ridgers, G. Sarri, G. M. Samarin, D. Symes, J. Warwick, M. Zepf, K. Krushelnick, and A. G. R. Thomas, *Review of Scientific Instruments* **89**, 113303 (2018).
- [205] N. P. Dover, M. Nishiuchi, H. Sakaki, M. A. Alkhimova, A. Y. Faenov, Y. Fukuda, H. Kiriya, A. Kon, K. Kondo, K. Nishitani, K. Ogura, T. A. Pikuz, A. S. Pirozhkov, A. Sagisaka, M. Kando, and K. Kondo, *Review of Scientific Instruments* **88**, 073304 (2017).
- [206] D. A. Mariscal, B. Z. Djordjević, E. S. Grace, R. Hollinger, T. Ma, G. G. Scott, H. Song, R. A. Simpson, J. J. Rocca, and S. Wang, *Plasma Physics and Controlled Fusion* **63**, 114003 (2021).

-
- [207] D. A. Mariscal, B. Z. Djordjević, R. Anirudh, T. Bremer, P. C. Campbell, S. Feister, E. Folsom, E. S. Grace, R. Hollinger, S. A. Jacobs, B. Kailkhura, D. Kalantar, A. J. Kemp, J. Kim, E. Kur, S. Liu, J. Ludwig, J. Morrison, R. Nedbailo, N. Ose, J. Park, J. J. Rocca, G. G. Scott, R. A. Simpson, H. Song, B. Spears, B. Sullivan, K. K. Swanson, J. Thiagarajan, S. Wang, G. J. Williams, S. C. Wilks, M. Wyatt, B. Van Essen, R. Zacharias, G. Zeraouli, J. Zhang, and T. Ma, *Review of Scientific Instruments* **94**, 023507 (2023).
- [208] R. L. Workman et al. (Particle Data Group), *Progress of Theoretical and Experimental Physics* **2022**, 083C01 (2022).
- [209] A. Thomas, M. Tzoufras, A. Robinson, R. Kingham, C. Ridgers, M. Sherlock, and A. Bell, *Journal of Computational Physics* **231**, 1051 (2012).
- [210] C. K. Birdsall and A. B. Langdon, *Plasma physics via computer simulation* (CRC Press, 1991).
- [211] T. D. Arber, K. Bennett, C. S. Brady, A. Lawrence-Douglas, M. G. Ramsay, N. J. Sircombe, P. Gillies, R. G. Evans, H. Schmitz, A. R. Bell, and C. P. Ridgers, *Plasma Physics and Controlled Fusion* **57**, 113001 (2015).
- [212] J. Derouillat, A. Beck, F. Pérez, T. Vinci, M. Chieramello, A. Grassi, M. Flé, G. Bouchard, I. Plotnikov, N. Aunai, J. Dargent, C. Riconda, and M. Grech, *Computer Physics Communications* **222**, 351 (2018).
- [213] K. Yee, *IEEE Transactions on Antennas and Propagation* **14**, 302 (1966).
- [214] W. H. Furry, *Physical Review* **81**, 115 (1951).
- [215] J. K. Daugherty and A. K. Harding, *The Astrophysical Journal* **273**, 761 (1983).
- [216] A. Di Piazza, M. Tamburini, S. Meuren, and C. H. Keitel, *Physical Review A* **98**, 012134 (2018).
- [217] A. Ilderton, B. King, and D. Seipt, *Physical Review A* **99**, 042121 (2019).
- [218] A. Di Piazza, M. Tamburini, S. Meuren, and C. H. Keitel, *Physical Review A* **99**, 022125 (2019).
- [219] D. Del Sorbo, D. Seipt, T. G. Blackburn, A. G. R. Thomas, C. D. Murphy, J. G. Kirk, and C. P. Ridgers, *Physical Review A* **96**, 043407 (2017).
- [220] D. Seipt, D. Del Sorbo, C. P. Ridgers, and A. G. R. Thomas, *Physical Review A* **98**, 023417 (2018).

-
- [221] B. King and S. Tang, *Physical Review A* **102**, 022809 (2020).
- [222] D. Seipt and B. King, *Physical Review A* **102**, 052805 (2020).
- [223] D. Seipt, C. P. Ridgers, D. D. Sorbo, and A. G. R. Thomas, *New Journal of Physics* **23**, 053025 (2021).
- [224] A. Gonoskov, T. G. Blackburn, M. Marklund, and S. S. Bulanov, *Reviews of Modern Physics* **94**, 045001 (2022).
- [225] H.-H. Song, W.-M. Wang, Y.-F. Li, B.-J. Li, Y.-T. Li, Z.-M. Sheng, L.-M. Chen, and J. Zhang, *New Journal of Physics* **23**, 075005 (2021).
- [226] H.-H. Song, W.-M. Wang, and Y.-T. Li, *Physical Review Letters* **129**, 035001 (2022).
- [227] K. Xue, T. Sun, K.-J. Wei, Z.-P. Li, Q. Zhao, F. Wan, C. Lv, Y.-T. Zhao, Z.-F. Xu, and J.-X. Li, *Physical Review Letters* **131**, 175101 (2023).
- [228] A. Macchi, M. Borghesi, and M. Passoni, *Reviews of Modern Physics* **85**, 751 (2013).
- [229] B. Qiao, S. Kar, M. Geissler, P. Gibbon, M. Zepf, and M. Borghesi, *Physical Review Letters* **108**, 115002 (2012).
- [230] A. McIlvenny, H. Ahmed, C. Scullion, D. Doria, L. Romagnani, P. Martin, K. Naughton, A. Sgattoni, D. R. Symes, A. Macchi, P. McKenna, M. Zepf, S. Kar, and M. Borghesi, *Plasma Physics and Controlled Fusion* **62**, 054001 (2020).
- [231] V. A. Vshivkov, N. M. Naumova, F. Pegoraro, and S. V. Bulanov, *Physics of Plasmas* **5**, 2727 (1998).
- [232] S. Palaniyappan, B. M. Hegelich, H.-C. Wu, D. Jung, D. C. Gautier, L. Yin, B. J. Albright, R. P. Johnson, T. Shimada, S. Letzring, D. T. Offermann, J. Ren, C. Huang, R. Hörlein, B. Dromey, J. C. Fernandez, and R. C. Shah, *Nature Physics* **8**, 763 (2012).
- [233] M. J. Duff, R. Wilson, M. King, B. Gonzalez-Izquierdo, A. Higginson, S. D. R. Williamson, Z. E. Davidson, R. Capdessus, N. Booth, S. Hawkes, D. Neely, R. J. Gray, and P. McKenna, *Scientific Reports* **10**, 105 (2020).
- [234] L. Yi, *Physical Review Letters* **126**, 134801 (2021).

-
- [235] L. Willingale, S. R. Nagel, A. G. R. Thomas, C. Bellei, R. J. Clarke, A. E. Dangor, R. Heathcote, M. C. Kaluza, C. Kamperidis, S. Kneip, K. Krushelnick, N. Lopes, S. P. D. Mangles, W. Nazarov, P. M. Nilson, and Z. Najmudin, *Physical Review Letters* **102**, 125002 (2009).
- [236] L. Yin, B. J. Albright, K. J. Bowers, D. Jung, J. C. Fernández, and B. M. Hegelich, *Physical Review Letters* **107**, 045003 (2011).
- [237] D. Jung, B. J. Albright, L. Yin, D. C. Gautier, R. Shah, S. Palaniyappan, S. Letzring, B. Dromey, H.-C. Wu, T. Shimada, R. P. Johnson, M. Roth, J. C. Fernandez, D. Habs, and B. M. Hegelich, *New Journal of Physics* **15**, 123035 (2013).
- [238] P. L. Poole, L. Obst, G. E. Cochran, J. Metzkes, H.-P. Schlenvoigt, I. Prencipe, T. Kluge, T. Cowan, U. Schramm, D. W. Schumacher, and K. Zeil, *New Journal of Physics* **20**, 013019 (2018).
- [239] P. Zhang, C. P. Ridgers, and A. G. R. Thomas, *New Journal of Physics* **17**, 043051 (2015).
- [240] M. J. Duff, R. Capdessus, D. D. Sorbo, C. P. Ridgers, M. King, and P. McKenna, *Plasma Physics and Controlled Fusion* **60**, 064006 (2018).
- [241] M. Chen, A. Pukhov, T.-P. Yu, and Z.-M. Sheng, *Plasma Physics and Controlled Fusion* **53**, 014004 (2010).
- [242] M. Tamburini, F. Pegoraro, A. D. Piazza, C. H. Keitel, and A. Macchi, *New Journal of Physics* **12**, 123005 (2010).
- [243] M. Tamburini, F. Pegoraro, A. Di Piazza, C. Keitel, T. Liseykina, and A. Macchi, *Nuclear Instruments and Methods in Physics Research Section A: Accelerators, Spectrometers, Detectors and Associated Equipment* **653**, 181 (2011).
- [244] M. Tamburini, T. V. Liseykina, F. Pegoraro, and A. Macchi, *Physical Review E* **85**, 016407 (2012).
- [245] R. Capdessus and P. McKenna, *Physical Review E* **91**, 053105 (2015).
- [246] E. G. Gelfer, A. M. Fedotov, and S. Weber, *New Journal of Physics* **23**, 095002 (2021).

- [247] B. Rus, F. Batysta, J. Čáp, M. Divoký, M. Fibrich, M. Griffiths, R. Haley, T. Havlíček, M. Hlavác, J. Hřebíček, P. Homer, P. Hříbek, J. Jand'ourek, L. Juha, G. Korn, P. Korouš, M. Košelja, M. Kozlová, D. Kramer, M. Krůs, J. C. Lagron, J. Limpouch, L. MacFarlane, M. Malý, D. Margarone, P. Matlas, L. Mindl, J. Moravec, T. Mocek, J. Nejd, J. Novák, V. Olšovcová, M. Palatka, J. P. Perin, M. Pešlo, J. Polan, J. Prokūpek, J. Řídký, K. Rohlena, V. Růžička, M. Sawicka, L. Scholzová, D. Snopek, P. Strkula, and L. Švéda, in *Diode-pumped high energy and high power lasers; eli: ultrarelativistic laser-matter interactions and petawatt photonics; and hiper: the european pathway to laser energy*, Vol. 8080, edited by L. O. Silva, G. Korn, L. A. Gizzi, C. Edwards, and J. Hein (International Society for Optics and Photonics, 2011), p. 808010.
- [248] M. Nishiuchi, N. P. Dover, M. Hata, H. Sakaki, K. Kondo, H. F. Lowe, T. Miyahara, H. Kiriya, J. K. Koga, N. Iwata, M. A. Alkhimova, A. S. Pirozhkov, A. Y. Faenov, T. A. Pikuz, A. Sagisaka, Y. Watanabe, M. Kando, K. Kondo, E. J. Ditter, O. C. Ettlinger, G. S. Hicks, Z. Najmudin, T. Ziegler, K. Zeil, U. Schramm, and Y. Sentoku, *Physical Review Research* **2**, 033081 (2020).
- [249] S. D. R. Williamson, R. J. Gray, M. King, R. Wilson, R. J. Dance, C. Armstrong, D. R. Rusby, C. Brabetz, F. Wagner, B. Zielbauer, V. Bagnoud, D. Neely, and P. McKenna, *New Journal of Physics* **22**, 053044 (2020).
- [250] L. Willingale, A. V. Arefiev, G. J. Williams, H. Chen, F. Dollar, A. U. Hazi, A. Maksimchuk, M. J.-E. Manuel, E. Marley, W. Nazarov, T. Z. Zhao, and C. Zulek, *New Journal of Physics* **20**, 093024 (2018).
- [251] N. P. Dover, C. A. J. Palmer, M. J. V. Streeter, H. Ahmed, B. Albertazzi, M. Borghesi, D. C. Carroll, J. Fuchs, R. Heathcote, P. Hilz, K. F. Kakolee, S. Kar, R. Kodama, A. Kon, D. A. MacLellan, P. McKenna, S. R. Nagel, D. Neely, M. M. Notley, M. Nakatsutsumi, R. Prasad, G. Scott, M. Tampo, M. Zepf, J. Schreiber, and Z. Najmudin, *New Journal of Physics* **18**, 013038 (2016).
- [252] M. King, R. Gray, H. Powell, D. MacLellan, B. Gonzalez-Izquierdo, L. Stockhausen, G. Hicks, N. Dover, D. Rusby, D. Carroll, H. Padda, R. Torres, S. Kar, R. Clarke, I. Musgrave, Z. Najmudin, M. Borghesi, D. Neely, and P. McKenna, *Nuclear Instruments and Methods in Physics Research Section A: Accelerators*,

- Spectrometers, Detectors and Associated Equipment **829**, 2nd European Advanced Accelerator Concepts Workshop - EAAC 2015, 163 (2016).
- [253] J. C. Fernández, D. Cort Gautier, C. Huang, S. Palaniyappan, B. J. Albright, W. Bang, G. Dyer, A. Favalli, J. F. Hunter, J. Mendez, M. Roth, M. Swinhoe, P. A. Bradley, O. Deppert, M. Espy, K. Falk, N. Guler, C. Hamilton, B. M. Hegelich, D. Henzlova, K. D. Ianakiev, M. Iliev, R. P. Johnson, A. Kleinschmidt, A. S. Losko, E. McCary, M. Mocko, R. O. Nelson, R. Roycroft, M. A. Santiago Cordoba, V. A. Schanz, G. Schaumann, D. W. Schmidt, A. Sefkow, T. Shimada, T. N. Taddeucci, A. Tebartz, S. C. Vogel, E. Vold, G. A. Wurden, and L. Yin, *Physics of Plasmas* **24**, 056702 (2017).
- [254] M. King, R. Wilson, E. F. J. Bacon, E. J. Dolier, T. P. Frazer, J. Goodman, R. J. Gray, and P. McKenna, *The European Physical Journal A* **59**, 132 (2023).
- [255] A. McIlvenny, D. Doria, L. Romagnani, H. Ahmed, N. Booth, E. J. Ditter, O. C. Ettliger, G. S. Hicks, P. Martin, G. G. Scott, S. D. R. Williamson, A. Macchi, P. McKenna, Z. Najmudin, D. Neely, S. Kar, and M. Borghesi, *Physical Review Letters* **127**, 194801 (2021).
- [256] J. Hornung, Y. Zobus, S. Roeder, A. Kleinschmidt, D. Bertini, M. Zepf, and V. Bagnoud, *Nature Communications* **12**, 6999 (2021).
- [257] F. Sauter, *Zeitschrift für Physik* **69**, 742 (1931).
- [258] L. L. Ji, A. Pukhov, I. Y. Kostyukov, B. F. Shen, and K. Akli, *Physical Review Letters* **112**, 145003 (2014).
- [259] F. N. Beg, A. R. Bell, A. E. Dangor, C. N. Danson, A. P. Fews, M. E. Glinsky, B. A. Hammel, P. Lee, P. A. Norreys, and M. Tatarakis, *Physics of Plasmas* **4**, 447 (1997).
- [260] M. G. Haines, M. S. Wei, F. N. Beg, and R. B. Stephens, *Physical Review Letters* **102**, 045008 (2009).
- [261] L. L. Ji, A. Pukhov, E. N. Nerush, I. Y. Kostyukov, B. F. Shen, and K. U. Akli, *Physics of Plasmas* **21**, 023109 (2014).
- [262] M. J. V. Streeter, C. Colgan, C. C. Cobo, C. Arran, E. E. Los, R. Watt, N. Bourgeois, L. Calvin, J. Carderelli, N. Cavanagh, S. J. D. Dann, R. Fitzgarrald, E. Gerstmayr, A. S. Joglekar, B. Kettle, P. McKenna, C. D. Murphy, Z. Najmudin,

- P. Parsons, Q. Qian, P. P. Rajeev, C. P. Ridgers, D. R. Symes, A. G. R. Thomas, G. Sarri, and S. P. D. Mangles, *High Power Laser Science and Engineering* **11**, e9 (2023).
- [263] H. Schwoerer, P. Gibbon, S. Düsterer, R. Behrens, C. Ziener, C. Reich, and R. Sauerbrey, *Physical Review Letters* **86**, 2317 (2001).
- [264] C. D. Chen, A. J. Kemp, F. Pérez, A. Link, F. N. Beg, S. Chawla, M. H. Key, H. McLean, A. Morace, Y. Ping, A. Sorokovikova, R. B. Stephens, M. Streeter, B. Westover, and P. K. Patel, *Physics of Plasmas* **20**, 052703 (2013).
- [265] S. Singh, C. D. Armstrong, N. Kang, L. Ren, H. Liu, N. Hua, D. R. Rusby, O. Klimo, R. Versaci, Y. Zhang, M. Sun, B. Zhu, A. Lei, X. Ouyang, L. Lancia, A. L. Garcia, A. Wagner, T. Cowan, J. Zhu, T. Schlegel, S. Weber, P. McKenna, D. Neely, V. Tikhonchuk, and D. Kumar, *Plasma Physics and Controlled Fusion* **63**, 035004 (2021).
- [266] A. Rousse, P. Audebert, J. P. Geindre, F. Fallières, J. C. Gauthier, A. Mysyrowicz, G. Grillon, and A. Antonetti, *Physical Review E* **50**, 2200 (1994).
- [267] R. D. Edwards, M. A. Sinclair, T. J. Goldsack, K. Krushelnick, F. N. Beg, E. L. Clark, A. E. Dangor, Z. Najmudin, M. Tatarakis, B. Walton, M. Zepf, K. W. D. Ledingham, I. Spencer, P. A. Norreys, R. J. Clarke, R. Kodama, Y. Toyama, and M. Tampo, *Applied Physics Letters* **80**, 2129 (2002).
- [268] J. Galy, M. Maučec, D. J. Hamilton, R. Edwards, and J. Magill, *New Journal of Physics* **9**, 23 (2007).
- [269] C. M. Brenner, S. R. Mirfayzi, D. R. Rusby, C. Armstrong, A. Alejo, L. A. Wilson, R. Clarke, H. Ahmed, N. M. H. Butler, D. Haddock, A. Higginson, A. McClymont, C. Murphy, M. Notley, P. Oliver, R. Allott, C. Hernandez-Gomez, S. Kar, P. McKenna, and D. Neely, *Plasma Physics and Controlled Fusion* **58**, 014039 (2015).
- [270] K. W. D. Ledingham, I. Spencer, T. McCanny, R. P. Singhal, M. I. K. Santala, E. Clark, I. Watts, F. N. Beg, M. Zepf, K. Krushelnick, M. Tatarakis, A. E. Dangor, P. A. Norreys, R. Allott, D. Neely, R. J. Clarke, A. C. Machacek, J. S. Wark, A. J. Cresswell, D. C. W. Sanderson, and J. Magill, *Physical Review Letters* **84**, 899 (2000).

- [271] T. Cowan, M. Perry, M. Key, T. Ditmire, S. Hatchett, E. Henry, J. Moody, M. Moran, D. Pennington, T. Phillips, T. Sangster, J. Sefcik, M. Singh, R. Snively, M. Stoyer, S. Wilks, P. Young, Y. Takahashi, B. Dong, W. Fountain, T. Parnell, J. Johnson, A. Hunt, and T. Kühl, *Laser and Particle Beams* **17**, 773 (1999).
- [272] B. Shen and J. Meyer-ter-Vehn, *Physical Review E* **65**, 016405 (2001).
- [273] A. M. Fedotov, N. B. Narozhny, G. Mourou, and G. Korn, *Physical Review Letters* **105**, 080402 (2010).
- [274] J. M. Cole, K. T. Behm, E. Gerstmayr, T. G. Blackburn, J. C. Wood, C. D. Baird, M. J. Duff, C. Harvey, A. Ilderton, A. S. Joglekar, K. Krushelnick, S. Kuschel, M. Marklund, P. McKenna, C. D. Murphy, K. Poder, C. P. Ridgers, G. M. Samarin, G. Sarri, D. R. Symes, A. G. R. Thomas, J. Warwick, M. Zepf, Z. Najmudin, and S. P. D. Mangles, *Physical Review X* **8**, 011020 (2018).
- [275] K. Poder, M. Tamburini, G. Sarri, A. Di Piazza, S. Kuschel, C. D. Baird, K. Behm, S. Bohlen, J. M. Cole, D. J. Corvan, M. Duff, E. Gerstmayr, C. H. Keitel, K. Krushelnick, S. P. D. Mangles, P. McKenna, C. D. Murphy, Z. Najmudin, C. P. Ridgers, G. M. Samarin, D. R. Symes, A. G. R. Thomas, J. Warwick, and M. Zepf, *Physical Review X* **8**, 031004 (2018).
- [276] T. Nakamura, J. K. Koga, T. Z. Esirkepov, M. Kando, G. Korn, and S. V. Bulanov, *Physical Review Letters* **108**, 195001 (2012).
- [277] C. S. Brady, C. P. Ridgers, T. D. Arber, and A. R. Bell, *Physics of Plasmas* **21**, 033108 (2014).
- [278] P. Hadjisolomou, T. Jeong, P. Valenta, D. Kolenaty, R. Versaci, V. Olšovcová, C. Ridgers, and S. Bulanov, *Journal of Plasma Physics* **88**, 905880104 (2022).
- [279] X.-L. Zhu, T.-P. Yu, M. Chen, S.-M. Weng, and Z.-M. Sheng, *New Journal of Physics* **20**, 083013 (2018).
- [280] H.-Z. Li, T.-P. Yu, J.-J. Liu, Y. Yin, X.-L. Zhu, R. Capdessus, F. Pegoraro, Z.-M. Sheng, P. McKenna, and F.-Q. Shao, *Scientific Reports* **7**, 17312 (2017).
- [281] D. J. Stark, T. Toncian, and A. V. Arefiev, *Physical Review Letters* **116**, 185003 (2016).
- [282] T. Wang, X. Ribeyre, Z. Gong, O. Jansen, E. d’Humières, D. Stutman, T. Toncian, and A. Arefiev, *Physical Review Applied* **13**, 054024 (2020).

-
- [283] K. Xue, Z.-K. Dou, F. Wan, T.-P. Yu, W.-M. Wang, J.-R. Ren, Q. Zhao, Y.-T. Zhao, Z.-F. Xu, and J.-X. Li, *Matter and Radiation at Extremes* **5**, 054402 (2020).
- [284] S. Chintalwad, S. Krishnamurthy, B. Ramakrishna, and C. P. Ridgers, *Physical Review E* **105**, 025205 (2022).
- [285] P. Hadjisolomou, T. M. Jeong, P. Valenta, G. Korn, and S. V. Bulanov, *Physical Review E* **104**, 015203 (2021).
- [286] D. Serebryakov and E. Nerush, *Quantum Electronics* **46**, 299 (2016).
- [287] Y. Zhao, J. Liu, Y. Li, and G. Xia, *Plasma Physics and Controlled Fusion* **61**, 065010 (2019).
- [288] W. Luo, S.-D. Wu, W.-Y. Liu, Y.-Y. Ma, F.-Y. Li, T. Yuan, J.-Y. Yu, M. Chen, and Z.-M. Sheng, *Plasma Physics and Controlled Fusion* **60**, 095006 (2018).
- [289] R. Capdessus, M. King, D. Del Sorbo, M. Duff, C. P. Ridgers, and P. McKenna, *Scientific Reports* **8**, 9155 (2018).
- [290] Z. Gong, R. H. Hu, H. Y. Lu, J. Q. Yu, D. H. Wang, E. G. Fu, C. E. Chen, X. T. He, and X. Q. Yan, *Plasma Physics and Controlled Fusion* **60**, 044004 (2018).
- [291] Y.-J. Gu, O. Klimo, S. V. Bulanov, and S. Weber, *Communications Physics* **1**, 93 (2018).
- [292] T. W. Huang, C. M. Kim, C. T. Zhou, M. H. Cho, K. Nakajima, C. M. Ryu, S. C. Ruan, and C. H. Nam, *New Journal of Physics* **21**, 013008 (2019).
- [293] K. V. Lezhnin, P. V. Sasorov, G. Korn, and S. V. Bulanov, *Physics of Plasmas* **25**, 123105 (2018).
- [294] X.-B. Wang, G.-Y. Hu, Z.-M. Zhang, Y.-Q. Gu, B. Zhao, Y. Zuo, and J. Zheng, *High Power Laser Science and Engineering* **8**, e34 (2020).
- [295] B. Martinez, E. d’Humières, and L. Gremillet, *Plasma Physics and Controlled Fusion* **60**, 074009 (2018).
- [296] W.-M. Wang, Z.-M. Sheng, P. Gibbon, L.-M. Chen, Y.-T. Li, and J. Zhang, *Proceedings of the National Academy of Sciences* **115**, 9911 (2018).
- [297] D. A. Serebryakov, T. M. Volkova, E. N. Nerush, and I. Y. Kostyukov, *Plasma Physics and Controlled Fusion* **61**, 074007 (2019).

-
- [298] Y. Zhao, J. Liu, G. Xia, and A. Bonatto, *Physics of Plasmas* **27**, 073106 (2020).
- [299] L. Fedeli, A. Sainte-Marie, N. Zaim, M. Thévenet, J. L. Vay, A. Myers, F. Quéré, and H. Vincenti, *Physical Review Letters* **127**, 114801 (2021).
- [300] F. Wan, C. Lv, M. Jia, H. Sang, and B. Xie, *The European Physical Journal D* **71**, 236 (2017).
- [301] J. Vyskočil, O. Klimo, and S. Weber, *Plasma Physics and Controlled Fusion* **60**, 054013 (2018).
- [302] J. Vyskočil, E. Gelfer, and O. Klimo, *Plasma Physics and Controlled Fusion* **62**, 064002 (2020).
- [303] S. Morris, A. Robinson, and C. Ridgers, *Physics of Plasmas* **28**, 103304 (2021).
- [304] B. Martinez, E. d’Humières, and L. Gremillet, *Physical Review Research* **2**, 043341 (2020).
- [305] C. S. Brady, C. P. Ridgers, T. D. Arber, and A. R. Bell, *Plasma Physics and Controlled Fusion* **55**, 124016 (2013).
- [306] B. Shahriari, K. Swersky, Z. Wang, R. P. Adams, and N. de Freitas, *Proceedings of the IEEE* **104**, 148 (2016).
- [307] P. I. Frazier, “Bayesian optimization”, in *Recent advances in optimization and modeling of contemporary problems* (INFORMS, 2018), pp. 255–278.
- [308] S. Jalas, M. Kirchen, P. Messner, P. Winkler, L. Hübner, J. Dirkwinkel, M. Schnepf, R. Lehe, and A. R. Maier, *Physical Review Letters* **126**, 104801 (2021).
- [309] R. J. Shalloo, S. J. D. Dann, J.-N. Gruse, C. I. D. Underwood, A. F. Antoine, C. Arran, M. Backhouse, C. D. Baird, M. D. Balcazar, N. Bourgeois, J. A. Cardarelli, P. Hatfield, J. Kang, K. Krushelnick, S. P. D. Mangles, C. D. Murphy, N. Lu, J. Osterhoff, K. Pöder, P. P. Rajeev, C. P. Ridgers, S. Rozario, M. P. Selwood, A. J. Shahani, D. R. Symes, A. G. R. Thomas, C. Thornton, Z. Najmudin, and M. J. V. Streeter, *Nature Communications* **11**, 6355 (2020).
- [310] E. J. Dolier, M. King, R. Wilson, R. J. Gray, and P. McKenna, *New Journal of Physics* **24**, 073025 (2022).
- [311] A. Gonoskov, E. Wallin, A. Polovinkin, and I. Meyerov, *Scientific Reports* **9**, 7043 (2019).

-
- [312] B. Z. Djordjević, A. J. Kemp, J. Kim, R. A. Simpson, S. C. Wilks, T. Ma, and D. A. Mariscal, *Physics of Plasmas* **28**, 043105 (2021).
- [313] Z.-H. He, B. Hou, V. Lebailly, J. A. Nees, K. Krushelnick, and A. G. R. Thomas, *Nature Communications* **6**, 7156 (2015).
- [314] Z.-H. He, B. Hou, G. Gao, V. Lebailly, J. A. Nees, R. Clarke, K. Krushelnick, and A. G. R. Thomas, *Physics of Plasmas* **22**, 056704 (2015).
- [315] S. J. D. Dann, C. D. Baird, N. Bourgeois, O. Chekhlov, S. Eardley, C. D. Gregory, J.-N. Gruse, J. Hah, D. Hazra, S. J. Hawkes, C. J. Hooker, K. Krushelnick, S. P. D. Mangles, V. A. Marshall, C. D. Murphy, Z. Najmudin, J. A. Nees, J. Osterhoff, B. Parry, P. Pourmoussavi, S. V. Rahul, P. P. Rajeev, S. Rozario, J. D. E. Scott, R. A. Smith, E. Springate, Y. Tang, S. Tata, A. G. R. Thomas, C. Thornton, D. R. Symes, and M. J. V. Streeter, *Physical Review Accelerators and Beams* **22**, 041303 (2019).
- [316] J. R. Smith, C. Orban, J. T. Morrison, K. M. George, G. K. Ngirmang, E. A. Chowdhury, and W. M. Roquemore, *New Journal of Physics* **22**, 103067 (2020).
- [317] K. Deb, “Multi-objective optimization”, in *Search methodologies: introductory tutorials in optimization and decision support techniques* (Springer US, 2014), p. 403.
- [318] M. T. M. Emmerich and A. H. Deutz, *Natural Computing* **17**, 585 (2018).
- [319] R. Roussel, A. Hanuka, and A. Edelen, *Physical Review Accelerators and Beams* **24**, 062801 (2021).
- [320] F. Irshad, S. Karsch, and A. Döpp, *Physical Review Research* **5**, 013063 (2023).
- [321] D. Wu, X. T. He, W. Yu, and S. Fritzsche, *High Power Laser Science and Engineering* **6**, e50 (2018).
- [322] F. Pedregosa, G. Varoquaux, A. Gramfort, V. Michel, B. Thirion, O. Grisel, M. Blondel, P. Prettenhofer, R. Weiss, V. Dubourg, J. Vanderplas, A. Passos, D. Cournapeau, M. Brucher, M. Perrot, and É. Duchesnay, *Journal of Machine Learning Research* **12**, 2825 (2011).
- [323] M. Hoffman, E. Brochu, and N. de Freitas, in *Proceedings of the twenty-seventh conference on uncertainty in artificial intelligence*, UAI (2011), p. 327.

- [324] P. M. Nilson, J. R. Davies, W. Theobald, P. A. Jaanimagi, C. Mileham, R. K. Jungquist, C. Stoeckl, I. A. Begishev, A. A. Solodov, J. F. Myatt, J. D. Zuegel, T. C. Sangster, R. Betti, and D. D. Meyerhofer, *Physical Review Letters* **108**, 085002 (2012).
- [325] E. N. Nerush, I. Y. Kostyukov, L. Ji, and A. Pukhov, *Physics of Plasmas* **21**, 013109 (2014).
- [326] R. J. Mason and M. Tabak, *Physical Review Letters* **80**, 524 (1998).
- [327] B. Albertazzi, S. N. Chen, P. Antici, J. Böker, M. Borghesi, J. Breil, V. Dervieux, J. L. Feugeas, L. Lancia, M. Nakatsutsumi, P. Nicolaï, L. Romagnagni, R. Shepherd, Y. Sentoku, M. Starodubtsev, M. Swantusch, V. T. Tikhonchuk, O. Willi, E. d’Humières, H. Pépin, and J. Fuchs, *Physics of Plasmas* **22**, 123108 (2015).
- [328] L. G. Huang, H. Takabe, and T. E. Cowan, *High Power Laser Science and Engineering* **7**, e22 (2019).
- [329] Z. Gong, F. Mackenroth, T. Wang, X. Q. Yan, T. Toncian, and A. V. Arefiev, *Physical Review E* **102**, 013206 (2020).
- [330] H. G. Rinderknecht, T. Wang, A. L. Garcia, G. Bruhaug, M. S. Wei, H. J. Quevedo, T. Ditmire, J. Williams, A. Haid, D. Doria, K. M. Spohr, T. Toncian, and A. Arefiev, *New Journal of Physics* **23**, 095009 (2021).